A CFD INVESTIGATION OF WIND TUNNEL INTERFERENCE ON DELTA WING AERODYNAMICS

Mark Allan, M.Eng.

Thesis submitted to the Faculty of Engineering,
University of Glasgow, for the Degree of Doctor of Philosophy

University of Glasgow
Department of Aerospace Engineering

October 2002

Declaration

I hereby declare that this dissertation is a record of work carried out in the Department of Aerospace Engineering at the University of Glasgow during the period from October 1999 to October 2002. The dissertation is original in content except where otherwise indicated.

October 2002

.....

(Mark Allan)

Abstract

Wind tunnel interference effects on delta wing aerodynamics are the subject of this thesis. To assess tunnel effects a three-dimensional RANS flow solver developed at the University of Glasgow has been used. Delta wings have been the subject of much research in the last four decades due to their advantageous characteristics in both low and high speed flight. The aerodynamics at low speed are primarily determined by the presence of leading edge vortices and the phenomenon of vortex breakdown. Due to the sensitivity of leading edge vortices to external influences, the effect of wind tunnel constraints on the flowfield has been the subject of (limited) research. Wind tunnel interference effects have been explored experimentally by various researchers, and according to the literature, wind tunnels have been observed to both promote and delay vortex breakdown, thus highlighting the complexity of the problem.

To explore the influence of wind tunnel test facilities on delta wing aerodynamics, the interference has been separated into two distinct types, wall interference and support structure interference. The wall interference effects have been split into three further components, tunnel blockage, side wall interference, and roof and floor interference. Splitting the tunnel influence in this way allows us to determine the most detrimental interference effects, thus allowing the wind tunnel engineer to design experiments accordingly.

Euler and more realistic RANS simulations of tunnel interference have been conducted. To reduce the question of grid dependence when comparing solutions, a common "farfield grid" was created and tunnel grids were extracted. Before doing RANS simulations an analysis of various turbulence models was conducted. It was found that turbulence models have difficulty in predicting turbulence levels in leading edge vortices. As such modifications have been applied to the models which improve predictions. Despite vortex breakdown being widely regarded as an invis-

cid phenomenon, dependence on turbulence modelling has been exhibited. This is due to the vortex properties being altered with turbulent diffusion of vorticity when turbulence levels are too high. Both 1- and 2-equation models were assessed and it was concluded that a modified 2-equation k-ω model was the most suitable of the models available (when compared against experimental results), and was therefore used in all subsequent simulations.

From both Euler and RANS simulations it has been concluded that the effect of sidewall proximity significantly promotes vortex breakdown. Side wall induced velocity components increase the mean effective incidence of the wing, the helix angle and the strength of the vortices. The combination of these effects promotes vortex breakdown. Roof and floor proximity has little effect on vortex breakdown as does the frontal area blockage. Pitching simulations have shown that the promotion of vortex breakdown is not consistent on both the upstroke and downstroke. Breakdown was observed to be promoted furthest at the higher incidence of the upstroke and on the downstroke. This highlights the dependency of tunnel interference on vortex strength.

Support simulations of a centred "aerodynamic" cross-sectional support have shown that vortex breakdown is delayed due to blockage effects. With a combination of both tunnel walls and a downstream support structure, it was shown that vortex breakdown moves downstream with the presence of the support (for the two support sizes considered). Such sensitivity to external influences indicates that conventional corrections are likely to be unsuitable for this type of flow field. A fully validated method of predicting specific tunnel interference effects for individual tests is therefore desirable.

Acknowledgements

I would like to express my sincere thanks to my supervisor Dr. Ken Badcock. His continual assistance, encouragement and relentless enthusiasm over the past three years has been greatly appreciated. I would also like to thank the other members of the CFD group, in particular Dr. George Barakos, Prof. Bryan Richards, and Mr. Ryan Menzies for all their help. I would like to thank all the members of the WEAG THALES JP12.15 and AVT-080 Task Groups, for many enlightening and fruitful discussions, and in particular Major A. Mitchell, of the United States Airforce Academy, for kindly providing the experimental data for the ONERA 70^o delta wing.

Finally I would like to thank my family, in particular my parents Bruce and Jane, for their endless support and encouragement.

This work was supported by a DERA Bedford scholarship.

Contents

List of Figures

Nomenclature

c_r	Root chord
c_p	Pressure coefficient
C_L	Lift coefficient
C_Lp	Potential lift coefficient
C_Lv	Vortex lift coefficient
C_D	Drag coefficient
C_M	Pitching moment coefficient
e	Energy
E	Total energy
$E(\kappa)$	Energy spectral density
f	Dominant (buffet) frequency
f_0	Pitching frequency
$\mathbf{F}, \mathbf{G}, \mathbf{H}$	Flux vectors
h	Enthalpy
h_0	Stagnation enthalpy
H	Total enthalpy
$\mathbf{i}, \mathbf{j}, \mathbf{k}$	Cartesian unit vectors
k	Reduced pitching frequency ($= 2\pi f_0 c_r / U_\infty$),
	Kinetic energy of turbulent fluctuations per unit mass
$\mathbf{I}$	Identity matrix
J	Jacobian matrix of transformation
K_P	Constant in potential flow lift equation
K_V	Constant in vortex lift equation
l	Characteristic eddy size

m_0	Offset
m_i	Amplitude of harmonic i
M_∞	Local Mach number
M_∞	Freestream Mach number
$\mathbf{n}$	Unit normal to a streamline (natural coordinates)
p_i	Phase of harmonic i
P, P^*	Non-dimensional pressure, dimensional pressure
P_k	Production of turbulent kinetic energy
P_ω	Production of specific dissipation rate
P_r	Prandtl number
ρ	Density
q	Dynamic pressure
q	Heat flux component
r	Ratio of the magnitude of the rate of strain tensor and the magnitude of vorticity
R	Radius
$\mathbf{R}$	Vector of residuals
Re	Reynolds Number (based on root chord length)
Re_T	Turbulent Reynolds number (μ_T/μ)
S	Entropy
$\mathbf{s}$	Direction along streamline (natural coordinates)
t, t^*	Non-dimensional time, dimensional time
T	Temperature
u, v, w	Cartesian velocity components
U, V, W	Axial, circumferential, and radial velocity components
U_∞, U_{inf}	Freestream velocity
$\mathbf{W}$	Vector of independent flow variables
x, y, z	Cartesian coordinate system

Greek Symbols

$\alpha(t)$	Instantaneous angle of attack
α_m	Mean angle of attack

α_0	Amplitude of pitching oscillation
$\Delta\mathbf{W}$	Vector of conservative updates
ϵ	Dissipation per unit mass
η	Spanwise distance from centreline non-dimensionalised by local span, Kolmogorov length scale
γ	Ratio of specific heats
Γ	Circulation
κ	Wavenumber
Λ	Sweep angle
μ	Molecular viscosity
μ_T	Turbulent eddy viscosity
ω	Specific dissipation rate, magnitude of vorticity vector
ϕ	Helix angle
ρ	Density
τ	Pseudo time
θ	Direction of streamline
Θ	Conical parameter
ξ, η, ζ	Curvilinear coordinates

Subscripts

l	Quantity relating to left hand side of system
L	Characteristic length
r	Quantity relating to right hand side of system
v	Viscous value
2	Values at outer edge of vortex
ω	Dissipation
∞	Freestream value

Superscripts

m	Pseudo time index

n	Time index
u	Unmodified
$*$	Dimensional quantity
$\bar{}$	Time averaged component i.e. $\bar{\rho}$
$'$	Turbulent fluctuation component i.e. ρ'
$\hat{}$	Vector of variables in conservative form i.e. $\hat{\mathbf{F}}$

Acronyms

AVT	Air Vehicles Technology
$BART$	Basic Aerodynamics Research Tunnel - NASA Langley
CFL	Courant-Friedrichs-Levy
$DERA$	Defence Evaluation and Research Agency
DLR	Deutsche Forschungsanstalt für Luft- und Raumfahrt
DES	Detached Eddy Simulation
DNS	Direct Numerical Simulation
DNW	Duits-Nederlandse Wind tunnel
FAB	Frontal Area Blockage
GCG	Generalised Conjugate Gradient
LES	Large Eddy Simulation
$N-S$	Navier-Stokes
PMB	Parallel multi-block
$RANS$	Reynolds-Averaged Navier Stokes
RET	Turbulent Reynolds number (μ_T/μ)
RTO	Research and Technology Organisation
S/H	Model span-to-tunnel height
S/W	Model span-to-tunnel width
TPL	Total Pressure Loss
$WEAG$	Western European Armaments Group

Chapter 1

Introduction

1.1 Overview

The demand for greater agility has played a major role in the design of fighter aircraft. The ability to manoeuvre at high angles of attack and high rates has proven to be a great advantage. As a result current and future aircraft design trends include reducing angle of attack limitations in low speed flight. The use of highly swept, slender, sharp leading edge delta wings, or variations on this planform, are common among high performance aircraft.

One of the early major design considerations was the prevention of flow separation. However as aircraft increased in speed, and the need to avoid compressibility effects increased, the sweep angle of aircraft wings increased and the thickness of the wings decreased. This led to difficulties in preventing flow separation and delta wing aerodynamics began to be studied in detail. These swept wings have desirable low drag characteristics at high speed and good high angle of attack characteristics at low speed.

Delta wings can continue producing lift up to angles of incidence of 40^o (with sufficient sweep). High aspect ratio finite wings stall at much lower incidences (from the root first due to the spanwise downwash distribution which is highest at the tip), where the flow separates completely from the wing upper surface resulting in a loss of lift. However, on a delta wing the flow separates from the leading edge at low incidence, around 5^o or less, and the vorticity generated at the leading edge is

convected downstream by the streamwise velocity components. When the vorticity shed from the leading edge balances with the convected vorticity, the separation vortices become stationary and produce suction near the leading edge. Thus the separation (and resulting vortical structure) contributes to the lift.

Although both computational fluid dynamics (CFD) and wind tunnels are now used for aircraft development, continued advances in computer technology and algorithms are giving CFD an increasing share of the process. This is particularly true in the early design stages, when engineers are establishing key dimensions and other basic parameters of the aircraft. Trial and error dominate this process, and wind tunnel testing is very expensive, requiring designers to build and test each successive model. Because of the increased role of CFD, a typical design cycle now involves between two and four wind-tunnel tests of wing models instead of the 10 to 15 that were once the norm [1].

Another advantage of computer simulations is the ability to simulate more realistic flight conditions. Wind tunnel tests can be contaminated by the influence of the tunnel walls and the structure that holds the model in place. Some of the flight vehicles of the future will fly at many times the speed of sound and under conditions too extreme for wind-tunnel testing. For hypersonic aircraft (those that will fly at up to twenty times the speed of sound) and spacecraft that fly both within and at the outer regions of the atmosphere, computational fluid dynamics is the only viable tool for design.

Several times in the past it has been predicted that with sufficiently powerful computers, the wind tunnel will become obsolete, and with it, the need to correct tunnel data. However, most scientists and engineers working in the aircraft industry would agree that the challenge of understanding turbulence will guarantee wind tunnels a long life. Neither the wind tunnel nor CFD can be used on its own, only an intelligent combination of both will enable the aerodynamicist to create a successful new design.

The aim of this thesis is to identify the main causes of tunnel wall interference on the flowfield around delta wings. The available literature on wind tunnel tests of delta wing flows shows a wide scattering of data [2], which to some extent, may be explained by the facilities used in the tests. Relatively little research has been

conducted on the influence of test facilities on delta wing flowfields, especially with respect to manoeuvring wings.

Two test cases are examined in detail in this thesis. The first is that of a cropped 65^o delta wing inside three arbitrary tunnels of different cross section, designated square, 3x2, and 2x3. The 3x2 and 2x3 cases were chosen as they permit experimental validation by simply rotating the wing 90^o in a wind tunnel to change from the 3x2 tunnel to the 2x3 tunnel. Careful consideration of support interference is also required. Another advantage of the 3x2 and 2x3 tunnel choice is that blockage is similar (frontal area blockage is equal) in both tunnels. Thus an important variable can be removed from the analysis. This wing was tested undergoing pitching, rolling, and yawing motion allowing validation of dynamic simulations. The second test case is that of the ONERA 70^o wing. This wing was tested in the ONERA F2 tunnel in France (full details are given in section 4.2.1). For this test case there is extensive validation data, both flowfield and surface measurements. This case has been considered to improve confidence in the realism of the solutions.

1.2 The leading edge vortex

On sharp edged delta wings with sweep angles greater than about 45^o, and at moderate incidence (generally less than 5^o), leading edge vortices form. The approaching flow attaches initially to the upper surface and turns towards the leading edge. Since the flow cannot negotiate the sharp turn around the leading edge, it separates and forms a shear layer or vortex sheet. A spanwise pressure gradient on the upper surface causes the shear layer to move inward and roll up to form a concentrated vortex. Flow moving over the vortex is swept downwards and reattaches on the lower surface. As the flow passes around the primary vortex and flows back towards the leading edge, an adverse pressure gradient causes the reattached flow to separate forming a secondary counter-rotating vortex (it is also possible to have tertiary structures in the vortex). This structure is illustrated in detail in figure 1.1.

The formation of the secondary vortex (which is most evident at high incidence) moves the primary vortex core inwards and upwards above the surface of the wing. This shift is greater if the boundary layer on the upper surface is laminar since flow

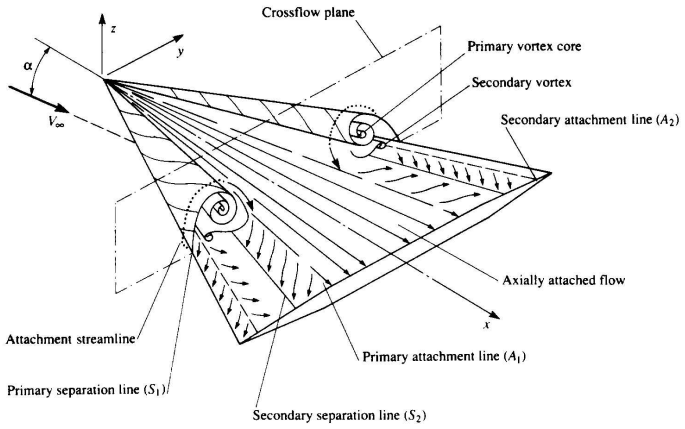

Figure 1.1: *Delta wing flowfield - by Stollery, J. (see [79] pp 360)*

separation is earlier and forms a larger secondary vortex. Reynolds number has little effect on the structure of the vortices on sharp leading edged delta wings [3]. For the case of a sharp edged delta wing at high incidence (with fully developed leading edge vortices) the flow pattern depends only weakly on Reynolds number. The secondary separation point is primarily dependent on whether the boundary layer is laminar or turbulent [4]. Hummel's experiments [4] showed for a 76^o delta wing that with laminar flow, secondary separation occurred at around 65% of the local semispan. With turbulent flow it was observed that secondary separation occurred at around 85% of the local semispan. A similar result is observed when transition occurs over the wing, i.e. the secondary separation line shifts towards the leading edge as transition to turbulent flow occurs. This can be seen clearly in the experiments of Mitchell [5](see figure 3.4, port half of the wing) at around $40\%c_r$. The secondary separation region is highlighted with red dye. Outboard of the secondary vortex core the flow reattaches and moves towards the leading edge, where it joins with the flow from the lower surface in the shear layer. Lowson [6] noted from published results that vortex locations from water tunnels are generally more inboard and off the wing when compared with wind tunnel tests, due to a large laminar secondary separation at low Reynolds number. He also noted that the effect of Reynolds number reduced with incidence which is consistent with smaller secondary separations at higher angles of incidence.

The leading edge vortices locally accelerate the flow. This causes a local suction

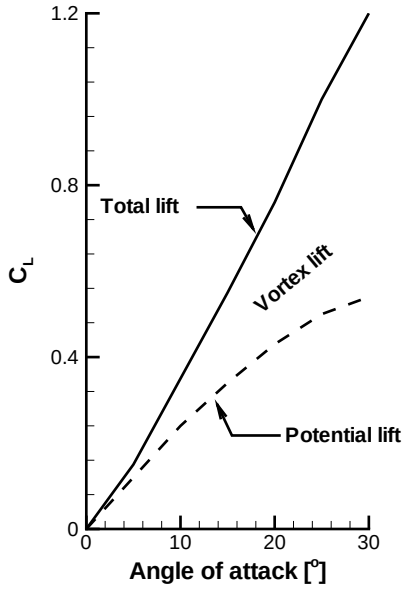

Figure 1.2: *Potential and vortex lift contributions for a 75^o delta wing - Polhamus [8]*

peak on the wing upper surface beneath the vortices. The location of the surface suction peaks more or less indicates the location of the primary leading edge vortices [7]. This results in an increase in lift - usually referred to as non-linear or vortex lift. Unsurprisingly, a large increase in induced drag also occurs. Polhamus [8] used a leading-edge suction analogy to develop analytical methods for predicting the low speed lift and drag-due-to-lift characteristics of sharp edged delta wings. Polhamus split total lift into two types, potential and vortex lift as shown in figure 1.2. From this diagram it is clear that the response and state of the vortices at high angles of attack are highly important, as any variation in vortex lift will heavily influence the forces and moments on the aircraft. The linear (C_{Lp}) and non-linear (C_{Lv}) increments were defined as

$$C_L = C_{Lp} + C_{Lv} = K_P sin(\alpha)cos^2(\alpha) + K_V sin^2(\alpha)cos(\alpha) \tag{1.1}$$

Here K_P is the normal force slope given by small disturbance potential flow lifting-surface theory, and K_V is determined by assuming that with reattached flow on

the upper surface, the normal force on the upper surface is the same as the suction obtained with attached flow around the leading edge (in the potential flow case).

It has been shown experimentally by Wentz and Kohlman [9] that as the sweep angle is increased, the strength of the leading edge vortices decreases (for a given incidence). Hemsch and Luckring [10] also showed analytically that the vortex strength (indicated by vortex circulation Γ) decreases with increasing leading edge sweep (Λ) via

$$\frac{\Gamma}{U_\infty} \sim l_{le} \frac{(tan\Lambda)^{0.2}}{\sqrt{1+tan^2\Lambda}} \tag{1.2}$$

where l_{le} is the length of the leading edge.

The size of the vortex core increases towards the trailing edge due to vorticity continually being fed from the leading edge. It has also been observed that the size of a vortex formed by roll up of a vortex sheet is independent of Reynolds number, although the radius of the viscous subcore decreases with increasing Reynolds number [11].

Wentz and Kohlman also showed that as flow incidence is increased, the strength (or circulation) of leading edge vortices increases. Visser and Nelson [12] measured the circulation and vorticity in the leading edge vortex of a 75^o delta wing. It was concluded that the flow upstream of vortex breakdown was near conical (in that properties remain constant along rays emanating from the apex) which was supported by the fact that spanwise vorticity and velocity distributions (pre-breakdown) scaled with the local geometry. The circulation was also found to grow linearly in the chordwise direction which indicated that the flow was conical. It was also concluded that since an increase in vortex strength is inevitably followed by breakdown, and that circulation grows despite vortex breakdown, it is not just the amount of circulation but the distribution of circulation associated with the axial vorticity which causes vortex breakdown. The circulation of delta wing vortices at incidence was also measured by Johari and Moreira [13] using a non-intrusive ultra-sound technique. The circulation over 60^o and 70^o wings was measured for various angles of incidence and at four chordwise stations. It was observed that at a given chordwise location circulation increased monotonically with incidence for both sweep angles up to a certain incidence, after which, the circulation remained constant or decreased. The

decreasing circulation was attributed to vortex sheet interaction. Circulation also increased linearly with chordwise location, and the rate of change of circulation with respect to incidence grew. The circulation was also found to increase irrespective of vortex breakdown occurring over the wing as the sum of the shed vorticity from the leading edge was unaltered. However Cornelius [14], using LDV measurements on a chined forebody fighter configuration, observed that positive circulation (obtained by integrating positive vorticity values) decreased after breakdown. This was due to a stonger turbulent mixing of positive (primary vortex) and negative (secondary vortex) regions of vorticity near the wing surface, reducing the amount of positive vorticity in the integration region. Honkan and Andreopoulous [15] measured the instantaneous three dimensional vorticity vectors over a 45^o delta wing using triple orthogonal hot-wire probes. Examining the mean vorticity and velocity levels it was found that the primary vortex was around three times as strong as the secondary. It was also observed that turbulent fluctuations, especially in the core, were small.

Axial velocities within a vortex core can reach up to three times freestream values. A qualitative explanation for this was given by Erickson [16] using a spiral sheet model of the vortex. The inclination of the spiralling vortex lines towards the vortex axis induces an additional downstream component of velocity along the vortex core. Profiles of velocity along a cross-section of the leading edge vortex can be found in (among others) references [17] and [5].

A study by Earnshaw [18] determined that leading edge vortices can be divided into three regions,

- The shear layer or vortex sheet which starts at the leading edge and feeds vorticity into the vortex core. The thickness of this shear layer increases with distance from the leading edge.

- The rotational core which is around 30% of the local semispan in diameter. The vorticity within the rotational core is assumed to be distributed continuously.

- The viscous subcore which is around 5% of the local semispan diameter. Within this region gradients of stagnation pressure, static pressure and velocity are very high. It is usually associated with the region where the swirl

velocity becomes zero at the vortex axis. Within the subcore (which rotates as a solid body) axial velocities can exceed three times that of the freestream velocity.

An interesting and informative theory for a leading edge vortex was presented by Hall [19]. Hall split the leading edge vortex into regions (as suggested by Earnshaw). Neglecting the shear layer (which is observed to diffuse rapidly and disappear after one revolution) the vortex was considered to consist of a continuous, inviscid, rotational, conical, and incompressible outer part, with a slender viscous subcore inner region where viscous diffusion is confined. This permitted both inner and outer solutions to be obtained. Considering only the outer region, by applying the axi-symmetric Navier-Stokes equations for a steady, incompressible, conical, inviscid flow, equations were derived for the axial, radial, and circumferential velocity components, as well as the pressure distribution through the vortex. For the outer flow solution the following four equations were derived for the velocity components and pressure distributions,

$$\frac{U}{U_2} = 1 - \left\{ \sqrt{(1+2\phi_2^2)} - 1 \right\} log\left(\frac{\Theta}{\Theta_2}\right) \tag{1.3}$$

$$\left(\frac{V}{V_2}\right)^2 = 1 - \left[\frac{\sqrt{(1+2\phi_2^2)}}{\phi_2}\right]^2 log\left(\frac{\Theta}{\Theta_2}\right) \tag{1.4}$$

$$\frac{W}{W_2} = \frac{\Theta}{\Theta_2} = \frac{R}{R_2} \tag{1.5}$$

$$\frac{P - P_2}{\rho V_2^2} = log\left(\frac{\Theta}{\Theta_2}\right) - \frac{1}{2}\left[\frac{\sqrt{(1+2\phi_2^2)}}{\phi_2}\right]^2 log^2\left(\frac{\Theta}{\Theta_2}\right) \tag{1.6}$$

where the subscript 2 represents values at the outer edge of the vortex. The upper-case lettering implies velocity components from the outer solution. The boundary conditions were taken to be

$$\Theta = 0, W = 0 \tag{1.7}$$

$$\Theta = \Theta_2, U = U_2, V = V_2, P = P_2 \tag{1.8}$$

Since the flow is conical the flow variables U (the axial component of velocity), V (the circumferential component of velocity), W (the radial component of velocity),

and P are functions of the conical parameter Θ (=R/x) only. It should be noted that the outer solution extends to the subcore, but in the subcore region the outer solution fails and is therefore switched to the inner solution. Clearly the radial component of velocity decreases linearly with decreasing distance from the vortex axis, and the axial and circumferential components increase. A final noteworthy point is that Hall's theory predicts that an increase in the helix angle (ϕ_2) increases the axial and circumferential velocity components, and increases the suction in the vortex core. An explanation for this (given by Hall) is that there is a focussing action of the spiralling streamlines which yields a high resultant velocity along the vortex axis.

Flow visualisation studies have indicated that the leading edge vortex changes location depending on incidence. For steady cases as the incidence of the wing is increased, the position of the primary vortex core was found to move inboard [20][21]. Green [22] found that the position of the vortex also varied along the chord. As a wing is pitched up the vortex core moves inboard, however, when breakdown nears a given chordwise station the primary vortex core is observed to move outboard. The vortex core is also found to move higher above the wing surface with increasing incidence. As the trailing edge is approached, the vortex core bends away from the wing surface towards the direction of the freestream.

Several investigations have observed the presence of streamwise structures in the shear layer [23][24][25][6][15][5]. Some investigations have suggested that these sub-structures rotate with the leading edge vortices [23][25], and some suggest the structures are spatially-fixed [24][6][15][5]. Although not universally accepted, the most popular explanation for these sub-structures is the well known Kelvin-Helmholtz instability, where between two parallel streams of different velocity, perturbations grow exponentially with downstream distance and are observed to roll up into discrete vortices, regardless of Reynolds number [25]. Other possible explanations are an interaction between the secondary vortical regions and the shear layer, or an instability due to curvature of the shear layer. Structures in the shear layer were also revealed in CFD simulations [26][27][28]. Vortical sub-structures were observed that rotate in the same sense as the primary vortex, which were identical to those observed in experiment [5]. These substructures were observed in both the pre- and

post-breakdown regions.

1.3 Vortex Breakdown

As the incidence of a delta wing increases the strength of the leading edge vortex increases. At some point along the vortex core an abrupt change occurs where the flow stagnates, and the vortex breaks down into full scale turbulence. This phenomenon is known as vortex breakdown. The earliest identification of this phenomenon is attributed to several researchers [29][30]. Peckham [31] and Elle [32] observed that the position of vortex breakdown is heavily dependent on both the incidence and sweep angles of the wing. As the angle of sweep increases the breakdown moves further downstream, and as the angle of attack of the wing increases the position of vortex breakdown moves towards the wing apex. This phenomenon and the detrimental effect on aircraft performance has been researched over the past four decades. A review of some of the most important features of vortex breakdown is now given.

Lambourne and Bryer [33] studied the phenomenon of vortex breakdown in detail and noted two distinct types can occur - the spiral (figure 1.3) and bubble (figure1.4) breakdown. A photograph from these experiments is shown in figure 1.5 and the two types are clearly visible. A more detailed view of the structure of the spiral breakdown is shown in figure 1.6.

The bubble breakdown is characterised by a stagnation point along the vortex axis followed by an oval separation region (as depicted in figure 1.4). The flow passes smoothly over the near-symmetric upstream half of the separation bubble, however the downstream half of the bubble is open and irregular, with the flow shedding as if from a bluff body. It was observed that the bubble is usually two or three core diameters in length. Downstream of the breakdown the vortex is turbulent and diffuses rapidly with increasing distance from the breakdown location. The flow downstream of the breakdown is still highly rotational. The spiral breakdown is characterised by a sudden deceleration of the fluid moving along the axis of the vortex, which is followed by a sudden kink where the vortex core is deflected into a spiral configuration (figures 1.3 and 1.6). This spiral persists for a few turns performing a whirling motion about the central axis. The vortex then breaks up

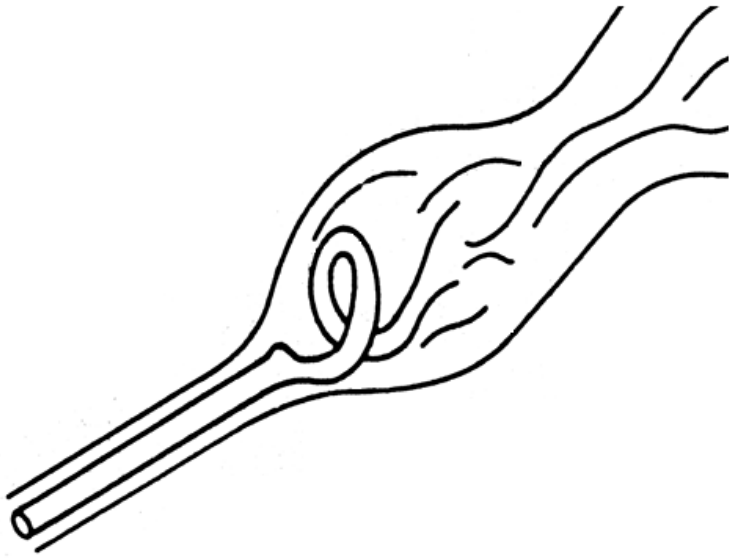

Figure 1.3: *Structure of spiral breakdown (adapted from [17])*

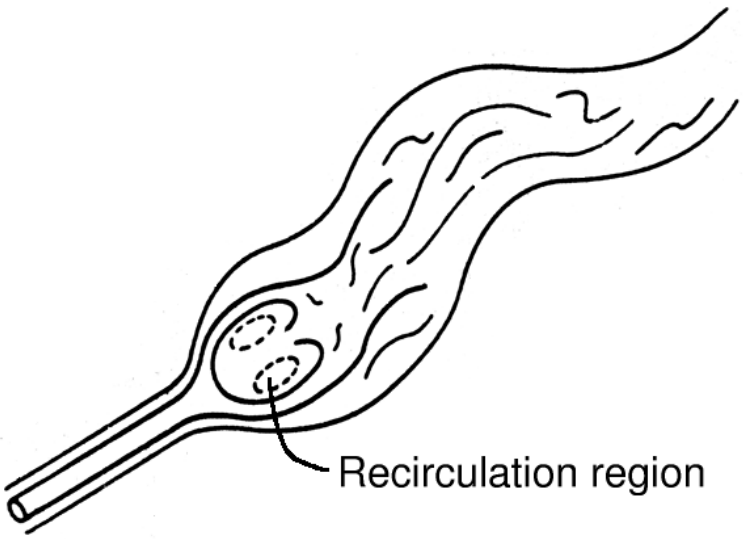

Figure 1.4: *Structure of bubble breakdown (adapted from [17])*

into full scale turbulence. The flow within the spiralling core continues to rotate in the sense of the vortex prior to breakdown, however the sense of the spiral was found to be the opposite of the vortex core. The expansion ratio (the ratio of the wake core diameter to approach flow diameter) of the spiral breakdown is found to be considerably less than the expansion ratio of the bubble breakdown [11]. Sarpkaya [34] observed that increasing the helix angle of a vortex (in a tube) switched the

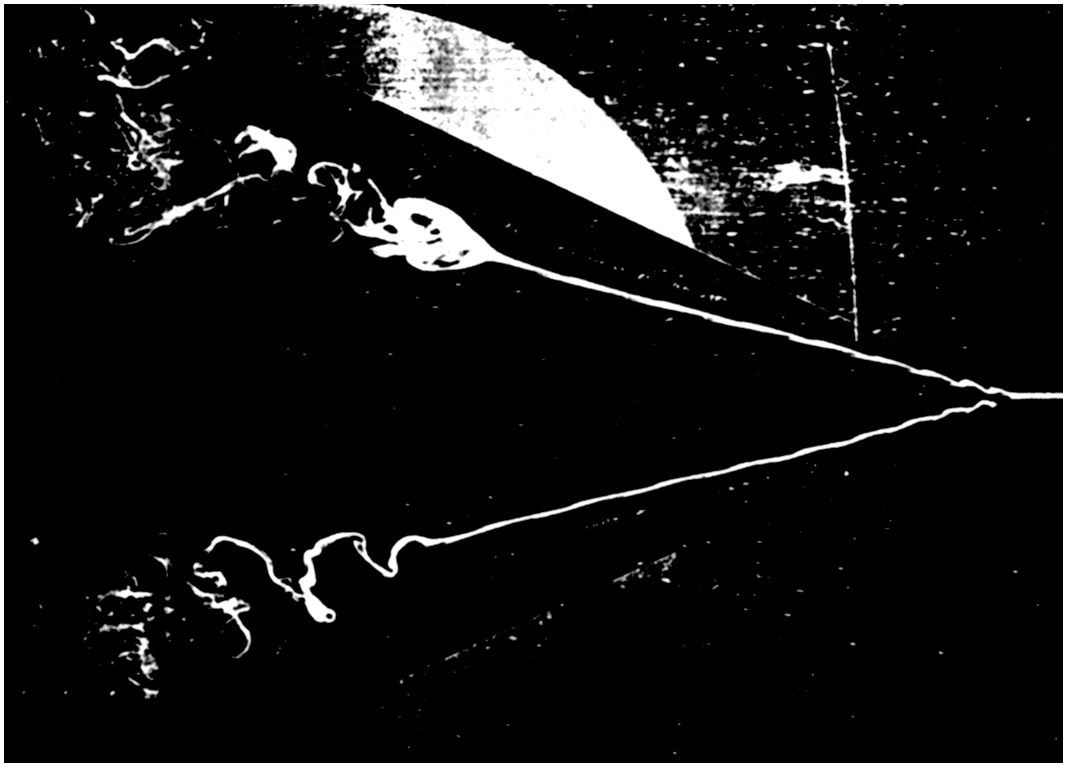

Figure 1.5: *Bubble (upper) and Spiral (lower) breakdowns - Lambourne and Bryer [33]*

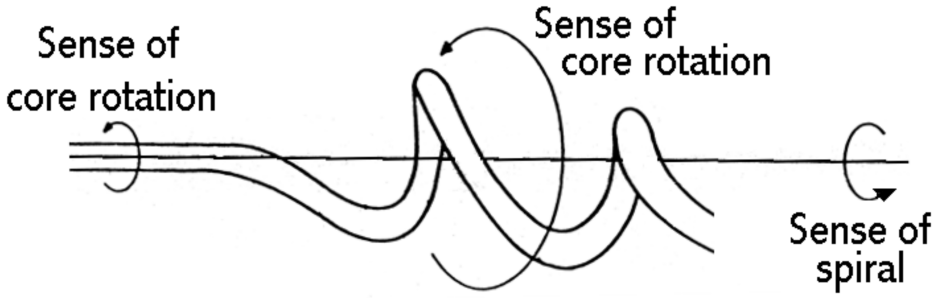

Figure 1.6: *Detailed structure of spiral breakdown (adapted from [17])*

breakdown type from the spiral to bubble type. Increasing the helix angle was also found to move the breakdown location upstream. As described by Leibovich [11], the spiral burst appears to be the most common form of breakdown above delta wings. Since in tubes this is the low swirl form of breakdown, this may imply that the swirl angle under conditions of aerodynamic interest is sufficiently low to prevent a bubble breakdown. Following the observation that increasing swirl angle promotes

vortex breakdown, as incidence is increased and the helix angle tightens, a leading edge vortex breakdown moves upstream as does its tube counterpart.

A flow visualisation and seven-hole probe survey of the leading edge vortices for 70^o to 85^o delta wings was conducted by Payne et al. [35]. The wings were tested at 10^o, 20^o, 30^o, and 40^o angle of attack at a Reynolds number of 85 thousand. It was observed that at high angles of incidence both the spiral and bubble types of breakdown occur and that these appear to be the extremes in a continuum of possible breakdown states. Intermediate forms were observed which exhibited characteristics of both spiral and bubble breakdown. The seven-hole probe surveys showed that leading edge vortices grow in size and strength with increasing angle of attack until breakdown occurs.

Steady flow water tunnel visualisation experiments were conducted by Lowson [36] on an 80^o delta wing. The presence of a static hysteresis was observed. As the wing was pitched up slowly (quasi-steady flow), breakdown passed the trailing edge at around 41^o. Once past the trailing edge breakdown moved quickly towards the apex settling at around $37.5\%c_r$, with an oscillation amplitude of around $10\%c_r$. After pitching up a little further and then pitching down, vortex breakdown remained over the wing moving slowly towards the trailing edge, which it passed at around 34^o angle of attack. This effect was observed at a range of flow velocities. A similar observation was made in the experiments of LeMay et al [37] using a 70^o delta wing, however the hysteresis effect was only noticeable as the breakdown approached the trailing edge. A static hysteresis was also observed by Thompson et al. [38] and in the computations of Visbal [39] for sweep angles as low as 65^o. A further observation by Lowson was the presence of a "yaw hysteresis". The breakdown on one half of the wing tended to lead the other (though which side changed randomly between tests). Once one side started to lead the other, past 40^o incidence the leading side tended to be closer to the apex during all of the pitch down. It should be noted that with sweep angles as large as 80^o there is likely to be considerable interaction between the two leading edge vortex sheets.

Factors found to vary the position of vortex breakdown are [33]

- Incidence - As incidence is increased the position of breakdown moves towards

the apex of the wing.

- Aspect Ratio - Since varying aspect ratio is similar to varying the sweep angle, as aspect ratio decreases breakdown moves downstream and vice versa. This holds for delta wings with sweep angles less than around 75^o [9].

- Acceleration - The position of breakdown varies with acceleration of the freestream flow. It was found that an increase in freestream velocity causes the position of breakdown to move upstream where it remains while the flow is accelerating. When the flow reaches its new velocity, the position of breakdown returns to its original position. Similarly breakdown moves downstream when the flow decelerates. An explanation of this is that at a point A upstream of a point B, the flow will be faster than that at B and thus will be at a lower static pressure. This forms an adverse pressure gradient which shifts the breakdown upstream (vice versa for decelerating flow). When the flow stops accelerating, A and B will have the same velocity (and hence pressure), thus eliminating the pressure gradient and allowing the breakdown to return to the original position.

- Flaps - The deflection of a flap downwards was found to have the effect of shifting the position of breakdown downstream and vice versa. This is due to a change in the chordwise pressure gradient caused by the flap deflection. A similar effect is observed when the wing is cambered.

Factors which do not vary the position of vortex breakdown are [33]

- Reynolds Number - In the range of $1 \times 10^4 \leq Re \leq 4.6 \times 10^6$, the influence of Reynolds number on the breakdown position was found to be small for wings with sharp leading edges. This suggests that laminar to turbulent transition is not a factor in vortex breakdown.

- Shear Layer modifications - Distortions to the shear layer were made by introducing wires, spoilers etc. near the leading edge. These were found to have no effect on the breakdown position. Similarly disruptions to the flow entering the vortex core (by the addition of a spoiler upstream of the wing) were made, and were found to have no significant effect on the breakdown position.

- Cropping - It was found by Wentz [40] that the removal of the wing tip had no significant effect on the position of breakdown.

- Trailing edge - It was also found by Wentz that the geometry of the trailing edge had no significant effect on breakdown.

The location of vortex breakdown has been found to fluctuate significantly in a number of investigations [36][41]. At low Reynolds numbers it was observed that the extent of the fluctuations is dependent on freestream velocity, with fluctuations increasing with decreasing freestream velocity [24]. Determining the position of breakdown is problematic as flow visualisation based methods are subjective and may account for some of the scatter of breakdown location in the literature (see for example figure 1.7). Also rarely is the method used to obtain the breakdown location given (for example the definition of the breakdown location or any associated unsteadiness). As described by O'Neil et al. [42], methods which rely on some gross characteristic of the bursting vortex (for example a substantial expansion of the vortex downstream of burst), tend to predict a more downstream burst location than using for example the occurance of core unsteadiness as the breakdown location. An interesting point from the results obtained by O'Neil et al. is the difficulty in locating breakdown locations on the aft portion of their 70^o wing. Figure 1.7 shows the breakdown location trajectory of 70^o delta wings as they are pitched up. Clearly around 30^o there are large discrepancies in breakdown locations. This may be attributed in part to the gradient of the curve at the lower incidences. In an incidence window of around 3-4 degrees, the breakdown moves from the trailing edge to the midchord. Such a low incidence window will make it hard to determine breakdown locations accurately.

A number of criteria for locating vortex breakdown have been suggested. Gursul [43] evaluated previously proposed parameters suggested to correlate with breakdown location. The aim was that if breakdown is plotted against these parameters, the breakdown locations should collapse onto a single curve. It was concluded that from the previous published criteria, the angle γ (the angle between the freestream and the leading edge) provided the best correlation with breakdown, although the correlation became worse close to the apex. The parameter $\Gamma/U_\infty x$ was also pro-

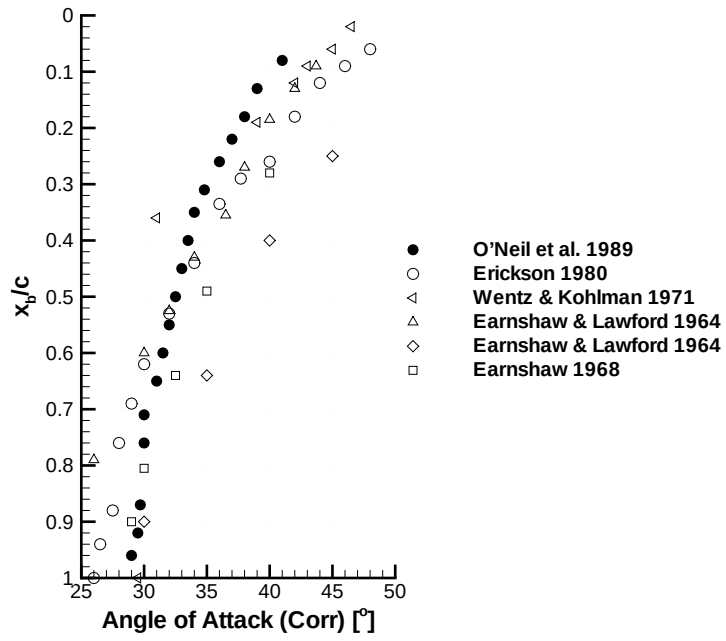

Figure 1.7: *Vortex burst locations : 70^o delta wings - Data taken from O'Neil et al. [42]*

posed by Gursul. This parameter provided good correlation along the entire length of the chord. Greenwell and Wood [44] suggested using surface pressure measurements to find the location of vortex breakdown. They noted that when vortex breakdown occurred there was a marked increase in the half width of the suction peak on the wing surface. Thus, by measuring the surface pressures, vortex breakdown location could be obtained. Robinson et al. [45] suggested using the Rossby number (the ratio of axial and circumferential momentum in a vortex). Where the Rossby number falls can be taken as the breakdown location. The critical Rossby number suggested by Euler and Navier-Stokes simulations was in the range of 0.9 to 1.4.

A number of theories for vortex breakdown have been given, though none have been universally accepted. Reviews have been made on vortex breakdown by Hall [46], Leibovich [11], Escudier [47], and Delery [48]. These reviews tend to concentrate on breakdown in tubes. In the early review by Hall (1972) the following conditions were specified for vortex breakdown - a maximum value of swirl (helix angle) of greater than 40^o upstream of breakdown (more recently Hawk et al. [49] indicated a

swirl angle of greater than 45^o for breakdown to occur), an adverse pressure gradient along the vortex core, and a divergence of stream tubes from the core. If the adverse pressure gradient or degree of divergence increases, a lower angle of swirl is required for breakdown.

In order to predict vortex breakdown, the analogy of breakdown as a failure of the quasi-cylindrical equations of motion (much like boundary layer separation is a failure of the boundary layer approximations) has been used [50]. The development of the flow can be calculated using the quasi-cylindrical equations of motion if the flow is assumed steady, laminar, incompressible and axi-symmetric. The idea of the analogy is that if the computed vortical flow exhibits appreciable axial gradients at some location, for example as a stagnation point is reached (which means the quasi-cylindrical approximation must fail there), then in the real case vortex breakdown will occur. Hall [46] also described a mechanism by which the axial gradients could be produced. It was shown that the pressure gradient along the vortex core consists of both the imposed external pressure gradient plus a swirl component (which increases with vortex strength). Thus it was demonstrated that a small change in pressure gradient at the edge of the vortex will result in much larger pressure gradients within the vortex core. Sarpkaya [51] later confirmed the strong influence of external pressure gradients on vortex breakdown in his vortex tube experiments. The best that can be hoped for in such simulations is a complete failure of the numerical calculation indicating a dramatic change in the structure of the flow. As commented by Escudier [47] it is clearly unsatisfactory to associate a physical phenomenon with the failure of a numerical computation.

Vortex breakdown has also been attributed to a hydrodynamic instability. In this theory it is proposed that breakdown is caused by spiral instabilities. A criterion for the flow to be unstable to spiral disturbances was given by Ludweig [52]. Providing the flow is unstable to spiral disturbances, it was suggested that after the onset of the instability, with suitable conditions, the disturbances will grow, retarding the core flow and cause a stagnation to occur. As commented by Hall [51], a major weakness of this theory is that it does not account for axi-symmetric breakdowns such as bubble breakdowns.

Another description of vortex breakdown given is that of a wave propagation

phenomenon. Several researchers have worked on this theory including [53][54][55]. For a full description see the review by Leibovich [11]. This theory was used by Gursul [56] to explain the time lag phenomenon of vortex breakdown associated with the unsteady motions of delta wings. Vortex breakdown can be estimated as the location at which critical conditions occur [11]. The flow is considered subcritical if waves can propagate upstream [54]. Thus any downstream disturbances, such as due to a trailing edge, will propagate upstream until the critical point is reached where breakdown can be assumed to occur.

A recent explanation is given in Brown and Lopez [57]. Brown and Lopez hypothesised that the physical mechanism of vortex breakdown is the production of negative azimuthal vorticity (which is required to stagnate the core flow). It was further hypothesised that a diffusion of vorticity in the core (where upstream of vortex breakdown vorticity tends to be confined) would lead to a radial redistribution of circulation, which in turn would increase the local tangential velocity component with radial distance, and therefore stretch or tilt the vortex lines. This could lead to a reduction in the initially positive component of azimuthal vorticity eventually becoming negative. Nelson and Visser [58], and Lin and Rockwell [59] provided experimental evidence for the theory proposed by Brown and Lopez. It was found just prior to vortex breakdown that the azimuthal vorticity component becomes negative. The work of Darmofal [60] also supports this hypothesis. Darmofal analytically examined mechanisms of producing negative azimuthal vorticity. It was shown that vortex stretching (which occurs due to core flow deceleration because of conservation of momentum) causes the core velocity to decrease rapidly (via a feedback mechanism) providing that negative azimuthal vorticity was already present. Further, it was shown that vortex tilting can occur due to a non-zero component of radial velocity (or equivalently an adverse pressure gradient), and as such azimuthal vorticity can be reduced. If a vortex core experiences an adverse pressure gradient the core velocity will decrease. From conservation of momentum the radial velocity must therefore increase and therefore the vortex tilting occurs. Vortex tilting will reduce the azimuthal vorticity thus slowing the core flow and if the adverse pressure gradient is strong enough, the azimuthal vorticity will become negative. In this case vortex stretching will increase the core slowing process, thus stagnating the flow.

Gursul [61] measured the fluctuating pressures on the surface of delta wings of sweep varying from 60^o to 75^o. Most data was collected at a Reynolds number of around 100,000. It was found that when the measurement point was beneath the breakdown region a sharp peak in the spectrum of pressure fluctuations was present, regardless of incidence and sweep angle. The non-dimensional dominant frequency was also observed to be independent of Reynolds number (for the Reynolds number range investigated). The pressure fluctuations were observed from flow visualistion (and pressure measurements at two spanwise locations) to be due to the helical mode instability. Once breakdown reached the apex there was no dominant frequency observed. The dominant frequency, f, was also observed to decrease with increasing distance from the apex. This is due to the radius of the spirals increasing with increasing distance from the apex. Non-dimensionalising by the distance from the apex, x, yielded a constant non-dimensional frequency (fx/U_∞) for all angles of incidence and sweep angles tested. The wavelength of the spiral disturbance was also observed to increase with incidence (and therefore circulation).

Mabey [62] stated that for a variety of tests on wing/fin configurations at RAE/DRA (Royal Aircraft Establishment / Defence Research Agency [UK]), the frequency parameter (fc/U_∞) varied with incidence according to the relation

$$\frac{fc}{U_\infty} Sin\alpha = const \tag{1.9}$$

Mabey used the results of Gursul, with an appropriate length scale for delta wings (found to be the wing semi-span), to derive the following expression for the wake non-dimensional frequency parameter

$$\frac{fcCot\Lambda}{U_\infty} Sin\alpha = 0.27 \pm 0.02 \tag{1.10}$$

Jupp et al [21] studied the surface pressure distribution above a stationary 60^o delta wing at various angles of incidence. Flow visualisation studies were also performed on a geometrically similar wing. Both the mean and root mean square (RMS) pressure distributions were examined. As incidence was increased two distinct regions of high RMS pressure were observed, one being inboard and one outboard of the primary mean suction peak. These were attributed to the primary attachment

and the formation of the secondary separation region. Unlike the mean c_p distribution, the RMS pressures did not decrease with distance from the apex. Another feature observed was a "waisting" of the primary RMS pressure region, which appeared to be attributed to the deceleration and subsequent stagnation of the vortex core, resulting in vortex breakdown. Downstream of this waisting there was an expansion of the high RMS region which was associated with the vortex breakdown.

1.3.1 Vortex breakdown - Pitching wing

When a delta wing is pitched or plunged there is a time lag response of the vortex flow, which can result in a temporary delay in vortex formation at low incidence, or a temporary delay in vortex breakdown at high incidence. For delta wings undergoing cyclic motions, a hysteresis develops in the vortex flow relative to the static case (or delay for ramping motion), which increases with the frequency or rate of motion [56]. As described by Ashley et al. [63] flow visualisation has been central to the understanding of delta wing loads.

Parker [20] investigated the effect of varying the freestream incidence on a 63^o delta wing at a mean incidence of 15^o. The freestream velocity was sinusoidally oscillated $\pm 8^o$ at frequencies of 2Hz and 4Hz. Flow visualisation and pressure data were taken. As the incidence of the wing increased breakdown moved towards the apex. However during the increasing incidence phase, at a given incidence the unsteady breakdown location lagged that of the static case. The most forward unsteady breakdown location was also noted to never reach as far forward as in the static case. There was also a lag in breakdown travel towards the trailing edge on the decreasing incidence phase of the cycle. The suction pressures in unsteady flow were also observed to lag those in the steady case, confirming that the vortices require a finite time to respond between incidence changes.

Gad-el-hak and Ho [64] visualised the effect of sinusoidally pitching a blunt leading edged 45^o and a sharp leading edged 60^o delta wing. They observed a hysteresis effect in the vortex location above the wing, with the vortex being higher above the wing on the downstroke compared with the upstroke for a given incidence. As the reduced frequency was increased, the position of the vortex above the wing

at the higher angles of incidence decreased. This observation was only present at the higher incidence. The hysteresis loop was found to be independent of Reynolds number for the range 25,000 to 340,000. Increasing the pitch rate was found to delay stall of the wing.

LeMay et al [37] studied the effect of sinusoidally pitching a 70^o delta wing from 29^o to 39^o. It was found that as the frequency of the pitching oscillation increased, the difference between breakdown locations at a given location on the upstroke and downstroke of the motion also increased. This led to thicker hysteresis loops in the breakdown location curves. It was also found that the chordwise range (x/c_r) over which breakdown occurs decreases. A similar effect was noted by Gursul [65] for the response of a leading edge vortex to fin oscillations (the dynamic response of vortex breakdown to these oscillations was likened to the response of a low-pass filter). This was due to the wing beginning its upstroke before breakdown could reach the aftmost position. It was also found that as the reduced frequency increases the hysteresis loops become more symmetrical around the static case. By measuring the phase lag over a range of reduced frequencies, it was found that there is a near linear relationship between phase lag and reduced frequency. A change in Reynolds number was found to have little effect on the phase lag.

Thompson et al. [38] investigated the response of the leading edge vortices from a 70^o delta wing to transient pitching motions. The range over which the wing was pitched was 30.5^o to 39.5^o at pitch rates up to $36.4^o/s$. It was found that the response of the breakdown to the transient motion was dependent on non-dimensional pitch rate, initial breakdown location, and direction of motion. The response of the breakdown location was also found to lag that found in the static case for a given angle of attack. As pitch rate was increased this lag increased. Reynolds number was found to have little influence on the results. The results from a pitch up manoeuvre were observed to be different from the pitch down manouevre, and that pitching up then pitching down produced different results to a continuous sinusoidal pitching.

Miau et al. [66] studied the nonuniform progression of vortex breakdown towards the apex during and after ramp up pitching motions around the mid chord. Flow visualisation studies of the breakdown location with pitch up and pitch down

motion showed that vortex breakdown remained near its initial point for a certain time before progressing towards the apex or trailing edge. The delay in breakdown progression (in terms of the instantaneous incidence where breakdown passes a given point) was observed to increase with pitch rate. A second delay in breakdown progression for the pitch up case was also observed which was most prominent with lower sweep angles. The occurrence of the second delay appeared to coincide with a shear layer instability. LDA results also indicated a large increase in the size of the secondary separation during the second delay which suppresses the primary vortex. Outwith the breakdown delays, breakdown travel towards the apex was near linear, indicating that nonlinear progression is solely due to delays in breakdown progression. This is consistent with other investigations [38][37]. It was suggested that the initial delay in breakdown progression to the apex during a ramp up manoeuvre was due to the underdevelopment of the primary vortex.

Rediniotis et al. [67] studied the flow over a ramping 75^o delta wing, at an average pitch rate of 40^o/s. The wing was ramped from 28^o to 68^o. It was observed that the breakdown appearance at the trailing edge was delayed in comparison to the static case. For the wing and pitching frequency chosen, it was ascertained from surface pressure data at two points beneath the vortex core (both mean and RMS), that once the breakdown passed the trailing edge, the progression towards the apex occurred at high speed. Within a 2^o increment in incidence the breakdown progressed to the mid-chord in the static case, and it was suggested (though unconfirmed due to the low temporal resolution) that the breakdown reached the apex within 2^o for the ramping case. It was also suggested from an apparent smooth increase in pressure beneath the burst vortex with increasing incidence, that the core breaks down first and this event radiates outwards. Seven hole probe data indicated a similar result.

Computational work has helped in the understanding of dynamic delta wing results. Visbal [68] computed the flow over a 75^o delta wing in ramping motion. Examining the flow after the motion had stopped, Visbal showed that well away from breakdown a stable focus exists (ie. the streamlines spiral into the vortex core). Prior to breakdown a stable limit cycle occurs (where the streamlines emanate from the core and spiral in from the leading edge) which was found to be due to vortex core compression (an axial deceleration of the flow prior to breakdown). These topologies

prior to vortex breakdown were observed experimentally through the use of PIV by Cipolla and Rockwell [69]. Cipolla and Rockwell further observed a nesting of limit cycles just prior to breakdown, then an unstable focus at breakdown (streamlines spiralling out), followed by an unstable limit cycle (streamlines spiralling into the core and no entrainment of the leading edge streamlines) post breakdown. Visbal [70] further studied the flow over the ramping 75^o delta wing. As in experiments a time lag in the breakdown motion was observed. As the wing was pitched around the trailing edge, an effective camber was induced. This reduced the effective incidence at the apex and lowered the suction in the vortex core. As the wing finished the ramping manoeuvre, the incidence at the apex increased and breakdown travelled to the apex. The move towards the apex was induced by an adverse pressure gradient along the vortex core which increased with incidence. It was concluded that the initiation of vortex breakdown was heavily dependent on the core pressure gradient. The time lag in the breakdown location travel to the apex was also seen in the core pressure distributions. As the wing adjusted to the new high incidence, the subsequent expansion in the vortex core near the apex propagated downstream at around freestream velocity, thus breakdown travelled to the apex via the developing adverse pressure gradient. Visbal and Gordnier [71] also showed that the time lags of breakdown motion in ramping motion were dependent on both pitch rate and pitch axis location. They found that increasing the pitch rate or moving the pitching axis location downstream delayed breakdown progression to the apex.

Lin and Rockwell [59] studied the transient structure of vortex breakdown after a pitch up manoeuvre. By pitching the wing from 25^o to 50^o angle of attack the motion and structure of the vortex breakdown as it propogated to the apex was examined. It was found that there is an initially high propogation speed of vortex breakdown, which increased following a transformation of the vortex structure. After the transformation the rate of breakdown motion decreased by around a factor of 20. It was concluded that rather than there being a series of quasi-steady states of breakdown motion as it moved towards the apex, there were a series of abrupt transformations. It was further concluded that the rapid motion of breakdown towards the apex was due to an abrupt transformation of the vortex structure. At larger times the degree of organisation increases and the rate of travel of breakdown

towards the apex slows down.

Coton et al. [72] studied the unsteady surface pressure distributions over a ramping 60^o delta wing. The wing was pitched at a constant pitch rate from -5^o to 45^o. As in the static testing of Jupp et al. [21], primary and secondary regions of high RMS pressure were observed at increasing incidence, associated with the primary attachment and secondary structure formation. The waisting of the primary RMS pressure ridge described in Jupp et al. [21] was seen to lag the static case with increasing pitch rate, indicating a lag in the breakdown progression upstream. This was confirmed via flow visualisation tests. As in the static case, at a given incidence in the pitch up manoeuvre, with increasing distance from the breakdown the centre buffet frequency decreases (since the wavelength of the helical waves increases with distance from the breakdown). It was also found that at a constant distance from the breakdown location, the dominant frequency of breakdown increases with increasing incidence. The tradeoff between these phenomena was given as the reason why the dominant frequency appears to decrease with increasing incidence at a given chordwise location for the static case. However in the pitching case it was found that with increasing incidence the centre buffet frequency remained near constant at a given chordwise location. This indicated an alteration in the balance of the frequency increase near breakdown and frequency decrease with distance from breakdown. As in the static case, the non-dimensional buffet centre frequency (fx/U_∞) just downstream of the breakdown ($0.1c_r$ from the breakdown location) was observed to be constant as breakdown progesses towards the apex, however, the non-dimensional frequency was observed to increase with increasing pitch rate.

1.4 Investigations into loads and moments on delta wings

Reviews of unsteady aerodynamic loading on delta wings have been given by Lee and Ho [73] (general motions) and Ashley et al. [63] (pitching wings).

Hummel and Srinivasan [74] studied the loads on a delta wing as the wing is pitched up. They found that at low incidence vortex breakdown is far downstream

of the trailing edge, and that increasing the incidence moves breakdown towards the apex. Also the incidence where breakdown passed the trailing edge increased with increasing sweep angle. When vortex breakdown passed the trailing edge, there was a loss in the slope of the load and moment curves, most noticeable in the pitching moment curves. This was attributed to a brief loss in lift as breakdown passes the trailing edge.

Wentz and Kohlman [9] found that for a 65^o delta wing, maximum lift occurs at an incidence when breakdown is between the trailing edge and the apex, i.e when breakdown is over the wing. For sweep angles less than 70^o, maximum lift occurs approximately when the burst location reaches the apex, whereas for higher swept wings, maximum lift is observed when the vortex breaks down in the vicinity of the trailing edge. As breakdown moves further towards the apex past the maximum lift incidence, the lift decreases and full flow separation occurs on the upper surface of the wing. It was found by Earnshaw and Lawford [75] that delta wings with sweep angles of around 65^o produced the best performance in terms of maximum lift coefficient.

In the review of unsteady loading on delta wings by Ashley et al. [63], the work of Jarrah [76] is discussed in detail. In Jarrah's work for a wing with aspect ratio of one (sweep angle of approximately 76^o), when the wing was pitched sinusoidally from 0^o to 30^o, the flow appeared quasi-steady (the aerodynamic coefficient hysteresis loops were thin). This indicates that in the absence of any vortex instability above the wing surface, the flow adjusts rapidly to changes in incidence and other boundary conditions. As the wing was pitched to higher incidence (up to 60^o and 90^o) where breakdown formed over the wing, hysteresis loops were present indicating a time lag in the propogation of vortex burst upstream. Increasing the aspect ratio of the wing had little influence on the hysteresis, however as aspect ratio increased the peak of the coefficients increased.

The effect of pitching oscillations on the lift and drag curves for a 70^o delta wing was studied by Soltani et al. [77]. For static cases, a 45% decrease in Reynolds number was found to increase the maximum lift by around 16%. A similar result was also found in the dynamic cases. It should be noted that the relatively strong dependence on Reynolds number may be attributed to the leading edge shape (the

leading edge was chamfered at 25^o on both the upper and lower surfaces). The wing was sinusoidally oscillated from 0^o to 55^o at reduced frequencies of 0.015 to 0.0815. The incidence at which the normal force gradient decreased was found to increase with increasing reduced frequency. This indicated a delay in the occurrence of vortex breakdown over the wing, which increased with increasing reduced frequency. The delay in breakdown reaching the apex resulted in higher values of maximum normal force coefficient. This increased normal force coefficient was found to have little effect on the maximum lift, however, the maximum drag increased with increasing reduced frequency. Once breakdown reached the apex, it was observed that there was a delay in vortex reformation during the downstroke. This lag resulted in the formation of hysteresis loops in the load and moment curves, however the hysteresis effect was dominant in the high incidence range where breakdown is present. From around 0^o to 20^o for the pitch rates considered, the curves from the upstroke and downstroke appear near coincident. A similar result was found from surface pressure measurements by Thompson et al. [78] where the surface pressures at $35\%c_r$, $55\%c_r$, and $75\%c_r$ root chord only showed strong hysteresis at high angles of attack. It was concluded that the surface pressures oscillated in phase with the wing motion. These results agree well with the findings of Jarrah [76]. The effect of a sideslip angle was also investigated. The lift and rolling moments were effected heavily with sideslip of the wing, most noticeably at high incidence when breakdown was observed to occur over one half of the wing earlier (the windward side) than the other.

1.5 Methodology

1.5.1 PMB3D

All simulations described in this thesis were performed using the University of Glasgow PMB3D (Parallel Multi-Block 3D) RANS solver. A full discussion of the code and turbulence models implemented is given in appendices A and B respectively.

PMB3D uses a cell centered finite volume technique to solve the Euler and Reynolds Averaged Navier-Stokes (RANS) equations. The diffusive terms are discretised using a central differencing scheme and the convective terms use Roe's scheme

with MUSCL interpolation offering third order accuracy. Steady flow calculations proceed in two parts, initially running an explicit scheme to smooth out the flow solution, then switching to an implicit scheme to obtain faster convergence. The pre-conditioning is based on Block Incomplete Lower-Upper (BILU) factorisation and is also decoupled between blocks to help reduce the computational time. The linear system arising at each implicit step is solved using a Generalised Conjugate Gradient (GCG) method. For time-accurate simulations, Jameson's pseudo-time (dual-time stepping) formulation is applied, with the steady state solver used to calculate the flow steady states on each physical time step (discussed fully in Appendix A).

Since PMB3D is an extension of the PMB2D (Parallel Multi-Block 2D) flow solver, the axis system is such that the x and y axes are in the longitudinal plane. Therefore for 3D wing calculations the x axis is the roll axis, the y axis is the yaw axis, and the z axis is the pitching axis (in body co-ordinates). This is in contrast to the standard "aerodynamic" axis system which uses the y axis as the pitching axis, and the z axis as the yawing axis.

For pitching motion of a delta wing inside wind tunnel walls, Trans-Finite Interpolation (TFI) of displacements is used [80]. Since deforming a mesh alters the cell volumes, a Geometric Conservation Law (GCL) is used to calculate the time varying cell volumes (which can be computed using the same method as the conservation laws), which is required to maintain the conservative properties of the computational scheme. Using TFI of displacements allows a fast and simple method for mesh deformation, and the original quality of the grid is generally maintained. Each block is treated seperately and the method is based on interpolation of block corner displacements. By interpolating block corner displacements, the displacement of the cell faces can be interpolated, and therefore the internal node displacements can be interpolated. Using the same interpolation procedure for all blocks ensures that there is a perfect matching of adjacent block faces.

1.5.2 Computational facility

The Computational Fluid Dynamics group at the University of Glasgow owns a cluster of PC's. The cluster is known collectively as Jupiter and is fully described by Badcock et al. [81]. There are 32 nodes of 750MHz AMD Athlon Thunderbird uni-processor machines, each with 768Mb of 100MHz DRAM. MPI (Message Passing Interface) is used to link up multiple nodes to create a virtual machine, which is used to execute computationally demanding problems. PMB3D balances the node loadings (number of cells per node) by spreading the blocks over all the nodes of the virtual machine. Halo cell values are passed between adjacent blocks using MPI.

1.6 Thesis outline

The structure of this thesis is such that each chapter starts with a detailed introduction to its topic. In this introductory chapter the flow topology on the leeward side of delta wings has been discussed. Chapter 2 describes results from the Euler simulations of wind tunnel interference for both static and pitching wings. Chapter 3 discusses the influence of turbulence modelling on vortical flows, and discusses the choice of turbulence model (and modifications made to improve predictions) used for RANS calculations. Chapter 4 presents results from RANS simulations of the wind tunnel interference which are used to confirm the conclusions drawn from the Euler study, and chapter 5 considers the effect downstream support structures can have using a RANS model of the flow. Trends highlighted and the relative magnitudes of each influence is assessed.

Chapter 2

Euler simulations of tunnel interference on delta wing flows

2.1 Introduction

Wind tunnels are used to test the aerodynamic characteristics of aircraft in the research and development stages. However, the influence of the tunnel walls must be taken into account when considering test results. Historically, wind tunnel corrections have been based on Linear Potential Flow Theory [82]. To obtain good quality and reliable test data, factors relating to wall interference, flow angularity, local variations in velocity, and support interference, must be taken into account. Karou [83] found that for delta wings with aspect ratio equal to one and spanning up to half the tunnel width, classical wall correction techniques can be used to correct flow field and force results up to 30^o angle of attack (it should be noted that vortex breakdown was unlikely to be present over the wing). Also, for swept wings with a blockage ratio (ratio of model planform area to tunnel cross-sectional area) of less than 0.08, tunnel interference effects can usually be considered negligible [84].

Clearly, the flow conditions within a wind tunnel will be different to those a wing would experience in free air. The interactions between the wing and wall flow fields induce longitudinal and lateral variations (streamline curvature and aerodynamic twist respectively) to the freestream, in addition to those attributed to the wing alone. These differences may result in a reduction in the average downwash

experienced by the model, a change in the streamline curvature about the model, an alteration to the local angle of attack along the span of the model, a change in dynamic pressure about the model due to solid and wake blockage, and in the buoyancy effect due to the axial pressure gradient along the tunnel test section. The magnitude of these effects increases with model size (increasing solid blockage).

This chapter examines the effect of wind tunnel wall interference using the Euler equations. The PMB3D flow solver (discussed in section 1.5) is used in all calculations. This simplified inviscid model provides a reliable and cheap alternative to the more realistic and expensive Reynolds-Averaged Navier-Stokes model. A novel approach to assessing tunnel interference is discussed, as well as the consideration of the tunnel effects on unsteady pitching wings.

2.2 Previous work

Previous investigations have been performed on static wings inside various tunnels. Generally the focus of these studies has been to find a method to correct force data through various methods. Frink [85] looked at variations in streamline curvature and aerodynamic twist due to the presence of the tunnel walls. He also found that the walls increased the suction peak on the wing beneath the leading edge vortices. This increased suction was explained by the upflow variation increasing the mean angle of attack.

Thomas and Lan [86] used a thin layer Navier-Stokes solver to compute the flow field around a wing inside the NASA Langley Basic Aerodynamics Research Tunnel (BART). Using the wall pressure signatures obtained from the Navier-Stokes simulations as a boundary condition for an Euler simulation, they used the wall pressure signature to calculate the interference flow field. Their results showed that the upwash along the chord of the wing increased towards the trailing edge. Hsing and Lan [87] used a similar method to derive correction charts. Their results also showed an increase in the suction peak beneath the primary vortices. Their computations of aerodynamic twist and upflow variations agreed well with those of Frink [85].

Weinberg [88] modelled the wind-tunnel walls with eight images of vortices inside

the test section. Two pairs of vortices were taken into account, the separated leading edge vortices and an additional pair of vortices to model the wing's bound vorticity. The leading edge vortices were modelled using straight lines for the vortex cores, and were positioned above the wing using experimental data. The results obtained by Weinberg were compared to the more accurate results of Frink [85], and were in good agreement.

Weinberg's computations showed (for a 70^o swept wing at 30^o incidence) that the induced upwash is relatively small near the wing's apex and grows larger toward the trailing edge, creating an effectively cambered wing under the influence of the test section walls. Previous experimental results have shown that a positively cambered wing (i.e. the local incidence of the trailing edge is greater than that at the apex) delays vortex breakdown travel to the apex. Based on the previous conclusions, Weinberg surmised that the effect of the induced camber caused by the presence of the wind tunnel walls would delay vortex breakdown travel towards the apex which is in direct contrast to the intuitive result that wall effects tend to increase angle of attack, thus promoting vortex breakdown travel towards the apex. Weinberg also conducted an experimental investigation into wall effects. He tested two sets of three wings (one set with 60^o sweep, and one set with 70^o sweep), each wing with a different span size. The experiment was performed in a square water tunnel (low Re) at a constant flow velocity of 11m/s. The tunnel size was 45cm x 45cm. He found that for the three wings with 70^o sweep, as the wing size was increased (kept at a constant angle of attack), vortex breakdown moved downstream. For the three wings with 60^o sweep, he found that as the wing span-to-tunnel width ratio increased from 0.175 to 0.35, the wall effects followed the computed trends (i.e. vortex breakdown was shifted downstream with increasing wing size). However, when the wing span-to-tunnel width ratio was increased from 0.35 to 0.7, no significant change was observed. This suggested that effective camber was not the only influence. For both the 60^o and the 70^o wings, the difference in breakdown location observed from the smallest model to the largest model, was of the order $25\%c_r$.

Thompson and Nelson [89] investigated experimentally the influence of tunnel walls on a 70^o delta wing by testing full, two thirds, and half scale models in a square tunnel (the largest model gave the ratios S/H = S/W = 0.364). Due to a steady

hysteresis effect the wing was tested for a quasi-steady upward and downward stroke. It was found that for the smallest model tested (S/H = S/W = 0.124) the breakdown location shifted downstream by as much as 15%c_r on both the quasi-steady upstroke and downstroke. For the half scale model and the full scale model, there appeared to be little difference in the breakdown locations. As stated by Thompson and Nelson, this shift downstream as model size is decreased is in contrast to the results of Weinberg [88]. It was noted that Weinberg used a Reynolds number an order of magnitude lower, and a constant velocity, as opposed to keeping the Reynolds number constant (as in the experiments of Thompson and Nelson). It was observed that the vortex suction on the model surface increased with model size.

Thompson and Nelson also conducted some unsteady experiments, varying the angle of attack from 0^o to 60^o. They found that the unsteady variation in breakdown location was unaffected by the wing size. A similar effect was stated to have occurred with a higher frequency of oscillation.

More recently Pelletier and Nelson [90] studied the effect of tunnel interference on 70^o delta wings. Experiments were conducted in a water tunnel with three different sized wings. These low Reynolds number tests agreed with the previous findings of Thompson and Nelson [89] who tested at higher Reynolds number, in that breakdown moved towards the apex with increasing wing size. Pelletier and Nelson used the method of images to explain this effect, concluding that the tunnel walls increased the mean incidence of the wing, thus promoting breakdown.

Lowson and Riley [91] investigated the possibility of tunnel and support interference being the cause of the scattering of experimental data for vortex breakdown locations for a given sweep angle. They tested several wings of identical geometry to those used in previous investigations. It was observed that tunnel wall proximity had little effect on vortex breakdown and that the geometry of the apex was the most important factor in vortex breakdown location. However, it was noted that when a 70^o wing was placed in a smaller tunnel, the breakdown moved downstream slightly, though this was not the case for all wings.

Verhaagen et al. [92] performed Euler simulations of the flow over a 76^o delta wing inside wind tunnels of increasing size. The wing span-to-tunnel width ratios considered were 0.292, 0.389, and 0.584 and the test section was octagonal. To model

the effect of a secondary separation, a small "fence" was placed where secondary separation would occur. It was found that decreasing the tunnel size (increasing the wing span-to-tunnel width ratio) increased the suction in the vortices and increased the velocities in the vortex core, due to an increase in circulation with decreasing tunnel size.

2.3 Flow separation from sharp leading-edges in Euler solutions

The use of the Euler equations in aerodynamic simulations offers a cheaper alternative to the full Navier-Stokes equations. This is at the cost of reducing the realism of the aerodynamic model, but, for flows where viscous effects are not dominant, Euler simulations can offer a reasonable solution [93][94][95][96][97][98][99].

Since pure delta wing flowfields are characterised by two leading edge vortices (which are a result of flow separation from the leading edge of the wing), it may initially seem strange to try to predict flow separation with the Euler equations, which by definition, have no boundary layers to deform. This section considers the mechanisms which allow inviscid flow separation from the sharp leading edges of delta wings.

2.3.1 Assumptions

The assumptions for the Euler model are that the flow is inviscid, adiabatic, and can be incompressible or compressible. Since viscosity is neglected no boundary layers are predicted in Euler simulations. As a result separation will not occur unless in special circumstances. However, it should be noted that if separation does occur at the leading edge of a delta wing, the Euler equations can correctly describe the transport of vorticity and entropy from the the leading edge, along the vortex sheet, to the roll up into the leading edge vortices.

2.3.2 Crocco's Theorem

A mechanism for the generation of vorticity in Euler flows is given by Crocco's Theorem. This relates entropy gradients to vorticity in frictionless, non-conducting, steady, adiabatic flows. The simplest form of Crocco's theorem is given in natural coordinates and is written as [100]

$$T\frac{dS}{d\mathbf{n}} = \frac{dh_0}{d\mathbf{n}} + u\omega \tag{2.1}$$

where $\mathbf{n}$ is the direction normal to a streamline, $\mathbf{s}$ is measured along the streamline, u is the velocity component along the streamline, and ω is the magnitude of the vorticity defined as (again in natural coordinates)

$$\omega = u\frac{\partial\theta}{\partial\mathbf{s}} - \frac{\partial u}{\partial\mathbf{n}} \tag{2.2}$$

where θ describes the direction of the streamline. Note $\frac{\partial\mathbf{s}}{\partial\theta}$ is effectively the radius of curvature of the streamline.

Crocco's theorem states that zero vorticity implies uniform entropy (S), provided the stagnation enthalpy is constant. Since the stagnation enthalpy is constant in most aerodynamic problems (h_0 = constant for a perfect gas), for vorticity to be generated in an inviscid flow, entropy layers must be present. In the case of Euler flows where the flow is adiabatic and inviscid, vorticity cannot be generated (in accordance with Kelvin's Laws). However, one source of entropy gradients in inviscid flows is the entropy rise across a non-uniform shock wave, since entropy is constant along streamlines unless that streamline passes through a shock. Therefore the presence of a shock near the leading edge of the wing could cause vorticity to be generated, which would be transported down the wing.

It was suggested by Rizzi (for the presence of the Kutta condition at sharp trailing edges in Euler simulations) [101] and Hitzel and Schmidt [102], that in the preliminary stages of the computational cycle, the flow is near that of potential. Very high velocities will therefore be generated around the sharp leading edges of delta wings. Since the Euler equations include compressibility effects, they respond with a shock to provide a fit to the surrounding flow. In accordance with Crocco's theorem vorticity could therefore be generated by the transient appearance of a

shock.

2.3.3 Numerical dissipation

All numerical schemes have some sort of numerical dissipation associated with them due to the discretisation of the derivatives [103]. The dissipative effect is also known as artificial viscosity and is especially important in regions with high flow gradients. As such, for flow around sharp leading edges where flow gradients are likely to be high there will be a significant amount of numerical dissipation, especially if the region is not adequately resolved. This numerical dissipation serves to increase the entropy (or decrease the total pressure) of the flow, and will allow the generation of vorticity in Euler solutions. For wings with rounded leading edges, interpretation of separated flow results requires more caution since the separation location is not fixed (as with sharp leading edges) [102][104]. The total pressure losses (or entropy gradients) due to numerical dissipation depend on the flow gradients, grid density and numerical algorithms.

Newsome [104] found that leading edge separation occurred on a 14:1 elliptic cone (round leading edged "delta"), however sufficiently refining the grid near the leading edge (thus reducing the numerical dissipation) eliminated the primary vortex in his Euler solutions. During the initial stages of his time accurate calculations he found the flow quickly expanded round the leading edge, producing supersonic velocities and a cross flow shock. No flow separation occurred after the crossflow shock. This expansion around the leading edge produced large entropy / vorticity errors which convected to the developing crossflow shock. This interaction caused flow separation to occur, the separated region expanded, and formed the large primary vortex. He did note, however, that the chain of events leading to the leading edge separation followed closely those described by Rizzi [101], however the origin of the vorticity required to cause flow separation originated from numerical error, not the presence of the shock. Refining the grid at the leading edge reduced the numerical error and vorticity generated, thus eliminating the separation.

Another possible mechanism for the generation of vorticity in an Euler solution was given by Hirschel and Rizzi [105] and Eberle et al. [106]. If we consider a shear

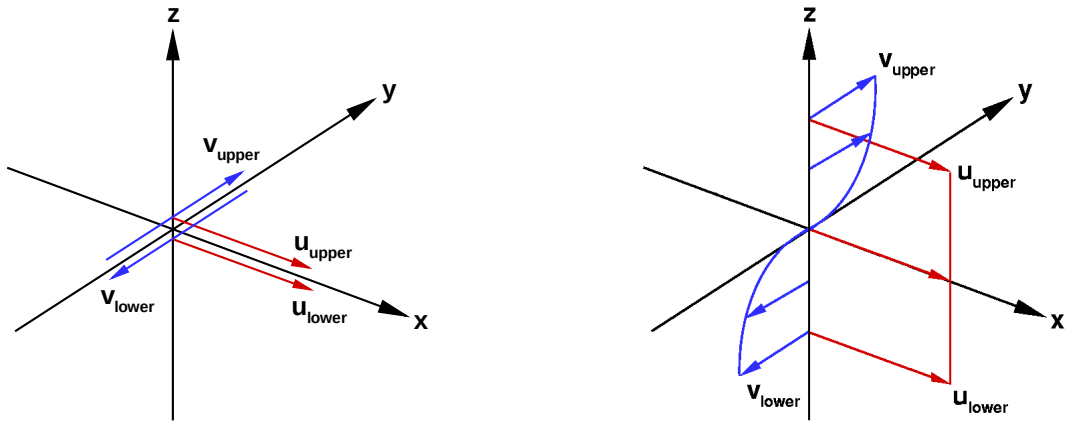

(a) Euler discontinuous shear layer

(b) Discontinuity layer widened by numerical smearing

Figure 2.1: *Three dimensional shear flows, adapted from [106] pp309*

flow in which the velocity vector has a constant component in the x direction, and opposite signed components in the y direction (zero normal velocity), in an ideal Euler model (as in potential flow) there is a discontinuity along the surface where the two streams meet. This is illustrated in figure 2.1(a). Along this discontinuity the magnitude of vorticity is infinite, but the vorticity is hidden in the discontinuity (this is in accordance with the fact that $\nabla \times \omega = 0$ only holds if the velocity field is continuous). However, analogous to the smearing of captured shock waves in discrete solutions, the ideal Euler discontinutity is smeared over a few grid cells. This smearing distorts the discontinuity as shown in figure 2.1(b), and the previously hidden vorticity appears in a shear layer of finite thickness.

2.4 Test case : WEAG-TA15 Wing

The test case used in the WEAG-TA15 Common Exercise IV [94] has provided a foundation for this research. The WEAG-TA15 WB1 model (see figure 2.2(a)) was tested at DLR Braunschweig by Löser [107]. Experiments were carried out at two Mach numbers (0.06 and 0.12) with Reynolds numbers based on the root chord of

1.55×10^6 and 3.1×10^6. The experiments were carried out in the $2.85m \times 3.2m$ low speed atmospheric wind tunnel (NWB) of DNW, located at DLR Braunschweig.

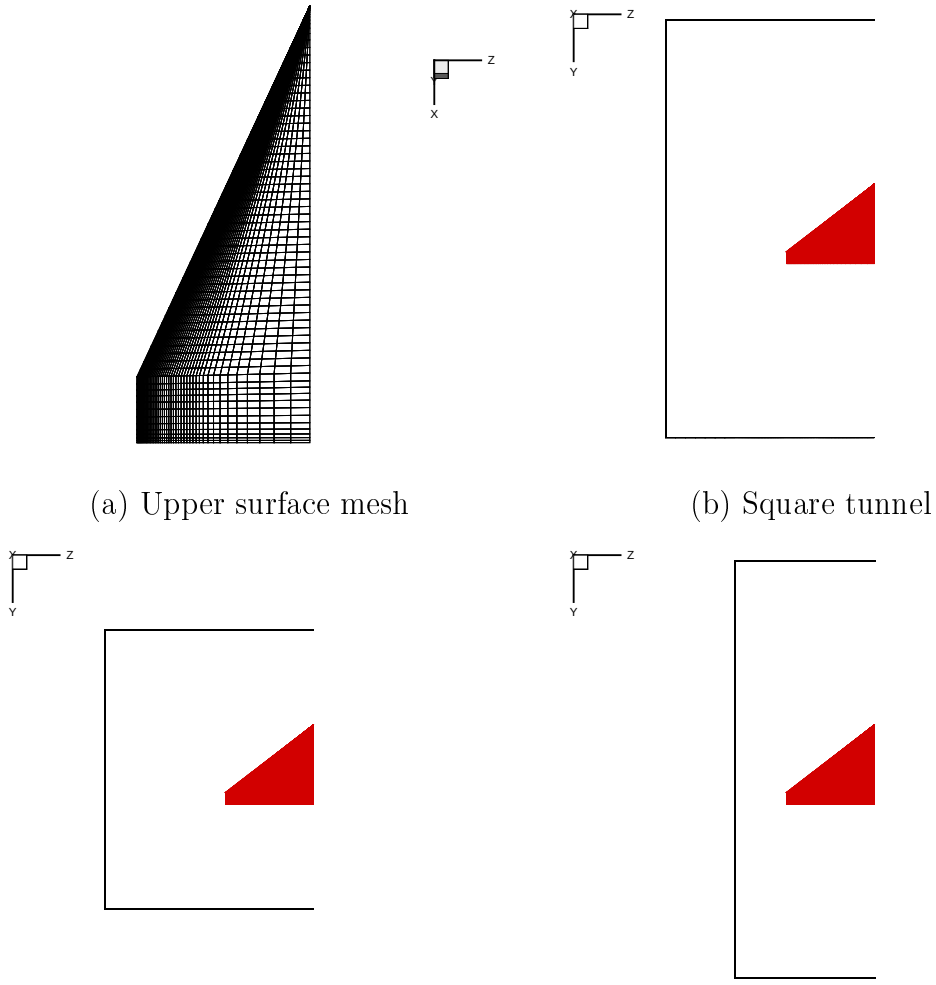

(a) Upper surface mesh

(b) Square tunnel

(c) 3x2 tunnel

(d) 2x3 tunnel

Figure 2.2: *WEAG-TA15 upper surface mesh and view upstream in the three wind tunnels considered*

The open test section was used. The wind tunnel model had an inner chord of 1200mm, a tip chord of 180mm, and a leading edge sweep of 65^o. The model is fully symmetric with a sharp leading edge which has a radius of 0.25mm. The aerofoil consists of an arc segment from the leading edge to 40% of the local chord, the region 40% to 75% of the local chord is defined by the NACA 64A005 aerofoil, and from 75% of the local chord to the trailing edge the aerofoil is a straight line inclined at 3^o.

The wind tunnel model has a fuselage of 160mm diameter built into the lower surface of the wing. The flow conditions for which static symmetric experimental data are available, are summarised in table 2.1. The flow conditions for which experimental pitching data are available, are summarised in table 2.2. For the static case surface pressures will be used for validation, and for the pitching cases load data will be used.

Incidence	-0.3^o, 9^o, 15^o, 21.2^o, 26.6^o, 41.4^o
Reynolds Number	1.55×10^6, 3.1×10^6
Mach number	0.06, 0.12

Table 2.1: Experimental flow conditions used by Löser [107] (Static testing)

Mean incidence	-0.3^o, 9^o, 15^o, 21^o, 7^o, 42^o
Reynolds Number	1.55×10^6, 3.1×10^6
Mach number	0.06, 0.12
Reduced pitching frequency	0.28, 0.56
Amplitude of pitching motion	3^o, 6^o

Table 2.2: Experimental flow conditions for pitching motion used by Löser [107]

The computational test cases in table 2.3 were considered. All computations in this chapter are inviscid, at a freestream Mach number of 0.4 (to eliminate the need for low Mach number pre-conditioning), with a pitching amplitude of 6^o, and reduced frequencies of motion of 0.56 and 1.5. The wing was meshed inside the tunnels at the mean incidence (α_m) of 21^o. The pitching motion is defined by

$$\alpha(t) = \alpha_m + \alpha_0 sin(kt) \tag{2.3}$$

For the pitching motion 50 time steps per cycle were used, and the computations were run until the removal of all transient effects (this is achieved after 4 complete cycles). A solution (not yet periodic) for the pitching wing inside the 3x2 tunnel, at the highest reduced pitching frequency of 1.5, using 100 time steps per cycle, is

shown in figure 2.3. It can be seen 50 time steps provides an adequate temporal resolution of the motion. It should be noted that the frequency of the helical motion of the vortex breakdown is too high to be resolved by the present computations, even with the smaller time step.

TUNNEL	S/W	S/H	α_m	α_0	k	M_∞
Experiment	-	-	21^o	-	-	0.12
Farfield	-	-	21^o	-	-	0.4
Square	0.42	0.42	21^o	-	-	0.4
3x2	0.42	0.63	21^o	-	-	0.4
2x3	0.63	0.42	21^o	-	-	0.4
Experiment	-	-	21^o	6^0	0.56	0.12
Farfield	-	-	21^o	6^o	0.56	0.4
Square	0.42	0.42	21^o	6^o	0.56	0.4
3x2	0.42	0.63	21^o	6^o	0.56	0.4
2x3	0.63	0.42	21^o	6^o	0.56	0.4

Table 2.3: WEAG-TA15 wing test cases - Inviscid flow

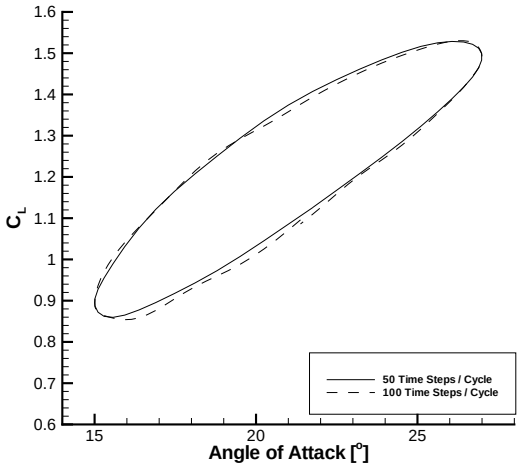

Figure 2.3: *WEAG-TA15 wing, temporal resolution study, 2x3 tunnel, k=1.5*

All simulations converged the residual six orders of magnitude with the maximum

residual being located at the leading edge of the wing near the apex.

2.5 Computational grids

The computational models consist of the half wing alone (no body, stings, mountings etc.) inside a farfield domain, a square tunnel, a 3x2 tunnel, and a 2x3 tunnel (tunnel details given in table 2.3). The tunnels are shown in figure 2.2. As described in section 1.5, the axis system used by the PMB3D flow solver has the x and y axes in the longitudinal plane, with the z axis spanwise. The frontal area blockages for each tunnel (with the wing at 21^o angle of attack) were 6.69% for the 2x3 and 3x2 tunnels, and 4.2% for the square tunnel. Consideration of the 2x3 and 3x2 tunnels allows the effect of tunnel wall proximity to be examined whilst keeping the frontal area blockage equal.

To allow a fair comparison between different tunnels one mesh was constructed in such a way that removing blocks would allow different tunnel shapes to be assessed. The topology that facilitated this with relative ease was the H-H topology.

There were 320 blocks in the "farfield" mesh with 1,770,000 grid points. This mesh had the farfield boundary condition applied at 20 c_r lengths from the wing in all directions. Extracting blocks from the farfield mesh gives the different tunnel grids. The square tunnel grid consists of 80 blocks with 923,000 grid points, the 3x2 tunnel grid has 40 blocks with 801,000 grid points, and the 2x3 tunnel grid 56 blocks with 811,000 grid points. The grid dimensions (considering only over the wing blocks) are given in table 2.4. All three tunnel grids have the farfield condition specified at the inlet and outlet, 20 c_r lengths from the wing, and the wing was meshed at an incidence of 21^o. The grid resolution near the leading edge is shown in figure 2.4. The initial normal to surface grid spacing was $0.002c_r$.

Since the simulations solve the Euler equations, no boundary layer develops on the tunnel walls, simulating the case of an ideal wind tunnel. Only the test section has been modelled without the presence of a contraction, diffuser, or settling chamber. These parts of the tunnel are assumed to have little influence since it is assumed the flow entering the test chamber is settled. No freestream velocity gradients are modelled though this could be achieved using experimentally obtained

distributions.

Test case	Streamwise	Spanwise	Normal to upper surface	Normal to lower surface	Grid total
Farfield	69	45	57	57	1,770,000
Square tunnel	69	45	49	49	923,000
3x2 tunnel	69	45	45	45	801,000
2x3 tunnel	69	45	49	49	811,000

Table 2.4: Grid dimensions for Euler tunnel interference study

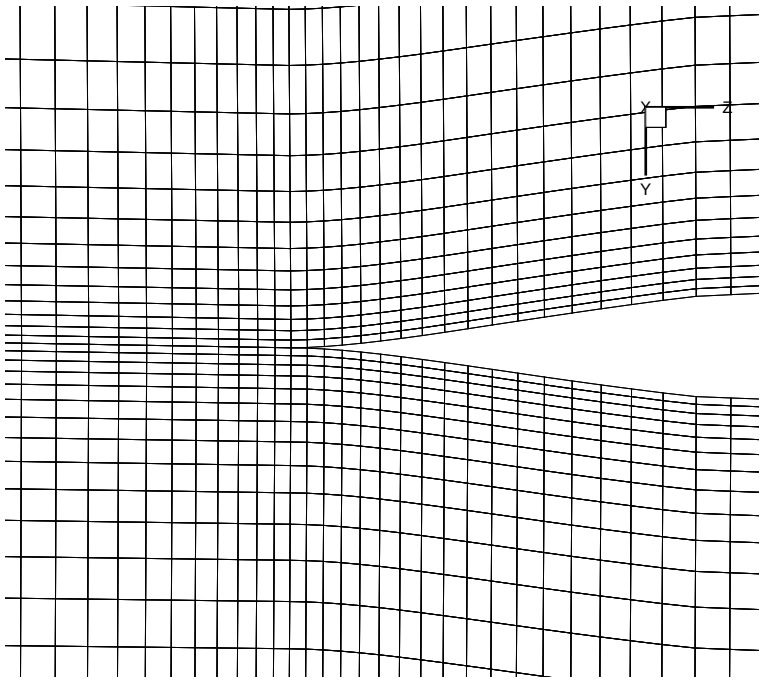

Figure 2.4: *WEAG-TA15 wing, grid point distribution near the leading edge of the wing, slice taken at the chordwise station 85%c_r*

Grid dependence study

A systematic study by Görtz and Rizzi [98] was undertaken to analyse the effect of grid resolution and topology when computing delta wing flows. The mesh generator

used was ICEMCFD Hexa (which has been used for the generation of all grids described in this thesis). They observed that for Euler simulations the solutions were dependent on both mesh topology and mesh refinement. The mesh topology has a strong influence on the resolution of particular regions. It was also concluded that the H-H topology performed best, but it must be stressed that no apex singularity was present in the grids. Strong grid dependency of Euler solutions has been observed by other researchers [108].

Various levels of refinement were examined in the current study. Due to the mechanism by which separation occurs (discussed in section 2.6) and vorticity is generated in the Euler solutions, the refinement around the leading edge was not altered significantly (apart from in the chordwise direction due to more points being added along the length of the leading edge). It is well known that varying the levels of refinement in the leading edge region drastically alters the solution [104]. Instead the vortical region was refined such that the levels of numerical dissipation in the vortex core would be reduced. The standard grid was refined in the chordwise, spanwise and normal directions by doubling the number of grid points in the respective direction. The surface pressure distributions at x/c_r=0.3 and 0.6 are shown in figures 2.5 and 2.6 respectively. The breakdown locations from each grid are given in table 2.5.

Grid	Breakdown location
Standard	$66.9\%c_r$
Refined chordwise	$65.1\%c_r$
Refined spanwise	$67.1\%c_r$
Refined normal	$69.9\%c_r$

Table 2.5: Summary of steady breakdown locations for grid refinement study

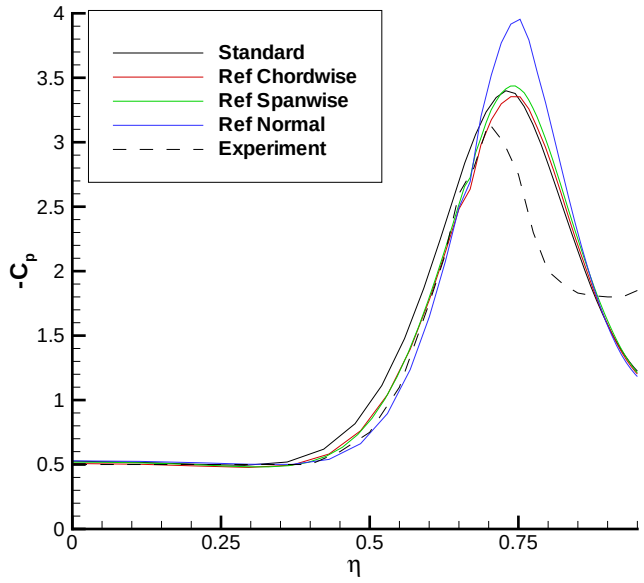

Figure 2.5: *WEAG-TA15 wing, Grid refinement study, comparison of surface pressure distributions at 30%c_r*

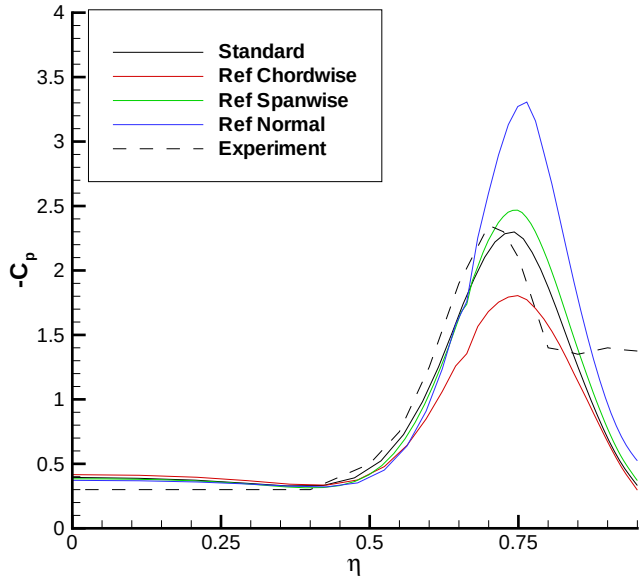

Figure 2.6: *WEAG-TA15 wing, Grid refinement study, comparison of surface pressure distributions at 60%c_r*

Considering the upper surface pressure distributions in figures 2.5 and 2.6, we see that the refinement in the chordwise and spanwise direction has had little effect. This is in contrast to the refinement in the normal to the surface direction which has produced much larger suction peaks at both the $30\%c_r$ and $60\%c_r$ stations. Considering the breakdown locations from the standard, and the refined in the chordwise and spanwise direction grids, it would appear the solutions are reasonably grid independent. However, resolving the grid in the normal to the surface direction again produces quite different results. It must be recalled however, that the gradients in the chordwise direction of a leading edge vortex are small in comparison to the other directions, and also, due to the shape of the wing and topology used, the refinement in the spanwise direction automatically increases towards the apex. Thus it might be expected that chordwise and spanwise refinement will have a lesser effect on the solution. Examination of the maximum axial velocities (which occurred just prior to vortex breakdown) revealed that the maximum axial velocity was 25% higher when the grid was refined in the normal to the surface direction, compared with the solutions from the other grids which appeared near equal. The increase in axial velocity is the most likely reason for the delay in vortex breakdown. Comparing the magnitude of the differences in breakdown location (maximum around $5\%c_r$) which is a highly sensitive parameter, it can be concluded that the standard grid produces reasonably accurate results and can be used in subsequent calculations.

Despite the exhibited grid dependency of the Euler solutions, since a common grid is being used to discretise the vortical region over the wing, each solution will suffer the same grid dependence. Therefore any differences in the solutions will arise solely as a result of the boundary conditions applied. In any case, the conclusions drawn from the Euler study are tested by including viscous effects in chapter 4.

2.6 Visualisation of the separation mechanism

The Euler separation mechanism from the sharp leading edges of the WEAG-TA15 wing is shown in figures 2.7 and 2.8. The total pressure loss contours shown in figure 2.7 indicate entropy rises, and the vorticity magnitudes shown in figure 2.8 indicate the generation of vorticity (in accordance with Crocco's theorem). The total

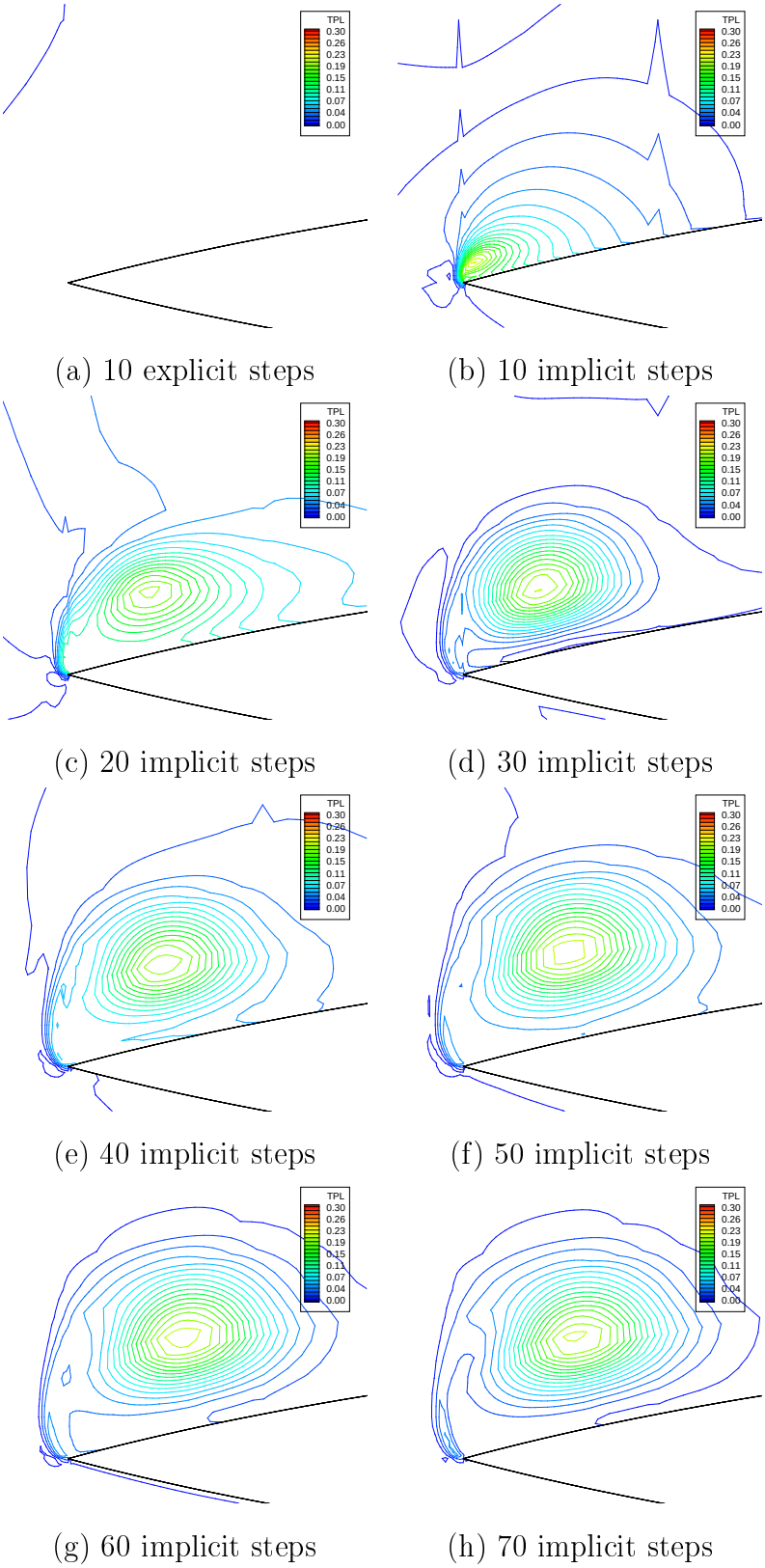

(a) 10 explicit steps (b) 10 implicit steps

(c) 20 implicit steps (d) 30 implicit steps

(e) 40 implicit steps (f) 50 implicit steps

(g) 60 implicit steps (h) 70 implicit steps

Figure 2.7: *Visualisation of Euler separation mechanism, total pressure loss contours*

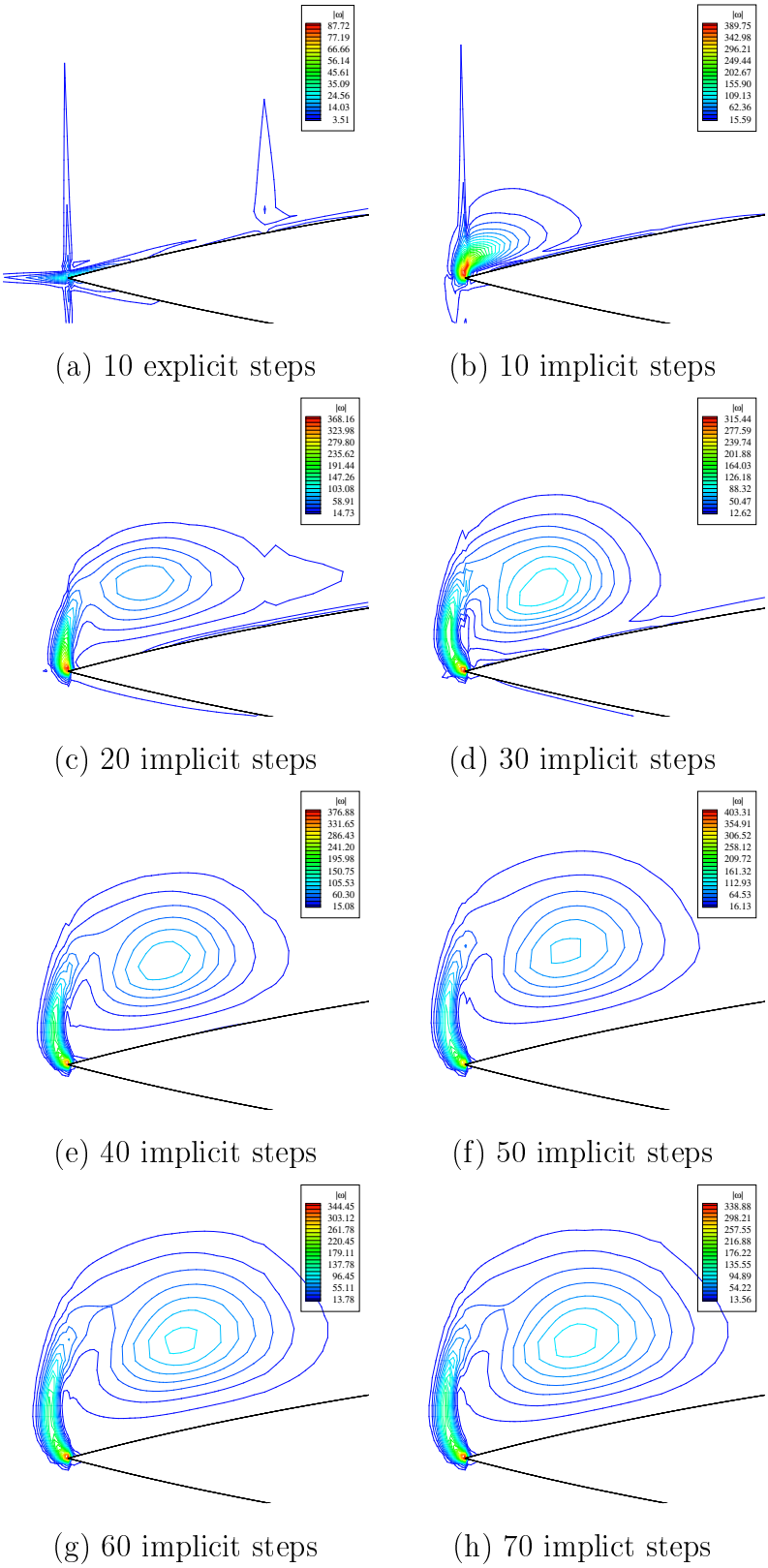

Figure 2.8: *Visualisation of Euler separation mechanism, vorticity magnitude contours*

pressure loss is defined as

$$TPL = 1 - \frac{P(1+\frac{\gamma-1}{2}M^2)^{\frac{\gamma}{\gamma-1}}}{\frac{1}{\gamma M_\infty^2}(1+\frac{\gamma-1}{2}M_\infty^2)^{\frac{\gamma}{\gamma-1}}} \tag{2.4}$$

where P is the local non-dimensional pressure, M is the local Mach number, and M_∞ is the freestream Mach number.

The solutions at $30\%c_r$ are shown for 7 intervals of 10 implicit steps at a CFL of 50 (after an initial 10 explicit steps at a CFL of 0.4). It should be noted that at no point in the computation does the flow become supersonic around the leading edge, and therefore the transient appearance of a shock is not the reason for inviscid separation in the current simulations. From figure 2.7 it is clear that as the flow begins to develop there is a loss in total pressure around the leading edge (figure 2.7(b)). As described by Eberle et al [106], in discrete Euler solutions in which a shear is present, a shear layer of finite thickness will be captured instead of fitting a contact discontinuity between the layers. If shear is present at the wing leading edge a vortex sheet will form. In accordance with Crocco's theorm an entropy rise will occur due to the captured vorticity in the shear layer, and a total pressure loss will result. As the computation progresses the region of total pressure loss expands forming a vortical structure near the leading edge (figures 2.7(c) and 2.8(c)). As the computation progresses further (figures 2.7(d)-(h) and 2.8(d)-(h)) the primary vortex moves into place, expanding and strengthening as the vorticity generation increases. Thus the primary vortices are formed.

2.7 Validation

Simulations were performed with farfield conditions at the outer boundary and were compared with the experiments of Löser [107]. Since the open test section was used the farfield solution will provide the fairest comparison. No corrections to the experimental data were made for effects of flow dispersion. The farfield simulations and their comparison to experimental data are discussed in this section. It should be noted that the open test section could be better modelled if pressure was measured

around the test section, thus allowing a pressure boundary condition to be added for a closer simulation of the experiment.

The test conditions of the experiment and simulations are detailed in table 2.6 for comparison.

	M_∞	Re	α_m	α_0	k
Simulation	0.4	Undefined	21^o	6^o	0.56
Experiment	0.12	3.1×10^6	21^o	6^o	0.56

Table 2.6: Experimental and computational test conditions

The computed surface pressure distributions for the stationary wing at 21^o angle of attack are compared with the experimentally obtained pressure distributions in figures 2.9 and 2.10 (the surface pressure distributions from the tunnel calculations are also shown and will be discussed later). The $30\%c_r$ and $60\%c_r$ stations have

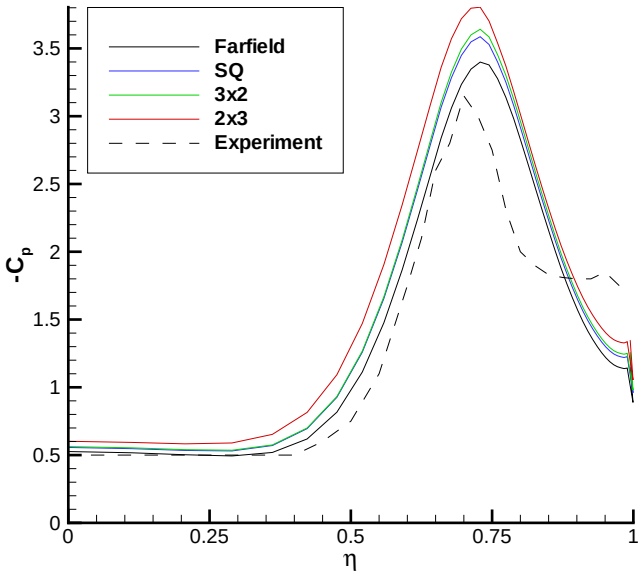

Figure 2.9: *WEAG-TA15 wing, Surface pressure distribution comparison at* $30\%c_r$

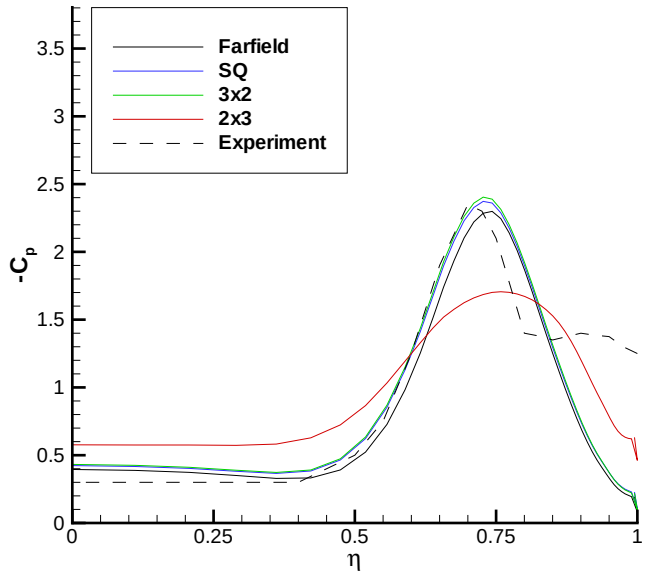

Figure 2.10: *WEAG-TA15 wing, Surface pressure distribution comparison at 60%c_r*

been extracted. At 30%c_r the Euler solutions predict the suction peak induced by the primary vortices, but no secondary vortices are present. The secondary vortices are due to boundary layer separation from the upper surface which clearly cannot be modelled with the Euler equations. It can be seen that the Euler code over-predicts the suction peaks of the primary vortices when compared to experiment, and also that the vortex core is more outboard (nearer the leading edge). The more inboard primary vortex is due to the lack of secondary vortices in the Euler solution, which tend to shift the primary vortex core inboard and off the surface. At 60%c_r the Euler suction peak is less than that of experiment and is also more spread out, indicating that vortex breakdown is occurring nearby [44] (as seen in figure 2.14(d)). It is concluded that the Euler solutions have predicted vortex breakdown too close to the apex.

For validation of the pitching simulations, the load curves for the reduced pitching frequency of 0.56 are given in figures 2.11 and 2.12. The pitching motion was performed by deforming the mesh using Trans-Finite Interpolation (discussed in section 1.5.1). A feature of figures 2.11 and 2.12, is that there is a distortion of the hysteresis loops near 27^o incidence on the downstroke. This is a direct result of the

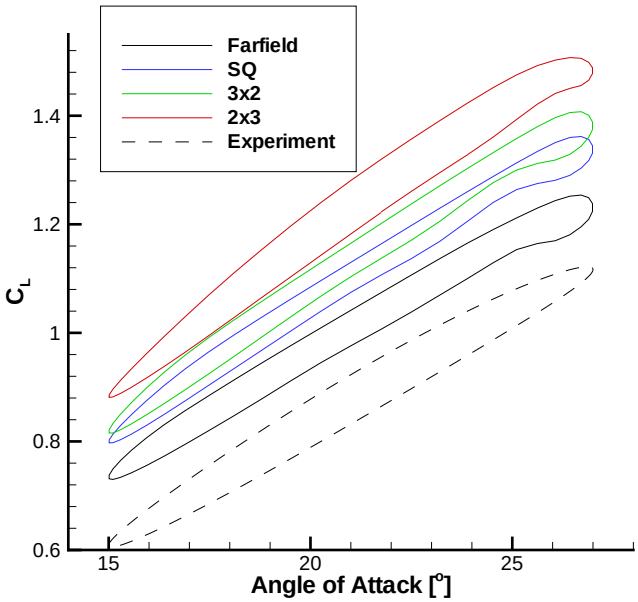

Figure 2.11: *WEAG-TA15 wing, Sinusoidal pitching lift curves, $k = 0.56$*

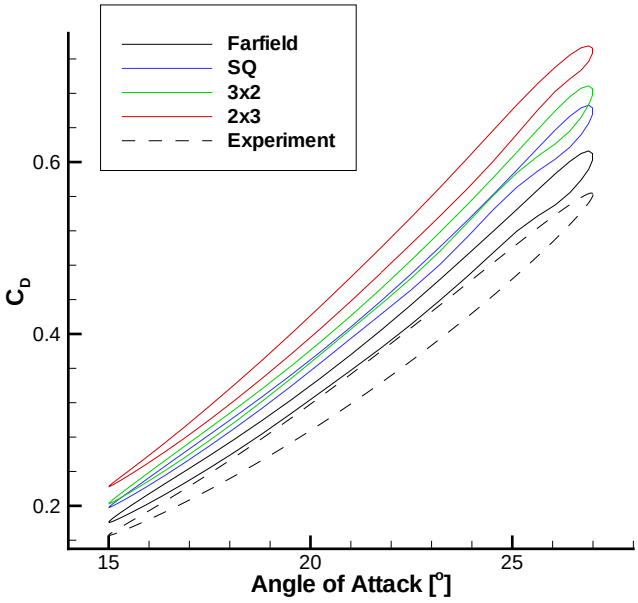

Figure 2.12: *WEAG-TA15 wing, Sinusoidal pitching Drag curves, $k = 0.56$*

early prediction of vortex breakdown in the Euler solutions, which has caused delta wing stall at the high incidence as the breakdown reaches the apex. A final feature of

figures 2.11 and 2.12 is the narrower hysteresis loop predicted by the Euler solutions when compared to those of experiment. This suggests that the unsteadiness (or time lag) is less pronounced in the Euler solutions. However, figures 2.11 and 2.12 show the Euler code is capable of predicting the hysteretic characteristics of pitching delta wings. Although the magnitude of the integrated forces is over predicted (when compared with experiment), it can be concluded that the Euler code is capable of predicting qualitative wind tunnel effects.

Since the experimental data was obtained at a freestream Mach number of 0.12, the effect of simulating the flow at a Mach number of 0.4 (which is more suitable for the flow solver as there is no need for low Mach number pre-conditioning) should be considered whan analysing the results. It is expected that at a freestream Mach number of 0.4, any compressibility effects in the solution are small, especially when observing solution trends. To test this a calculation was performed at a freestream Mach number of 0.2. The upper surface pressure distributions are compared with those from with a freestream Mach number of 0.4 in figure 2.13.

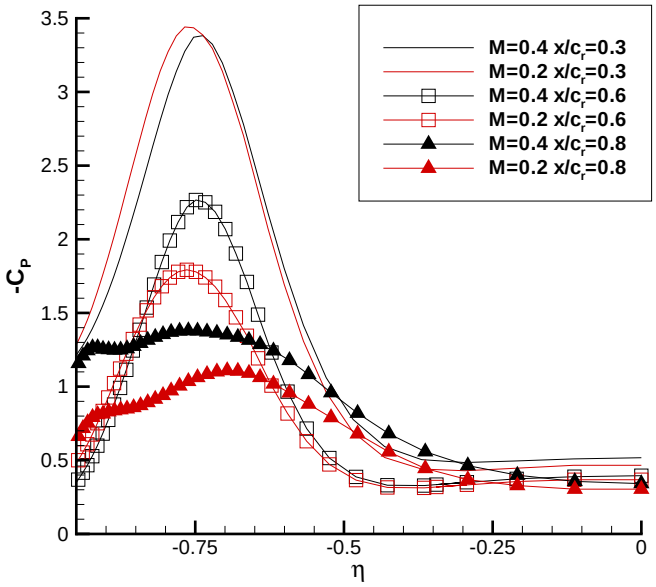

Figure 2.13: *WEAG-TA15 wing, Effect of Mach number on upper surface pressure distribution, farfield solution*

At $x/c_r = 0.3$ the suction levels are similar, though the primarysuction peak has moved outboard with the lower Mach number [109]. At $x/c_r = 0.6$, the suction peak with the freestream Mach number of 0.2 has lowered indicating an earlier vortex breakdown. However, qualitatively the solutions are comparable, so the use of a Mach number of 0.4 will allow a fair comparison with experimental data. For thin slender wings at moderate incidence, the influence of Mach number on the vortices is small providing the Mach number normal to the leading edge is less than 0.7 [3]. Further evidence of the minimal effect of compressibility in the Euler solutions will be given in chapter 4 where the RANS simulations are run at a lower Mach number of 0.2.

Given the previous discussion it appears that Euler simulations can quite accurately predict the leeside flow over delta wings (with a suitably refined grid). However, throughout this chapter it must be kept in mind that the Euler solutions can only highlight trends in wind tunnel influences due to the strong grid dependency of the solutions (discussed in section 2.5).

2.8 Results and discussion

2.8.1 Steady results

Before unsteady calculations were performed, steady calculations were made for each of the tunnels considered. The steady computations had the wing stationary at 21^o angle of attack. Figure 2.14 shows the steady breakdown locations for the farfield solution and the three tunnels. Figure 2.15 shows the steady tunnel pressure distributions as well as the farfield pressure distribution at the closest wall locations (for comparison purposes).

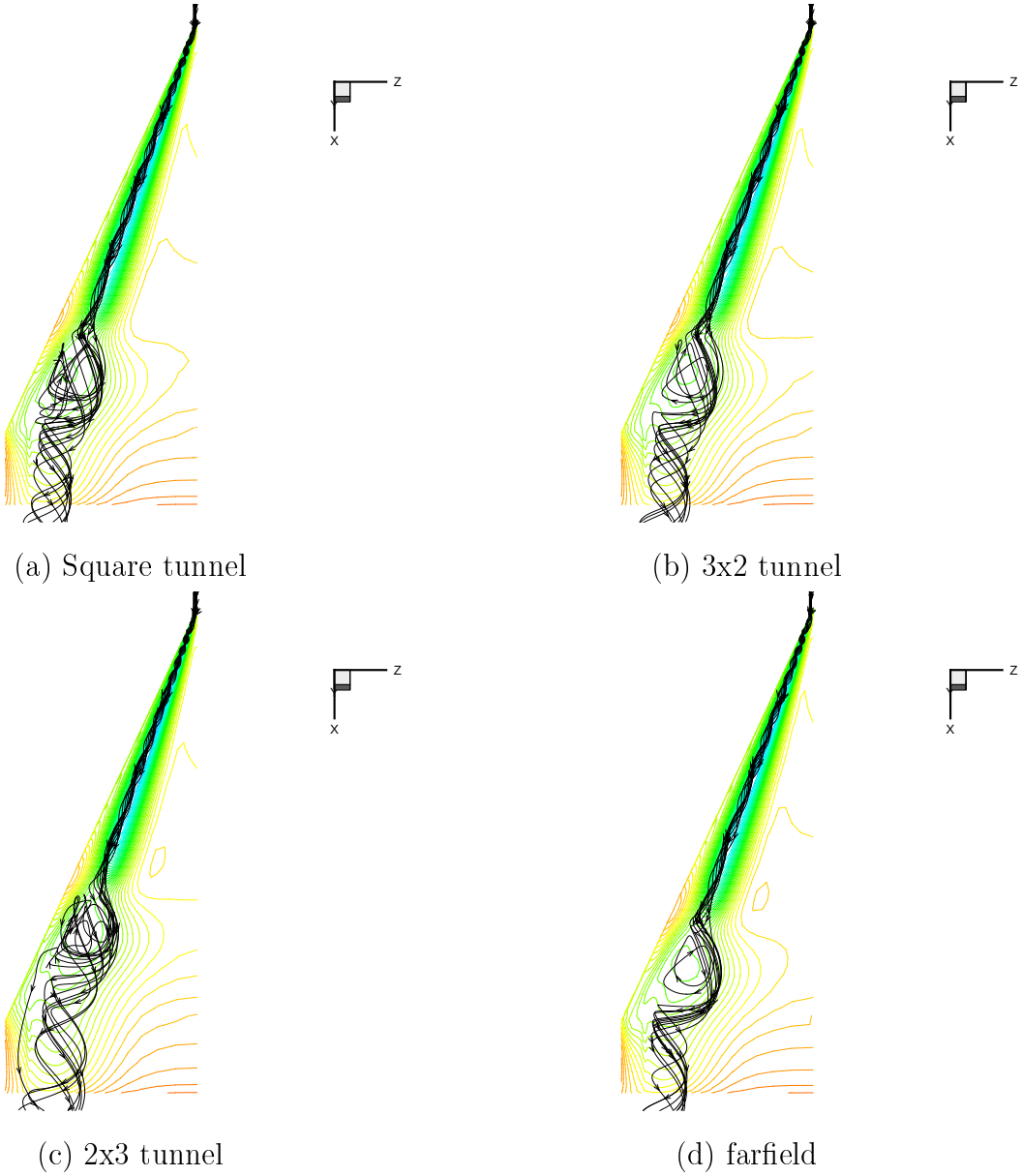

(a) Square tunnel

(b) 3x2 tunnel

(c) 2x3 tunnel

(d) farfield

Figure 2.14: *WEAG-TA15 wing, Upper surface pressure distributions and steady breakdown locations*

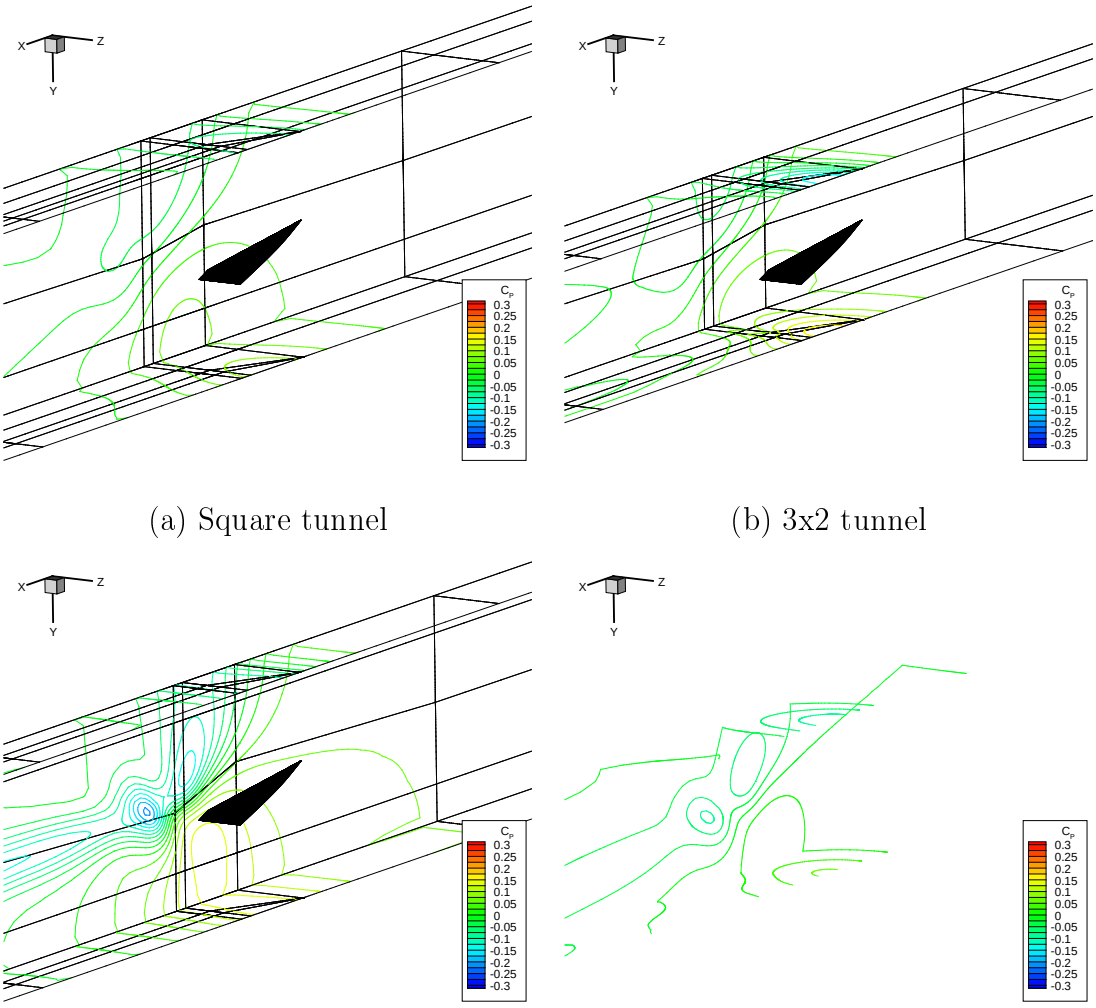

(a) Square tunnel

(b) 3x2 tunnel

(c) 2x3 tunnel

Farfield at z/c_r = -0.63, $y/c_r = \pm 0.63$

Figure 2.15: *WEAG-TA15 wing, Steady flow tunnel wall pressure distributions*

Considering first the vortex breakdown locations it can be seen from figure 2.14 that the most noticeable difference occurs in the 2x3 tunnel, shifting the breakdown location from approximately 64.9%c_r (farfield solution) to 60.0%c_r with these distances measured from the apex. The breakdown position has been determined by inspecting where the streaklines diverge from the core. Given that there is no significant shift in the breakdown locations when the roof and floor of the tunnel are brought closer to the wing (going from the square to the 3x2 tunnel), it can be concluded that the strongest interference must be due to the side walls. The steady breakdown locations are summarised in table 2.7.

TUNNEL	S/W	S/H	Breakdown Location
FARFIELD	-	-	66.9%c_r
SQUARE	0.42	0.42	66.6%c_r
3 X 2	0.42	0.63	66.5%c_r
2 X 3	0.63	0.42	60.0%c_r

Table 2.7: Summary of steady breakdown locations for wing at 21^o angle of attack

If we now consider the pressure distributions on the side walls (given in figure 2.15) for each of the steady solutions, we can see that there are quite significant differences when compared with similar locations from the farfield solution. The farfield pressure distributions were obtained by extracting slices at z/c_r = -0.63, and $y/c_r = \pm 0.63$. These locations correspond to the most inner wall positions considered. It is clear from figure 2.15 that the side walls of all the tunnels have a favourable pressure gradient (in the vicinity of the wing) in the axial direction. This is expected as the vortices move closer to the side wall as they extend towards the trailing edge of the wing. Near the trailing edge of the wing at the cropped tip, the side wall induced upwash is greatest, inducing the largest suction. The pressure gradient on the wall becomes more favourable as the side wall is moved closer to the wing, which is seen as we move from the square to the 2x3 tunnel. Another feature of the wall pressure distributions, on the 2x3 tunnel side wall in particular, is the presence of a clear vortical flow pattern on the side wall downstream of the wing's trailing edge. It is well known from experiment that the strong rotational

flow extends down the tunnel, even though the vortex may have burst over the wing. This vortical flow pattern (which extends $20c_r$ lengths down the tunnel, requiring the farfield boundary condition to be applied well away from the wing) is observed for the three tunnels, reducing in strength with decreasing S/W ratio [87].

The pressure distribution along the centreline of the tunnels and the farfield solution can be seen in figure 2.16. The change from the pressure to the suction side

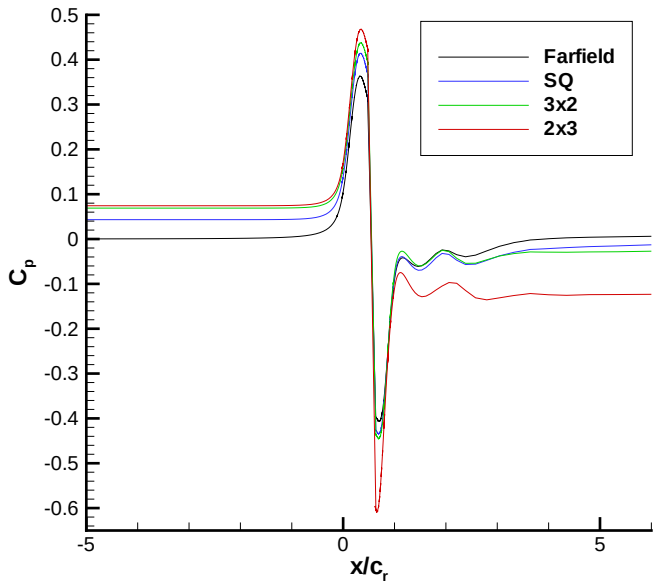

Figure 2.16: *WEAG-TA15 wing, Pressure distribution along centreline of the tunnel and farfield solutions*

of the wing is shown by the discontinuity near $x/c_r = 0.5625$. It is clear that the 2x3 tunnel produces the greatest blockage, as the static pressure upstream of the wing increases the most (implying lower dynamic pressure). This blockage reduces slightly in the 3x2 tunnel, and even further in the square tunnel. Interestingly, downstream of the wing the static pressure at the centreline is considerably lower in the 2x3 tunnel when compared to the other solutions. This is due to the fact that the highly rotational downstream flow is deflected upwards by the wall induced velocity components. This can be clearly seen in figure 2.15(c), and reduces with decreasing S/W ratio. Comparing the blockage from the 3x2 and 2x3 tunnels which

is almost equal upstream of the wing, it is suggested that tunnel blockage is not the major influence promoting vortex breakdown.

The steady pressure distribution beneath the vortex core line on the surface of the wing is shown in Figure 2.17. Clearly the largest suction occurs near the apex of the wing which agrees well with experimental results [21]. It is clear that with the 2x3 tunnel there is the largest increase in suction due to the tunnel walls. There are slight increases in suction with the square and 3x2 tunnels, however this increase is not to the same extent as in the 2x3 tunnel. An increase in suction beneath the vortex core due to tunnel walls was observed experimentally by Thompson and Nelson [89], who found that as the S/W ratio increased, the suction peak beneath the vortex core also increased.

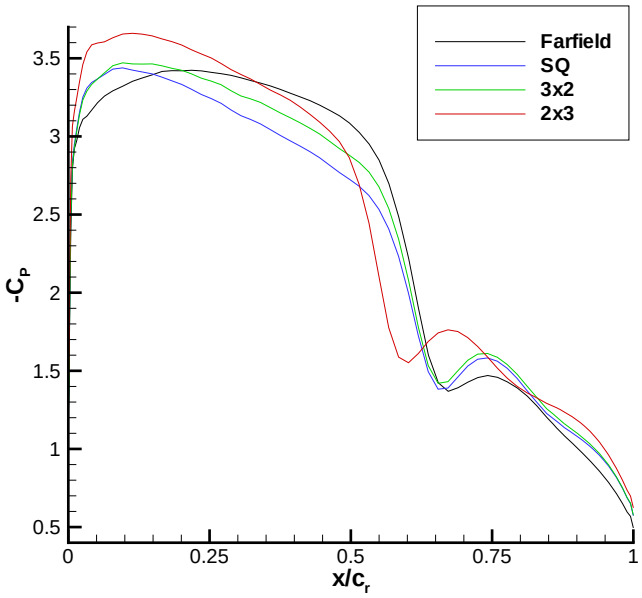

Figure 2.17: *WEAG-TA15 wing, Surface pressure distributions beneath the vortex core*

Figure 2.18 shows the flow angle (the angle at which the freestream has been turned up) in all tunnels at the spanwise location of $z/c_r \simeq -0.63$, the location of the 2x3 tunnel side wall. As expected, the proximity of the side wall induces the highest upwash along the wing when compared to that of the square and 3x2 tunnels. It is also clear that the mean effective incidence the wing experiences in

the 2x3 tunnel is much higher than that of the wing in the square and 3x2 tunnels. This can explain the suction peak increases seen in figure 2.17 as the wing is placed in the various tunnels. It is also clear that the 2x3 tunnel produces the greatest wall induced camber, since the induced upwash (subtracting the farfield flow angles from those in the tunnel solution) clearly rises quickest in the 2x3 tunnel. Weinberg [88] surmised that this induced camber effect will delay vortex breakdown in accordance with the experiments of Lambourne and Bryer [33] for a positively cambered wing. However it is clear from the measured breakdown locations in the tunnel solutions that the higher mean effective incidence appears to be the dominant influence on vortex breakdown.

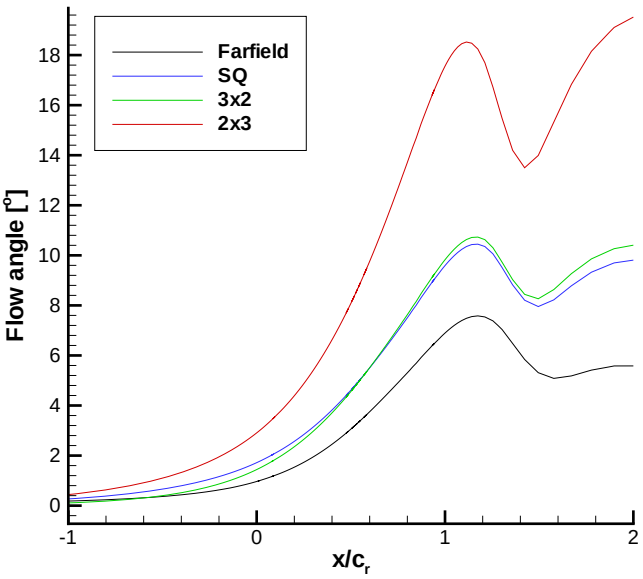

Figure 2.18: *WEAG-TA15 wing, Flow angles centred between roof and floor on the location of the 2x3 tunnel side wall, farfield and tunnel solutions*

Returning to figures 2.9 and 2.10, we see the surface pressure distributions from the four solutions at $30\%c_r$ and $60\%c_r$ respectively. At the $30\%c_r$ location, the 2x3 tunnel induces the highest suction peak, and also shifts the vortex core inboard the furthest (the location of the surface suction peak indicates the position of the primary vortex core [7]). This can be attributed to the side wall induced velocities which provide an additional upward velocity component. This will shift the vortex

core upwards and inwards. This increase in the suction peak was observed in previous investigations [89][87]. At the 60%c_r location it is clear the suction peaks are lowering and becoming wider, with the peak from the 2x3 tunnel being lowest and widest. This indicates the vortex is burst in the 2x3 tunnel while the others are nearing breakdown [44]. The increasing suction beneath the vortices indicates that they become stronger when placed within wind tunnel constraints.

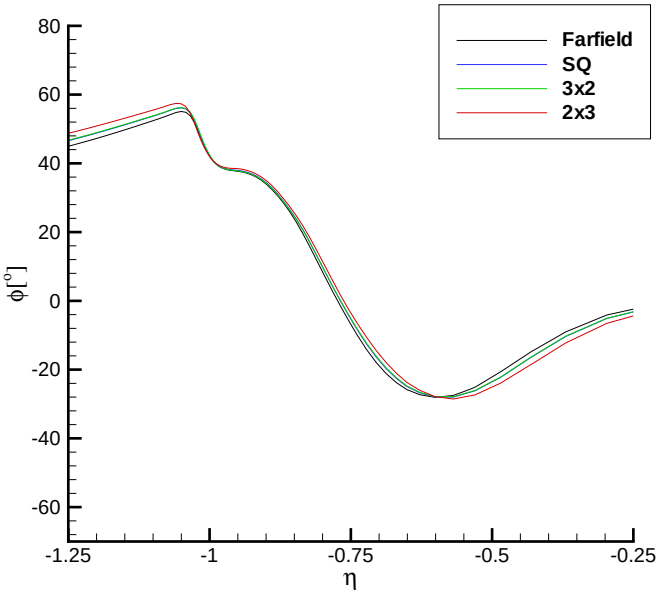

Figure 2.19: *WEAG-TA15 wing, Comparison of helix angles through vortex, x/c_r=0.3*

The helix angle distribution through the vortex core is shown in figure 2.19. The helix angle is defined as

$$\phi = tan^{-1}\left[\frac{-v}{u}\right] \tag{2.5}$$

where u and v are the components of velocity in the chordwise and normal-to-surface directions respectively (in body axes). Recalling the wall induced upflow demonstrated in figure 2.18, it is clear that the additional upward velocity component has tightened slightly the helix angle of the vortex. A tightening of the helix angle was observed to promote vortex breakdown in tubes [34]. The helix angles for the

square and 3x2 tunnels are very similar, incremented in comparison to that from the farfield solution. The helix angle for the 2x3 tunnel is even larger (the increment being twice as large as that from the square and 3x2 tunnels) as expected due to the closer side wall proximity.

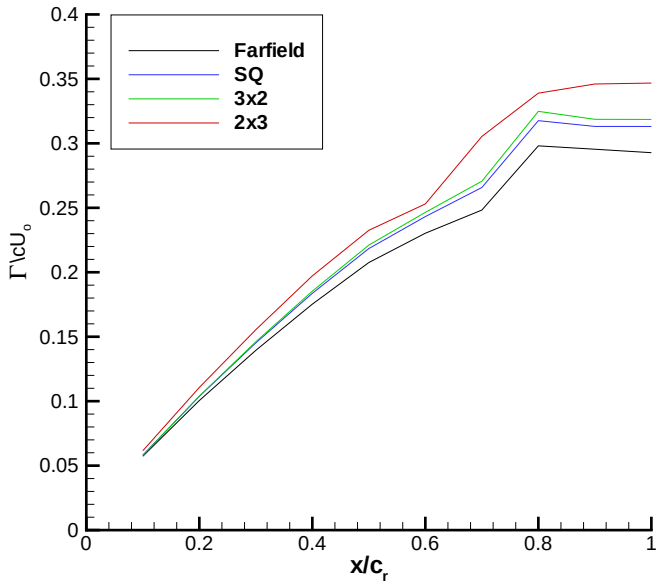

Figure 2.20: *WEAG-TA15 wing, Comparison of circulation distributions*

Figure 2.20 shows the circulation distribution (indicating the vortex strength) in the chordwise direction. The circulation was calculated by integrating the axial component of vorticity, ω_x, over slices along the wing. Clearly when a delta wing is placed inside a wind tunnel the leading edge vortices increase in strength. This is also shown by the increased suction peaks on the wing surface beneath the vortices. Evidently as vorticity is continually shed from the leading edge of the wing into the vortex, the circulation increases in the chordwise direction. The circulation curves from the square and 3x2 tunnels are very similar. This is a strong indication that the side walls are the main cause of strengthening the vortices, thus incrementing the circulation. This is seen again when the side walls are brought even closer to the wing (in the 2x3 tunnel) which increases the circulation further.

The distributions of ω_y and ω_z components of the vorticity vectors are shown in figures 2.21 and 2.22 respectively. The distributions are given at two chordwise

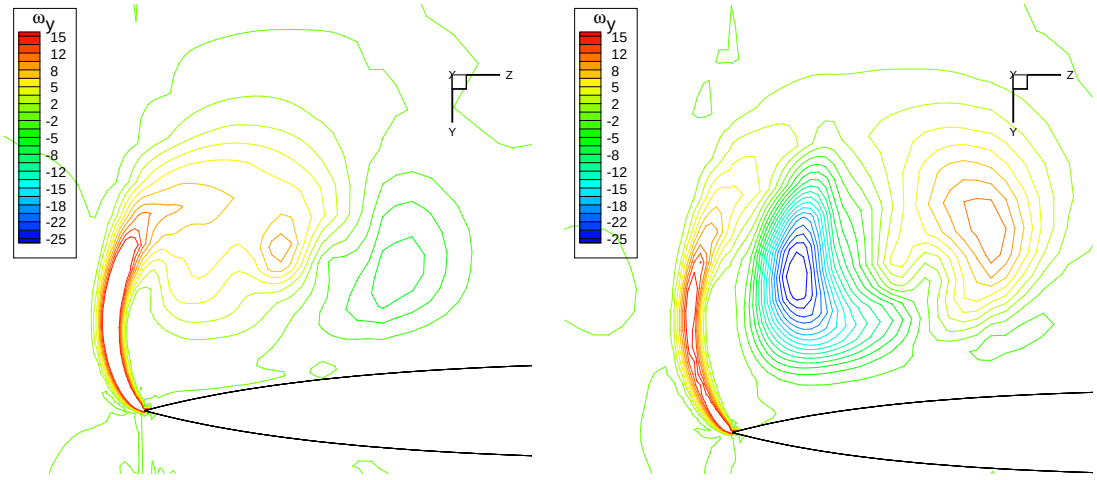

(a) x/c_r=0.6 (b) x/c_r=0.65

Figure 2.21: *WEAG-TA15 Wing, Distribution of ω_y components of vorticity, farfield solution*

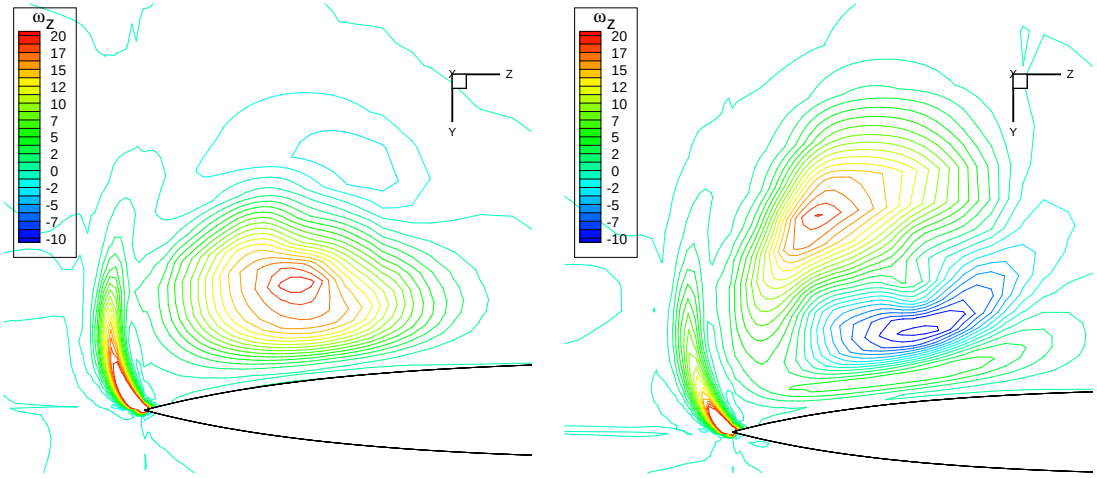

(a) x/c_r=0.6 (b) x/c_r=0.65

Figure 2.22: *WEAG-TA15 Wing, Distribution of ω_z components of vorticity, farfield solution*

stations of x/c_r=0.6 and x/c_r=0.65 for the farfield solution. Both these locations are upstream of vortex breakdown (breakdown was found at 66.9%c_r). If we contrast the signs of the two components at x/c_r=0.6 and x/c_r=0.65, we see that both the ω_y and ω_z components change sign. At the chordwise station of x/c_r=0.6 the components

of ω_y and ω_z are such that the rotation is in the sense that would tend to accelerate the flow in the vortex core. Now considering the sense of the rotations at x/c_r=0.65 we see that the ω_y and ω_z components are in the sense that would decelerate the core flow. Thus prior to vortex breakdown negative azimuthal vorticity is produced. The production of negative azimuthal vorticity was first proposed as an inviscid mechanism for vortex breakdown by Brown and Lopez [57]. A fuller discussion is given in section 3.7.3 for RANS solutions. The same behaviour is seen for the tunnel solutions.

2.8.2 Pitching results

Unsteady pitching calculations were performed at two reduced frequencies, k = 0.56 (experimental reduced frequency), and k = 1.5 (artificially large pitching frequency). The lift and drag curves for the k = 0.56 case are shown in figures 2.11 and 2.12, and for the k = 1.5 case in figures 2.23 and 2.24.

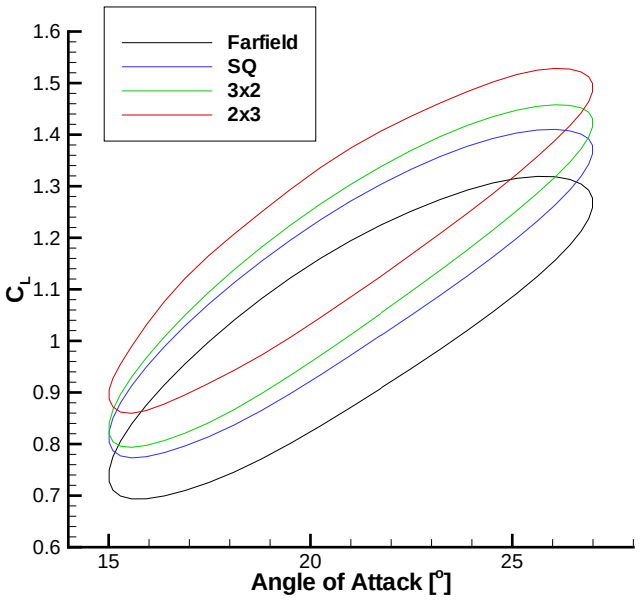

Figure 2.23: *WEAG-TA15 wing, Sinusoidal pitching lift curves, k = 1.5*

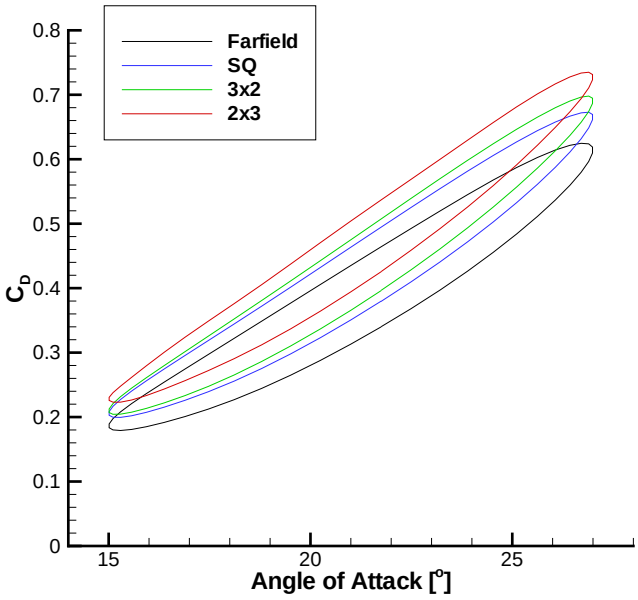

Figure 2.24: *WEAG-TA15 wing, Siusoidal pitching drag curves, k = 1.5*

As mentioned in the validation section, for the lower reduced frequency of k = 0.56 with farfield conditions at the outer boundaries, there appears to be a deformation of the hysteresis loop around 27^o angle of attack on the downstroke of the motion. This can be attributed to the fact that vortex breakdown is near the apex of the wing, as seen in figure 2.25. For this reason the higher reduced frequency of k = 1.5 was computed as vortex breakdown is expected to never get close to the apex, thus yielding more typical hysteresis loops shown in figures 2.23 and 2.24.

Figure 2.25 summarises the vortex breakdown locations at each point in the pitching cycle for the reduced pitching frequency of k = 0.56. It should be noted that the breakdown locations were taken as the point on the vortex core where the velocity magnitude was at a minimum. Although not presented here, it was observed that for the artificially large pitching frequency (k = 1.5), there was an increase in the phase lag of the breakdown motion [56], and a reduction in the magnitude of the breakdown location maxima and minima [37][65]. In order to visualise the extent of the tunnel wall interference for each tunnel considered, the wall pressure distributions are given at eight points in the pitching cycle in figures 2.26 to 2.28. It is clear from figure 2.25 that the 2x3 tunnel influences the breakdown locations

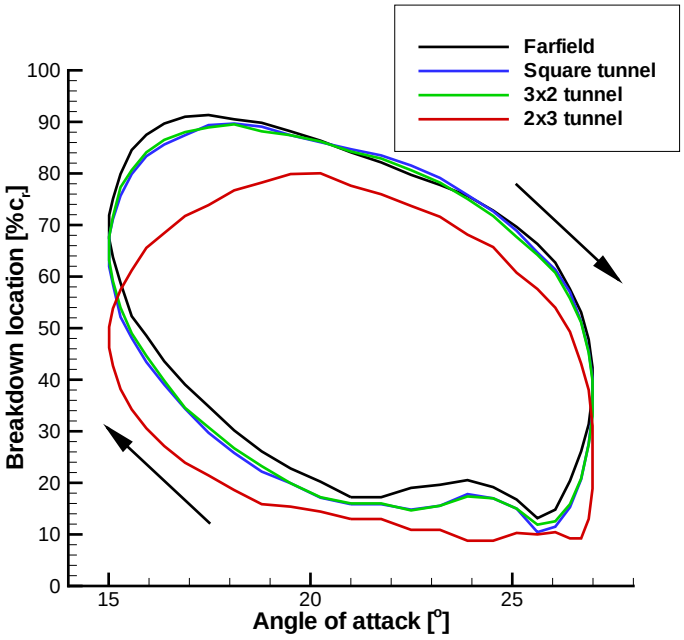

Figure 2.25: *WEAG-TA15 wing, Summary of sinusoidal pitching vortex breakdown locations, $k = 0.56$*

the most (as in the steady case), promoting vortex breakdown. Figure 2.25 also shows that the square and 3x2 tunnels tend to produce similar breakdown locations, which on the downstroke and the beginning of the upstroke, are slightly promoted in comparison to the farfield breakdown locations. It is therefore concluded that bringing in the roof and floor has little influence on the unsteady breakdown locations, indicating that roof and floor proximity is not a dominant factor in these unsteady flows. This is in contrast to the effect of bringing in the side walls. Comparing the square and 2x3 tunnel solutions, there is clearly a large variation in the breakdown location as the side walls come closer to the wing. This is a further indication that side wall proximity is the most dominant factor in tunnel wall interference on delta wing aerodynamics. If we look closely at figure 2.25 we see that the largest deviation of the breakdown locations from those obtained in farfield conditions occurs after the vortex has burst and is reforming (during the downstroke and the start of the upstroke). This is a consistent result from all three tunnels. A final obvious difference between the breakdown curves from the tunnel and farfield solutions is the gradients of the breakdown hysteresis loops. The large deviations in breakdown

locations during the vortex reformation (due to tunnel effects), appear to increase the phase lag of the breakdown motion in the tunnels relative to that in the farfield solution.

As mentioned previously, figures 2.26 to 2.28 show the wall pressure distributions at eight points around the pitching cycle. From the eight incidences shown in figure 2.28, it is clear that the highest tunnel interference appears to correspond to the highest incidences of the wing (figure 2.28(g)). Similarly the lowest tunnel interference appears to correspond to the lowest incidences of the wing.

If we examine the incidence at which the largest deviation between breakdown loops from the 2x3 tunnel and farfield solutions occurs, around 16.9^o on the upstroke, examination of the tunnel wall pressure distributions at this point (figure 2.28(d)) suggests there is little interference in comparison to that at high incidences (figures 2.28(f-h)). This suggests that the tunnel interference is not in phase with its effect on the breakdown location. Like the effect of increasing incidence, the effect of high tunnel interference on the breakdown location appears to lag the motion of the wing. Thus the high interference effect at 27^o, for example, will not be seen on the breakdown location until some point on the downstroke (similar to the effect of the maximum incidence not being seen until during the downstroke). Recalling figure 2.25 we see that the breakdown location appears to be held near the apex slightly longer in the 2x3 tunnel, compared with the other solutions. If we look at each of the tunnel wall pressure distributions at the high incidences (figures 2.26(f-h), 2.27(f-h), and 2.28(f-h) for the square, 3x2, and 2x3 tunnels respectively), we see that the tunnel interference from the 2x3 tunnel is much stronger in comparison to the square and 3x2 tunnels. Since it appears that the tunnel interference effect on the breakdown motion lags the motion of the wing, the effect of high tunnel interference at high incidence is mainly seen during the vortex reformation phase.

It should be noted that on the upstroke of the pitching motion, despite a phase lag in the breakdown motion, the tendency is for vortex breakdown to move towards the apex (after reaching its most downstream location). As was discussed in the previous steady simulations, tunnel side walls tend to promote vortex breakdown. Thus the combination of the increasing incidence and the effect of the side walls is to cause breakdown to move to the apex. Here both effects have the same influence, to

cause breakdown to travel to the apex. Considering the downstroke of the motion, again despite a phase lag in breakdown motion due to the pitching motion, we see that the decreasing incidence causes breakdown to move to the trailing edge. However, the side walls still tend to promote vortex breakdown. Thus it can be expected that the side walls hinder the reformation of the vortex (especially after the higher incidences where tunnel effects are strongest) and thus, with the high interference effect at high incidences, the largest tunnel interference occurs during the vortex reformation.

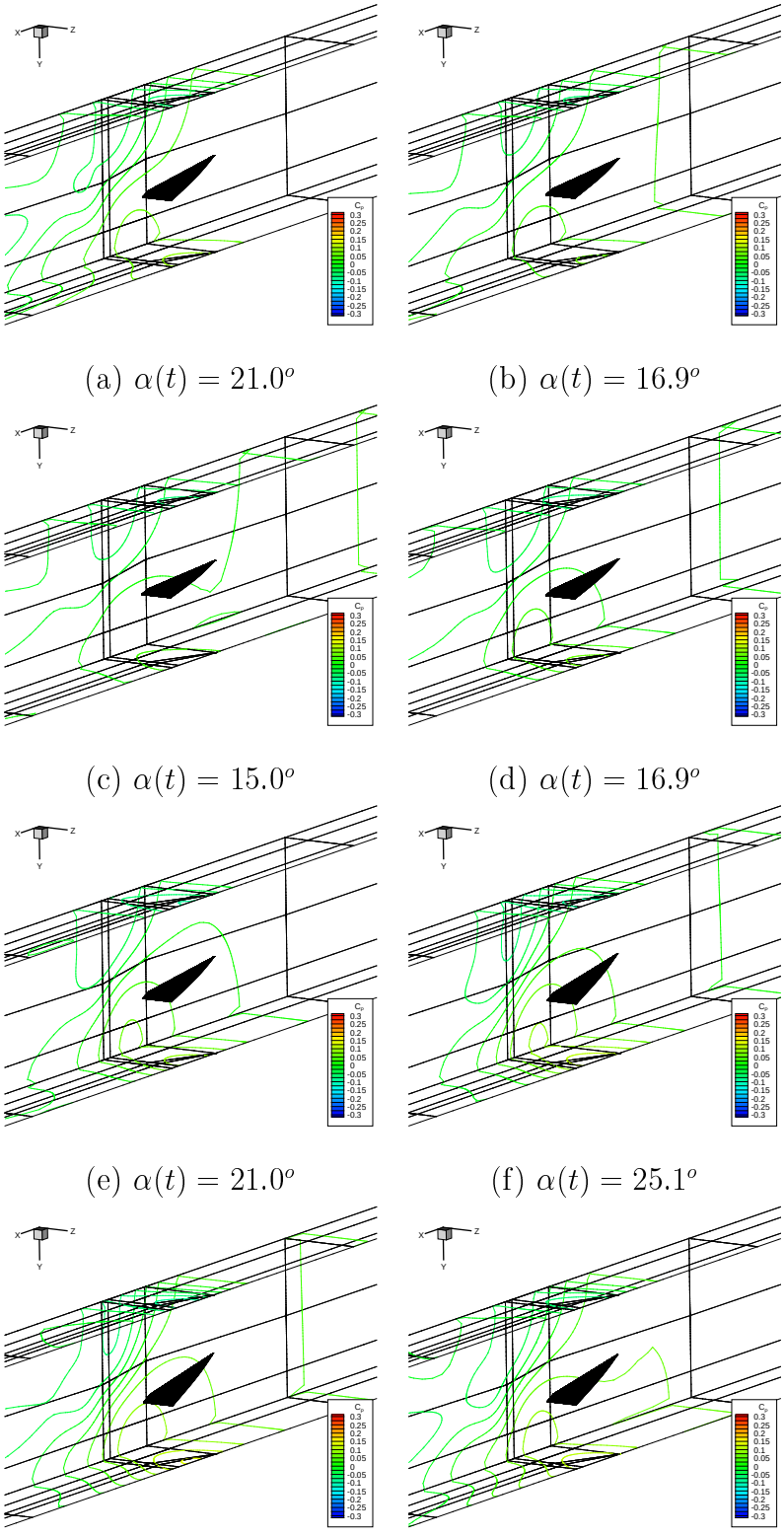

(a) $\alpha(t) = 21.0^o$ (b) $\alpha(t) = 16.9^o$

(c) $\alpha(t) = 15.0^o$ (d) $\alpha(t) = 16.9^o$

(e) $\alpha(t) = 21.0^o$ (f) $\alpha(t) = 25.1^o$

(g) $\alpha(t) = 27.0^o$ (h) $\alpha(t) = 25.1^o$

Figure 2.26: *WEAG-TA15 wing, Sinusoidal pitching, tunnel wall surface pressures within square tunnel, k = 0.56*

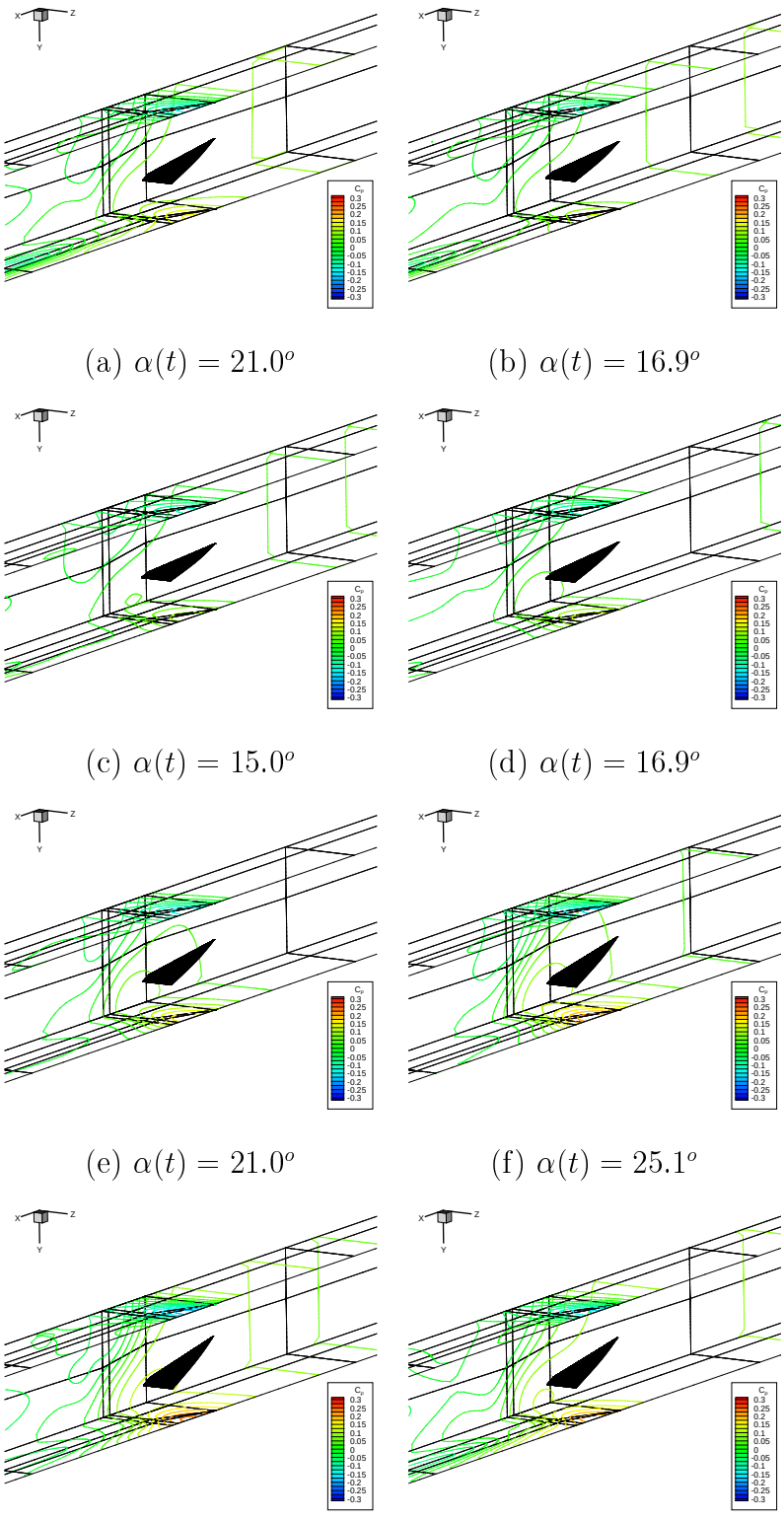

(a) $\alpha(t) = 21.0^o$ (b) $\alpha(t) = 16.9^o$

(c) $\alpha(t) = 15.0^o$ (d) $\alpha(t) = 16.9^o$

(e) $\alpha(t) = 21.0^o$ (f) $\alpha(t) = 25.1^o$

(g) $\alpha(t) = 27.0^o$ (h) $\alpha(t) = 25.1^o$

Figure 2.27: *WEAG-TA15 wing, Sinusoidal pitching, tunnel wall surface pressures within 3x2 tunnel, k = 0.56*

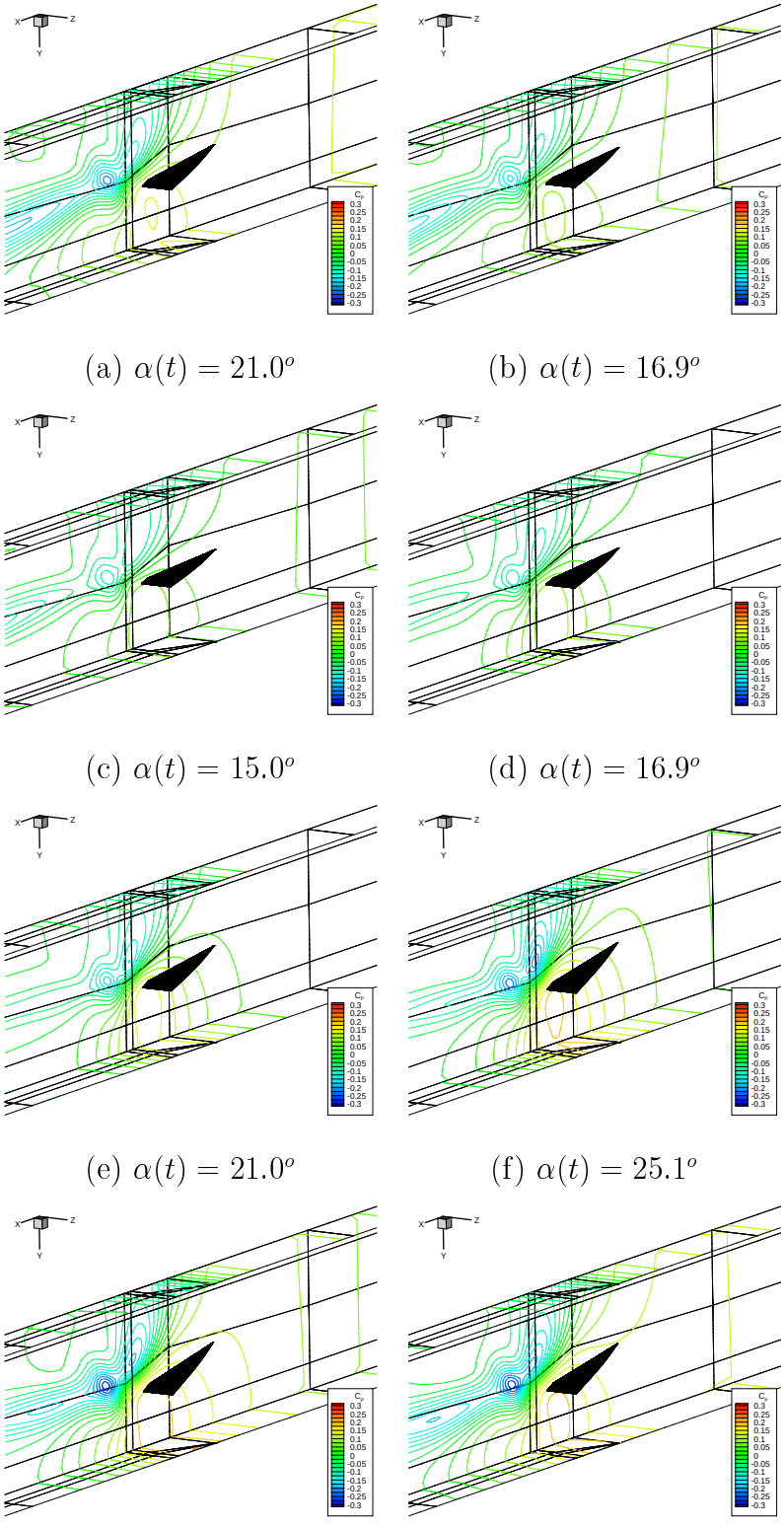

(a) $\alpha(t) = 21.0^o$ (b) $\alpha(t) = 16.9^o$

(c) $\alpha(t) = 15.0^o$ (d) $\alpha(t) = 16.9^o$

(e) $\alpha(t) = 21.0^o$ (f) $\alpha(t) = 25.1^o$

(g) $\alpha(t) = 27.0^o$ (h) $\alpha(t) = 25.1^o$

Figure 2.28: *WEAG-TA15 wing, Sinusoidal pitching, tunnel wall surface pressures within 2x3 tunnel, k = 0.56*

2.9 Conclusions

The effect of wind tunnel wall constraints on steady and pitching delta wing aerodynamics has been investigated using solutions of the Euler equations. It has been shown in both the current and previous investigations that Euler simulations can adequately model the primary vortices which occur on delta wings at incidence, and their response to manoeuvres. Taking into account the limitations of the Euler model the following conclusions can be drawn :

- Wind tunnel wall constraints promote vortex breakdown. This result agrees qualitatively with the experimental results of Thompson and Nelson [89] and Pelletier and Nelson [90].

- For rectangular shaped wind tunnels the presence of the roof and floor has little influence on vortex breakdown. This was observed by comparing the square and 3x2 tunnel breakdown locations.

- Tunnel side walls appear to be the dominant influence promoting vortex breakdown. The close proximity of the 2x3 tunnel side walls significantly promoted vortex breakdown.

- Wind tunnel blockage has little or no influence on vortex breakdown. This was observed by comparing the 3x2 and 2x3 tunnel blockages, and the vortex breakdown locations obtained.

- Tunnel side walls increase the mean effective incidence of the wing. Despite the presence of a possible induced camber effect, it appears the effect of an increase in the mean effective incidence is dominant in promoting vortex breakdown.

- Downstream of the wing it has been shown that the tunnel side walls displace the rotational post breakdown flow upwards towards the centre of the wind tunnel.

- The presence of tunnel side walls increases the helix angles of the vortices. This increase in helix angle increases the strength of the leading edge vortices. Comparing the solutions from the square and 3x2 tunnels we see that the

vortex strengths are similar indicating that the roof and floor proximity has little effect on vortex strength.

- Tunnel wall constraints tend to promote vortex breakdown when the wing undergoes sinusoidal pitching motion. Like the static cases the side walls have the dominant influence promoting breakdown.

- For sinusoidal pitching motion the extent of the tunnel influences is dependent on whether the wing is on its upstroke or downstroke.

- Vortex reformation is delayed by tunnel side walls which tend to promote vortex breakdown. As the wing pitches down and tunnel interference lowers, breakdown reaches its most downstream location later in the cycle, compared with the farfield solution. This is due to the delay of vortex recovery which is due to the high tunnel interference at high incidence.

- The side wall influence tends to be greatest on the downstroke of the motion. This has been shown in the simulations as large deviations in the breakdown locations between the 2x3 tunnel solutions and the farfield solutions. This is due to the fact that the wing is moving from a state of high tunnel interference to low tunnel interference.

The results of this study indicate that when testing delta wings in a wind tunnel, the model should be orientated such that the side walls are as far away from the model as possible. It has also been shown that for testing with a S/W ratio less than 0.42, tunnel wall influences are likely to be minimal.

Navier-Stokes calculations need to be performed in order to assess the viscous effects. The effect of tunnel influences on the secondary vortices must also be investigated as the presence of the secondary vortices influences the position of the primary ones. It is expected that the trends will not vary with viscous flow but this must be confirmed.

As with all CFD simulations validation of the solutions via comparison with experiment is imperative. These simulations have been designed in such a way that experimental validation is possible. Although careful consideration of support

interference must be taken into consideration, a plausible experimental program could involve steady tests on a delta wing in a 3x2 tunnel with below model vertical mounting, then mounting the wing on the side wall which would effectively be testing the wing in a 2x3 tunnel. Unsteady simulations will be much harder due to the support structures required for dynamic testing.

Chapter 3

Peformance of turbulence models for delta wing flows

3.1 Introduction

Three dimensional Navier-Stokes computations are necessary to correctly predict the complex leeward side flow characteristics of delta wings. As shown in chapter 2, Euler simulations can't predict the presence of secondary vortices, due to the inviscid flow assumption eliminating boundary layer separation. Further more at high Reynolds' numbers, the flow becomes turbulent requiring the turbulent fluctuations to be modelled. In fact, most practical flows of engineering interest are turbulent. Even a flow which has a mean which is steady is subjected to disturbances which amplify downstream, producing larger fluctuations of the flow variables from the mean, eventually becoming completely turbulent with a continuous range of frequencies and wavelengths [110]. Turbulent flows tend to transfer some of the mean flow kinetic energy to turbulent scales. This is known as the cascade process which transfers kinetic energy from the larger to the smaller eddies. Dissipation of kinetic energy to heat occurs via the smallest eddies. The rate at which the larger scale eddies supply energy is given by parameters such as ϵ, the dissipation per unit mass, or ω, the specific dissipation rate. In the past, turbulence modelling of complex flows mainly employed algebraic turbulence models such as the Baldwin-Lomax model [111] amongst others.

In recent years, turbulence modelling based on turbulent transport equations has become the standard [112]. Prandtl postulated computing a characteristic velocity scale for turbulence. He chose the specific turbulent kinetic energy, k. Models employing several transport equations are currently in use by CFD practitioners, though most of these employ the Boussinesq approximation. This implies that the Reynolds stress tensor is aligned with the mean flow tensor. The one-equation models are incomplete as they relate the turbulent length scale to some typical flow dimension. This is application dependent and consequently two-equation models provide an equation for the turbulence length scale and are therefore independent of ad-hoc assumptions regarding the scales of turbulent structures. Two equation eddy viscosity models are the most widely used models today.

Other families of turbulence models aiming at improving the generality of predictions have been developed. One example is Large Eddy Simulation (LES). Figure 3.1 shows a typical energy spectrum of a turbulent flow. LES involves computing the largest eddies as they are considered to be directly effected by the boundary conditions, and therefore must be computed. On the other hand it is assumed that the smallest eddies are independent of boundary conditions and thus can be modelled. LES models are spatially filtered, ie. it is the cell dimensions of the computational grid which determine how much of the energy spectrum is modelled and how much is computed [112]. Thus as a grid is refined the amount of turbulence modelling is reduced. However, LES does have trouble with near wall solutions as the grid requirements approach that of Direct Numerical Simulation.

Direct Numerical Simulation (DNS) of turbulent flows is a complete time-dependent solution of the equations of conservation of mass, momentum and energy. In prinicple, the computational grid must be fine enough to resolve even the smallest eddies, i.e. the complete energy spectrum of figure 3.1. The problem with this is obvious; the mesh sizes required are enormous at practical Reynolds numbers. As estimated by Wilcox [112], for a DNS simulation of a channel flow with a Reynolds number of 230,000, 2.1×10^6 grid points are required, with 114,000 timesteps for time accuracy of the solution. With these requirements for a simple channel flow it is evident that high Reynolds number DNS simulations of flow around aircraft is currently beyond the capabilities of modern computers.

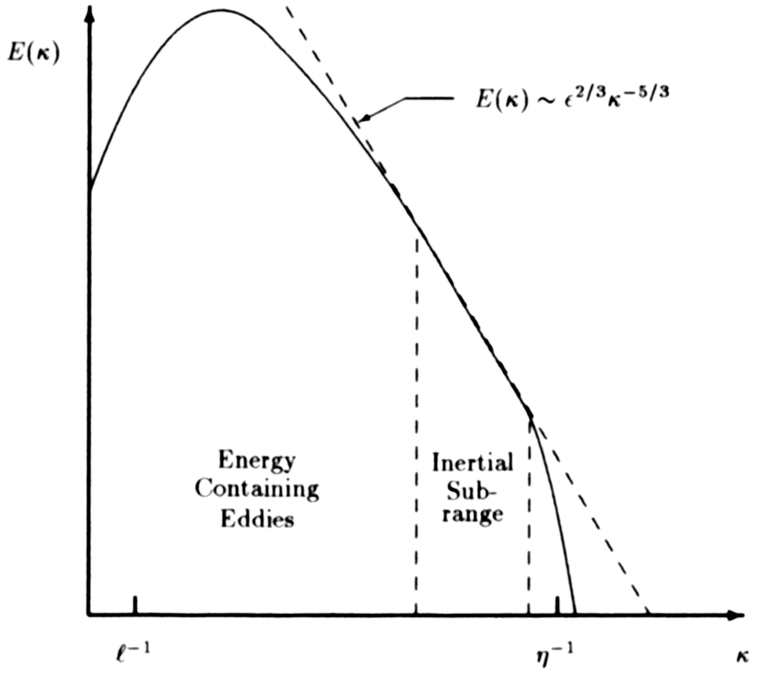

Figure 3.1: *Energy spectrum for a turbulent flow - log-log scales - [112] p317*

In order to improve turbulence modelling whilst working within current computational constraints, Detached Eddy Simulation (DES) was suggested by Spalart et al. [113]. DES is a hybrid method in which a RANS turbulence model is used to simulate turbulence in the boundary layer, but elsewhere LES is used. RANS turbulence models are known to predict boundary layers at low computational cost, and LES can accurately predict large regions of separated flow. Still this approach requires *a-priori* knowledge of the solution in order to estimate the limits of the RANS region.

The aim of this chapter is to apply various turbulence models in order to provide an assessment of their performance, and to allow the selection of the most appropriate model for viscous tunnel calculations (chapters 4 and 5). The PMB3D flow solver (discussed in section 1.5) is used in all calculations. In this chapter, the turbulence models implemented in PMB3D will be briefly described, and their ability to predict delta wing aerodynamics will be discussed. Conclusions on the most suitable model are drawn.

3.2 Previous Work

Several CFD investigations on delta wings have been performed using a laminar flow assumption, thus eliminating the need for turbulence modelling. Such simulations have produced fairly realistic results [70][104][114][26][115][71][116][117]. However, clearly we cannot realistically model high Reynolds number turbulent flows with a laminar flow assumption.

Previous work on high Reynolds number turbulent delta wing flows have highlighted the deficiencies of current RANS turbulence models when predicting vortical flows. Investigations have been conducted using the Baldwin-Lomax algebraic turbulence model with the Degani-Schiff [118] modification [119][120][121][45][109][122] [123][124]. This turbulence model by its very nature only accounts for turbulence in the boundary layers on the wing surface, therefore the turbulence in the shear layer (which rolls up forming the primary vortex) is not modelled. A final point is the need to specify a turbulence length scale, which for separated flows can be difficult and ambiguous.

Morton et al. [27] applied the Spalart-Allmaras one-equation model to a 70^o delta wing with and without a vortical flow correction. Without the vortical flow correction it was found that the turbulent eddy viscosity was excessively high, dissipating vorticity and eliminating vortex breakdown. The solutions were considerably improved with the vortical flow correction (an additional destruction term was included to limit the production of eddy viscosity in regions of high vorticity), which were noted to compare remarkably well with Detatched Eddy Simulation solutions (discussed below).

In order to eliminate the need for specifying a length scale, higher-order turbulence models can be used. Gordnier [125] used the 2-equation k-ϵ turbulence model to predict the flow over a 65^o delta wing. It was found that too much eddy viscosity was produced in regions of high vorticity (such as in vortex cores), and therefore modifications to the model were made, similar to those of Menter [126] (equation 3.3) and Dacles-Mariani et al. [127]. Dacles-Mariani et al. applied the Baldwin-Barth one equation turbulence energy model to the flow of a wing tip vortex and found excessive levels of turbulence with the standard model. They therefore ap-

plied a modification to the production term, limiting it by a linear function of the vorticity magnitude. These modifications to the $k-\epsilon$ model limited the production of turbulent kinetic energy improving the flow predictions.

Recently two-equation models have been used for the prediction of the flow around rolling and coning delta wings, in transonic flows. The four participants (one of which was Glasgow University) of the WEAG THALES JP12.15 Common Exercise 1 [128] used various forms of the $k-\omega$ turbulence model, each requiring modifications to reduce the eddy viscosity levels in the vortex cores. Modifications used by two of the participants (NLR and Glasgow University), which were proposed by Brandsma et al. [129], will be discussed later in this chapter.

A DES model using the Spalart-Allmaras RANS turbulence model has been used recently by Morton et al. [27], and Mitchell et al. [28], for the prediction of the unsteady flow around a 70^o delta wing (the case considered in this chapter) with very promising results. It should also be noted that using LES has the advantage that as the grid is refined the turbulence modelling is used less, since LES only models turbulence length scales smaller than the local cell dimensions.

3.3 Test case : ONERA 70^o Wing

We consider a subsonic case for a 70^o delta wing at 27^o angle of attack. At this incidence vortex breakdown is occurring over the wing. Extensive flow visualisation data is available for validation purposes [5][130] and this wing has been used in previous investigations [131].

The wing has a leading edge sweep of 70^o, a root chord length of 950mm, a trailing edge length of 691.5mm, flat upper and lower surfaces, and a leading edge bevel of 15^o. The wind tunnel model had a blunt trailing edge 20mm thick which has been beveled (15^o bevel) in the computational model to simplify grid generation.

The wing was tested in the ONERA F2 tunnel (situated at Le Fauga-Mauzac Center, near Toulouse, France) which has a working section of height 1.8m, width 1.4m, and length 5m (see figure 3.2). It is a subsonic, continuous, closed-return tunnel. The wing was also tested in the ONERA S2Ch tunnel situated at the Chalais-Meudon Centre (ONERA) which is of quasi-circular cross-section with a

diameter of 3m and a test section length of 4.93m.

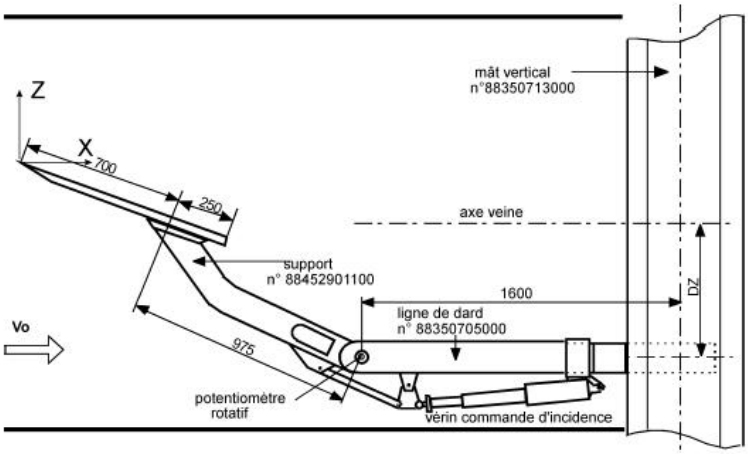

Figure 3.2: *Schematic of ONERA F2 tunnel, taken from reference [5], page 96*

The flow conditions for which extensive experimental data from the ONERA F2 tunnel are available are given in table 3.1.

Incidence	27^o
Reynolds number	1.56×10^6
Freestream velocity	24m/s ($M_\infty = 0.069$)

Table 3.1: Experimental conditions for testing of ONERA 70^o wing in ONERA F2 tunnel

For these flow conditions, flow visualisation of velocity components, vorticity components, turbulent kinetic energy components and local static pressure are available in various planes. This data was obtained using three dimensional LDV. Vortex breakdown locations are also available based on where the axial component of velocity becomes negative.

It should be noted that in the simulations the Reynolds number has been matched, however the Mach number is 0.2, compared with the lower Mach number of 0.069 in the experiment. Since the current work is based on a high speed flow solver, a freestream Mach number of 0.2 was used to avoid any possible convergence issues. Despite the higher Mach number of the simulations, it is assumed that since

the Mach number is low subsonic, compressibility will be negligible and the vortex structure will not alter significantly and therefore the vortex should be adequately modelled. Visbal and Gordnier [109] investigated the effects of compressibility on vortex breakdown for a 75^o delta wing at $34 - 35^o$ angle of attack, by varying the freestream Mach number from 0.2 to 0.95, holding the Reynolds number constant at 2×10^6. For the static case, prior to breakdown there did not appear to be any significant difference in the vortex structure. However, the secondary separation line tended to move inboard with increasing Mach number.

All computations were conducted on a coarse grid which was extracted from the finer grid. The coarse grid was obtained by extracting a level in all three directions. The solution from the coarse grid was then used as a starting solution for the fine grid allowing faster convergence on the fine grid. For the turbulence model study, 10 explicit steps at a CFL of 0.4, and 1000 implicit steps at a CFL of 10 were used on the coarse grid. The fine grid calculations used 3000 implicit steps at a CFL of 5 (a conservative value) when being started from the coarse grid calculations.

In summary the test case flow conditions used for the turbulence model study are given in table 3.2.

Incidence	27^o
Freestream Mach Number	0.2
Reynolds Number	1.56×10^6

Table 3.2: RTO Task Group AVT-080 on "Vortex breakdown over slender wings" - Test case conditions

Transition was observed to occur at around $40\%c_r$ in experiment, however the CFD simulations assume a fully turbulent flow. Since the effect of Reynolds number on breakdown is minimal, the effect of transition is expected to solely alter the position of the primary vortex and secondary separation location [132].

3.4 Computational grid

For all preliminary computations an H-H topology was used. The wing was meshed at 0^o angle of attack with the freestream velocity vector being rotated for the flow at incidence. As described in section 1.5, the axis system used by the PMB3D flow solver has the x and y axes in the longitudinal plane, with the z axis spanwise. The non-dimensional cell height normal to the wing surface was $10^{-6}c_r$. As with the WEAG-TA15 wing used in chapter 2, no support has been modelled (the support is an elbow connected to the windward surface of the wing [5], see figure 3.2). For further ease of grid generation no tunnel walls have been included. The tunnel influence is discussed in detail in chapter 4. Only half of the wing was considered.

Total number of grid points	3,969,810
Normal to upper surface	117
Normal to lower surface	75
Streamwise	99
Spanwise	79

Table 3.3: Turbulence model study grid dimensions

The dimensions of the grid used for the turbulence model study are given in table 3.3

3.5 Results and discussion

Preliminary calculations with the three turbulence models implemented in PMB3D have been applied to this test case. As described in Appendix B the models are the 2-equation k-ω and SST models, and the 1-equation Spalart-Allmaras (SA) model. Examination of the convergence histories indicates that in all simulations the mean flow residual converged at least four orders of magnitude.

The upper surface pressure distributions predicted with the three turbulence models can be seen in figure 3.3. On the port half of the wing the experimental surface pressure distribution is shown (taken from reference [5]), and on the star-

board half the computed surface pressure distributions. Qualitatively the solutions from all turbulence models appear to compare well with measurements, including the prediction of at least a primary vortex structure. Comparing the suction levels, the suction peaks have also been predicted reasonably well.

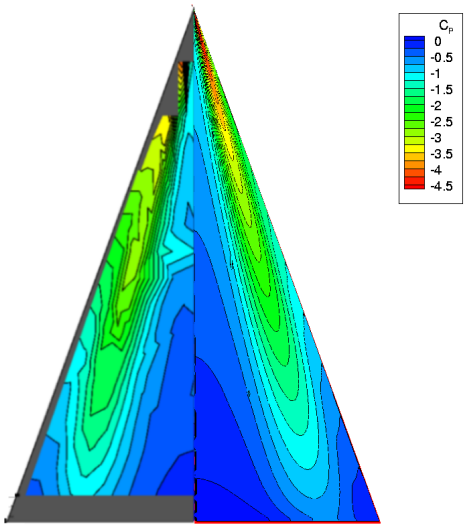

(a) Spalart-Allmaras

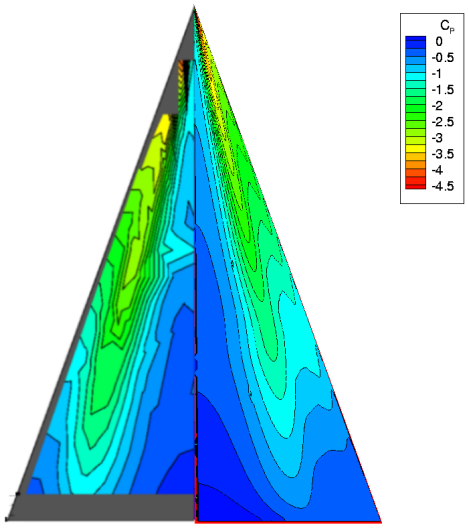

(b) SST

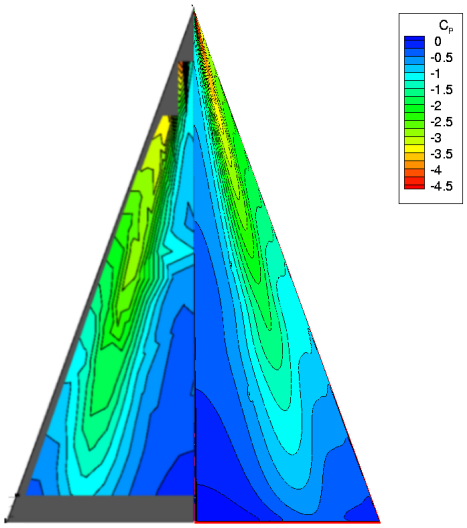

(c) Standard k-ω

Figure 3.3: *ONERA 70^o wing, Upper surface pressure distributions*

The upper surface skin friction distributions and shear stress streamlines are given in figure 3.4. The experimental oil flow visualisation is on the port half of the

wing, and on the starboard side is the computed result. As described in reference [5], the experimental secondary separation line is seen at the intersection of the green and red dye regions (two different colours of dye were used in the experiment to highlight the secondary separation).

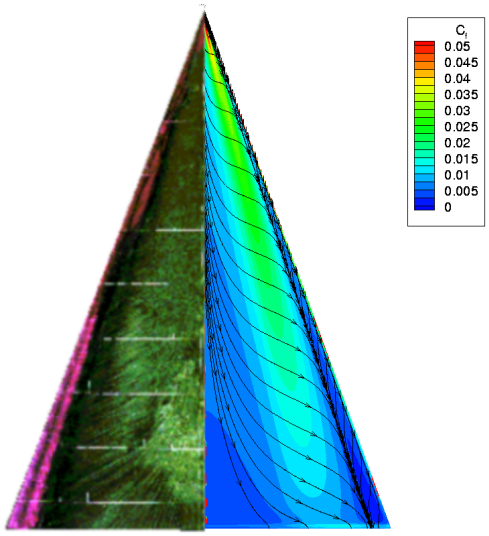

(a) Spalart-Allmaras

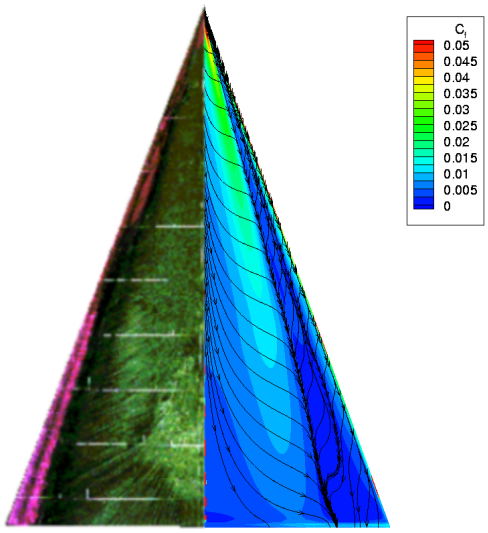

(b) SST

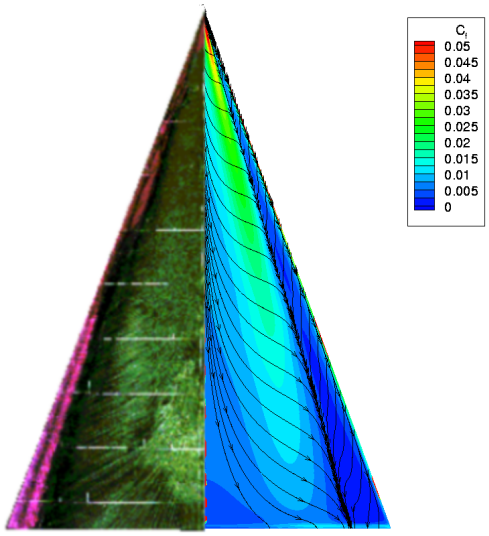

(c) Standard k-ω

Figure 3.4: *ONERA 70° wing, Upper surface skin friction distributions with shear stress streamlines*

From the computed results it is clear that the skin friction is highest beneath the primary vortex core where the flow reattaches to the upper surface, whilst the skin friction decreases rapidly after the secondary separation. Comparing the results from the 2-equation turbulence models we see that the secondary separation locations are predicted early in comparison to experiment. The secondary separation line from the SST model is predicted earliest (implying the lowest turbulence levels in the reattached boundary layer), followed by the k-ω and Spalart-Almaras models respectively. Finally it can be seen that the levels of skin friction from each turbulence model are similar. Interestingly with the SST model there is an additional separation within the secondary separation region, indicating the presence of tertiary structures. The early secondary separation could be due to the higher Mach number [109] or possibly to the assumption of fully turbulent flow (in experiment as transition occurs the secondary separation line was noted to shift outboard at around 40%c_r).

Figures 3.5 to 3.7 show the surface pressure distributions at three chordwise stations. Vortex breakdown does not appear to occur at all in the solutions from the Spalart-Allmaras turbulence model. In contrast to the Euler simulations of chapter 2, there is a plateau between the primary vortex suction peak and the leading edge in the 2-equation model solutions, representing the presence of a secondary vortex. Comparing the solutions from the 2-equation models we see that the standard k-ω model produces the strongest suction peak followed by the SST model. Another noticeable difference is the more inboard location of the primary vortex in the SST solution. A lower turbulent eddy viscosity within the boundary layer leads to an earlier secondary separation, which pushes the primary vortex more inboard. This earlier separation has produced a stronger secondary separation region (indicated by the secondary suction peak in the SST solution) which has induced a tertiary separation as seen in figure 3.4(b). The k-ω model produces the best agreement with experiment for the upper surface pressure distribution, in terms of both primary vortex suction and location. The Spalart-Allmaras model produces the highest suction but there is no significant secondary separation in the solution due to high turbulence levels in the vortex. It can also be seen from figures 3.5 to 3.7 that as the vortex extends downstream the suction peak decreases in comparison to experiment.

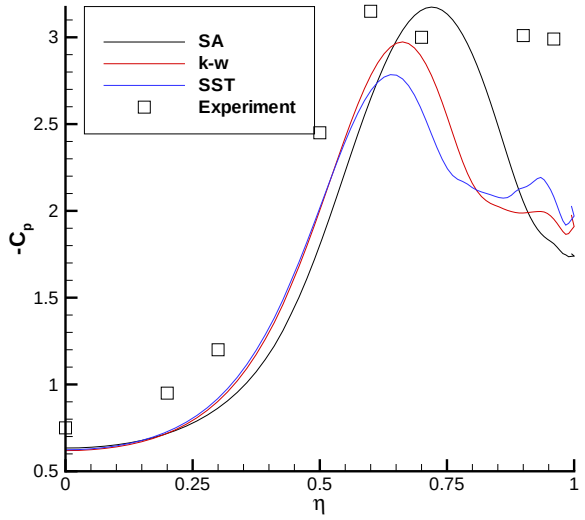

Figure 3.5: *ONERA 70° wing, Comparison of upper surface pressure distributions,* $x/c_r = 0.32$

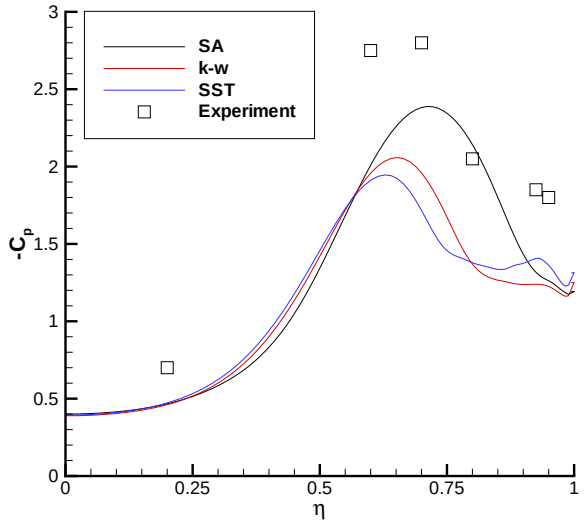

Figure 3.6: *ONERA 70° wing, Comparison of upper surface pressure distributions,* $x/c_r = 0.52$

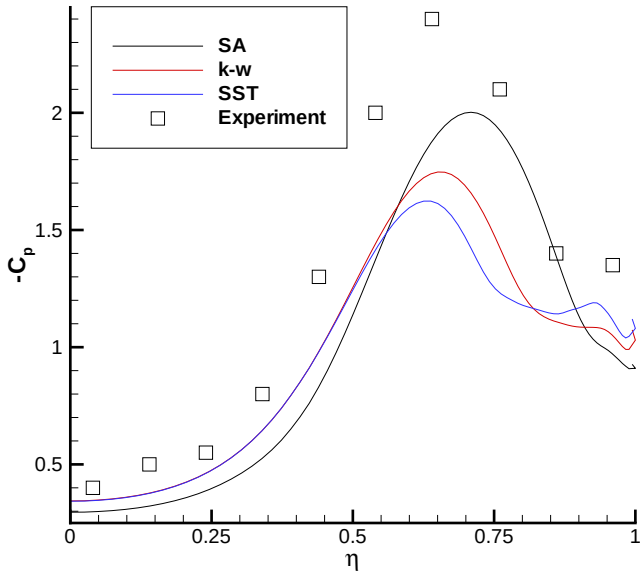

Figure 3.7: *ONERA 70° wing, Comparison of upper surface pressure distributions,* $x/c_r = 0.63$

The total pressure loss (TPL) distribution (defined by equation 2.4) through the vortex core at a chordwise location of $x/c_r = 0.32$ can be seen in figure 3.8. At this chordwise location vortex breakdown is downstream. TPL occurs due to dissipative effects such as molecular diffusion and turbulence. In regions of high eddy viscosity we would expect to see the largest TPL. An entropy increase (which again occurs due to dissipative effects) will be highlighted by a TPL increase. The TPL contours show clearly the structure of the predicted leading edge vortices. In all solutions there is a clear secondary separation which is represented by a rise in TPL towards the leading edge. However, in the Spalart-Allmaras model solution, the secondary separation occurs very close to the leading edge. From the smearing of the TPL contours it can be expected that there is an excess of eddy viscosity predicted in the vortex core (this is due to the source term in equation B.3 depending on the local vorticity magnitude). Turbulence levels within the vortex will be discussed below. The high eddy viscosity is the cause of the delay in secondary separation (a more turbulent boundary layer will delay secondary separation). Comparing figures 3.8

(b) and (c), the solutions from the 2-equation models, we see a very similar flow structure. Clearly the SST model predicts the largest secondary separation which is as suggested from the surface pressure distributions of figures 3.5 to 3.7.

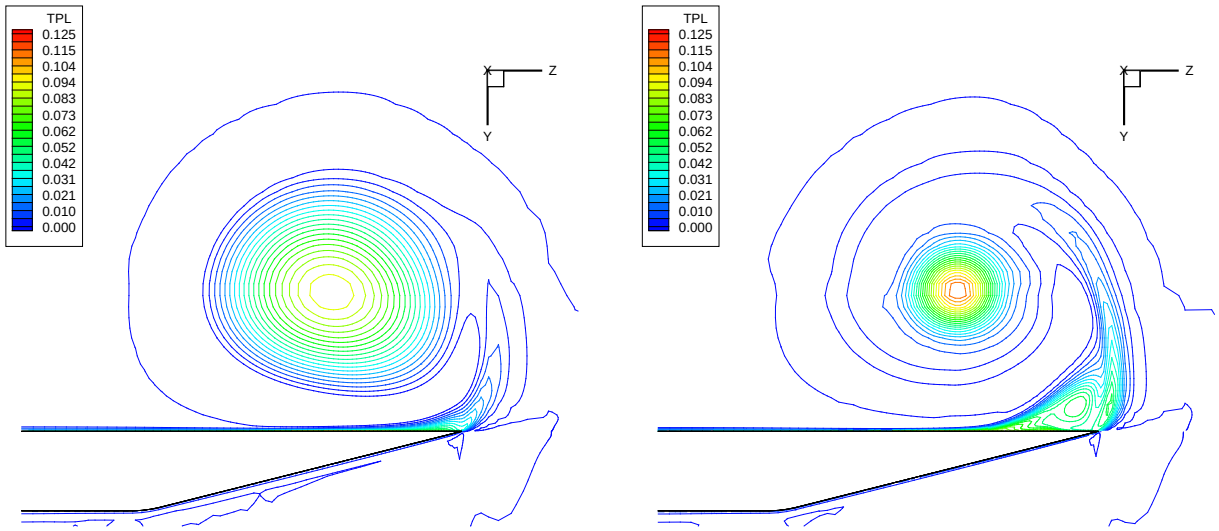

(a) Spalart-Allmaras

(b) SST

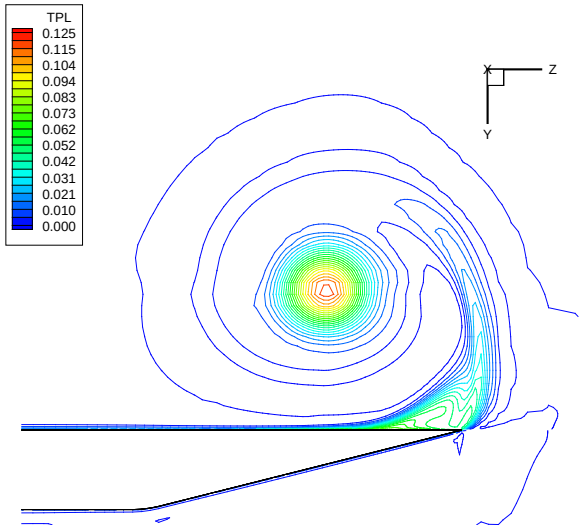

(c) Standard k-ω

Figure 3.8: *ONERA 70° wing, Total pressure loss contours through vortex,* $x/c_r = 0.32$

The structure of the vortex (secondary separation location in particular), the location of vortex breakdown, and the strength of the vortex is clearly dependent on the levels of turbulence generated. The amount of turbulence generated will determine how much kinetic energy is in the vortex (the lower the kinetic energy the earlier breakdown will occur as the flow will not be able to withstand the adverse pressure gradient in the vortex core for as long).

Figure 3.9 shows the turbulence Reynolds number levels along a vertical slice

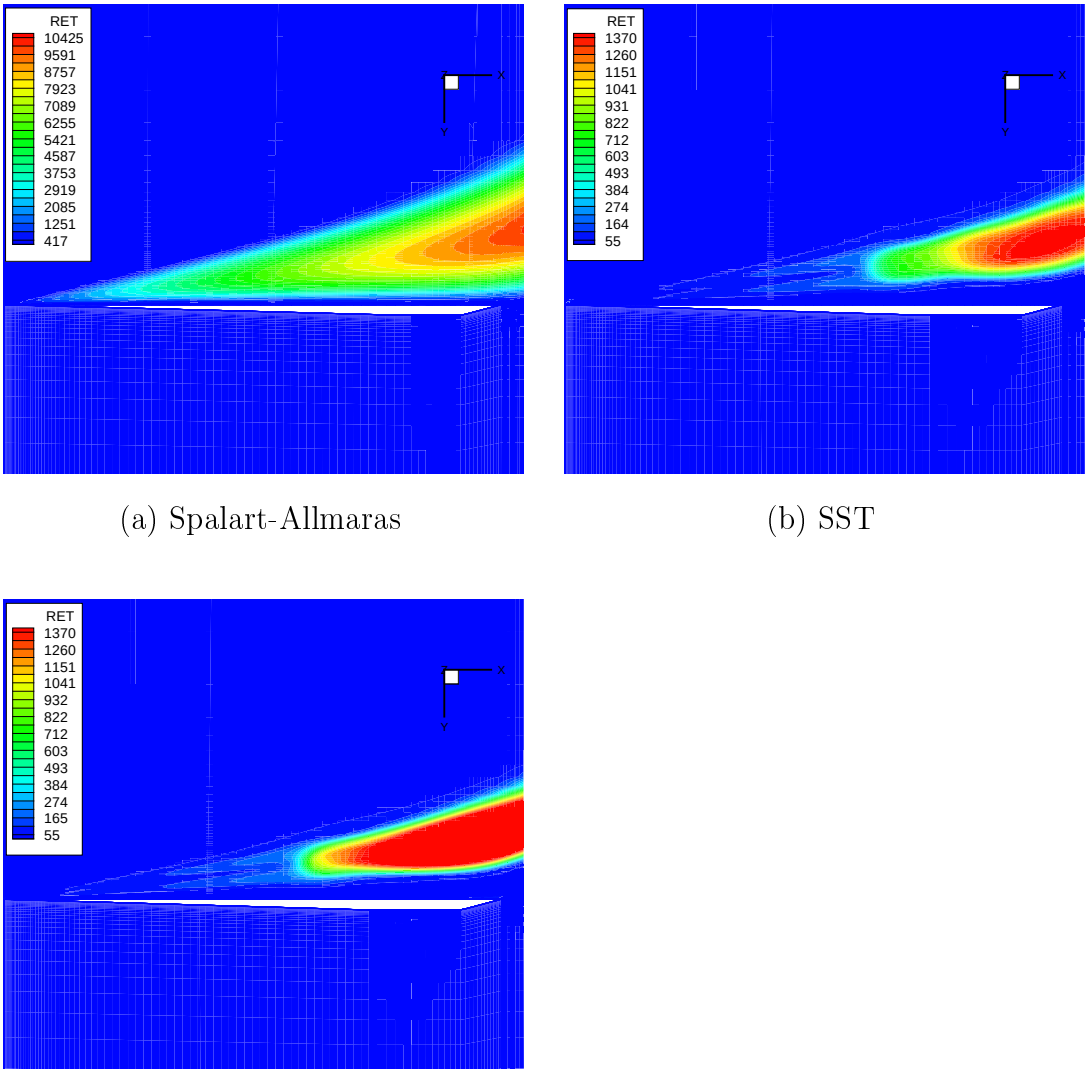

(a) Spalart-Allmaras

(b) SST

(c) Standard k-ω

Figure 3.9: *ONERA 70^o wing, Vertical slice through vortex core, Turbulence Reynolds number contours*

through the core of the vortex in each solution. The turbulence Reynolds number is the ratio of turbulent eddy viscosity to molecular viscosity [$Re_T = \mu_T/\mu$]. Note the scale for the Spalart-Allmaras model solution is ten times greater than those from the 2-equation models, which are plotted on the same scale. As expected from the upper surface pressure and TPL plots, the Spalart-Allmaras model predicts the highest levels of turbulence in the vortex. This increase in turbulence diffuses the vorticity in the vortex core (see figure 3.10(a)) and eliminates vortex breakdown. The levels of turbulence in the Spalart-Allmaras solution also explain the delay in secondary separation. The elimination of vortex breakdown with the Spalart-Allmaras model due to high eddy viscosity was also found by Morton et al. [27]. Considering the turbulent Reynolds number distribution through the vortices from the 2-equation models, they appear to be very similar, both in turbulence levels and distribution. Most of the turbulence is concentrated in the vortex core where the shear and vorticity is high. Considering the source terms in the 2-equation models this is as expected. Post breakdown both 2-equation models predict a large increase in turbulence which would appear to agree qualitatively with experiment (see figure 3.18(d)). Considering the vorticity levels through the vortex (figures 3.10(b) and (c)) it can be seen that the 2-equation models predict very similar solutions.

The vortex breakdown locations predicted by the three turbulence models are given in table 3.4

Model	Breakdown location
Spalart-Allamaras	Breakdown not present
SST	$62.1\%c_r$
k-ω	$60.4\%c_r$
Experiment	$65\pm5\%c_r$

Table 3.4: Breakdown locations from preliminary turbulence model study

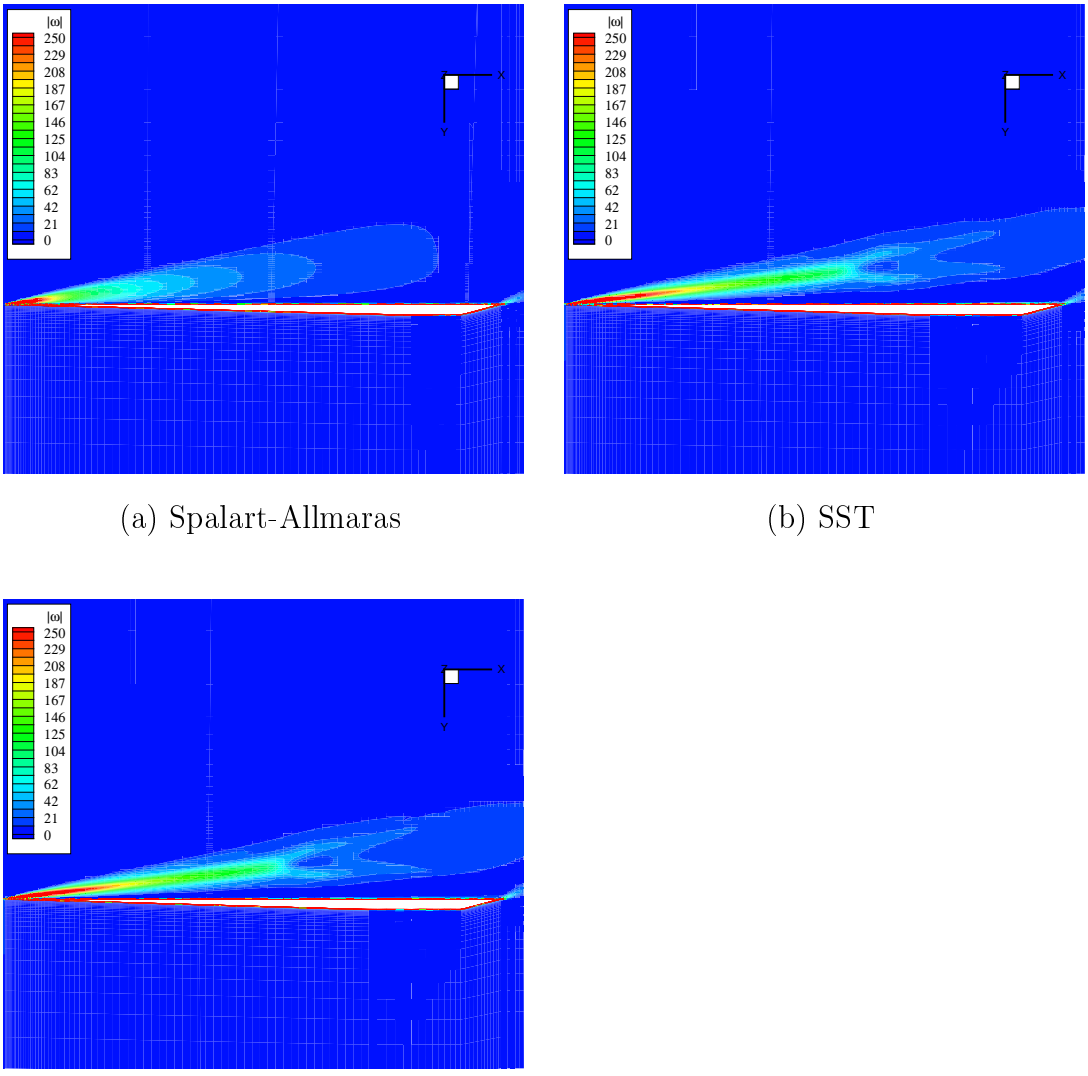

(a) Spalart-Allmaras

(b) SST

(c) Standard k-ω

Figure 3.10: *ONERA 70° wing, Vertical slice through vortex core, Vorticity magnitude contours*

3.6 Modifications to the k-ω turbulence model for vortical flows

From the previous analysis it is concluded that the k-ω model produces the most favourable results from the turbulence models available in PMB3D. This conclusion is based on primary vortex strength, primary vortex location, secondary separation location (which determines primary vortex location), turbulence levels, and turbulence distribution. This section investigates two modifications to the k-ω model which are expected to improve the realism of the model in this case. These modifications are specifically for vortical flows. In this section the tunnel walls will be considered to allow a more accurate comparison with experimental data, and provide insight into which modification, if any, will yield the best results.

It is well known that most 2-equation turbulence models over-predict the eddy viscosity within vortex cores, thus causing too much diffusion of vorticity [125]. This weakens the strength of the vortices and can eliminate secondary vortices, especially at low angles of attack where the vortices are already weak. This section deals with modifications to the k-ω turbulence model suggested by Brandsma et al. [129], to reduce the eddy-viscosity in vortex cores. These modifications were supplied in the PMB3D flow code.

The two suggested modifications to the standard k-ω model were implemented in PMB3D and are

$$P_k = min\{P_k^u, (2.0 + 2.0min\{0, r-1\})\rho\beta^* k\omega\} \tag{3.1}$$

$$P_\omega = \frac{P_\omega^u}{min\{r^2, 1\}} \tag{3.2}$$

Here P_k^u is the unlimited production of k, P_ω^u is the unlimited production of ω, and r is the ratio of the magnitude of the rate-of-strain and vorticity tensors.

The first modification is an extension of the one proposed by Menter [126] which uses the dissipation of k as a limiter. Menter's modification is given as

$$P_k = min\{P_k^u, 20\rho\beta^* k\omega\} \tag{3.3}$$

When k is over predicted in the vortex core, it will be limited to a value relative to the dissipation in that region. Previous experience by this author with this modification has shown it to be the least effective in reducing turbulence levels in the vortex core and as such will not be considered in the comparisons shown. The modification suggested by Brandsma et al. [129] replaces the constant "20" with a linear function of r. In vortex cores where the flow approaches pure rotation and the vorticity is high, r becomes much less than 1.0 and therefore in vortex cores the production of k is reduced and even turned into a dissipative term in equation B.7. This modification will be referred to as the NLR P_k limiter.

The second modification is equivalent to dividing the production of ω in equation B.8 by $min\{r^2, 1\}$. As in the first modification turbulence levels are limited by a function of r. Clearly with the second modification, when vorticity is high and the value of r is much less than 1.0, turbulent kinetic energy dissipation increases thereby reducing the eddy viscosity. This modification will be refered to as the NLR P_ω enhancer.

Brandsma et al. [129] concluded that the NLR P_ω enhancer produced the most favourable results. The test case considered was that of a 65^o cropped delta wing (identical in geometry to that described in chapter 2, section 2.4) at 10^o incidence, a freestream Mach number of 0.85, and a Reynolds number of 9×10^6. It should be noted that at 10^o angle of attack the leading edge vortices are weak in comparison to those formed when the wing is at high incidence. Therefore, as observed by Brandsma et al., the dissipation due to eddy viscosity is strong enough to weaken the vortices enough to eliminate a secondary separation. At high incidence it may be expected that the vortices are strong enough so that they will not be dissipated sufficiently to prevent a secondary separation. Therefore, how much these modifications influence the solutions at high incidence needs to be assessed.

3.7 Comparison of modifications with experiment

3.7.1 Computational grid

In order to validate and assess the predictions of the modifications to the k-ω model, the ONERA 70^o wing inside the ONERA F2 tunnel is considered. This grid is identical to the ONERA F2 grid used and described in chapter 4 and an indication of the grid resolution is given in figure 3.11. The only difference between the current and previous calculations is the presence of the tunnel walls. All flow parameters are as defined in section 3.3. No attempt has been made to alter any coefficients. The effect of the support structures will be discussed in chapter 6.

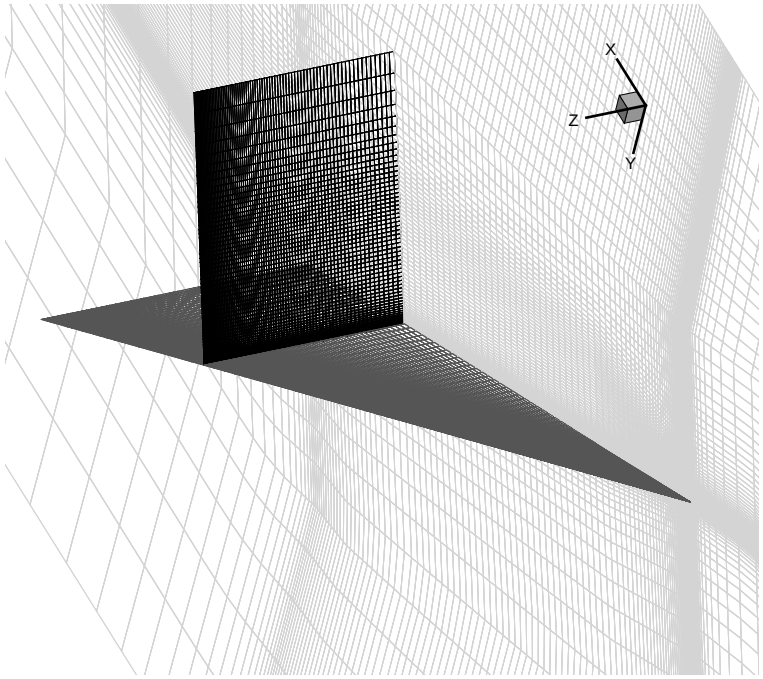

Figure 3.11: *ONERA 70^o wing, View of ONERA F2 tunnel mesh*

Again the mesh is of H-H topology with only half the wing modelled, however, the wing has been meshed at 27^o in the ONERA F2 tunnel. The first cell height normal to the wing surface is $10^{-6}c_r$ as in the previous grid. This yields an average y^+ value of 0.1. Representative boundary layer profiles calculated near the centre of the wing on the upper surface with the three k-ω variants are given in figure 3.12. The boundary layer profiles are as expected with the k-ω model. The turbulent

kinetic energy (k) is zero at the wall, increasing in the centre and decreasing towards the edge of the boundary layer. Similarly the profile of the specific dissipation rate (ω) is as expected, being low at the edge of the boundary layer, and increasing asymptotically as the wall is approached [112]. A slip condition is applied at the tunnel walls eliminating the need for clustering points in the tunnel wall boundary layer.

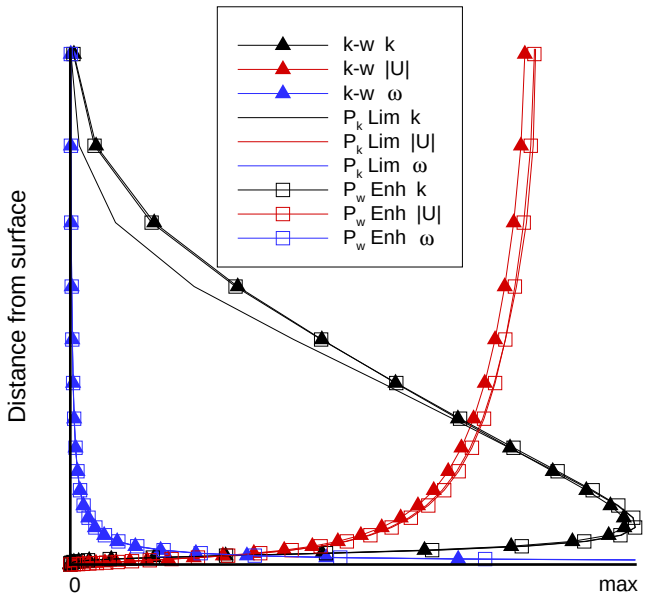

Figure 3.12: *ONERA 70^o wing, Boundary layer profiles from k-ω variants taken near the centre of the wing on the upper surface*

3.7.2 Grid dependence study - ONERA 70^o wing

In order to attempt to verify the accuracy of the solutions, a limited grid dependency study has been conducted. Due to the high computational power requirements to solve the flow with the fine grid, only a comparison with the coarse grid solution is presented. Since it is the resolution of the vortical region that is of interest, the following grid dimensions in table 3.5 are for above the upper surface of the wing with no off-wing blocks being discussed. The "standard" grid is that used in the computations of chapter 4, and the "coarse" grid is extracted from the standard

grid.

Grid	Chordwise	Spanwise	Normal to upper surface
Standard	99	79	103
Coarse	45	40	52

Table 3.5: ONERA 70^o wing, grid refinement study grid dimensions

The upper surface pressure distributions are given in figure 3.13. The breakdown locations from the coarse and standard grids are $59.6\%c_r$ and $64.7\%c_r$ respectively. Clearly as we go from the coarse to standard grids the suction peaks increase in strength and vortex breakdown moves downstream.

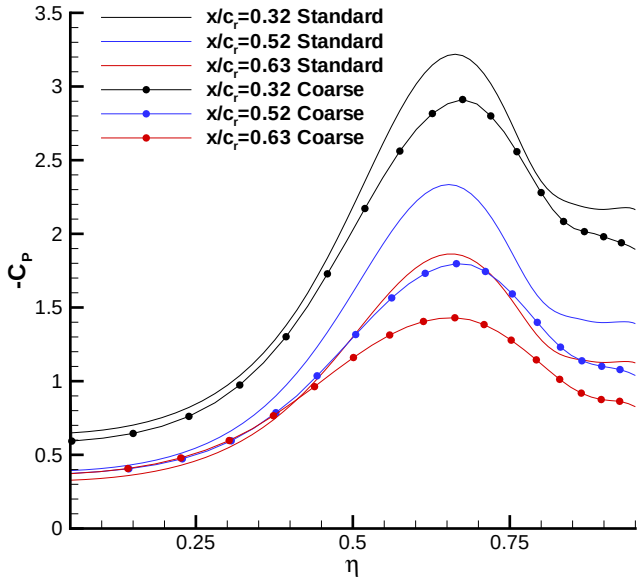

Figure 3.13: *ONERA 70^o wing, Dependency of upper surface pressure distribution with grid refinement*

Flow visualisation of the solutions indicates that a grid refinement increases the core properties (higher suction, higher axial velocities, higher vorticity) and increases turbulence levels within the vortex. Clearly as breakdown is delayed going from the

coarse to the standard grid, the increase in the core properties is dominant over the dissipation of kinetic energy in the vortex, allowing the core flow to negotiate the adverse pressure gradient a little further. It should be noted that Visbal and Gordnier [109] observed for simulations on a 75^o delta wing at 25^o angle of attack, with Reynolds number equal to 2×10^6, and freestream Mach number of 0.2, that on a coarse grid (H-H topology) vortex breakdown was located upstream to that computed on a finer grid. It should be noted that the fine grid was coarser than the standard grid used in this study and the Baldwin-Lomax turbulence model was employed.

Since the grids used for the tunnel calculations have been extracted from a common farfield grid, the grid dependency of each solution will be similar. As such, despite the fact that further refinement of the vortices is required (which is not currently feasible due to computing limitations), the grid dependency is equal for all cases and therefore solution to solution comparisons for tunnel effects is still valid.

3.7.3 Results

Again the convergence of the solutions was checked first. In all solutions the mean flow residual converged at least four orders of magnitude. It should be noted, however, that fluctuating loads were obtained with the NLR P_ω enhancer. The fluctuating loads are shown in figure 3.14.

For the standard k-ω and NLR P_k limiter models, we see that the solution achieves a steady state. However the solution from the NLR P_ω enhancer does not. Recalling the unsteady nature of vortex breakdown, the fluctuating loads may be attributed to unsteadiness in either the breakdown location [41][5] or the helical mode instability of vortex breakdown [61][62][21][72][28]. Fluctuating loads have been observed in other steady state computations [98]. As will be shown later, the NLR P_ω enhancer kills most of the turbulence in the breakdown region, which will dissipate the vorticity in the standard k-ω and NLR P_k limiter solutions (allowing a steady state solution to be achieved).

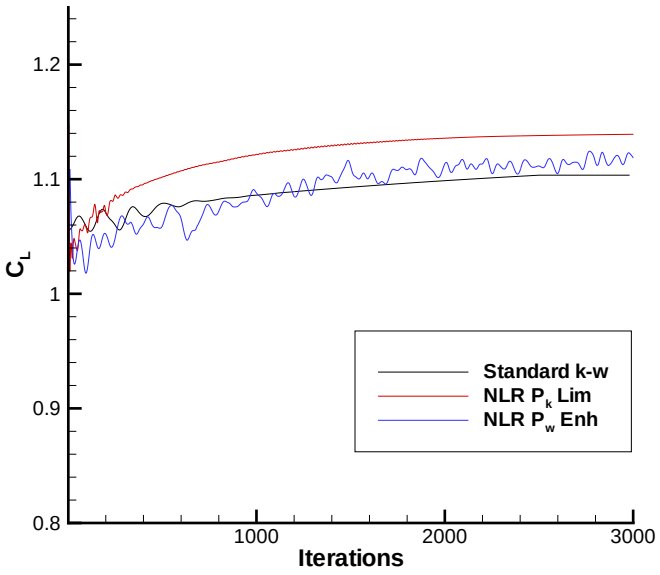

Figure 3.14: *ONERA 70° wing, Lift convergence history*

If we look at the upper surface pressure distributions at the chordwise stations of $x/c_r = 0.32$, 0.52, and 0.63 (figures 3.15, 3.16, and 3.17 respectively) we see that the modifications do not alter significantly the vortex induced suctions on the wing near the apex (at x/c_r=0.32). Examination of the surface pressure distributions at x/c_r=0.52 indicates that the standard k-ω model predicts vortex breakdown earlier in comparison to the other two variants. The early breakdown is indicated by a sharp drop in the primary suction peak. It is also clear that as mentioned previously, the variation in vortex strength in the chordwise direction reduces faster in the CFD solutions in comparison to experiment, almost equally with each variant. This may be due to the vertical position of the vortex being poorly predicted (possibly due to the laminar / turbulent transition in experiment varying the position of the vortex core), or that the grid resolution is insufficient. However, it is unlikely to be due to the levels of turbulence predicted, since as will be discussed later, the NLR P_ω enhancer effectively destroys almost all turbulence. It should be remembered that the H-H mesh topology expands the cell sizes in the chordwise direction along a delta wing.

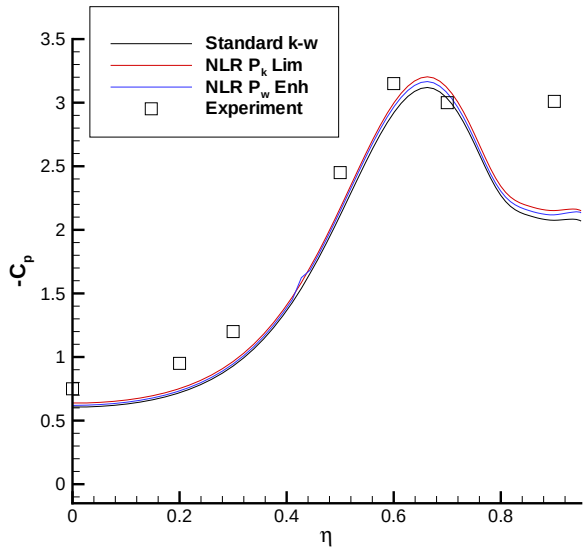

Figure 3.15: *ONERA 70^o wing, Comparison of upper surface pressure distributions,* $x/c_r = 0.32$

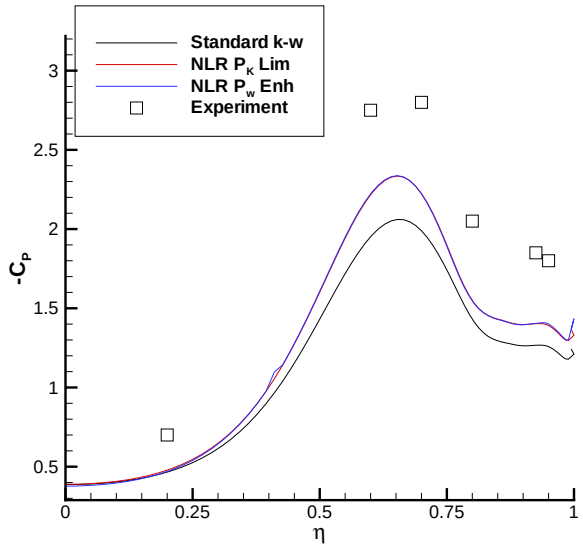

Figure 3.16: *ONERA 70^o wing, Comparison of upper surface pressure distributions,* $x/c_r = 0.52$

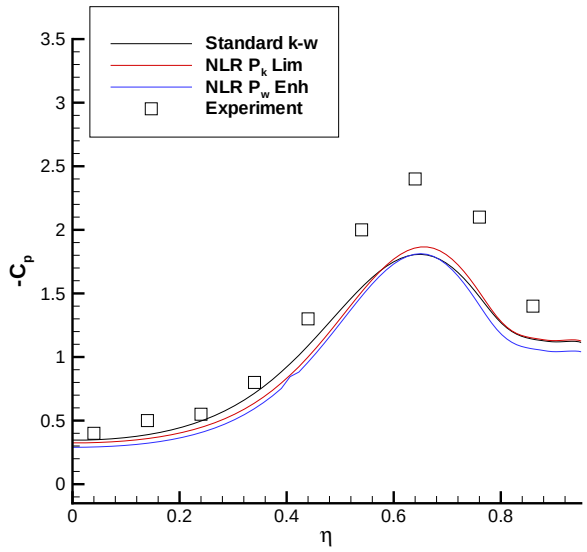

Figure 3.17: *ONERA 70^o wing, Comparison of upper surface pressure distributions,* $x/c_r = 0.63$

However, in general the upper surface pressure distributions are predicted well with all k-ω variants, especially closer to the apex. The suction levels near the apex (where the flow is highly resolved) compare well with experiment, despite the strength of the secondary vortex possibly being under-predicted (it should be recalled however that in the experiment the flow is laminar until around 40%c_r, which may explain the weaker secondary vortex near the apex). Further downstream the structure of the vortex is visible despite the vortex weakening in comparison to experiment.

The turbulent kinetic energy, k, distributions from each k-ω variant are given in figure 3.18. For comparison the experimentally obtained distribution of k is given in figure 3.18(d). The experimental distribution of turbulence shows that there is a large increase in turbulent kinetic energy as the vortex breaks down. Before breakdown the flow appears to be fairly ordered with low turbulent fluctuations. Comparing the predicted distributions of k it is evident that by far the largest difference in the solutions occurs with the NLR P_ω enhancer. Clearly most of the turbulent kinetic energy is eliminated (even when the vortex breaks down) by the

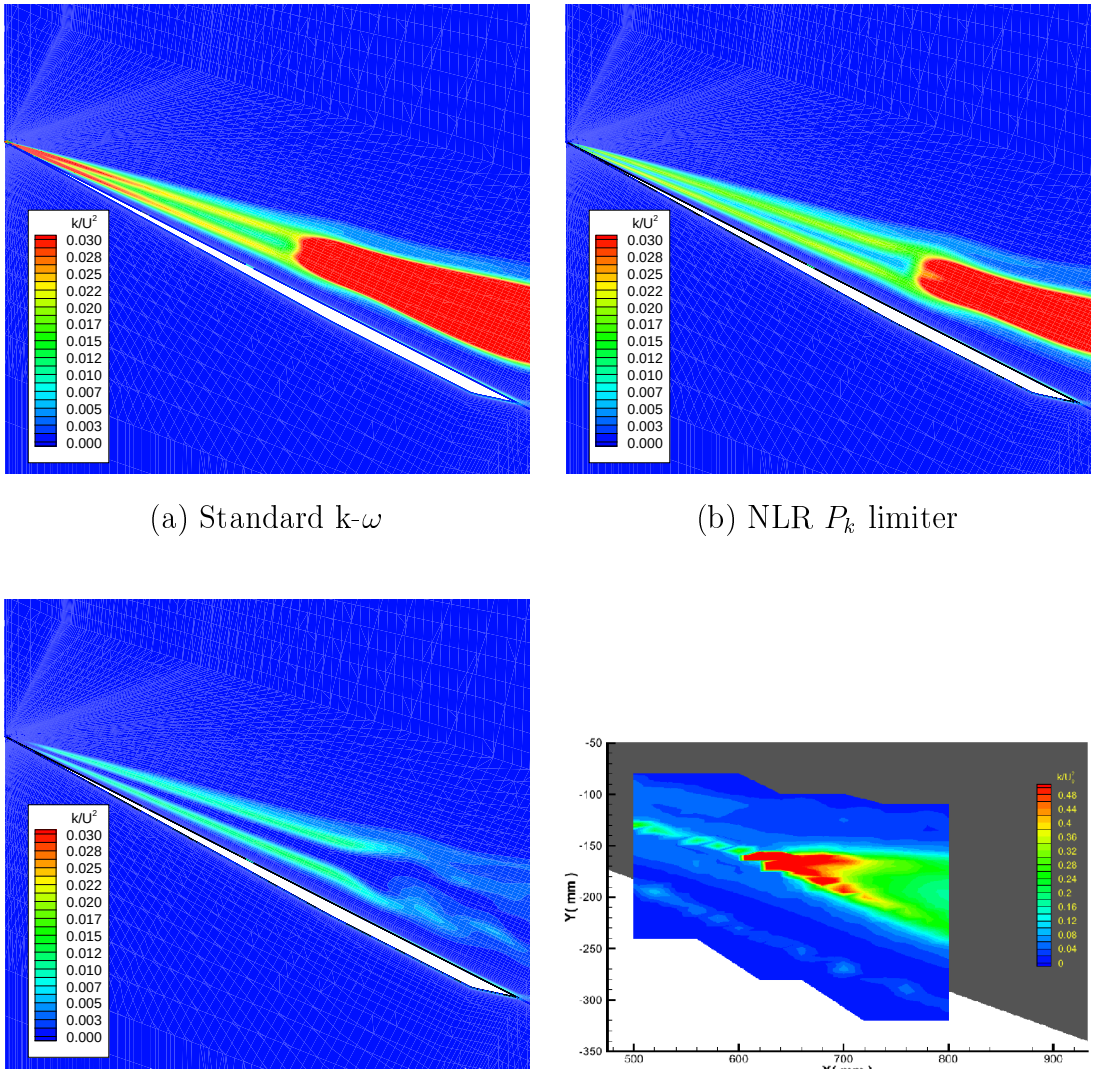

(a) Standard k-ω

(b) NLR P_k limiter

(c) NLR P_ω enhancer

(d) Experiment [5] p195

Figure 3.18: *ONERA 70^o wing, Vertical slice through vortex core, Turbulent kinetic energy contours*

production of too much turbulence dissipation. This suggests that the NLR P_ω enhancer modification is too strong making the flow more laminar in the post-breakdown region. The NLR P_k limiter has less influence as the turbulence levels do not appear to be too much different from those predicted by the standard k-ω model. It should be noted that with the 2 equation k-ω model, there is an effective balancing of the production of turbulent kinetic energy and the dissipation of turbulent kinetic energy. Therefore if the turbulent kinetic energy is reduced the dissipation reduces.

It can therefore be expected that altering the P_k term in the "k-equation" will have a smaller influence than altering the P_ω term in the "ω equation". The effect of limiting the production of k can be seen best in the turbulence levels in the vortex core. The turbulence levels are reduced and the turbulence generated at the apex is effectively eliminated. Another noticeable difference is in the gradients of k throughout the vortex, i.e. there is no longer a smooth distribution of turbulence throughout the vortex which is clearly artificial. During vortex breakdown where the flow changes from an orderly rotational flow to complete turbulence, it can be seen that both the standard k-ω model and the NLR P_k limiter show a large increase in turbulent kinetic energy. This is in strong contrast to that predicted by the NLR P_ω enhancer. The excessive loss of turbulent kinetic energy (and therefore eddy viscosity) predicted by the NLR P_ω enhancer is likely to be the cause of the fluctuations observed in the load curves, as fluctuations are not seen when using the other k-ω variants.

The distribution of turbulent Reynolds number through the vortex core for each of the k-ω variants can be seen in figure 3.19. As mentioned earlier this variable is very useful when considering the levels of turbulent eddy viscosity in the vortex. From the previous discussion, as expected it can be seen that most eddy viscosity is eliminated with the NLR P_ω enhancer. The turbulence levels are also reduced with the NLR P_k limiter, especially in the vortex core where the turbulence should be low [15]. Both limiters have reduced the turbulence levels in the vortex core and as mentioned previously, it appears that the NLR P_ω enhancer modification is too strong.

The distribution of vorticity magnitude through the vortex can be seen in figure 3.20. The effect of the modifications on breakdown location can clearly be seen. Both modifications have delayed vortex breakdown. On the scale plotted, the levels of vorticity appear similar with all modifications, with the main difference being how far downstream the high vorticity regions extend. Comparing the locations of vortex breakdown, it is clear that the standard k-ω model predicts breakdown closest to the apex (56.1%c_r), followed by the NLR P_k limiter (64.7%c_r), and finally the NLR P_ω enhancer (68.0%c_r). It can also be seen that in the NLR P_ω enhancer there are "pockets" of vorticity in the breakdown region which are not observed in the

solutions from the other variants. This may indicate structures in the breakdown region causing the fluctuation loads seen in figure 3.14.

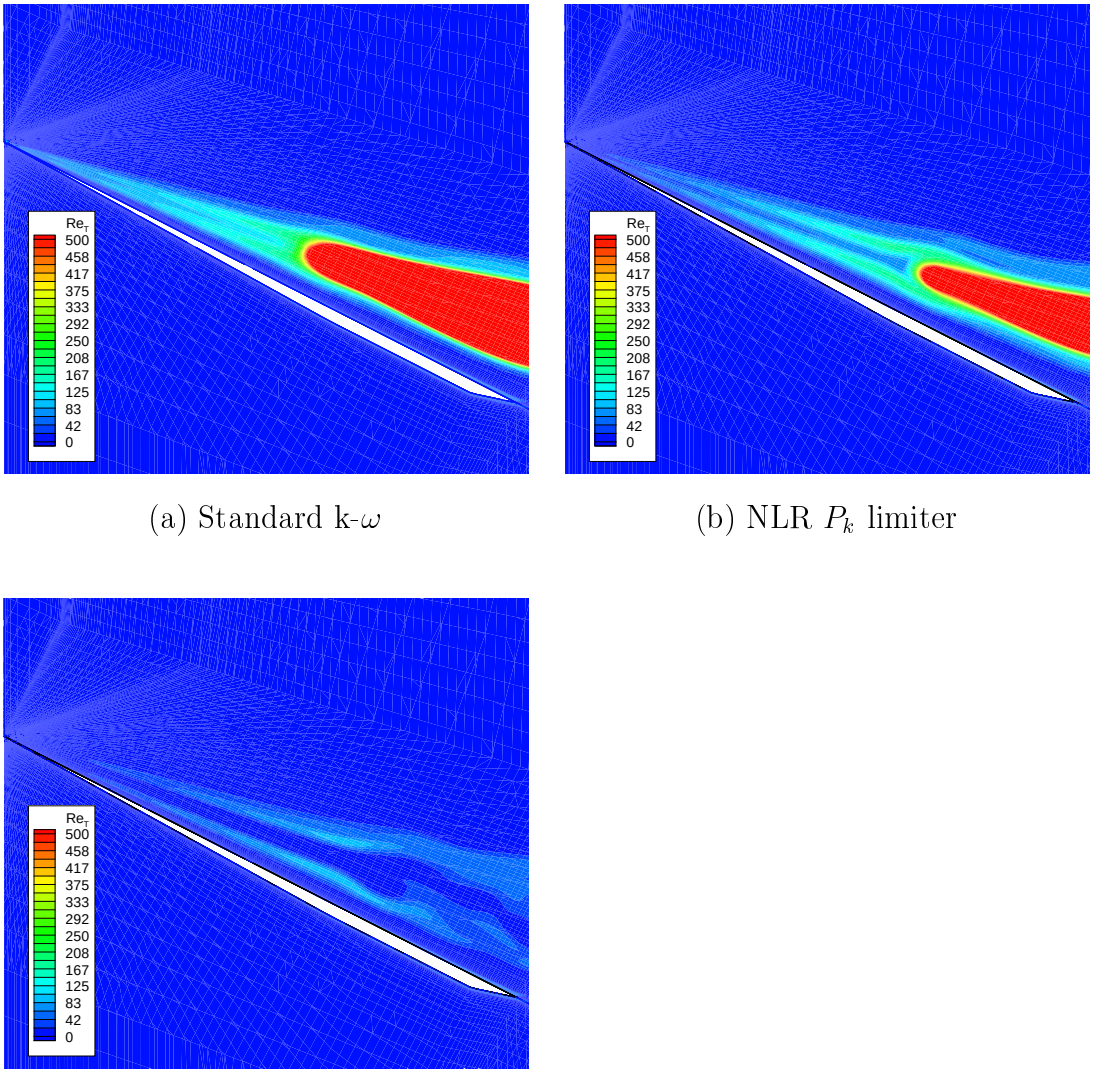

(a) Standard k-ω

(b) NLR P_k limiter

(c) NLR P_ω enhancer

Figure 3.19: *ONERA 70° wing, Vertical slice through vortex core, Turbulence Reynolds number contours*

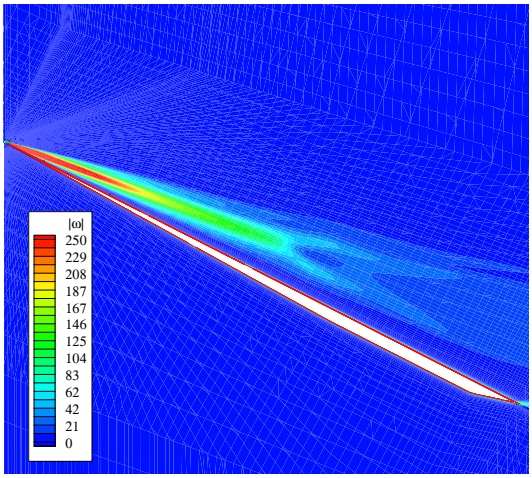

(a) Standard k-ω

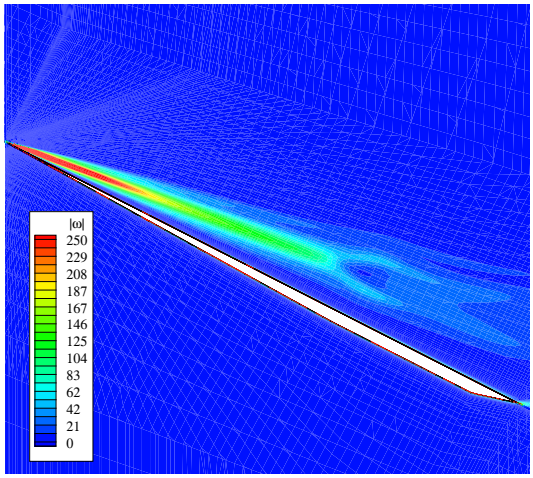

(b) NLR P_k limiter

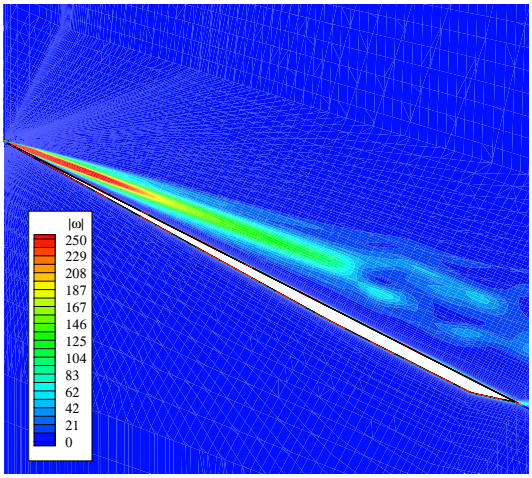

(c) NLR P_ω enhancer

Figure 3.20: *ONERA 70° wing, Vertical slice through vortex core, Vorticity magnitude contours*

The distributions of the ω_x component of vorticity at the chordwise location of x/c_r=0.52, are shown in figure 3.21 for the three k-ω variants. It should be noted the scales of the CFD solutions are consistent, however the limits are narrower than the experimental scale (varying from -100 to 100 in the CFD solutions and -200 to 200 in the experimental distribution). Considering the standard k-ω model solution it is clear that vortex breakdown is occurring nearby as the ω_x component of vorticity has reduced dramatically as breakdown is approached. However, in general for the

other two variants the distribution of the ω_x component of vorticity agrees well with experiment. However is should be noted that the core vorticity levels are predicted much lower in comparison with experiment. This indicates that the computed vortex strengths are likely to be lower than those found in experiment which follows from the lower suction peaks at x/c_r=0.52 and 0.63.

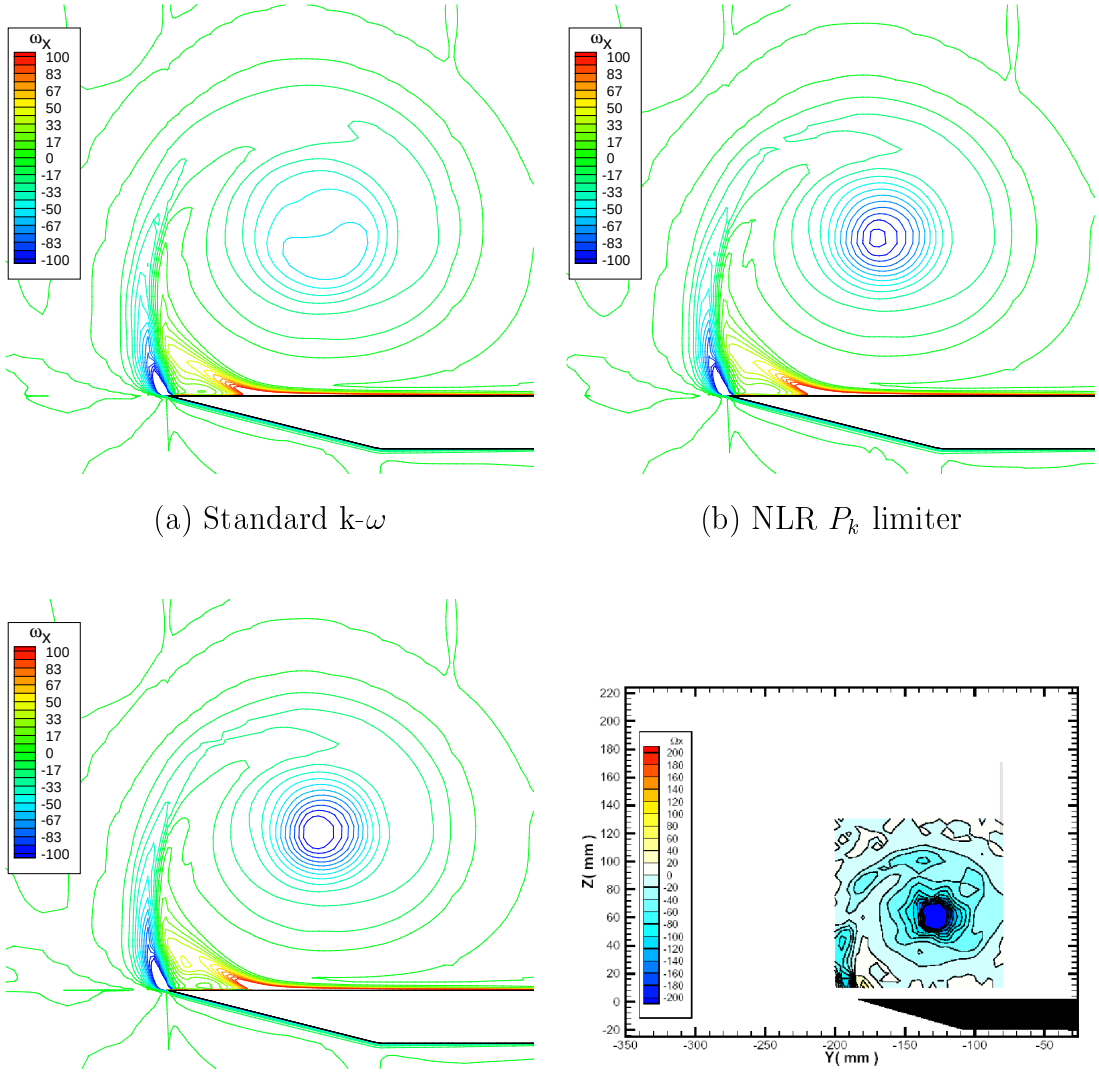

(a) Standard k-ω (b) NLR P_k limiter

(c) NLR P_ω enhancer (d) Experiment [5] p188

Figure 3.21: *ONERA 70^o wing, axial components of vorticity*

Figure 3.22 shows the dynamic pressure along the vortex core. According to the 1st Law of thermodynamics energy can be neither created nor destroyed, only converted into other forms. Therefore if we increase the amount of turbulence (and therefore dissipation of energy) in the vortex core (i.e. use the standard k-ω model) the kinetic energy in the core must be reduced. It would therefore seem reasonable that a vortex core of lower kinetic energy would be more susceptible to the core adverse pressure gradient, and therefore vortex breakdown. Indeed it is understood that increasing the momentum in the core delays breakdown, as the adverse pressure gradient can be overcome a little further [133].

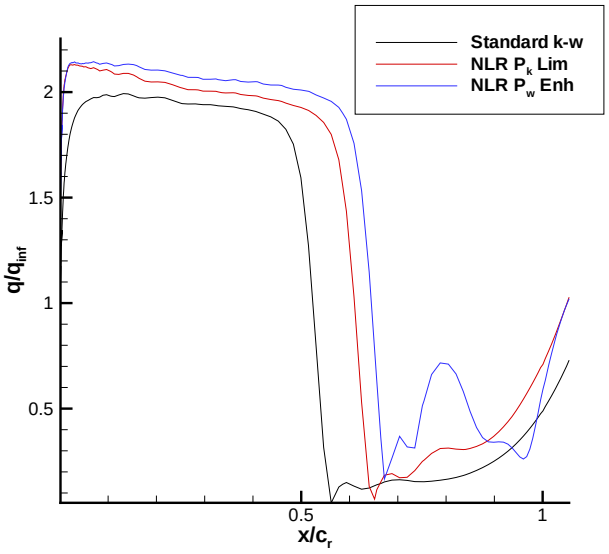

Figure 3.22: *ONERA 70^o wing, Dynamic pressure distributions extracted from the vortex cores*

The axial velocity distribution can be seen in figure 3.23 for the chordwise location of x/c_r=0.52. Considering figure 3.23 we see immediately that the axial velocity in the core of the vortex does not reach the values found in experiment. The effect of the early breakdown can also be seen at x/c_r=0.52 in the standard k-ω solution,

where the axial velocity has dropped significantly in comparison to the other solutions. It can also be seen that the velocity peak from the NLR P_ω enhancer is highest followed by that from the NLR P_k limiter solution. The velocity outwith the vortex core region compares reasonably well with that from experiment. Examination of the core velocity along the entire vortex length shows that the maximum core velocities are around 2.25 times freestream.

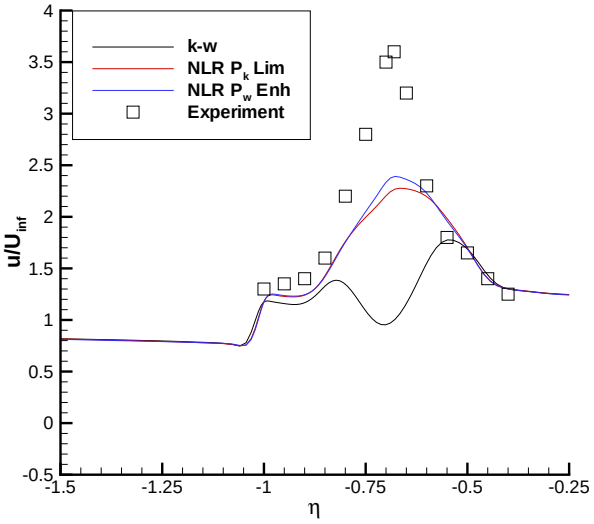

Figure 3.23: *ONERA 70° wing, Distribution of axial velocity through vortex core at* x/c_r*=0.52*

The helix angles through the vortex at $x/c_r = 0.52$ are shown in figure 3.24. The helix angle is as defined by Mitchell [5] (with the z axis spanwise), and is given by equation 2.5. It is seen in figure 3.24, outwith the vortex core, that the helix angles have been predicted well. As the core of the vortex is approached, in experiment there is a sharp decrease in helix angle with a changing in sign as the core is traversed. The computed distributions show a similar trend, however the change in sign of the helix angle occurs at a slower rate. It is evident that the largest discrepancy between CFD and experiment occurs in the core region which can be attributed to the fact that the magnitude of the axial velocity in the core is not well predicted, thus yielding a lower gradient. The different turbulence models

can clearly be seen to have little influence on the helix angle (although it should be recalled breakdown proximity will effect the helix angle distribution).

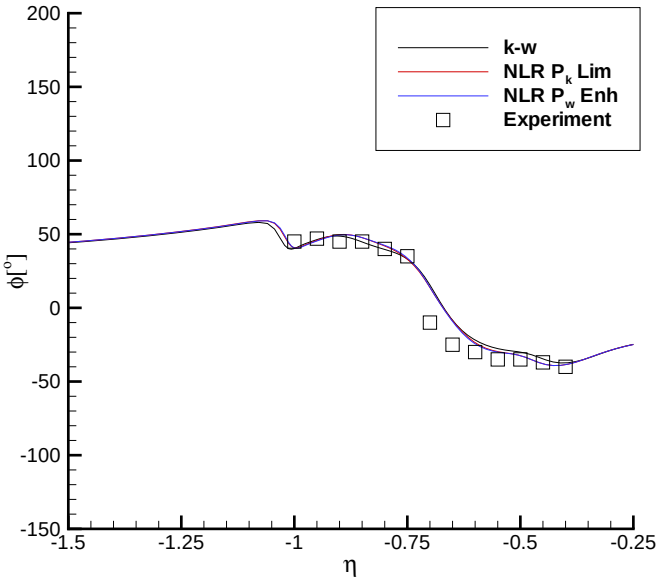

Figure 3.24: *ONERA 70° wing, Distribution of helix angle through vortex core at* x/c_r*=0.52*

A final point about the solutions is the orientation of the vorticity vectors prior to vortex breakdown. Figures 3.25 and 3.26 show the magnitudes of the ω_y and ω_z components of the vorticity vector, at the chordwise stations of x/c_r=0.52 and x/c_r=0.63. The figures were obtained from the results using the NLR P_k limiter, though the following discussion applies regardless of the modification used. It is well understood that prior to vortex breakdown the vorticity vector is predominantly in the axial direction (which in the current solutions is effectively the ω_x component). At the chordwise station of x/c_r=500 we see that the components ω_y and ω_z of the vorticity vector are relatively low (though not zero since ω_x is not exactly along the vortex axis). Also the sign of these components indicates that they are rotating in the sense that would accelerate the core flow. If we now consider the ω_y and ω_z distributions at x/c_r=0.63, we see that the components have changed sign near the core when compared with the distributions at x/c_r=0.52. This change of sign was

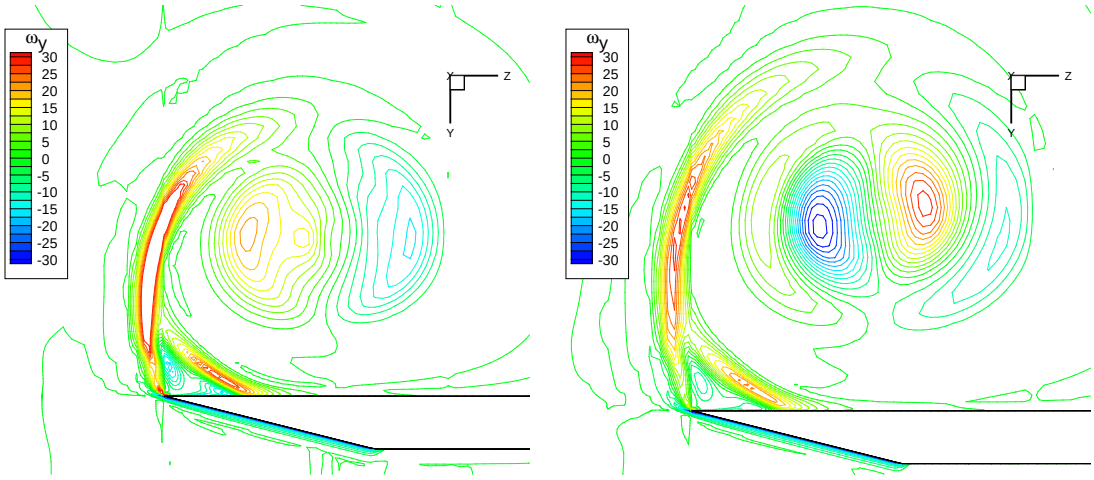

(a) x/c_r=0.52 (b) x/c_r=0.63

Figure 3.25: *ONERA 70^o Wing, NLR P_k limiter solution, ω_y components of vorticity*

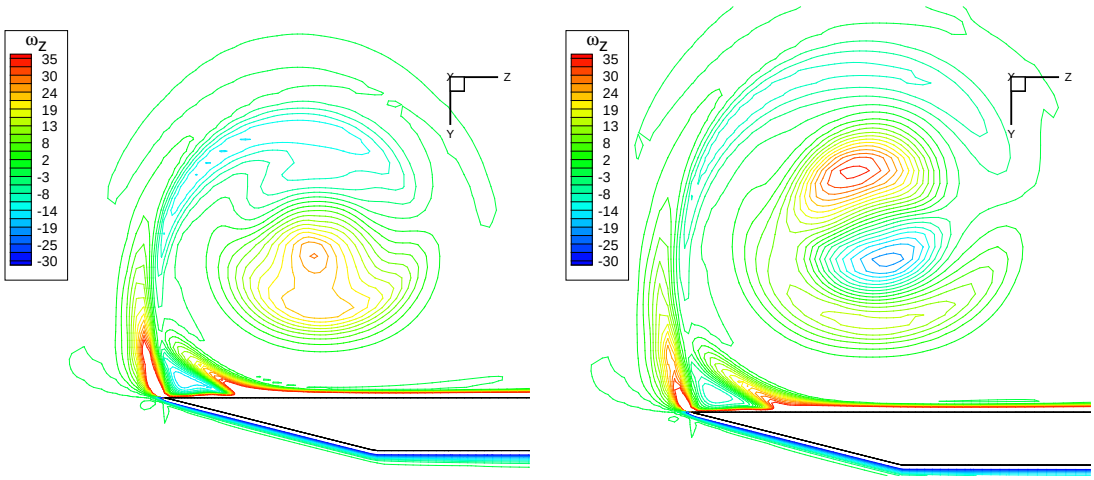

(a) x/c_r=0.52 (b) x/c_r=0.63

Figure 3.26: *ONERA 70^o Wing, NLR P_k limiter solution, ω_z components of vorticity*

seen in the Euler solutions of chapter 2. Thus the sense of the rotation of the ω_y and ω_z components at x/c_r=0.63 are opposing the motion of the core flow. At x/c_r=0.63

negative azimuthal vorticity has been produced. In chapter 4 (figure 4.9), we will see that at x/c_r=0.63 in the ONERA F2 tunnel solution the core pressure is rising rapidly. This is due to the flow decelerating towards the stagnation point associated with vortex breakdown. As described by Darmofal [60] and initially suggested by Brown and Lopez [57], when the core flow decelerates the radial components of velocity increase (due to conservation of mass), therefore the vorticity vector tilts. Eventually tilting and stretching of the vorticity lines can produce negative azimuthal vorticity which tends to slow the core flow. This would appear to be the case in the current simulations and the cause of vortex breakdown. Negative azimuthal vorticity near breakdown was also observed in the measurements of Nelson and Visser [58] and Lin and Rockwell [59].

3.8 Application of NLR P_k limiter to WEAG-TA15 test case

3.8.1 Description of test case

This test case was discussed in chapter 2. For a full discussion of the wing geometry and the available experimental data, see section 2.4. The simulation conditions have farfield outer boundaries, a Mach number of 0.2, and a Reynolds number of 3.1×10^6. It should be noted that a lower Mach number of 0.2, compared with the Mach number of 0.4 in the Euler solutions of chapter 2, is used which is closer to that of the experiment (M_∞=0.12). This reduces the question of compressibility effects which may have been present in the Euler simulations of chapter 2. The y^+ values for an initial wall spacing of $1 \times 10^{-6} c_r$ were found to be on average 0.1. Boundary layer profiles with the NLR P_k limiter, at the centre of the wing, are given in figure 3.27. The extracted profiles indicate a well resolved boundary layer featuring the trends for k and ω as described by Wilcox [112].

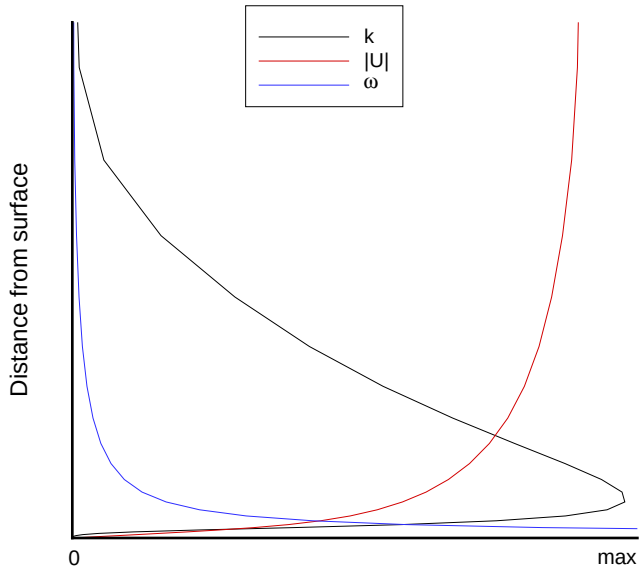

Figure 3.27: *WEAG-TA15 wing, Boundary layer profiles from NLR P_k limiter variant taken near the centre of the wing on the upper surface*

3.8.2 Grid dependence

Like the 70^o wing case, in order to attempt to verify the accuracy of the solutions, a limited grid dependency study has been conducted. Again due to the high computational power requirements to solve the flow with the fine grid, only a comparison with the coarse grid solution is presented. The resolution of the vortical region is given in table 3.6 with no off-wing blocks being discussed.

Grid	Chordwise	Spanwise	Normal to upper surface
Standard	99	79	103
Coarse	45	40	52

Table 3.6: WEAG-TA15 wing, grid refinement study grid dimensions

The upper surface pressure distributions are given in figure 3.28. The breakdown

locations from the coarse and standard grids are 74.3%c_r and 77.4%c_r respectively. Clearly as we go from the coarse to standard grids the suction peaks increase in strength and vortex breakdown moves downstream. The discussion for the ONERA 70^o wing grid dependence study given in section 3.7.2, also applies in this case. The mesh used in all subsequent WEAG-TA15 wing calculations is shown in figure 3.29.

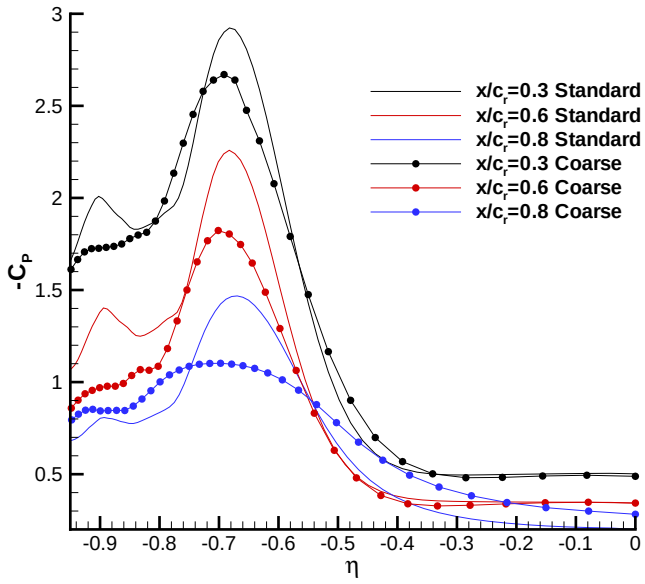

Figure 3.28: *WEAG-TA15 wing, Dependency of upper surface pressure distribution with grid refinement*

3.8.3 Validation

Since the experimental data of Löser [107] was obtained in an open test section wind tunnel, a farfield solution will be used for validation of the steady and unsteady solutions. As discussed in chapter 2, a more accurate validation could be conducted if the pressure distribution around the test section was measured. This pressure distribution could be used as a boundary condition for a more accurate simulation of the open test section.

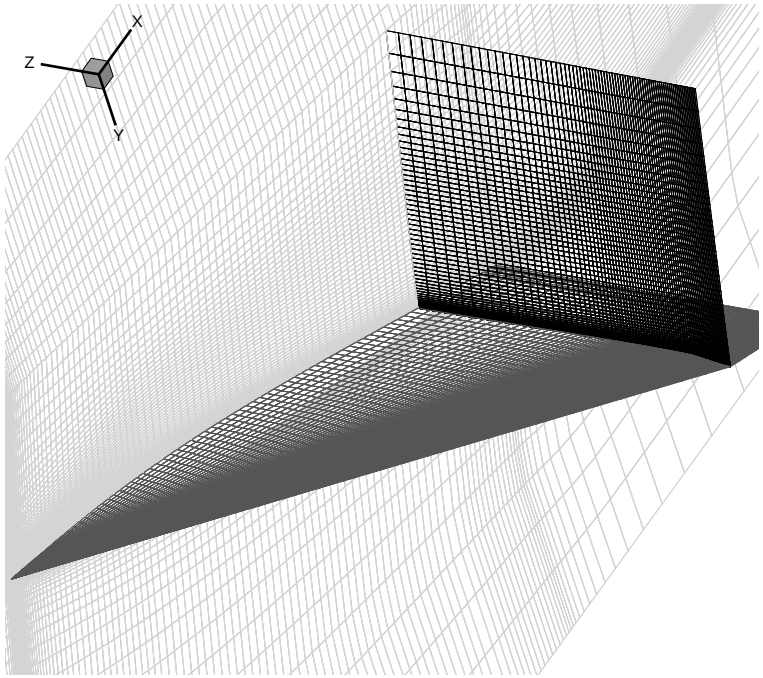

Figure 3.29: *WEAG-TA15 wing, View of mesh near the* 65^o *wing test cases*

A comparison of the computed and experimental surface pressures at three chordwise locations is given in figure 3.30. As can be seen the primary vortex suction levels compare very well with experiment at the chordwise locations of x/c_r=0.3, x/c_r=0.6, and x/c_r=0.8. However, one noticeable difference is the location of the primary vortex core. In the CFD solution the primary vortex core is clearly more inboard than was observed in experiment (most evident at the chordwise locations of x/c_r=0.3 and 0.6). This indicates that the secondary vortex is too large, as a larger secondary vortex will push the primary vortex core inboard [6][21]. It is also clear that the secondary suction region predicted by CFD is more peaky (again most evident at the chordwise locations of x/c_r=0.3 and 0.6) than that found in experiment. This indicates a stronger secondary flow in the CFD solutions when compared to experiment. The early secondary separation can be attributed to the turbulence levels in the boundary layer predicted by the NLR P_k limiter (a reduction in turbulence was shown in chapter 3 to cause earlier secondary separation). Interestingly, at the chordwise location of $x/c_r = 0.8$, the primary and secondary suction levels compare very well with experiment, and as such the primary vortex

core location is also well predicted. Note that at this chordwise location there is a smaller spanwise pressure gradient (due to the vortices being burst), thus reducing the dependency of the solution on the boundary layer profile. Despite the more inboard primary vortex in the CFD solutions, it is concluded that the flow over the WEAG-TA15 wing has been well predicted.

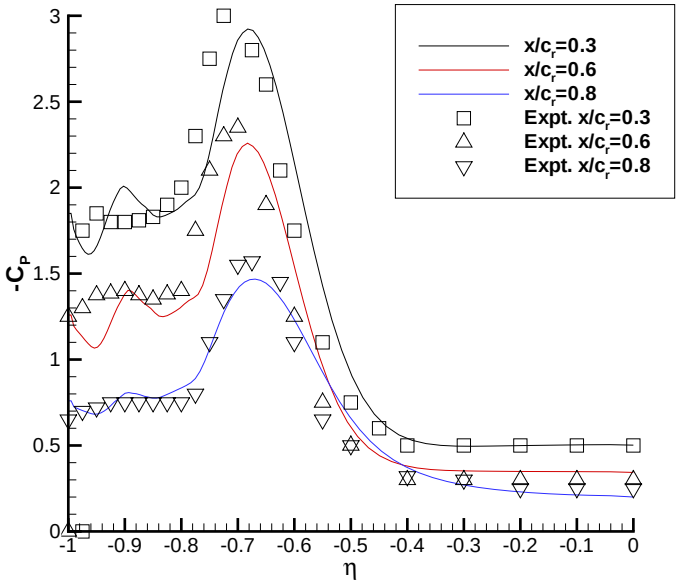

Figure 3.30: *WEAG-TA15 Wing, Comparison of upper surface pressure distributions with experiment*

3.9 Conclusions

The performance of the turbulence models implemented in PMB3D for predicting vortical delta wing flows has been examined. It has been found that turbulence modelling influences vortex strength, diffusion of vorticity, secondary separation location and strength (and therefore primary vortex core location). The vortex breakdown location has been observed to be influenced by turbulence modelling which is due to the varying core properties predicted with different turbulence models. Generally the 2-equation models were found to perform better than the 1-equation Spalart-

Allmaras turbulence model.

A preliminary study showed the solutions from the k-ω turbulence model of Wilcox [112] produced the most realistic solutions (based on the characteristics of the primary and secondary structures). This encouraged an analysis of some available k-ω variants [129]. These variants involved altering the source terms in the k and ω equations, depending on the magnitude of the ratio of the rate-of-strain tensor and the magnitude of vorticity. The NLR P_ω enhancer was found to eliminate most turbulence in the vortex, pre- and post-breakdown. The levels of turbulent dissipation were such that the highly turbulent post-breakdown region was eliminated, yielding an unconverged solution. The NLR P_k limiter was found to be a much weaker modification in comparison to the NLR P_ω enhancer, yielding qualitatively similar turbulence levels to the standard k-ω model. However, the turbulence levels in the vortex core (where turbulence levels should be low [12]) are reduced, and as such breakdown is delayed in comparison to the standard k-ω model. All versions of the k-ω model have predicted similar suction levels, and secondary separation.

Considering the surface pressure distributions and vorticity magnitudes in the vortex core, it can be concluded that the leading edge vortices predicted are lower in strength compared to those found in experiment. This should be kept in mind when considering tunnel interference which is dependent on vortex strength.

Considering suction levels, vortex structure, distribution of turbulent eddy viscosity, core velocity components, and breakdown locations, it has been concluded that best comparison with experiment is obtained with the NLR P_k limiter. As such this model will be used in all RANS simulations of chapters 5 and 6. The NLR P_k limiter was applied to the WEAG-TA15 test case of chapter 2, and was found to produce accurate results.

It is concluded that the PMB3D RANS solver can adequately predict the vortical flow around delta wings and can be used for further wind tunnel interference simulations.

Chapter 4

RANS simulations of tunnel interference on delta wing flows

4.1 Introduction

In chapter 2 we studied tunnel wall effects using the Euler equations. However, as discussed in chapter 3 we need the Reynolds Averaged Navier-Stokes (RANS) equations to model more realistically the lee side flow over delta wings. Therefore to improve correlation with experiment, and to confirm the conclusions of chapter 2, the simulations have been repeated with a RANS model of the flow. As in previous chapters the PMB3D flow solver (discussed in section 1.5) is used in all calculations. The main conclusions from chapter 2 are as follows

- Wind tunnel wall constraints promote vortex breakdown.
- For conventionally shaped wind tunnels the presence of the roof and floor has little influence on vortex breakdown.
- Tunnel side walls appear to be the dominant influence promoting vortex breakdown.
- Wind tunnel blockage has little or no influence on vortex breakdown.
- Tunnel side walls increase the mean effective incidence of the wing.

- Downstream of the wing it has been shown that the tunnel side walls displace the rotational post breakdown flow upwards towards the centre of the wind tunnel.
- The tunnel side walls increase the helix angles and therefore vortex strengths. The tunnel roof and floor have little influence on vortex strengths.
- Tunnel wall constraints tend to promote vortex breakdown when the wing undergoes sinusoidal pitching motion. The extent of the tunnel influence is dependent on whether the wing is on its upstroke or downstroke.
- Side walls have a strong effect on the rate of motion of the vortex breakdown, delaying vortex recovery.
- The side wall influence tends to be greatest on the downstroke of the motion.

4.2 Test cases

Two test cases are considered for the RANS simulation of wind tunnel effects on delta wing aerodynamics. The first case is the ONERA 70^o delta wing discussed in chapter 3, and the second is the WEAG-TA15 wing discussed in chapter 2. These cases provide experimental validation for both steady and pitching solutions respectively. The experimental results of Mitchell [5] have been used for validation of the ONERA 70^o wing case in chapter 3. For this case flow visualisation data exists for a static incidence of 27^o. The experimental results of Löser [107] are used as validation for the WEAG-TA15 case. Although no flow visualisation data is available surface pressure data and unsteady load data is available for comparison. Drawing on the conclusions of section 3.9, for all calculations the 2-equation k-ω turbulence model with the NLR P_k limiter is used.

For all tunnel test cases, a slip condition (inviscid wall boundary) has been applied at the tunnel walls. This eliminates the need to resolve the tunnel boundary layers thus reducing the grid sizes dramatically. A consequence of this is that the favourable pressure gradient within the test section, due to tunnel wall boundary layer growth, is not modelled. However it is expected that the lack of tunnel wall

boundary layers in the present simulations will not effect the trends observed when considering wall induced velocities.

4.2.1 Test case 1 : ONERA 70^o wing - steady

For this wing three boundaries have been chosen. The first has the wing in free air (farfield), the second represents the ONERA F2 tunnel (discussed in section 3.3), and the third the ONERA F2 tunnel side walls brought closer to the wing (increasing the S/W ratio). Full details of these configurations as well as flow parameters can be found in table 4.1.

Tunnel	S/W	S/H	α_m	M_∞	Re
Farfield	-	-	27^o	0.2	1.56×10^6
ONERA F2	0.49	0.38	27^o	0.2	1.56×10^6
S/W0.63	0.63	0.38	27^o	0.2	1.56×10^6

Table 4.1: ONERA 70^o wing test cases - Fully turbulent flow

Mitchell [5] tested this wing in both the ONERA S2Ch and ONERA F2 tunnels and it was noted there were significant differences in the results from the two facilities. As described in section 3.3 the ONERA F2 tunnel is of rectangular cross-section with height 1.8m, width 1.4m, and length 5m. The ONERA S2Ch tunnel is of quasi-circular cross-section with a diameter of 3m and test section length 4.93m. These values given S/W=0.49 and S/H=0.38 for the ONERA F2 tunnel, and S/W=0.23 and S/H=0.55 (taking into account off tunnel centreline location of wing) for the ONERA S2Ch tunnel. Despite the flow conditions being similar in both tunnels, the mean breakdown locations were closer to the apex in the ONERA F2 tunnel (the smaller of the two), when compared with those measured in the ONERA S2Ch tunnel (see figure 4.1). This suggests some test facility interference, which could be due to either the support structure or tunnel wall interference. It should also be noted that there is an asymmetry in the breakdown locations when comparing the values from the port and starboard halves of the wing. The most probable reason given was a small yaw angle of the model.

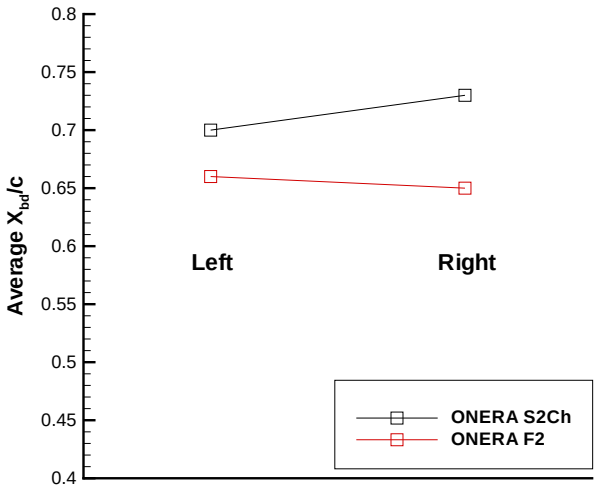

Figure 4.1: *Measured breakdown locations in ONERA F2 tunnel and ONERA S2Ch tunnel, taken from reference [5], page 136*

4.2.2 Test case 2 : WEAG-TA15 wing - steady and pitching

This test case was discussed in chapter 2. For a full discussion of the wing geometry and the available experimental data, see section 2.4. Table 4.2 lists the computational test cases and the flow conditions considered. As in chapter 2, Trans-Finite Interpolation (discussed in section 1.5.1) is used to deform the mesh to allow pitching motion inside the wind tunnels.

It should be noted that a lower Mach number of 0.2 is used in the RANS simulations. This Mach number is closer to that of the experiment and further reduces the question of compressibility effects which may have been present in the simulations of chapter 2.

4.3 Grids

The strategy implemented in chapter 2 will be used for all computations. This involves the creation of one grid (a "farfield" grid) for each test case, constructed in such a way that wind tunnels can be created by extracting the outer blocks.

TUNNEL	S/W	S/H	α_m	α_0	k	M_∞	Re
Farfield	-	-	21^o	-	-	0.2	3.1×10^6
Square	0.42	0.42	21^o	-	-	0.2	3.1×10^6
3x2	0.42	0.63	21^o	-	-	0.2	3.1×10^6
2x3	0.63	0.42	21^o	-	-	0.2	3.1×10^6
Farfield	-	-	21^o	6^o	0.56	0.2	3.1×10^6
Square	0.42	0.42	21^o	6^o	0.56	0.2	3.1×10^6
3x2	0.42	0.63	21^o	6^o	0.56	0.2	3.1×10^6
2x3	0.63	0.42	21^o	6^o	0.56	0.2	3.1×10^6

Table 4.2: WEAG-TA15 wing test cases - Fully turbulent flow

This methodology has the advantage of eliminating grid variations in the region of interest, removing the question of grid dependence when comparing solutions.

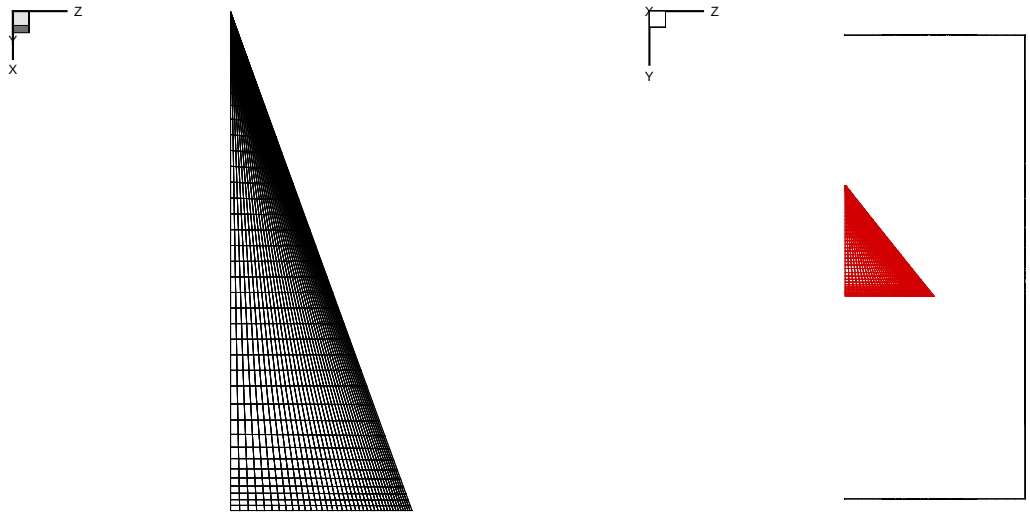

Figure 4.2: *ONERA 70^o delta wing upper surface mesh (every second grid point removed for clarity) and view upstream in ONERA F2 Tunnel*

The ONERA 70^o wing upper surface mesh, and the wing in the ONERA F2

tunnel is shown in figure 4.2. A representation of the ONERA 70^o wing grid resolution was also given in figure 3.11. The upper surface mesh for the WEAG-TA15 wing is shown in figure 4.3, and the wing in the tunnels can be seen in figure 2.2. A representation of the WEAG-TA15 wing grid resolution was given in figure 3.29. Again all grids are of H-H topology with only half the wing modelled. The ONERA 70^o wing and the WEAG-TA15 wing have been meshed at 27^o and 21^o respectively.

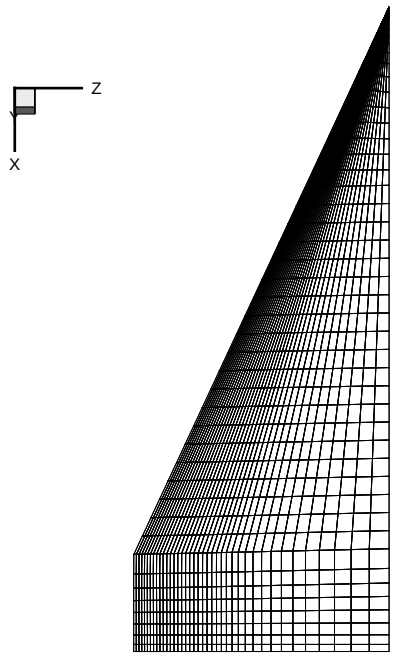

Figure 4.3: *WEAG-TA15 upper surface mesh (every second grid point removed for clarity)*

For complete grid dimensions see table 4.3. Note that the streamwise and spanwise values are over the wing (not including off wing blocks), and the total is the full grid size. As described in section 1.5, the axis system used by the PMB3D flow solver has the x and y axes in the longitudinal plane, with the z axis spanwise. The first cell height normal to the wing surface is $10^{-6}c_r$ in all grids, yielding y^+ values of less than 1.0 for the ONERA 70^o and WEAG-TA15 wings respectively. This cell spacing provides an adequate resolution of the wing boundary layer (a full discussion is given in the validation described in chapter 3).

Test case	Streamwise	Spanwise	Normal to upper surface	Normal to lower surface	Total
ONERA 70^o FF	99	79	117	75	3,969,810
ONERA 70^o F2	99	79	103	61	2,904,660
ONERA 70^o S/W=0.63	99	79	103	61	2,664,090
WEAG-TA15 FF	99	79	109	81	3,966,306
WEAG-TA15 SQ	99	79	95	65	2,995,888
WEAG-TA15 3x2	99	79	89	61	2,809,808
WEAG-TA15 2x3	99	79	95	65	2,594,998

Table 4.3: Viscous grid dimensions

The ONERA 70^o wing and WEAG-TA15 RANS solutions have been verified and validated in chapter 3.

4.4 Results and discussion

4.4.1 Steady results

Test case 1 : ONERA 70^o Wing

In order to obtain the breakdown locations on the ONERA 70^o wing, the location at which the axial component of velocity becomes zero was used. This is consistent with the method used in experiment. To do this a vertical slice through the vortex core was taken and the point where the axial velocity becomes zero was measured. The breakdown locations for the three test cases are given in table 4.4.

TUNNEL	S/W	S/H	Breakdown Location
Farfield	-	-	$68.8\%c_r$
ONERA F2	0.49	0.38	$64.7\%c_r$
ONERA S/W=0.63	0.63	0.38	$60.3\%c_r$
Experiment	0.49	0.38	$65\pm5\%c_r$

Table 4.4: Summary of steady breakdown locations for ONERA 70^o wing at 27^o angle of attack

The promotion of vortex breakdown is comparable in magnitude (though possibly a little lower) to the promotion of vortex breakdown seen experimentally when going from the larger ONERA S2Ch tunnel to the smaller ONERA F2 tunnel (see figure 4.1). It should be kept in mind that, as discussed in chapter 3, the vortex strengths are underpredicted (and therefore so will the tunnel wall interference) and support effects have been omitted in the CFD solutions. As in chapter 2, increasing the S/W ratio has the effect of promoting vortex breakdown.

The wing upper surface pressure and shear stress streamline distributions are shown for the three cases in figure 4.4. It can be seen that the suction (especially at the apex) from the leading edge vortices increases as the wing becomes closer to the tunnel side wall. The secondary separation lines are clearly visible and the primary attachment line occurs along the centre of the wing as in experiment. Figures 4.5 to 4.7 show the spanwise surface pressure distributions at the chordwise locations of $x/c_r = 0.32$, $x/c_r = 0.52$, and $x/c_r = 0.63$ respectively. Vertical coloured lines at the x/c_r=0.63 station represent the secondary separation locations (taken where τ_z changes sign). When the flow is confined by the ONERA F2 tunnel the suction peak increases, and increases further as the side wall is brought closer (the S/W=0.63 tunnel). Interestingly at the chordwise location x/c_r=0.63 (figure 4.7) the secondary separation location has moved outboard. This occurs at the earlier stations on the wing, however as the wing narrows the variations become less evident. It can also be seen that the secondary vortex increases in strength (almost equally in comparison to the primary suction peak) with increasing S/W.

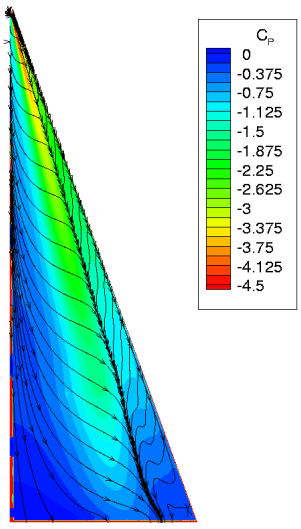

(a) Farfield

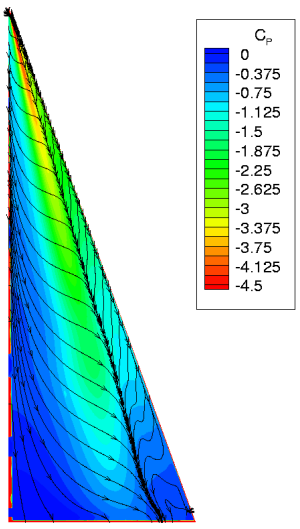

(b) ONERA F2 tunnel

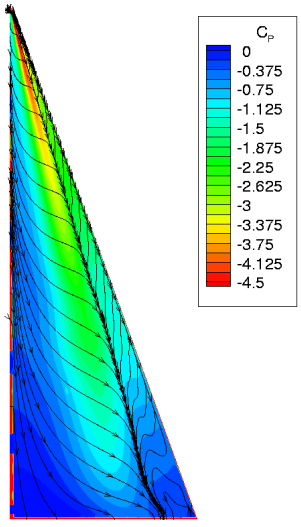

(c) S/W = 0.63 Tunnel

Figure 4.4: *ONERA 70° wing, Steady flow wing surface pressure distributions with shear stress streamlines*

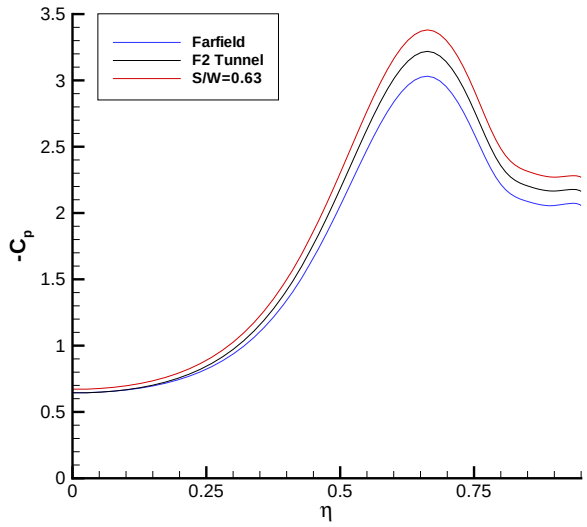

Figure 4.5: *ONERA 70^o Wing, Comparison of upper surface pressure distributions,* $x/c_r = 0.32$

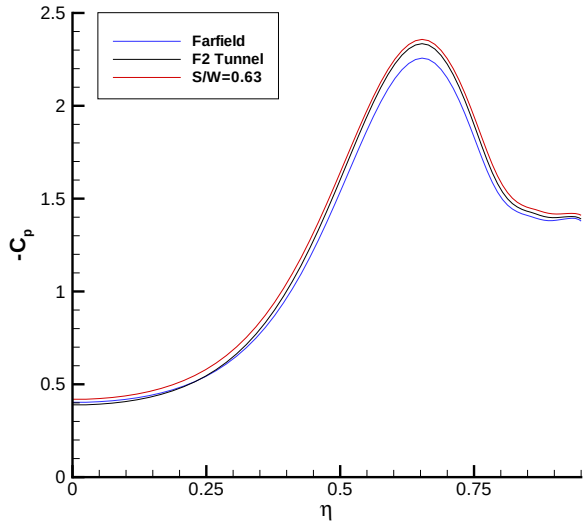

Figure 4.6: *ONERA 70^o Wing, Comparison of upper surface pressure distributions,* $x/c_r = 0.52$

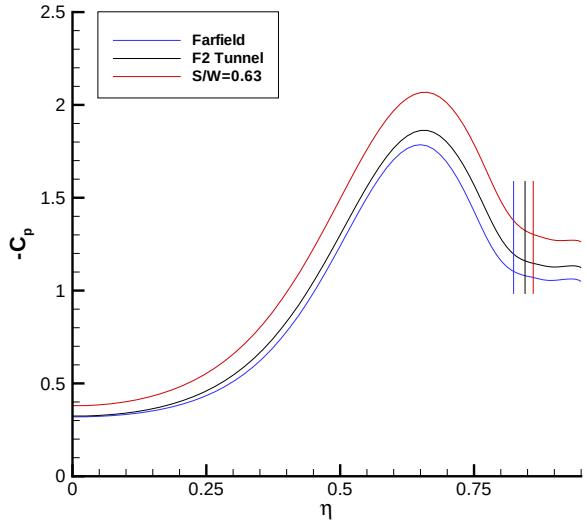

Figure 4.7: *ONERA 70^o Wing, Comparison of upper surface pressure distributions,* $x/c_r = 0.63$

The tunnel wall pressure distributions on the ONERA F2 and the S/W = 0.63 tunnels are shown in figure 4.8. As in the Euler cases a clear vortical flow pattern can be seen on the side walls. The flow patterns appear similar for the ONERA F2 tunnel and the S/W=0.63 tunnel, with the strength of the pressure distribution increasing with increasing S/W ratio. Clearly most interference is induced by the side wall.

In order to assess the adverse pressure gradient experienced by the vortex core, the pressure distribution along the vortex core in each tunnel is shown in figure 4.9. Visbal [70] found that vortex breakdown was heavily dependent on the pressure gradient along the vortex core. As the wing is placed within wind tunnel wall constraints, the suction in the vortex core prior to breakdown increases. This implies that when the vortices are placed within wind tunnels, they become stronger than those in farfield conditions. With this additional suction the adverse pressure gradient experienced by the core flow increases, thus vortex breakdown is expected to be promoted. This agrees qualitatively with the results of Visbal.

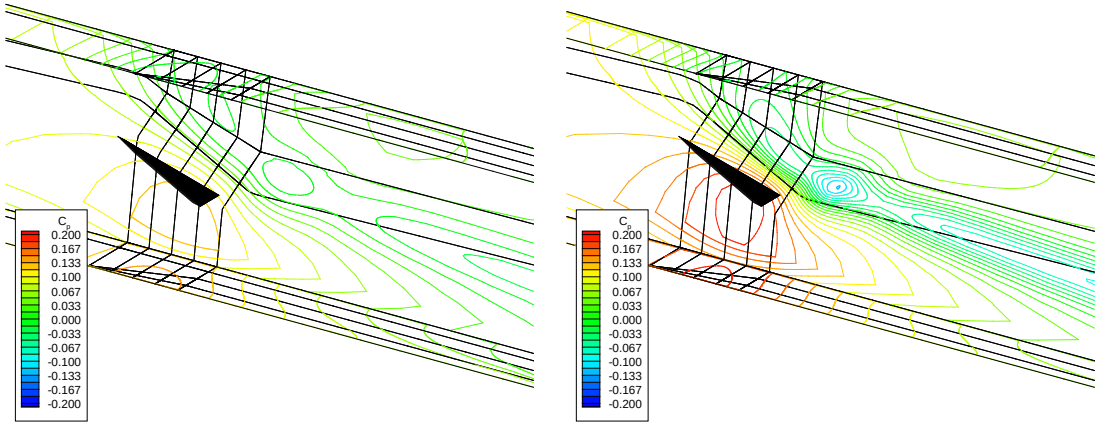

(a) ONERA F2 tunnel (b) S/W = 0.63 Tunnel

Figure 4.8: *ONERA 70° wing, Steady flow tunnel wall pressure distributions*

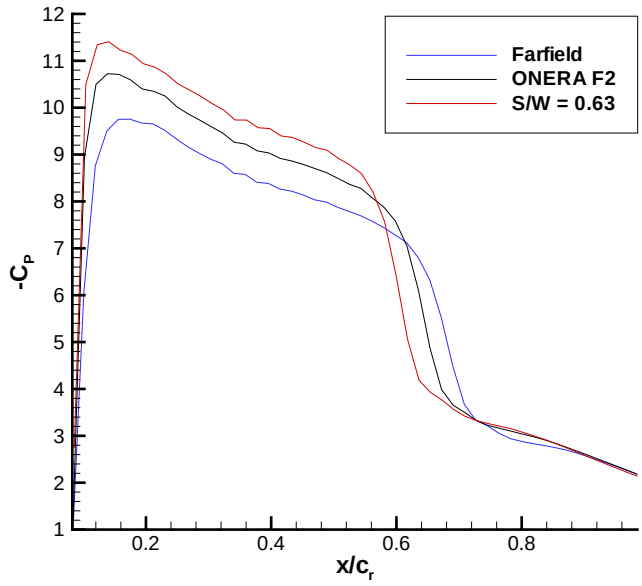

Figure 4.9: *ONERA 70° wing, Pressure distributions along vortex cores*

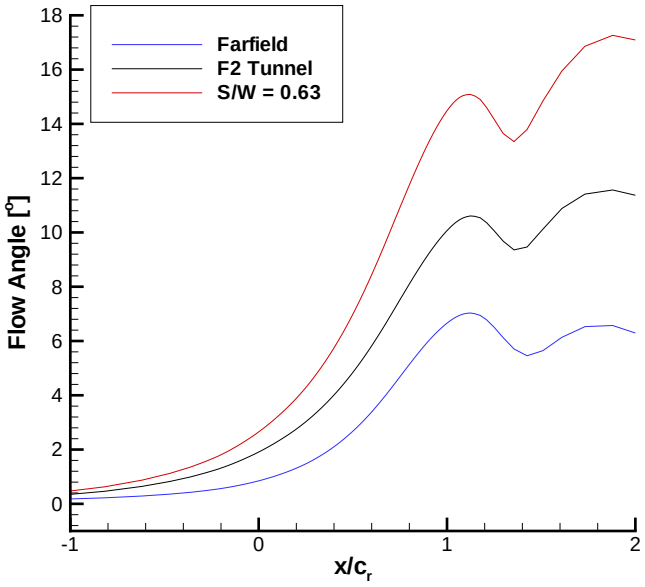

Figure 4.10: *ONERA 70^o wing, Flow angles at 1.5 wing span lengths from wing*

The flow angle (the angle at which the freestream is turned up due to the presence of the wing and side walls) variation in the streamwise direction can be seen in figure 4.10. Both tunnels increase the flow angle ahead of the wing in comparison to the farfield solution, and also increase the rate at which the flow angle increases along the wing. As with the Euler results there are two possible effects present, an increase in the mean effective incidence and induced camber. Both these effects increase with increasing S/W. Since breakdown has moved towards the apex it is expected that the increase in the mean effective incidence is the dominant effect.

Figures 4.11 shows the distribution of the helix angle (defined by equation 2.5) through the midline of the vortex core at the chordwise location of $x/c_r = 0.52$. At this chordwise location the vortex is unburst in all solutions. The experimental helix angle obtained in the ONERA F2 tunnel is also given for comparison. As the tunnel walls are brought closer to the wing it can be seen that the helix angle increases (the turns of the vortex tighten) which can cause a promotion of vortex breakdown [34]. This is due to the side wall induced vertical velocity components which also increase in the mean effective incidence of the wing. The tightening of the vortex increases

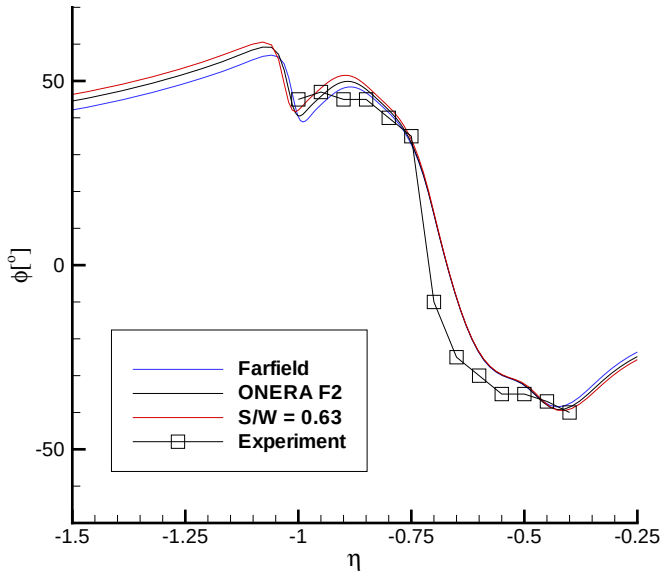

Figure 4.11: *ONERA 70° wing, Comparison of helix angles through vortex cores at* x/c_r*=0.52*

the crossflow momentum. Given that the adverse pressure gradient experienced by the wing boundary layer as it passes from beneath the primary vortex core to the secondary separation region, is unchanged (the secondary suction also increases with the primary suction), the likely cause of the delay in secondary separation in the tunnels is an increase in crossflow momentum due to the tighter winding of the vortex. It can also be seen that the location at which the helix angle changes sign (as we pass through the vortex core) does not appear to move significantly with increasing S/W ratio, indicating the vortex core does not move spanwise significantly at this chordwise station.

The static pressure distribution along the centreline of the tunnels and the farfield solution can be seen in figure 4.12. As the centreline passes through the wing the switch from the pressure side to the suction side can be seen as a jump in the curve at approximately x/c_r=0.75. It is evident that as the tunnel size decreases the static pressure beneath the wing increases (as expected due to increasing frontal area blockage). The suction over the wing upper surface also increases with decreasing

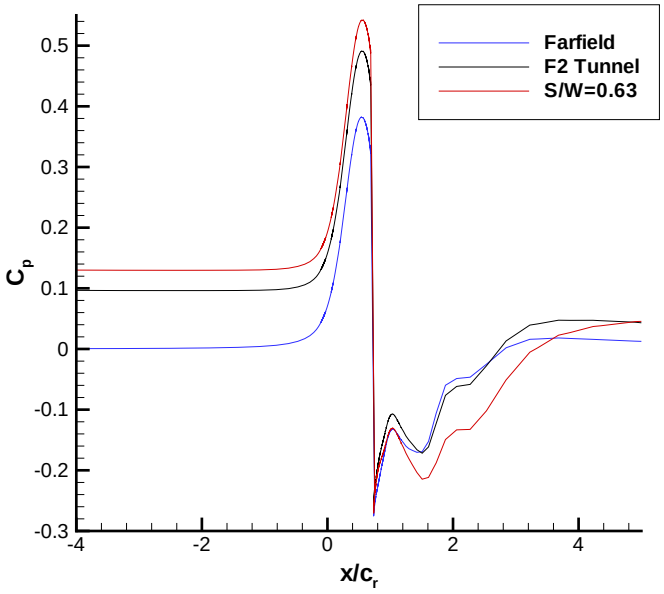

Figure 4.12: *ONERA 70° wing, Tunnel centreline pressure distributions*

tunnel size. The effect of the lifting of the broken down vortex system into the centre of the tunnel can also be seen. Behind the wing the tunnel pressure distributions are slightly above that of the farfield. However, it should be recalled that there are two effects, the blockage increasing the static pressure within the tunnel, and the vortex lifting which decreases the pressure in this region. Thus it is the difference between the pressure increment ahead of the wing and behind the wing that shows the extent of the vortex lifting. The displacement of the vortices has been confirmed with flow visualisations.

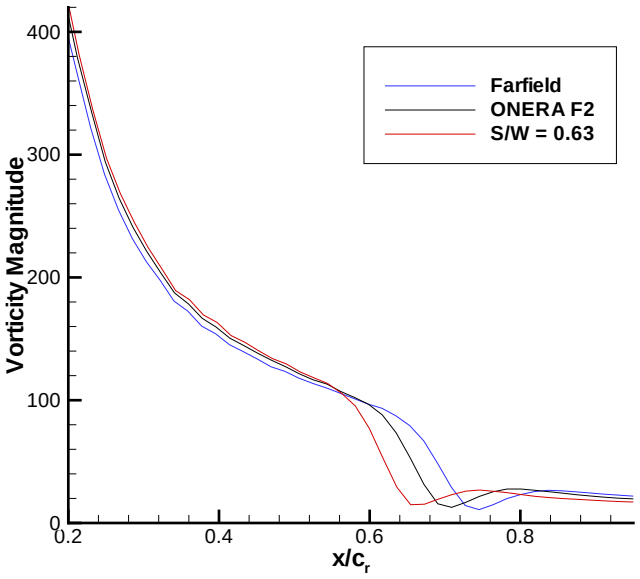

Figure 4.13: *ONERA 70° wing, Data extracted from vortex core - vorticity magnitudes*

In order to assess the levels of vorticity, the magnitude of the vorticity vectors has been extracted along the vortex core. As seen in figure 4.13, when tunnel wall constraints are applied to the flow the vorticity in the core increases. It is also evident that the highest vorticity occurs near the apex of the wing. Cross-sectional slices of the vorticity distribution through the vortex have been taken at the chordwise location of $x/c_r = 0.63$ (figure 4.14). This gives an excellent depiction of the vortex structure. Close inspection of the vortex core locations confirms that the vortex is displaced above the wing in the wind tunnels as suggested by figure 4.12. It should be recalled that for the flow in the ONERA F2 and S/W=0.63 tunnel, vortex breakdown occurs nearby in comparison to the farfield solution. This can be seen by the decrease in vorticity magnitude at the core. The total pressure loss (TPL) contours (figure 4.15) at the same chordwise location again give an excellent depiction of the vortex structure. In this figure the nearby presence of vortex breakdown can be seen as an increase in the TPL at the vortex core (as breakdown begins to occur turbulence and entropy increase, thus increasing the TPL).

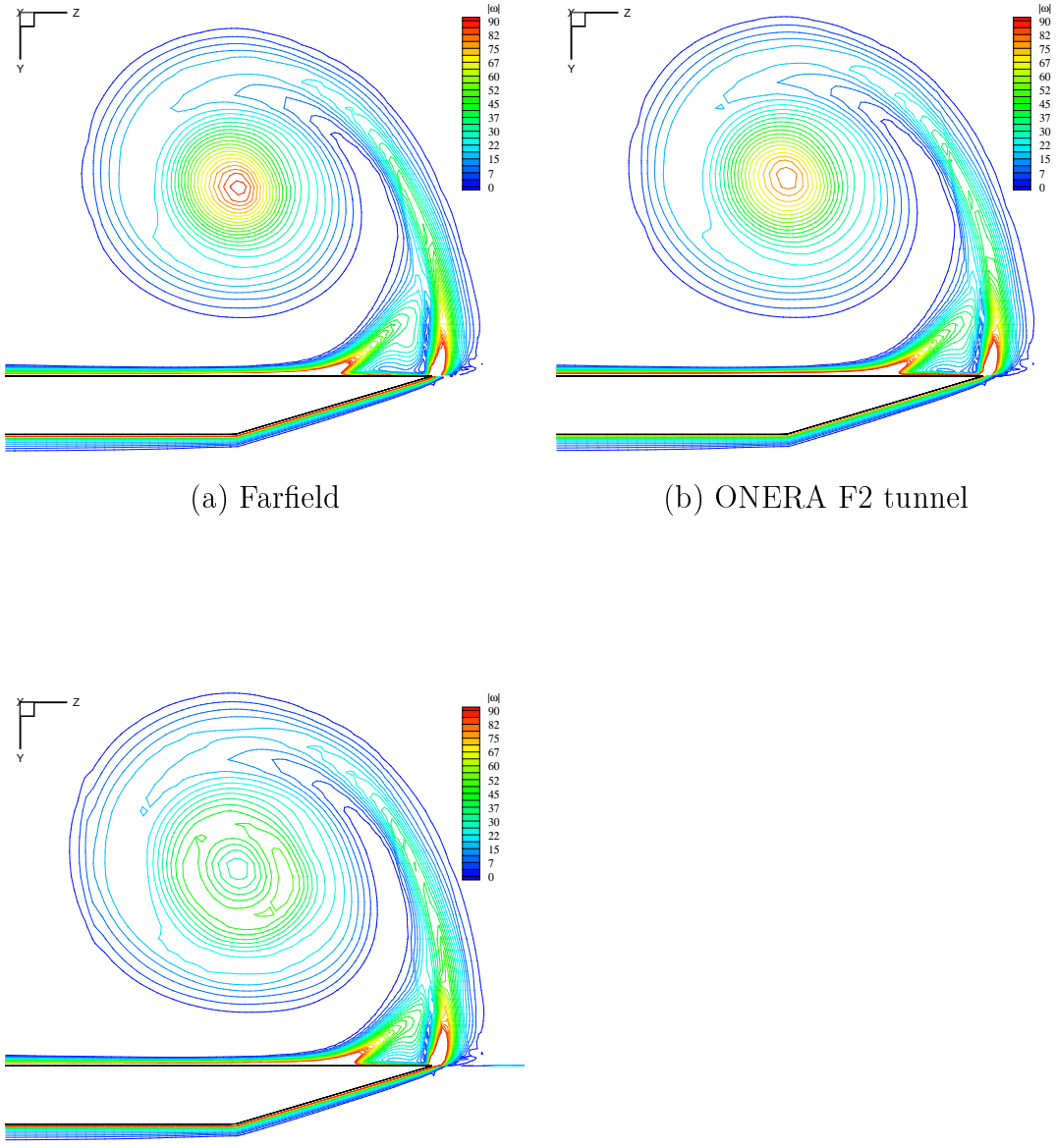

(a) Farfield

(b) ONERA F2 tunnel

(c) S/W = 0.63 Tunnel

Figure 4.14: *ONERA 70^o wing, Steady flow vorticity magnitude contours,* x/c_r = 0.63

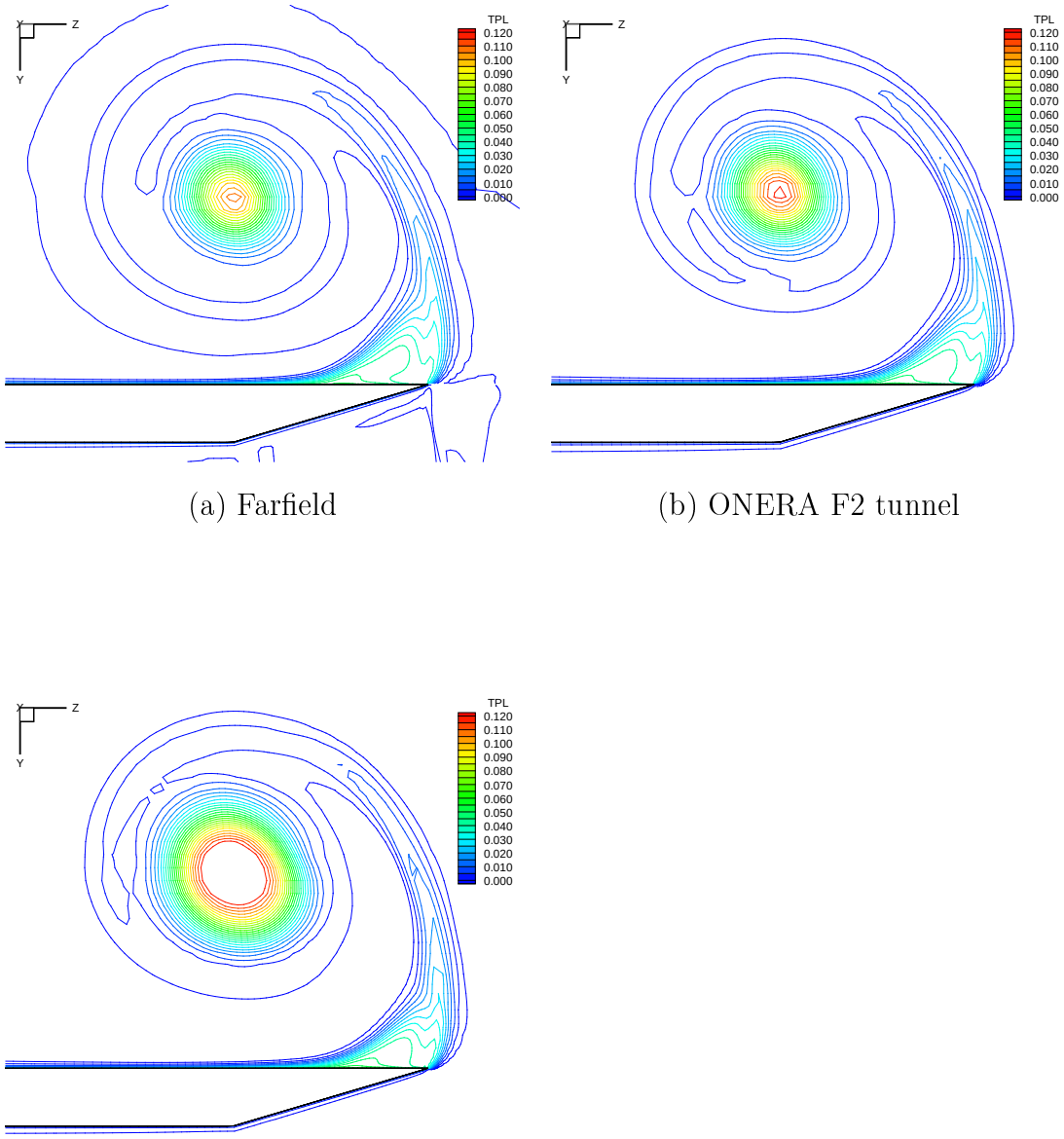

(a) Farfield

(b) ONERA F2 tunnel

(c) S/W = 0.63 Tunnel

Figure 4.15: *ONERA 70^o wing, Steady flow total pressure loss contours,* $x/c_r = 0.63$

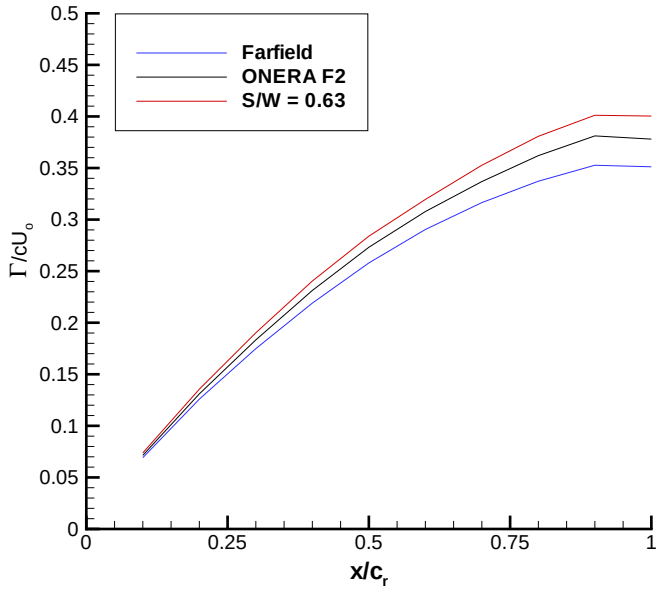

Figure 4.16: *ONERA 70^o wing, Comparison of circulation distributions*

The chordwise variation in circulation along the vortex is given in figure 4.16. The circulation was obtained by integrating the ω_x component of the vorticity vector over ten chordwise slices. The oppositely signed secondary separation region was omitted (which would have the effect of lowering the circulation). From the apex to around the midchord position it can be seen there is a relatively linear growth in circulation in the chordwise direction, after which the rate of growth in circulation decreases [12]. Despite vortex breakdown occurring the circulation continues to increase in the chordwise direction [13], eventually becoming near constant as the trailing edge is reached. The integrations were performed over an entire extracted plane, thus it would appear rather than there being a loss in the ω_x component of vorticity, it is dispersed throughout the vortex. If the integration region is not large enough to encompass this dispersion, it may appear that there is a loss in circulation. The circulation curves further indicate that as the wing is placed in wind tunnels the vortices become stronger, strengthening with increasing S/W ratio.

Test case 2 : WEAG-TA15 Wing

The breakdown locations for the four WEAG-TA15 wing test cases are given in table 4.5. Note that no experimental breakdown locations are available.

TUNNEL	S/W	S/H	Breakdown Location
Farfield	-	-	$77.4\%c_r$
Square	0.42	0.42	$75.7\%c_r$
3x2	0.42	0.63	$75.4\%c_r$
2x3	0.63	0.42	$70.8\%c_r$

Table 4.5: Summary of steady breakdown locations for WEAG-TA15 wing at 21^o angle of attack

As for the ONERA 70^o wing cases the breakdown locations were obtained by extracting a vertical slice through the vortex core and finding the point where the axial velocity component becomes negative. Recalling the results of the Euler simulations of chapter 2, it can be seen that the trends of breakdown location within tunnel wall constraints predicted by the RANS solver are similar to those predicted by the Euler solver. For the square and 3x2 tunnel it can be seen that the breakdown locations are almost identical, slightly nearer the apex in comparison to the farfield results, indicating that the roof and floor proximity has little influence. This result is in agreement with the Euler simulations. Comparing the 2x3 tunnel breakdown locations with those from the square and 3x2 tunnels, we clearly see that the largest influence on breakdown location is due to the side wall proximity. This again agrees with the Euler results.

Figure 4.17 shows the upper surface pressure distributions for the farfield and tunnel solutions. Upper surface shear stress streamlines have also been shown. The secondary separation and reattachment locations are clearly visible. Between the secondary separation and reattachment lines there is also another set of separation and attachment lines. This is due to a small region of separation just after the secondary vortex core. It is possible that this additional separation may not be present in experiment as it has already been observed that the secondary vortex

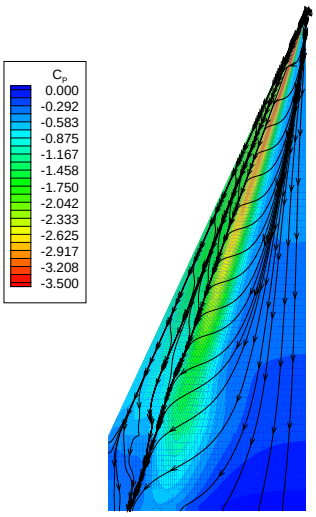

(a) Farfield

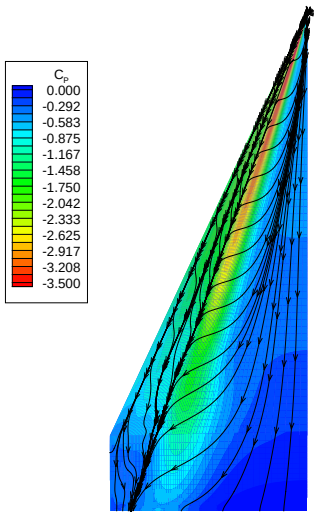

(b) Square tunnel

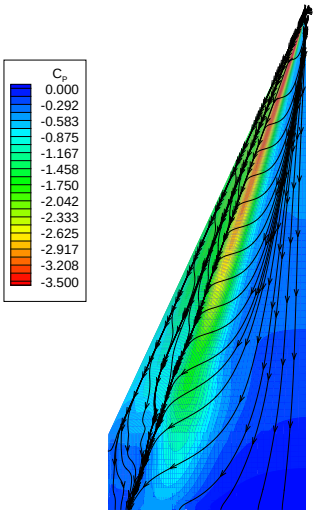

(c) 3x2 tunnel

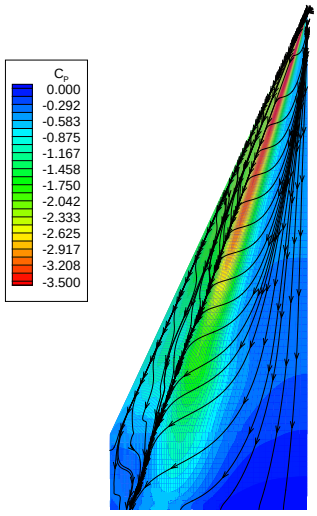

(d) 2x3 tunnel

Figure 4.17: *WEAG-TA15 wing, Steady flow wing surface pressure distributions with shear stress streamlines*

appears stronger in the CFD solutions, and also that the boundary layer profile may not be as full as in experiment (recall the early secondary separation discussed in section 3.8.3). This small structure can be seen later in figures 4.27 and 4.28.

A comparison of the upper surface pressure distributions at three chordwise locations is given in figures 4.18 to 4.20. As with the Euler and ONERA 70^o wing simulations it is clear that as the wing enters tunnel constraints, the suction peak beneath the primary vortex core increases. Although not presented here, there is a very minor shift in the secondary separation location towards the leading edge of the wing when in the tunnels. This trend is in agreement with the ONERA 70^o wing simulations although it should be noted that the shift is not to the same extent as in the solutions with the ONERA 70^o wing. Any delay in secondary separation is dependent on the upper surface shape (the WEAG-TA15 wing has a convex upper surface), the primary suction peak, and the crossflow momentum. Inboard of the primary vortices (near the centreline) it can seen that there is additional suction on the wing upper surface due to the blockage effect of the tunnels. This further increments the lift. Looking closely at the pressure distributions at x/c_r=0.6, the

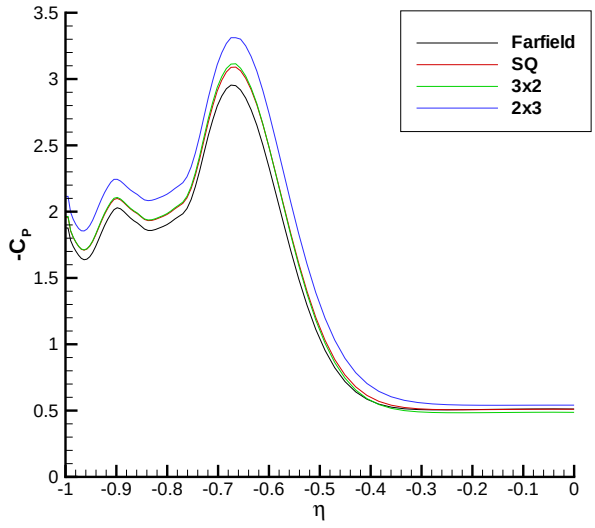

Figure 4.18: *WEAG-TA15 Wing, Comparison of upper surface pressure distributions, x/c_r = 0.3*

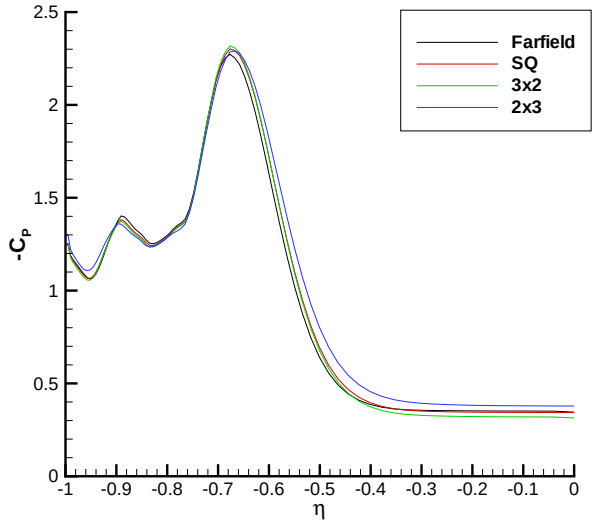

Figure 4.19: *WEAG-TA15 Wing, Comparison of upper surface pressure distributions, $x/c_r = 0.6$*

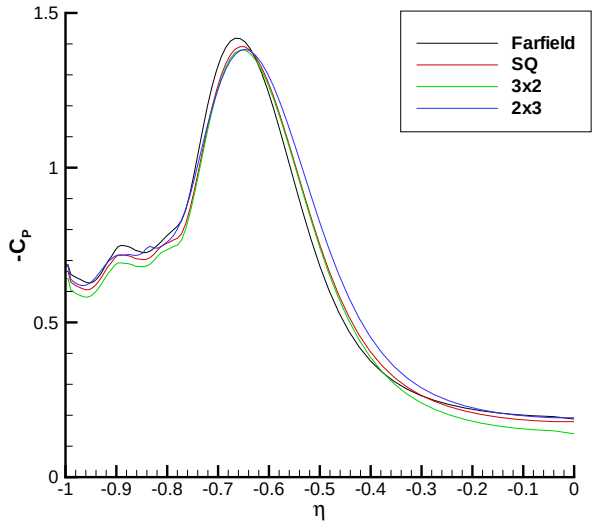

Figure 4.20: *WEAG-TA15 Wing, Comparison of upper surface pressure distributions, $x/c_r = 0.8$*

effect of the promotion of vortex breakdown towards the apex can be seen. All the pressure curves become much closer to the pressure distribution from the farfield solution. This is due to vortex breakdown being closer to the x/c_r=0.6 station in the tunnel solutions than in the farfield solution. A similar situation is seen at x/c_r=0.8, where the farfield solution shows the largest suction peak. Again this is due to the promotion of vortex breakdown which yields fully broken down vortical flow in the tunnel solutions. It is also evident that when the roof and floor are brought closer to the wing there is little change in the suction peak (compare the 3x2 and square tunnel solutions), which indicate that roof and floor proximity has little bearing on the strength of the vortices.

The tunnel wall pressure distributions for all three tunnels are given in figure 4.21. As in the Euler solutions for these cases, there is a clear favourable pressure gradient in the axial direction. This is expected as the vortices become closer to the side wall as they extend towards the trailing edge of the wing. At the cropped tip of the wing the side wall induced upwash will be greatest producing the largest suction on the wall. Looking at the strength of the pressure contours, the pressure gradient on the wall becomes more favourable as the side wall is moved closer to the wing, which is seen as we move from the square to the 2x3 tunnel. Again as seen in the Euler and ONERA 70^o wing solutions there is a clear vortical flow pattern on the side wall downstream of the wing's trailing edge. This vortical flow pattern extends the length of the tunnel. The vortical flow pattern on the side walls is observed for the three tunnels, reducing in extent with decreasing S/W ratio [87]. It is clear that the close proximity of the 2x3 tunnel side wall induces the largest favourable pressure gradient, indicating that the side wall produces most interference.

In order to assess the adverse pressure gradient experienced by the vortex core in the tunnels, the pressure distribution along the leading edge vortex core is shown in figure 4.22. As the vortex is placed within tunnel constraints it can be seen that the suction in the vortex core increases, with the largest increment being observed in the 2x3 tunnel. The square and 3x2 tunnels produce a similar increment in suction. This increase induces a stronger adverse pressure gradient as seen in figure 4.22. As described in the results of the ONERA 70^o wing case, the increase in the adverse pressure gradient promotes vortex breakdown.

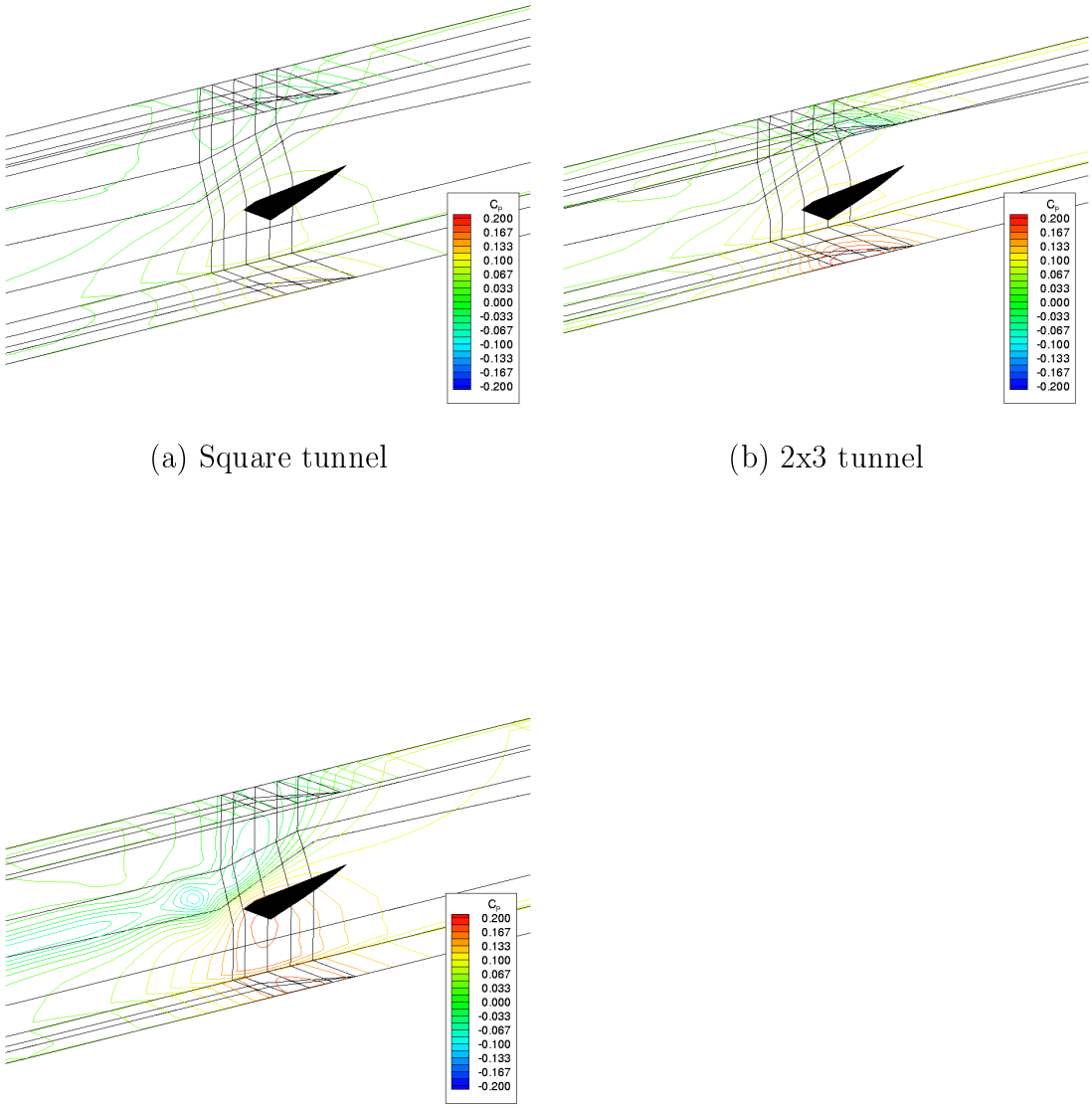

(a) Square tunnel

(b) 2x3 tunnel

(c) 3x2 tunnel

Figure 4.21: *WEAG-TA15 wing, Steady flow tunnel wall pressure distributions*

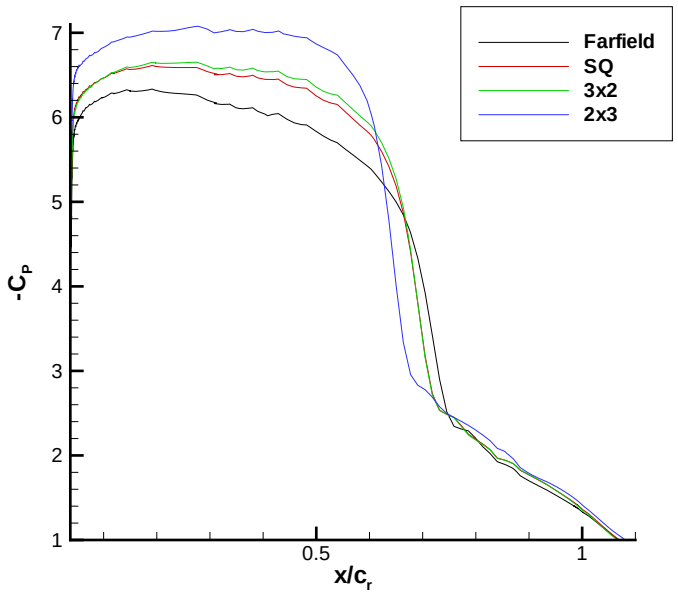

Figure 4.22: *WEAG-TA15 wing, Pressure distributions along vortex core*

The flow angles at the 2x3 tunnel side wall location are shown in figure 4.23. As in the Euler results of chapter 2 it can be seen that the presence of the side walls has increased the flow angles (the angle the freestream is turned up) along the wing thus increasing the mean effective incidence of the wing. Evidently the proximity of the 2x3 tunnel side wall induces the largest mean incidence, followed by the square and 3x2 tunnels which induce a near equal mean incidence. As mentioned in the Euler and ONERA 70^o wing results, the mean incidence effect would appear to be dominant over a possible induced camber effect.

The helix angle of the flow through the the vortex core can be seen in figure 4.24. This data was extracted at a chordwise location of x/c_r=0.6 where breakdown is downstream. As seen in the ONERA 70^o wing results, the helix angle increases due to the side wall induced velocity components. As shown previously, the roof and floor (as expected) have little effect on the helix angle. The vortex tightens the most in the 2x3 tunnel, followed by the square and 3x2 tunnels which are near equal.

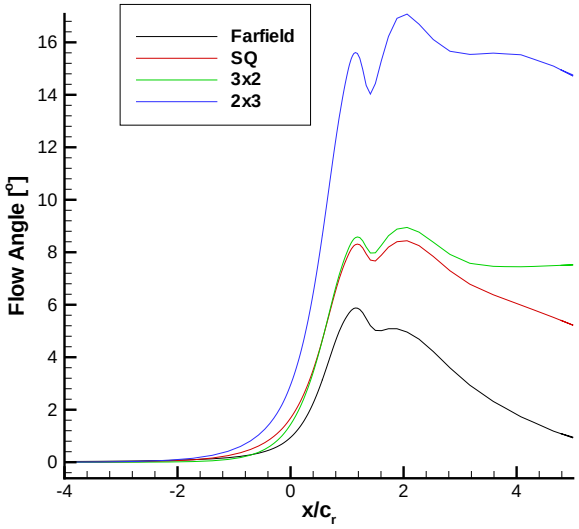

Figure 4.23: *WEAG-TA15 wing, Flow angles at 2x3 tunnel side wall location*

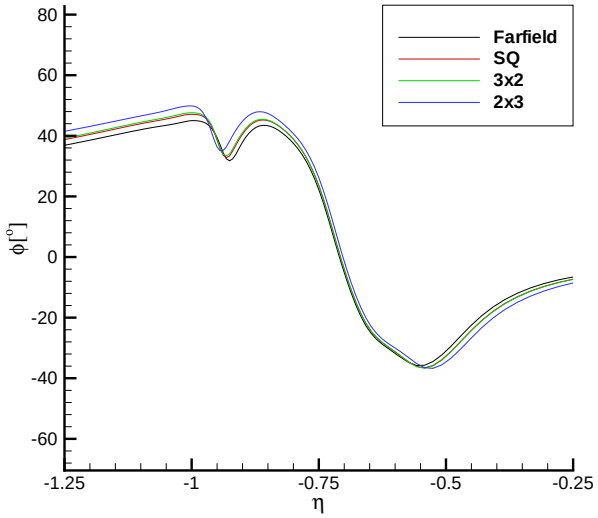

Figure 4.24: *WEAG-TA15 Wing, Comparison of helix angles, $x/c_r = 0.6$*

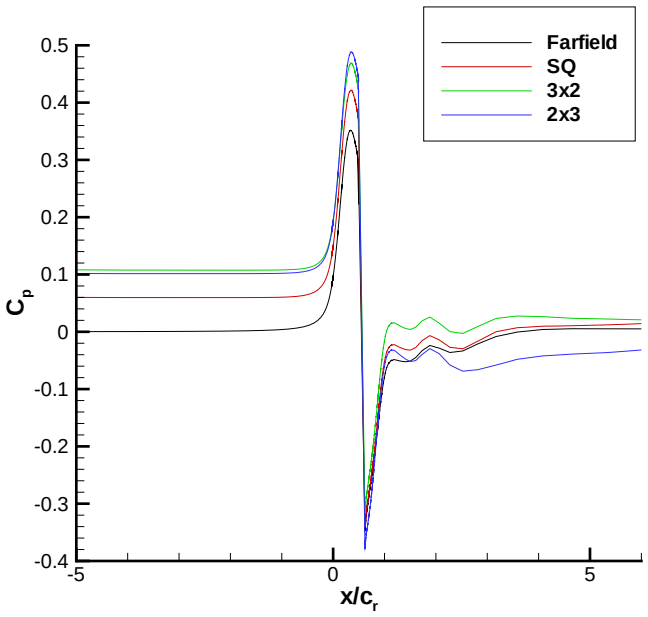

Figure 4.25: *WEAG-TA15 wing, Tunnel centre line pressure distributions*

The tunnel centreline pressure distributions can be seen in figure 4.25. As was discussed in chapter 2, the side wall induced upwash lifts the vortical system up into the centre of the tunnel. A similar trend is seen with the RANS solutions given in figure 4.25. Like the Euler solutions it can seen that the 3x2 and 2x3 tunnels produce similar blockage levels ahead of the wing. The jump from the pressure side to the suction side of the wing can be seen around x/c_r=0.5625. As previously observed, when the wing is placed within tunnel test sections the static pressure increases on the lower surface and decreases on the upper surface due to the blockage effect. As in the Euler and ONERA 70^o cases, well downstream of the wing the pressure distributions indicate the location of the broken down vortical system. Like the Euler solutions it can seen that the vortical flow in the 2x3 tunnel is displaced upwards to the centre of the tunnel (this is indicated by a low pressure in comparison to the farfield, square, and 3x2 tunnel solutions). Nearer the trailing edge where the flow on the lower surface is expanding past the trailing edge, the 2x3 tunnel solution exhibits characteristics of the vortical flow being displaced upwards to the centreline of the tunnel. Despite the pressure near the trailing edge being

higher than in the farfield solution, one must recall the increment in pressure due to blockage, thus deducting the effect of blockage it is clear the flow near the trailing edge is also lifted off the surface of the wing in comparison to the farfield, square, and 3x2 tunnel solutions. This was confirmed via flow visualisation.

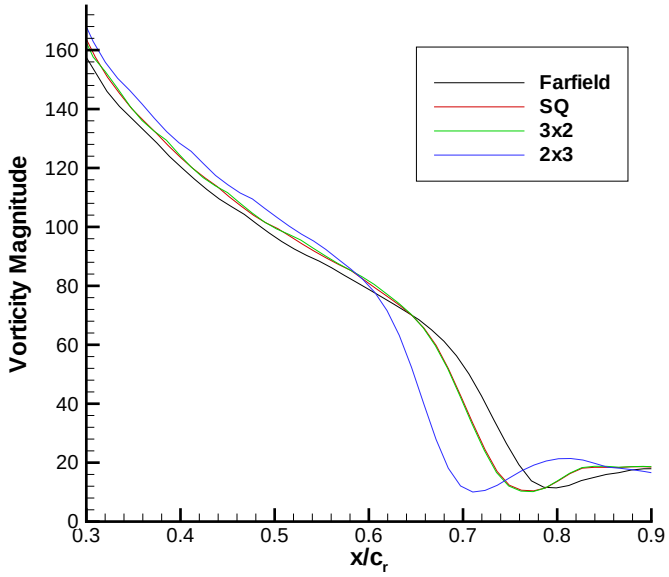

Figure 4.26: *WEAG-TA15 wing, Data extracted from vortex core - vorticity magnitudes*

The vorticity magnitude along the centre of the vortices is given in figure 4.26. Due to the very large vorticity magnitudes at the apex, this region has been omitted from the figure (most vorticity is generated at the apex). As with the suction in the vortex core, when the wing is placed within wind tunnel constraints the magnitude of the vorticity vectors along the vortex core increases. As seen for the ONERA 70^o wing, this indicates that the vortex becomes stronger in the tunnels. The 2x3 tunnel can be seen to increase in strength the most, followed by the square and 3x2 tunnels which produce similar vorticity values in the vortex centre. This confirms that side wall proximity is the dominant influence. The vorticity magnitude distribution through the vortex cores at the chordwise location x/c_r=0.5, can be seen in figure 4.27. The vorticity in the core is highest in the 2x3 tunnel, followed by the near

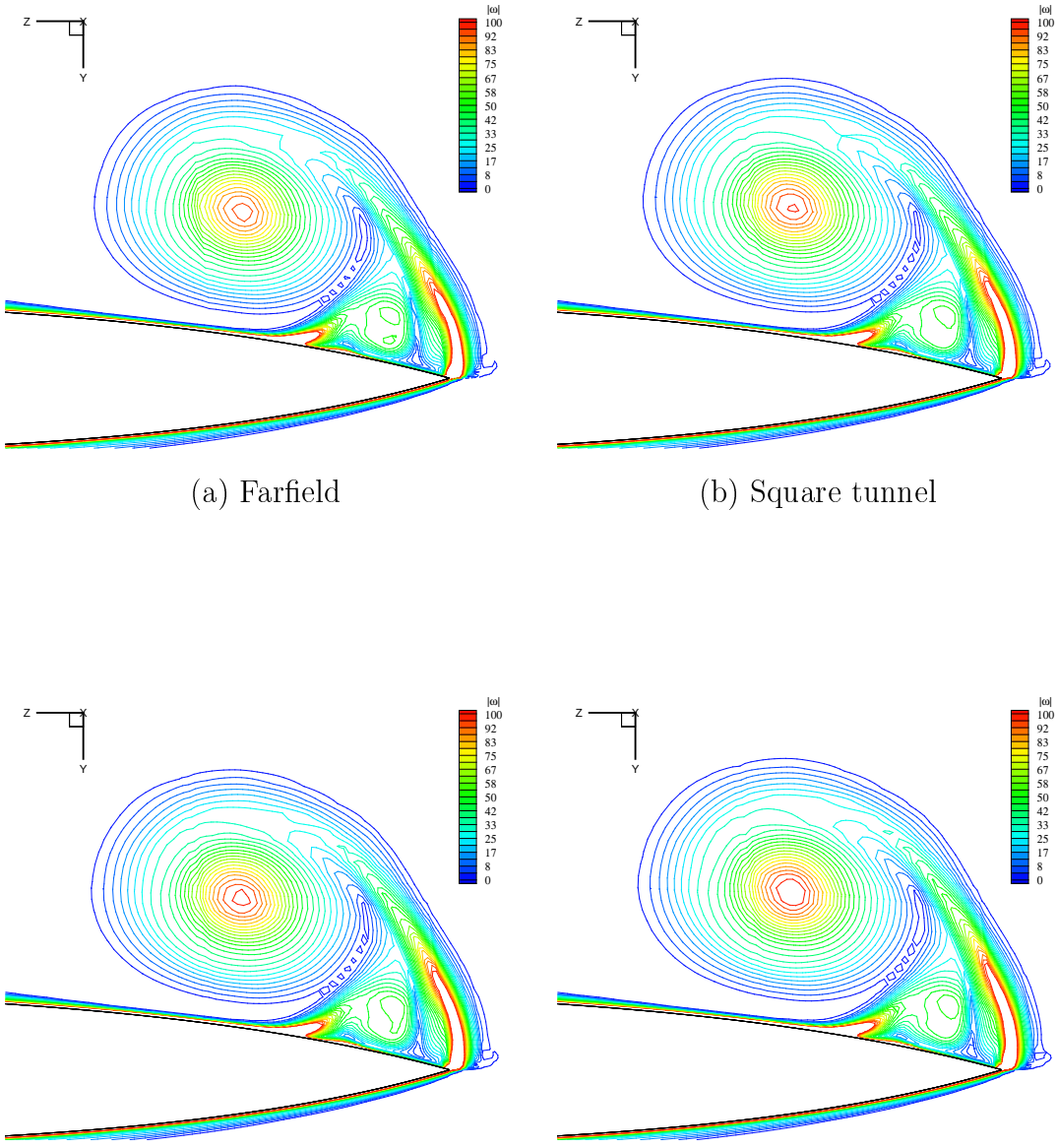

(a) Farfield

(b) Square tunnel

(c) 3x2 tunnel

(d) 2x3 tunnel

Figure 4.27: *WEAG-TA15 wing, Steady flow vorticity magnitude contours,* $x/c_r = 0.5$

equal square and 3x2 tunnel results. Recalling the results of the pressure distributions along the centre of the tunnels it can be observed that as the wing is placed in the tunnels (most noticeably the 2x3 tunnel), there is a shift upwards (off the surface of the wing) of the primary vortex core. Close inspection of the region between the primary and secondary vortices (near the wing surface), shows the presence of a small tertiary structure. Examination of the sign of the axial component of vorticity shows that the rotation is in the same sense as the primary vortex. This tertiary structure appears to be too small to be adequately resolved with the current grid resolution. It is this tertiary structure which causes the additional separation and attachment lines seen in figure 4.17. The TPL contours through the vortex core (figure 4.28) highlight the structure of the leading edge vortices. The secondary vortex is much larger than that observed on the ONERA 70^o wing. It is thought that the convex shape of the upper surface allows a more distinct secondary vortex to form.

The circulation along the chordwise direction is given in figure 4.29. As with the ONERA 70^o wing cases, the secondary vortex was eliminated from the calculation of circulation. Clearly the tunnel walls increase the strength of the vortices in the chordwise direction, with the 2x3 side wall inducing the strongest vortices. The almost equal circulation near the apex, and the steeper gradient of the circulation curve in the tunnels indicates that the effect of the tunnel side walls increases down the leading edge as expected. Since the square and 3x2 tunnels produce similar strength vortices, the roof and floor have little influence on vortex strength.

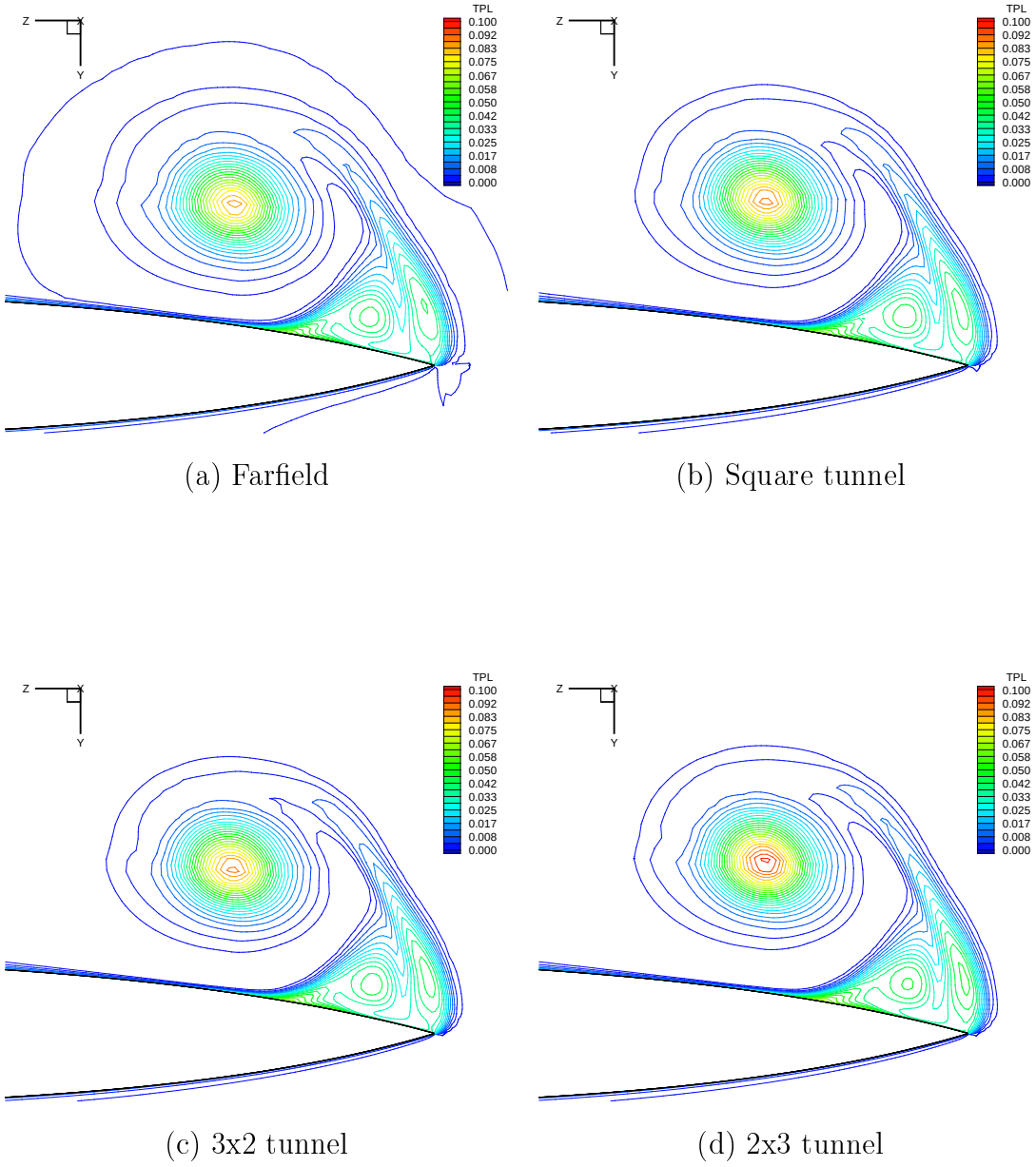

(a) Farfield

(b) Square tunnel

(c) 3x2 tunnel

(d) 2x3 tunnel

Figure 4.28: *WEAG-TA15 wing, Steady flow total pressure loss contours,* $x/c_r = 0.5$

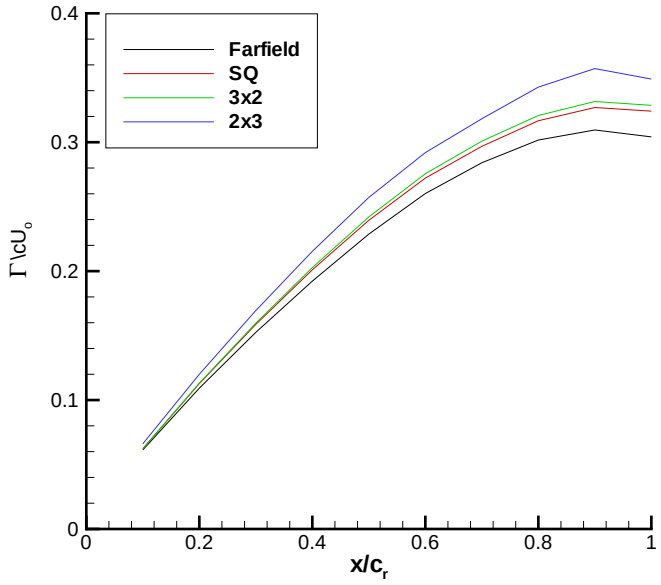

Figure 4.29: *WEAG-TA15 wing, Comparison of circulation distributions*

4.4.2 Pitching cases

Verification

In order to ensure a sufficient number of time steps per cycle were chosen to resolve the pitching motion, a time step refinement study was conducted by increasing the number of time steps per cycle from 50 to 100. It should be noted that the time step refinement study was conducted on a grid extracted from the finer WEAG-TA15 farfield mesh, since the coarse grid adequately predicts the pitching trends, and the coarse grid calculations are considerably cheaper. As can be seen the lift, drag and pitching moment curves in figure 4.30 compare well, indicating that 50 time steps provides an adequate temporal resolution.

Validation

The lift, drag, and pitching moment curves from each of the pitching cases considered are compared with the experimentally obtained loads and moments in figures 4.31 to 4.33. For validation purposes the farfield solution is considered as previously

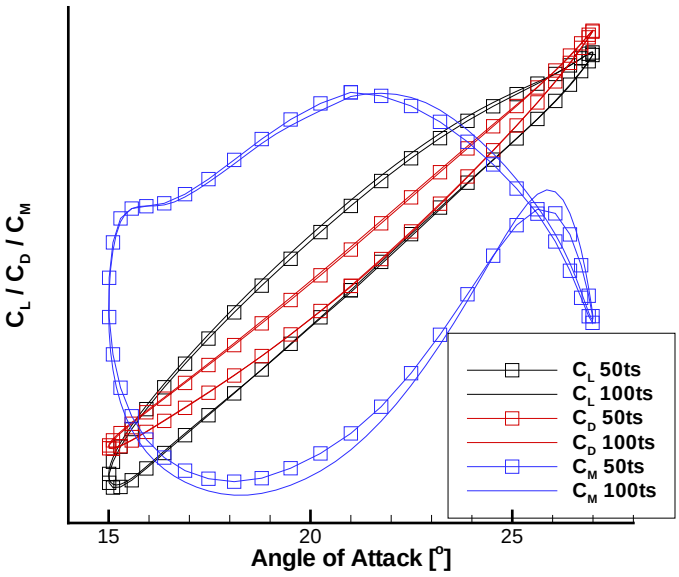

Figure 4.30: *WEAG-TA15 wing, Time step refinement study for pitching motion*

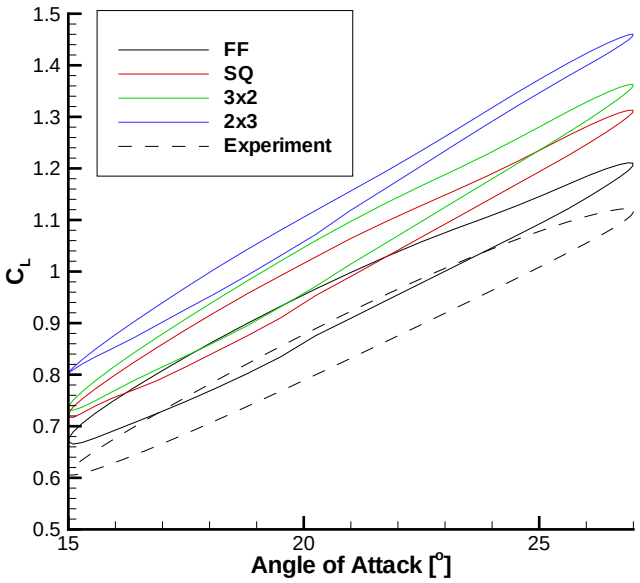

Figure 4.31: *WEAG-TA15 wing, $C_L - \alpha$ curves for pitching motion*

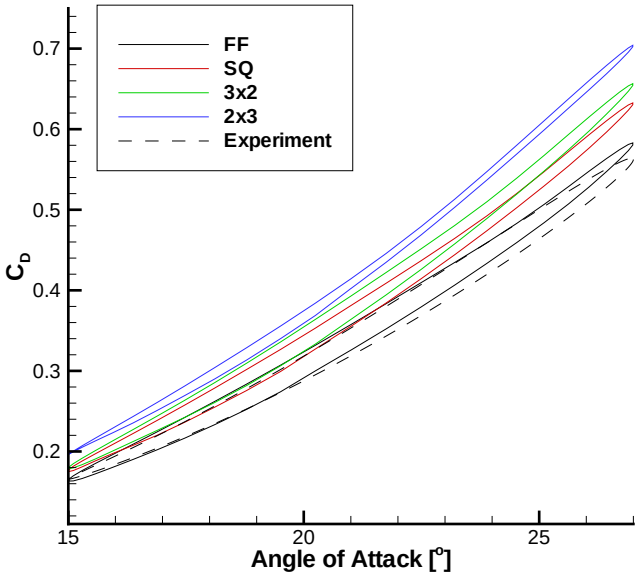

Figure 4.32: *WEAG-TA15 wing, $C_D - \alpha$ curves for pitching motion*

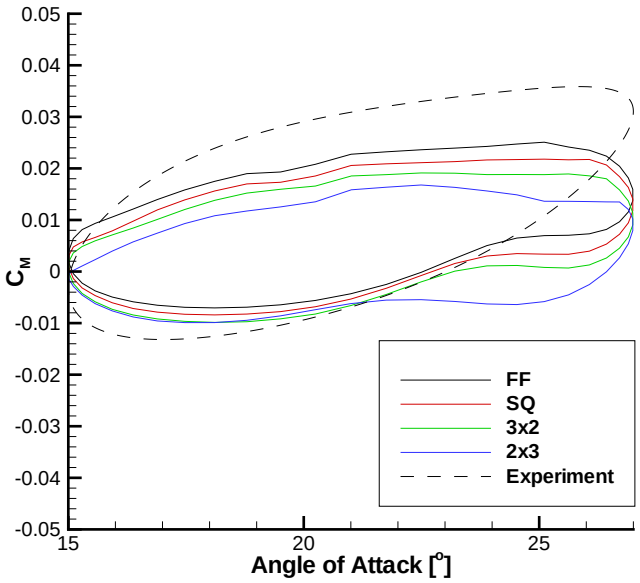

Figure 4.33: *WEAG-TA15 wing, $C_M - \alpha$ curves for pitching motion*

discussed in chapter 2. The lift and drag curves can be seen to have been predicted well, with the lift being slightly over predicted. The magnitude of the pitching moment curves have also been predicted well, though the trend is not so well predicted. However it must be kept in mind that parameters such as pitching moment are very sensitive to vortex breakdown location and vortex strength, which are hard to predict to a high level of accuracy. As can be seen, particularly in the lift curve, there is a thinning of the hysteresis loop as the angle of attack is increased. This is due to a region of reduced lift curve slope occurring at around 23^o angle of attack. At this incidence it is observed from flow visualisations that vortex breakdown has crossed the trailing edge, resulting in a reduction in the lift curve slope [74]. The resulting non-linearity is not observed in the experimental data which may be a result of the data presentation. The experimental data is given in the frequency domain (via Fourier transformation) [107]. The resulting load curves are described by the position signal

$$\alpha(t) = \alpha_0 + \Delta\alpha Cos\varphi \qquad 0 \leq \varphi \leq 2\pi \tag{4.1}$$

and the corresponding load or moment coefficient value given by

$$m(t) = m_0 + \sum_{i=1}^{3} m_i Cos(i\varphi + p_i) \tag{4.2}$$

where t=0 is taken to be the point where the position signal (or incidence in the case of pitching motion) reaches its maximum. m_i and p_i are the amplitude and phase respectively, of the first three harmonics.

Clearly the response of the vortices to pitching motion is predicted well and as such comparisons of vortex response to pitching motion in tunnels can be considered.

Discussion of results

Considering first the lift curves and drag curves in figures 4.31 and 4.32, we initially see that the tunnels have a considerable influence on the shape and positions of the curves. As the wing is placed into the square tunnel we see an increment of the lift curve. There is also a narrowing of the curve, most evident at the higher incidence. This can be attributed to the vortex breakdown passing the trailing edge

at a slightly lower angle of attack when compared with the farfield solution. A similar situation is seen in the 3x2 tunnel where the curve is further incremented due to increasing blockage effects. As expected the location at which the lift curve slope drops (when breakdown crosses the trailing edge) appears to be similar in the square and 3x2 tunnels. Finally comparing the 2x3 tunnel solution with that from the farfield solution, we see a further increment in lift as expected with the stronger vortices. Also it is evident that by far the thinnest loops occur for the 2x3 tunnel solution. Again this is due to the fact that vortex breakdown has crossed the trailing edge earliest in the 2x3 tunnel. A similar situation is seen with the drag curves.

If we compare the described lift and drag curves with those from the Euler solutions in chapter 2 (figures 2.11 and 2.12), we see considerably different trends. However, there are two important differences between the RANS and Euler solutions which must be remembered. First of all that the suction peaks predicted by the Euler code are higher than those in the RANS solutions (this is due to the vortices being closer to the surface of the wing in the Euler solutions as there is no secondary vortex), and second, that the effect of breakdown crossing the trailing edge is not seen in the Euler solutions (breakdown is constantly over the wing in the Euler solutions). Since the effect of increasing blockage is to increment the lift and drag, the vortex lift contribution (recalling Polhamus' suction analogy [8]) becomes a lower percentage of the total lift. Since the vortex lift in the RANS solutions is lower than in the Euler solutions (the RANS suction peaks are lower), the effect of increasing blockage on the thickness of the load curves is more apparent. Also since the vortices are closer to the wing in the Euler solutions, an increase in vortex strength (i.e. as incidence or S/W ratio increases) will be more apparent on the suction peaks (and therefore the vortex lift) in comparison to the RANS solutions.

The pitching moment curves provide a good measure of how much the flow structure varies at a given point in the pitching cycle due to tunnel wall constraints. Since breakdown locations are unavailable once breakdown has passed the trailing edge, the pitching moment curves provide a great deal of insight as to how the tunnel walls are influencing the flow at the low incidences, being sensitive longitudinal flow variations. The understanding of the side wall influences on breakdown location gained from the steady results, and the effect that blockage has on the loads and

moments, allows a great deal of information to be interpreted solely from the pitching moment curves. Figure 4.33 shows the pitching moment curves obtained from each solution. Clearly the smallest difference is in the angle of attack region between 15^o to 21^o on the upstroke of the pitching motion. Recalling that the blockage in the 2x3 and 3x2 tunnels is similar (which will have an effect on the pitching moment), it can be concluded that since the pitching moment curves in the 2x3 and 3x2 tunnels are almost identical in the low incidence range, the tunnel side walls have little effect on the vortices. It should also be remembered that wind tunnel wall interference will depend heavily on vortex strength, which increases with incidence (the mirror images strengthen as the leading edge vortices strengthen). Thus we would expect the greatest interference to occur at high incidence. It can therefore be assumed that at low incidence, the difference between the 2x3 and 3x2 tunnel curves, and those from the square and farfield solutions, is purely due to blockage. As the incidence is increased and the influence of the tunnel side walls increases, the effect of the promotion of vortex breakdown crossing the trailing edge early in the 2x3 tunnel can be seen at around 22^o on the upstroke. As the breakdown forms just past the trailing edge there is a slight increase in the nose down pitching moment due to the breakdown region acting like a bluff body in the CFD solutions (a small suction peak is observed on the wing surface beneath the vortex breakdown region). This provides additional suction near the trailing edge increasing the nose down pitching moment slightly. As the incidence increases further and breakdown moves completely onto the wing, a loss of the nose down pitching moment occurs as expected (this occurs earliest in the 2x3 tunnel at around 24.5^o). The solutions from the other two tunnels and the farfield solution follow a similar pattern though this occurs later in the pitching cycle. At around 25^o it is evident that vortex breakdown is well established over the wing in all the solutions (figure 4.34), which is highlighted by a sharp decrease in the nose down pitching moment. Now considering only the 2x3 tunnel pitching moment curve, it can be seen that from 27^o to around 25^o on the downstroke that the pitching moment remains relatively constant. In this region vortex breakdown is held at its most upstream location (see figure 4.34 for confirmation) due to the increased influence of the tunnel walls at high incidence, which are promoting vortex breakdown. It can be concluded that as in the Euler

simulations of chapter 2, there is a delay in vortex recovery. From around 25^o to 22^o it is observed that the 2x3 tunnel solution begins to tend towards that of the other tunnels, which is due to the reducing tunnel interference. From around 22^o downwards it can be seen that the pitching moment curve from all tunnels follow a similar trend to that of the farfield solution as the tunnel inteference lowers. Most attention has been paid to the 2x3 tunnel solution, however, it is also clear that the square and 3x2 tunnels have influenced the curves, both in blockage terms and from a slight promotion of vortex breakdown.

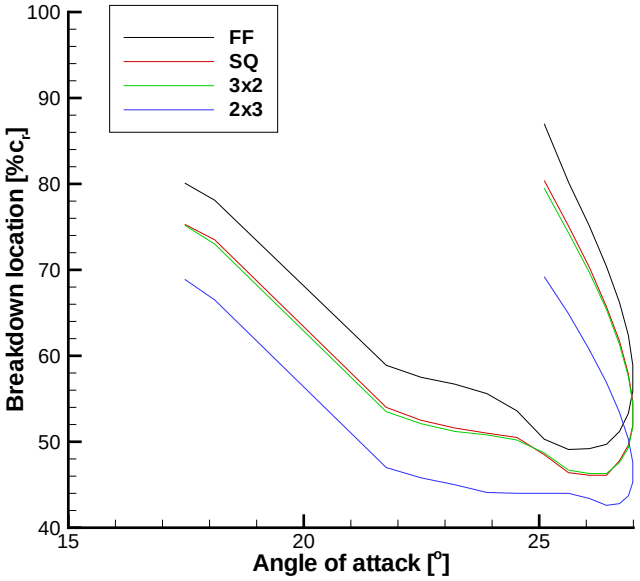

Figure 4.34: *WEAG-TA15 wing, Unsteady breakdown locations for sinusoidal pitching motion*

The vortex breakdown locations for the RANS pitching calcs are given in figure 4.34. Locations at which breakdown is over the wing are only shown. Downstream of the trailing edge the grid coarsens, and as such, breakdown locations cannot be obtained in this region. It should be noted that on the upstroke the vortex breakdown location has been taken where the axial component of velocity becomes zero. However, on the downstroke of the motion where vortex breakdown is moving downstream it is not possible to use this criterion for breakdown, as the motion of the

breakdown location prohibits this (the axial velocity does not become zero). As such, for the downstroke the breakdown location was defined as the location where the turbulent Reynolds number (or equally the eddy viscosity) increases rapidly. A turbulence Reynolds number of near 600.0 (where eddy viscosity is 600 times greater than the molecular viscosity) was chosen as the breakdown location which corresponded well with where the axial velocity was observed to become zero on the upstroke. As the wing pitches up the breakdown clearly moves upstream in a near linear manner reaching it's most upstream value at around 26^o on the downstroke. In the 2x3 tunnel in particular it can be seen that the breakdown is held near its most upstream location until around 24^o on the downstroke. Recalling the tendency of the side walls is to promote vortex breakdown, at the high incidence the tendency to promote vortex breakdown is strong therefore breakdown is held upstream. Eventually the tunnel interference begins to lower as the wing pitches down and the breakdown begins to move downstream at a similar rate to the farfield solution. A similar trend was observed with the Euler simulations of chapter 2. It is clear that the initial progression of breakdown downstream is non-linear [66].

In order to visualise the extent of the interference with incidence the tunnel wall pressure distributions are given in figures 4.35 to 4.37 for the square, 3x2, and 2x3 tunnels respectively. Considering the side wall pressure distributions on the square and 3x2 tunnels we see very similar interference patterns, with the interference increasing with incidence. The side wall interference is much clearer in the solutions from the 2x3 tunnel. As the wing pitches up and the vortices become stronger we see a much stronger interference pattern on the side walls. It is this strong interference at high incidence which causes the delay in vortex recovery in the 2x3 tunnel. The effect of blockage can also be seen as a high pressure beneath the wing, increasing with frontal area blockage and incidence.

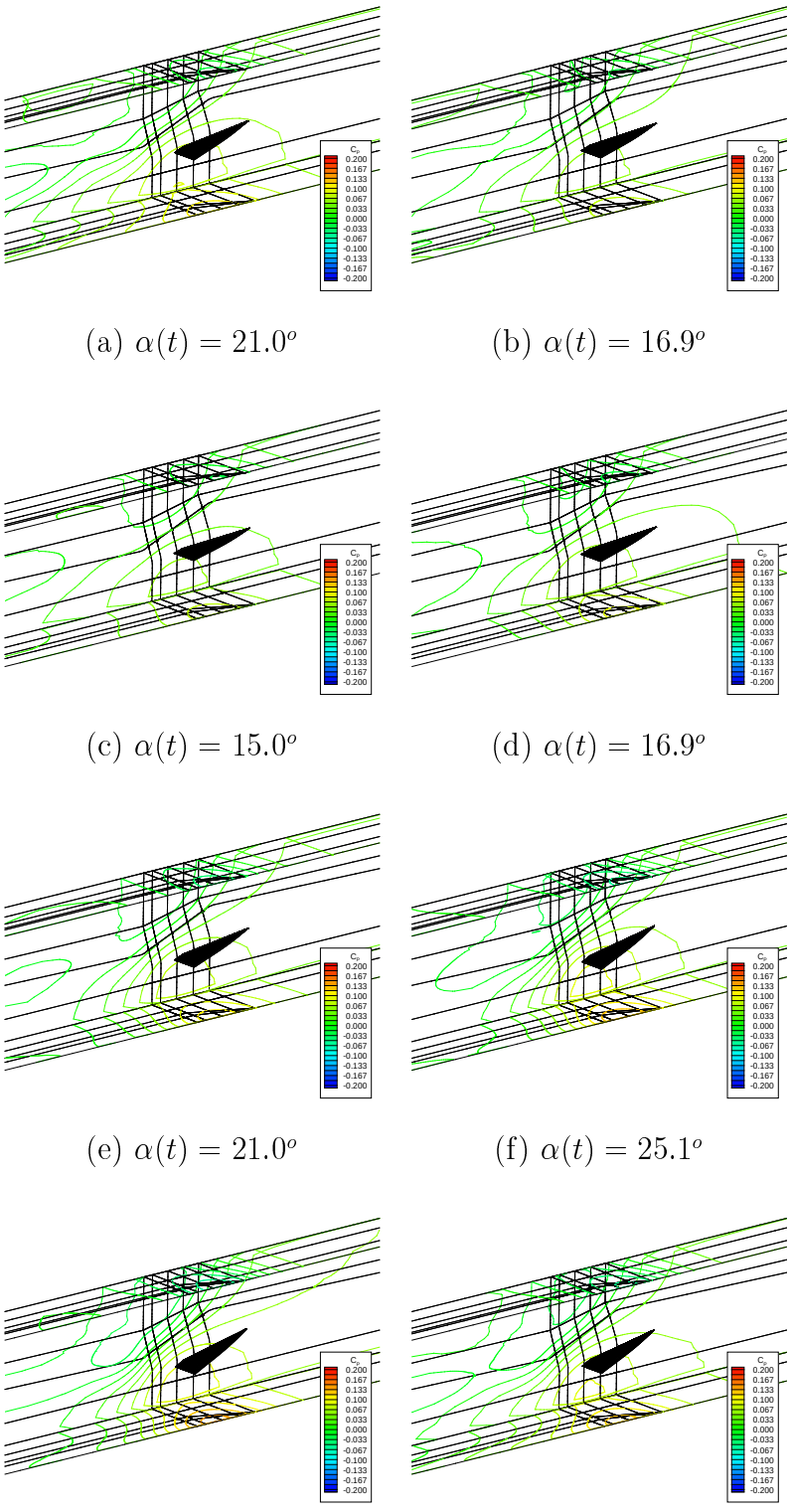

(a) $\alpha(t) = 21.0^o$ (b) $\alpha(t) = 16.9^o$

(c) $\alpha(t) = 15.0^o$ (d) $\alpha(t) = 16.9^o$

(e) $\alpha(t) = 21.0^o$ (f) $\alpha(t) = 25.1^o$

(g) $\alpha(t) = 27.0^o$ (h) $\alpha(t) = 25.1^o$

Figure 4.35: *WEAG-TA15 wing, Sinusoidal pitching, tunnel wall surface pressures within square tunnel, k = 0.56*

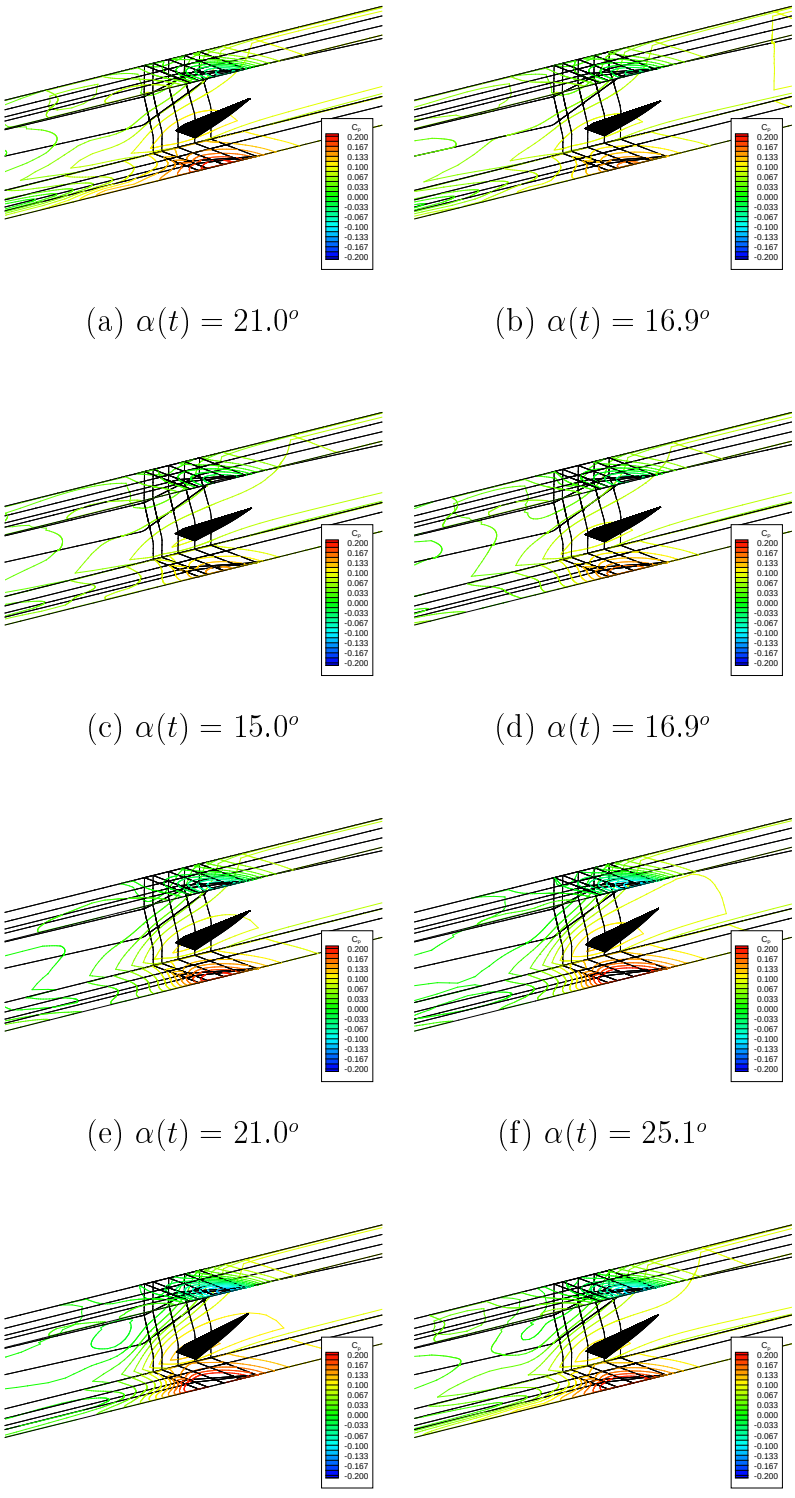

(a) $\alpha(t) = 21.0^o$ (b) $\alpha(t) = 16.9^o$

(c) $\alpha(t) = 15.0^o$ (d) $\alpha(t) = 16.9^o$

(e) $\alpha(t) = 21.0^o$ (f) $\alpha(t) = 25.1^o$

(g) $\alpha(t) = 27.0^o$ (h) $\alpha(t) = 25.1^o$

Figure 4.36: *WEAG-TA15 wing, Sinusoidal pitching, tunnel wall surface pressures within 3x2 tunnel, k = 0.56*

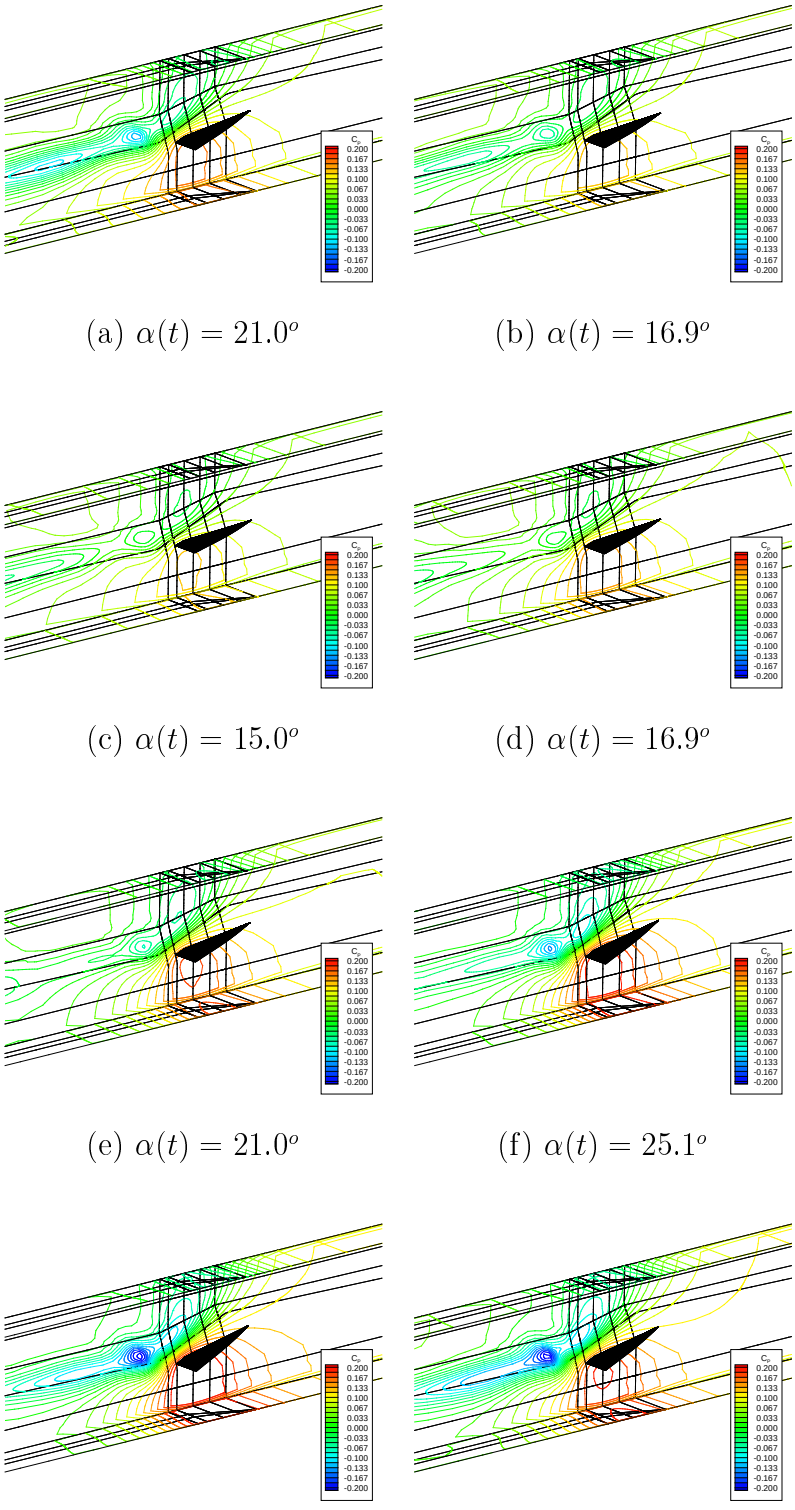

(a) $\alpha(t) = 21.0^o$ (b) $\alpha(t) = 16.9^o$

(c) $\alpha(t) = 15.0^o$ (d) $\alpha(t) = 16.9^o$

(e) $\alpha(t) = 21.0^o$ (f) $\alpha(t) = 25.1^o$

(g) $\alpha(t) = 27.0^o$ (h) $\alpha(t) = 25.1^o$

Figure 4.37: *WEAG-TA15 wing, Sinusoidal pitching, tunnel wall surface pressures within 2x3 tunnel, k = 0.56*

4.5 Conclusions

4.5.1 Steady cases

The influence of wind tunnel test section walls on delta wing aerodynamics has been examined with a RANS method. Drawing on the results from the steady test cases (with the WEAG-TA15 and ONERA 70^o wings) the following observations are noted

- Tunnel side walls promote vortex breakdown
- Roof and floor proximity has little influence on vortex strength or breakdown
- Tunnel blockage appears to have little influence on breakdown location
- Tunnel constraints increase strength and suction of the vortices
- Tunnel contraints increase effective angle of attack of the wing
- The helix angle and therefore vortex strength increases when a delta wing is placed in tunnels due to side wall induced upwash
- Secondary separation is delayed in tunnels due to increased cross flow momentum (extent is likely to be dependent on wing shape)
- Side walls displace vortices upwards off the wing surface due to side wall induced upwash

The RANS simulations have confirmed the conclusions drawn in the Euler study in chapter 2.

4.5.2 Pitching cases

The following conclusions are drawn from the RANS pitching cases

- Tunnel walls consistently promote vortex breakdown in pitching motion
- Tunnel side walls cause vortex breakdown to cross the trailing edge earlier in the pitching cycle distorting the pitching moment curve on the upstroke

- With high interference at high incidence, vortex recovery occurs later in the pitching cycle in the 2x3 tunnel solutions in particular
- As the wing pitches down the pitching moment curves tend towards that of the farfield solution, however they differ due to the consistently further upstream location of vortex breakdown
- Tunnel wall influences are strongest at the high incidences and on the downstroke
- At the low incidence range of the upstroke tunnel interference appears minimal

Chapter 5

RANS simulations of support structure interference

5.1 Introduction

The work in Chapters 2 and 4 has concentrated on the effect of the wind tunnel walls alone. Another aspect of tunnel interference which has not yet been considered is that of the support structures required to hold the wing in the tunnel. For unsteady testing these support structures can be fairly large [135][136][137][138], as they deliver the driving mechanism for high rate manoeuvres.

As discussed in chapter 2, experimental studies have been conducted to assess the interference effects of test facilities on vortex breakdown. The work in this thesis has so far shown that tunnel side walls promote vortex breakdown. This agrees with some experiments [89][90], yet disagrees with others [88]. All experimental studies require support structures to hold the model in place. The experimental studies also increase the wing size as opposed to decreasing the tunnel size, hence changing the model to support interference ratio. The effect of these support structures on the experimental studies must therefore be considered. As described by Taylor et al. [139], even very basic issues such as the effects of support geometry and location, and the variation of support interference with amplitude and frequency of manoeuvring tests are unknown.

The test case of the ONERA 70^o wing in the ONERA F2 tunnel is used but with

a CFD model of a support structure downstream of the wing. The support structure modelled is intended to mimic a downstream pressure disturbance propogating upstream. No sting or wing mounting is considered due to the added complexity of the problem, both in terms of grid generation and flow physics behind a solid sting. The aim of this chapter is to indicate the effect and extent of support structure interference. The PMB3D flow solver (discussed in section 1.5) was used in all calculations.

5.2 Previous work

Hummel [140] observed that the presence of an obstacle one chord length downstream of the trailing edge of a delta wing caused vortex breakdown to shift towards the apex by up to $40\%c_r$. The obstacle considered was unrealistically large (wider than the span of the delta wing), however, this early observation highlighted the possible effects that support structures can have.

Recently Taylor et al. [139] varied the position of various obstacles behind the wing trailing edge to find the effect support proximity had on vortex breakdown. It was concluded that when an obstacle was placed in the vortex core, breakdown was promoted due to the adverse pressure gradient which formed in front of the obstacle. As the obstacle was moved away from the vortex core, breakdown was observed to move downstream. It can be expected that the degree of support interference will be dependent on support size, vortex strength and trajectory.

Although possibly not considered as support interference, fuselages on delta wing models can effect the breakdown location. Some sting mounted tunnel models have upper surface fuselages to connect the model to the sting. The effect of such fuselages has been considered in a number of investigations, each of which have shown significant variations in breakdown location for a given sweep angle and incidence. See for example [141][142][143]. A possible reason for the variation in the breakdown locations was given by Ericsson [142] in which the effect of the fuselage was described as an induced camber effect. The induced camber effect alters the location of vortex breakdown, either delaying or promoting breakdown depending on the fuselage.

5.3 Test cases

It is well understood that if an obstacle is placed in the path of a vortex core breakdown will occur. This is due to a local adverse pressure gradient forming in front of the obstacle (as the flow approaches stagnation). To try and assess the effect of the tunnel support interference in the experiments of Mitchell [5], a vertical support was placed in the centre of ONERA F2 tunnel downstream of the ONERA 70^o wing. Since supports in dynamic testing tend to be fairly large (driving mechanisms must also be housed) a thick support cross-sectional area was chosen. The cross-sectional area of the support considered in the computations is larger than that used in the experiments of Mitchell [5]. The support is a cylinder with a straight taper in the downstream direction (to eliminate any computational anomolies with flow behind a frictionless bluff body). Figure 5.1 shows the support structure and dimensions. To avoid grid generation complications, the support attaching the wing to the vertical support is omitted. It may be expected that there is some interference from this mounting. The downstream support gives a frontal area blockage of around 12%.

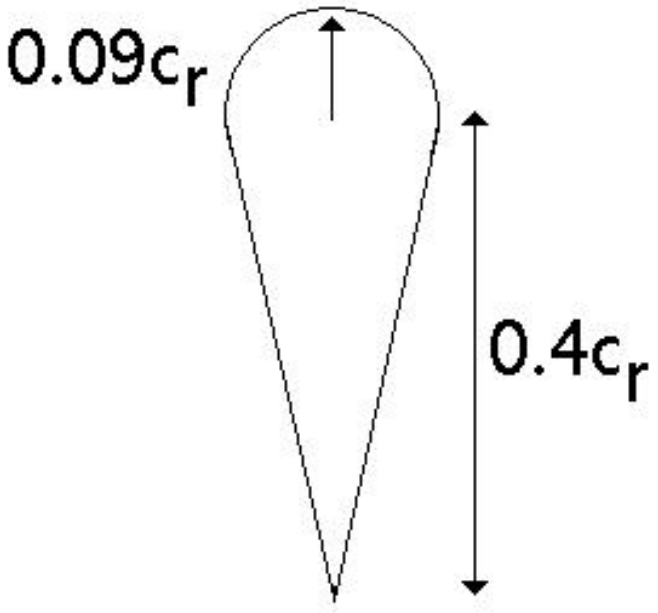

Figure 5.1: *Support geometry and dimensions*

The support was placed at two locations, $0.5c_r$ and $1c_r$ from the trailing edge of the wing. Angles of incidence of 23^o and 27^o were considered, as vortex breakdown is present near the trailing edge of the wing at 23^o and near the centre of the wing at 27^o. At 27^o angle of attack the grids used for the support interference simulations are identical over the wing to those used in chapter 4, with the ONERA 70^o wing in the ONERA F2 tunnel. Therefore there is no change in grid resolution in the vortical region above the wing. A depiction of the grid around the ONERA 70^o wing was given in figure 3.11. For the incidence of 23^o, the 27^o grids were deformed using Trans-Finite Interpolation (TFI) to generate the new meshes. The 27^o mesh was altered downstream of the wing to allow the presence of the support. For this grid resolution the solution has been validated in chapter 3.

As in chapter 4, the ONERA F2 tunnel walls have been modelled with an inviscid wall boundary condition, and in the current simulations the supports have also been modelled with an inviscid wall boundary condition. Neglecting wall and support structure boundary layes reduces the mesh sizes significantly. Upstream a farfield boundary condition has been placed $10c_r$ from the apex of the wing, and downstream of the wing a first order extrapolation boundary condition has been placed at $10c_r$ from the trailing edge. The k-ω turbulence model with the NLR P_k Limiter [129] is used in all calculations.

5.4 Results and discussion

The breakdown locations observed in the calculations are given in table 5.1. As in chapter 4, the breakdown locations have been taken where the axial velocity equals zero.

If we consider first the 27^o case, it can be seen that when the support is $1c_r$ from the trailing edge there appears to be a small influence on breakdown, with breakdown being delayed slightly in comparison to the case without support structures. Since the vertical support used in the experiments of Mitchell [5] was placed around $2c_r$ from the trailing edge of the wing, it can be safely concluded that its interference effect is minimal. As the support is brought closer to the trailing edge of the wing (at $0.5c_r$ from the trailing edge) it can be seen that breakdown shifts back towards

the trailing edge by around 16.3%c_r. This is in contrast to what may be considered as the common understanding that downstream supports induce vortex breakdown due to pressure disturbances propogating upstream.

Incidence	Support location	Breakdown location
27	$0.5c_r$	81.0%c_r
27	$1c_r$	65.9%c_r
27	NONE	64.7%c_r
23	$0.5c_r$	92.0%c_r
23	$1c_r$	81.7%c_r
23	NONE	80.0%c_r

Table 5.1: Vortex breakdown locations

To find the reason for the tendency of the supports to delay vortex breakdown, the structure of the vortices prior to breakdown is examined. First of all the flow angles (the angle at which the freestream is deflected due to the presence of the wing) along the wing are shown in figure 5.2. There is little change in the flow angles when supports are placed in the tunnel. This is due to the flow angles only being altered by the proximity of the vortices to the side wall (which induce vertical velocity components increasing the mean incidence of the wing). Indeed provided the vortices do not increase in strength due to the supports, the flow angles should remain the same. For the majority of the wing this is seen to be the case, however, there is a noticeable deviation after the midchord position when the support is placed $0.5c_r$ from the wing. This is due to the delay in vortex breakdown altering the vorticity distribution in what was originally the post-breakdown region. This alters the wall effect in this region.

The surface pressure distributions above the wing at x/c_r =0.32, 0.52, and 0.63 can be seen in figures 5.3 to 5.5 respectively. At x/c_r=0.32 there is little difference in the upper surface pressure distributions, both in core location and strength. The minor differences are likely due to blockage effects. This is confirmed when we examine the axial vorticity distributions through a horizontal traverse across the

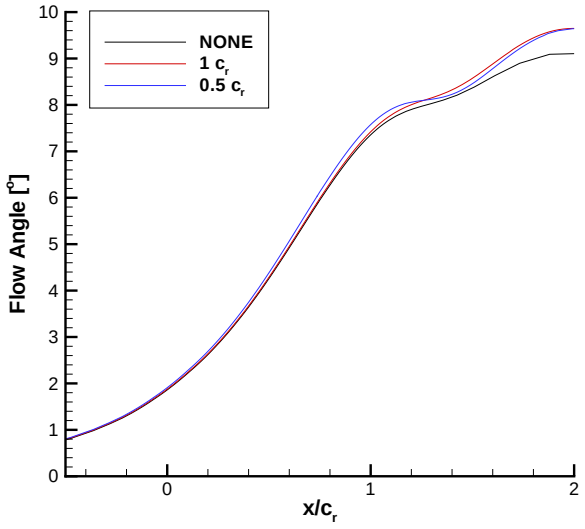

Figure 5.2: *Flow angles along side wall of ONERA F2 tunnel between roof and floor, 27^o Angle of attack*

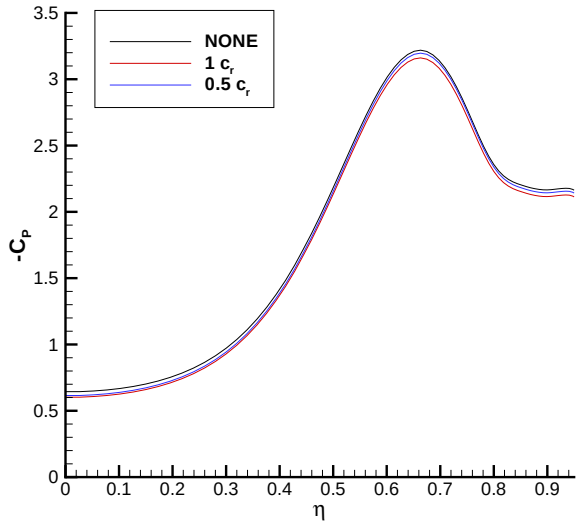

Figure 5.3: *27^o angle of attack, upper surface pressure distributions with and without supports, $x/c_r = 0.32$*

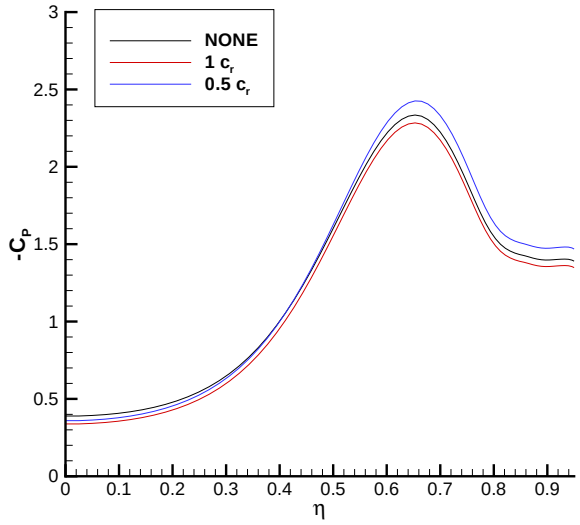

Figure 5.4: 27^o *angle of attack, upper surface pressure distributions with and without supports,* $x/c_r = 0.52$

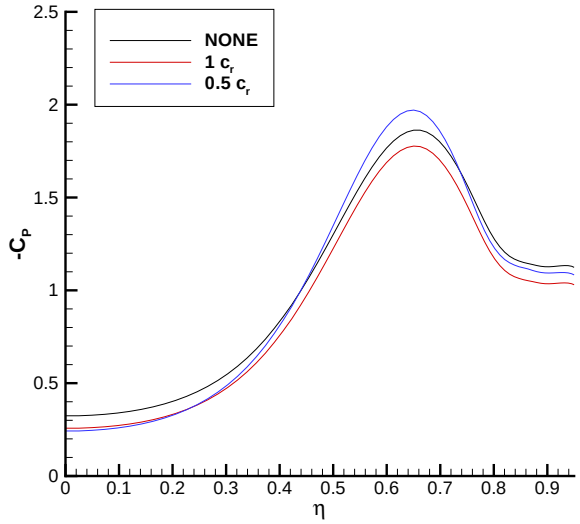

Figure 5.5: 27^o *angle of attack, upper surface pressure distributions with and without supports,* $x/c_r = 0.63$

leading edge vortices (figure 5.6). At x/c_r=0.32 which is well ahead of breakdown, there is clearly little difference in the flow when supports are added. At $x/c_r = 0.52$ and 0.63, the differences are more apparent as the variations in breakdown location are more local at these chordwise stations. Since the breakdown locations without and with the support at $1c_r$ from the trailing edge are similar, the differences in the pressure distributions are again likely due to blockage effects. The highest suction peaks at $x/c_r = 0.52$ and 0.63 occur when the support is placed $0.5c_r$ from the trailing edge, due to the larger delay in vortex breakdown.

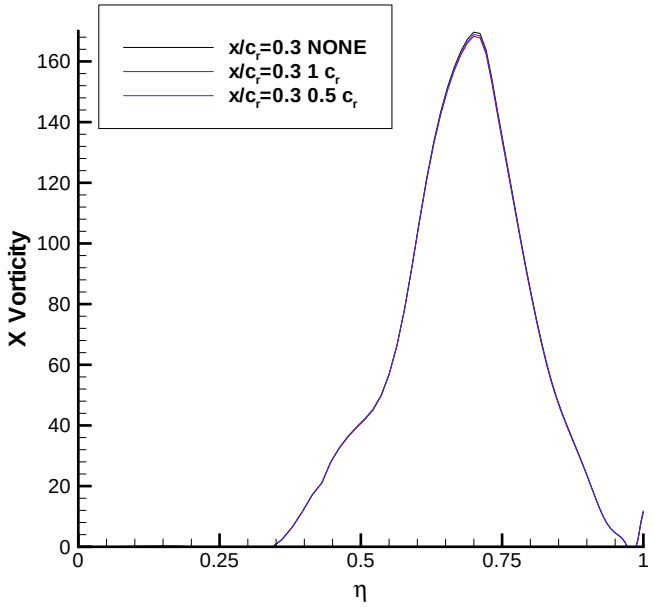

Figure 5.6: 27^o *angle of attack, Comparison of axial component of vorticity through vortex core*

As a final check on the strengths of the vortices, the circulation distribution in the chordwise direction is given in figure 5.7. There is little or no difference in the strengths of the vortices prior to vortex breakdown. There appears to be a slight increase in the strength of the vortices when the support is placed at $0.5c_r$ from the trailing edge of the wing in the breakdown delay region. However, this would appear to be due to the locally higher effective incidence experienced by the wing.

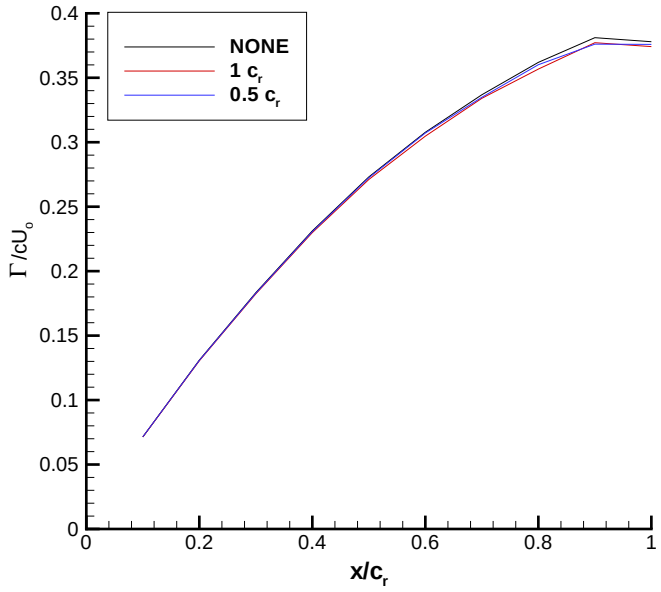

Figure 5.7: *Variation in circulation in the chordwise direction, 27^o Angle of attack*

Figure 5.8 shows the pressure distribution along a horizontal plane at the midpoint between the tunnel roof and floor for each incidence and support location. The flow direction is from top to bottom and the intersection of the horizontal plane with the wing is clearly seen upstream of the support. Evidentally the vortical flow negotiates the support as opposed to impinging on it as in the experiments of Taylor et al. [139][144]. Since the mean effective incidence of the wing and strength of the vortices is unaltered prior to vortex breakdown, the only explanation for the delay in vortex breakdown is the change in the pressure gradients in the tunnels. It is well understood that vortex breakdown is sensitive to external pressure gradients [51]. The effect of the supports on the axial pressure gradient within the tunnels can be seen in figure 5.9. The data were extracted near the tunnel sidewall at the midplane between the roof and floor. Note that if the data were extracted from the centreline of the tunnel an adverse pressure gradient would appear as the support was approached due to the stagnation region at the front of the support. Since the vortex does not impinge on this region the pressure distribution near the side wall is more representative of the external pressure gradients experienced by the vortex.

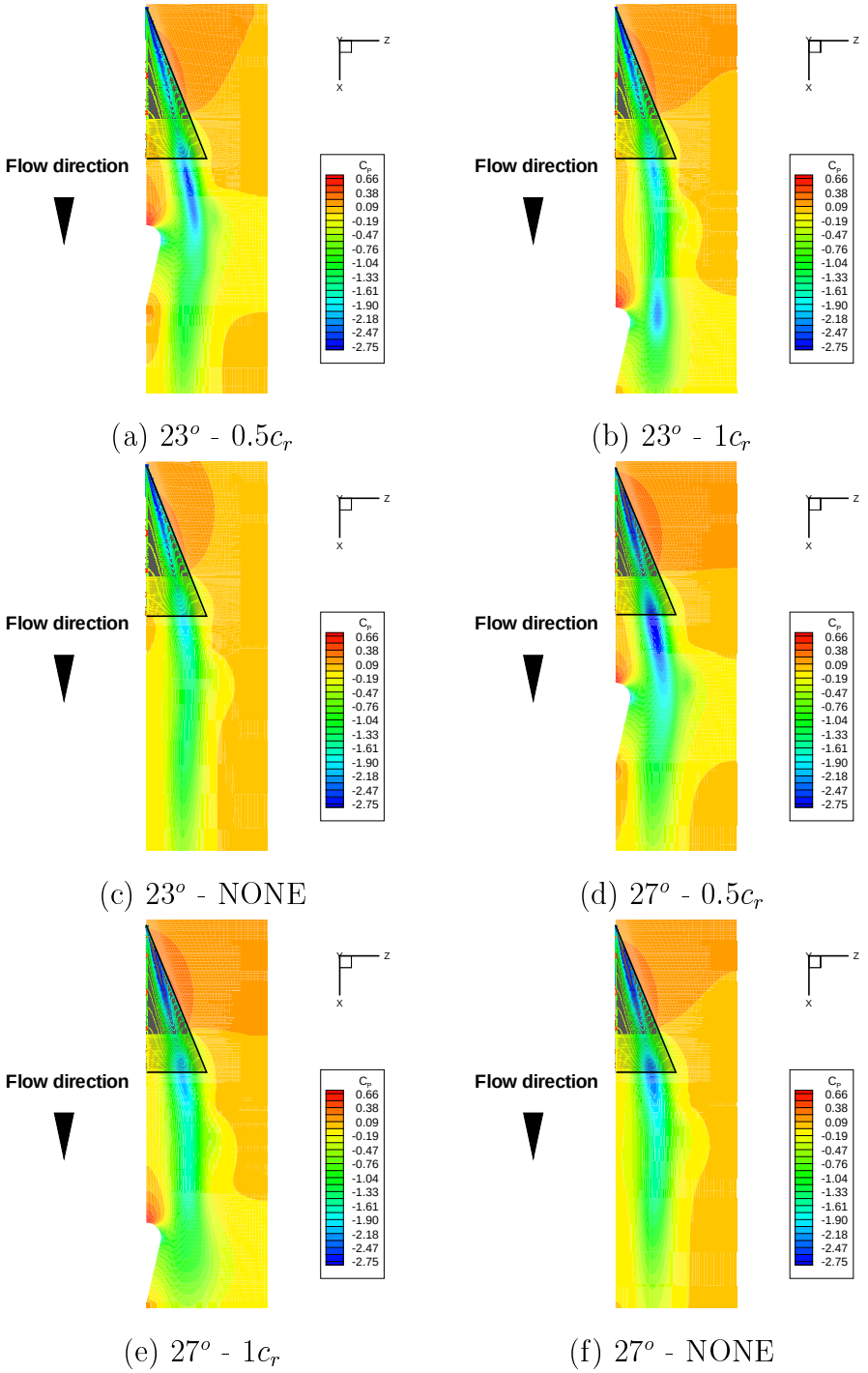

(a) 23^o - $0.5c_r$ (b) 23^o - $1c_r$

(c) 23^o - NONE (d) 27^o - $0.5c_r$

(e) 27^o - $1c_r$ (f) 27^o - NONE

Figure 5.8: *Pressure distribution along a horizontal plane between ONERA F2 tunnel roof and floor*

As the support is brought near the wing it is clear that a local (to the wing) favourable pressure gradient develops. This is due to an acceleration of the flow as it negotiates the support, thus reducing the local static pressure around the support. To have an effect on vortex breakdown the favourable pressure gradient must be local with respect to the vortices, and so when the support is placed $1c_r$ from the wing, the favourable pressure gradient around the support has a smaller effect.

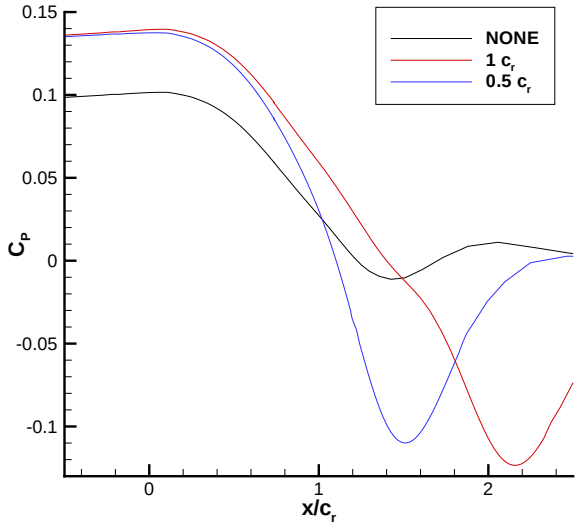

Figure 5.9: *Pressure distribution along side wall of ONERA F2 tunnel between roof and floor, 27^o Angle of attack*

From the previous discussion it is clear that the downstream support structures have the sole effect of altering the pressure gradient within the tunnel. There is little or no change to the vortex structure prior to vortex breakdown. As such the calculations at the lower incidence of 23^o will be discussed from the point of view of the pressure gradients experienced by the vortices. The 23^o case will be used to assess how much the support influences weaker vortices, where the breakdown is naturally more downstream. Regarding the breakdown locations at 23^o it appears that even at the lower incidence the breakdown is only slightly effected by the support when it is placed at $1c_r$ from the wing. Observing the pressure distribution along the ONERA F2 side wall when the wing is $1c_r$ from the wing (figure 5.10),

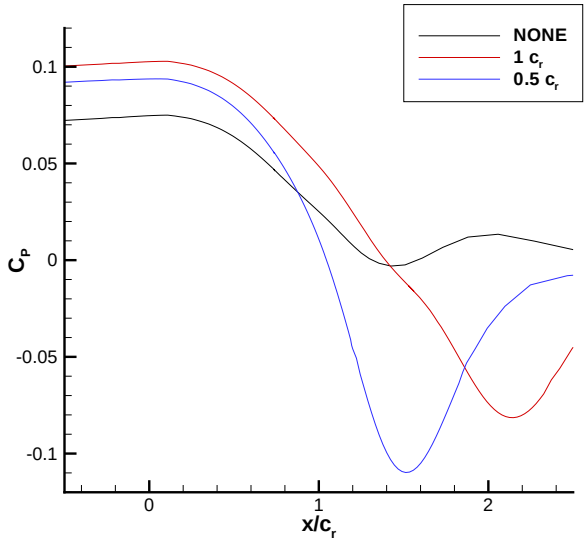

Figure 5.10: *Pressure distribution along side wall of ONERA F2 tunnel between roof and floor, 23^o Angle of attack*

we see that the pressure gradient near the wing is only slightly effected by the downstream structure. As the support is brought closer to the wing we see an increasing favourable pressure gradient which delays the breakdown further as seen in the breakdown locations of table 5.1.

Clearly the shape and size of the support considered in this study alters the pressure gradients in the tunnels due to blockage. The acceleration of the flow around the support causes a favourable pressure gradient to form, and if this pressure gradient is local with respect to the vortices breakdown is delayed. However there is also a stagnation region ahead of the support so it is possible that if the blockage effect was lower and the stagnation effect may become dominant and breakdown will be promoted. To assess any possibility of this a narrower support was placed at $0.5c_r$ from the trailing edge of the wing, with the wing at 27^o angle of attack. The geometry is identical to that described in figure 5.1, however the radius of the cylindrical section was reduced from $0.09c_r$ to $0.045c_r$. This effectively halves the support frontal area blockage from approximately 12% to 6%. The breakdown was observed to shift from $64.7\%c_r$ to $73.8\%c_r$. The tunnel mid plane pressure

distributions are shown in figure 5.11. Clearly despite the blockage being reduced the previous discussion applies to thinner supports. As long as the vortex cores negotiate the support breakdown can be delayed. This seems to be the case for "streamlined" tunnel-centred support structures.

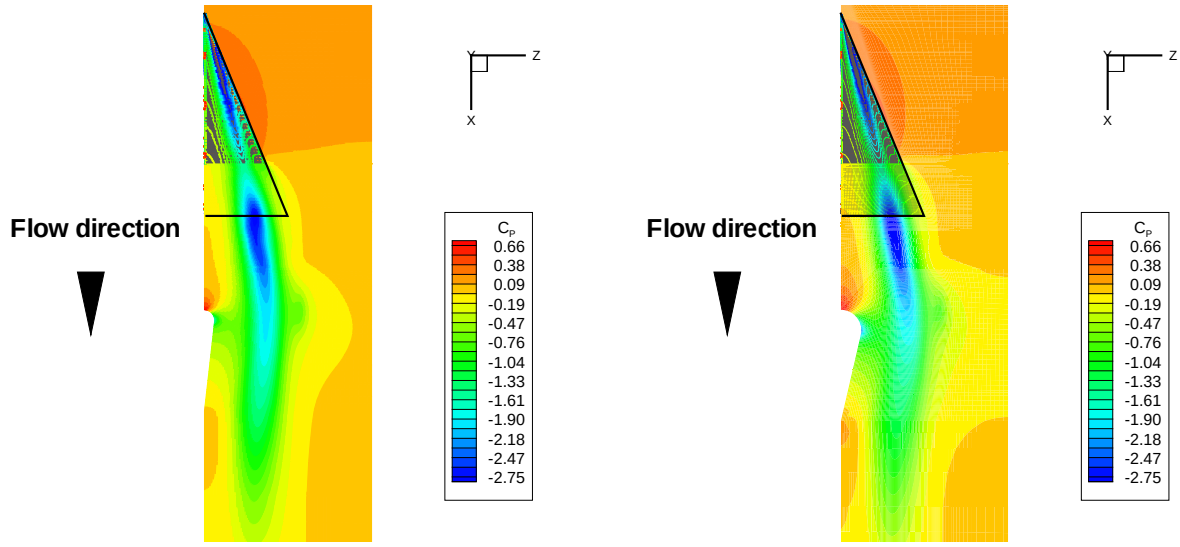

(a) Support radius $0.045c_r$ (b) Support radius $0.09c_r$

Figure 5.11: *Pressure distribution along a horizontal plane between ONERA F2 tunnel roof and floor, 27° angle of attack, large and small supports*

5.5 Discussion of possible support interference in experimental studies

As described in chapter 3, the experimental study by Weinberg [88] shows that vortex breakdown moves downstream with increasing model size, yet the experimental studies by Thompson and Nelson [89] and Pelletier and Nelson [90] show that vortex breakdown moves upstream with increasing model size. The effect of support structures was not discussed in any of these studies. Support structure interference (and the clear influence it can have on delta wing flows) is therefore an unexplored possible reason for the opposite trend observed by Weinberg in experiment.

It has been shown in chapters 3 and 5 that tunnel walls tend to promote vortex

breakdown. A possible mechanism for delaying vortex breakdown has been discussed in the current chapter. Taylor et al. [139] have also shown experimentally that if a leading edge vortex impinges on a support structure, vortex breakdown is promoted due to a local adverse pressure gradient.

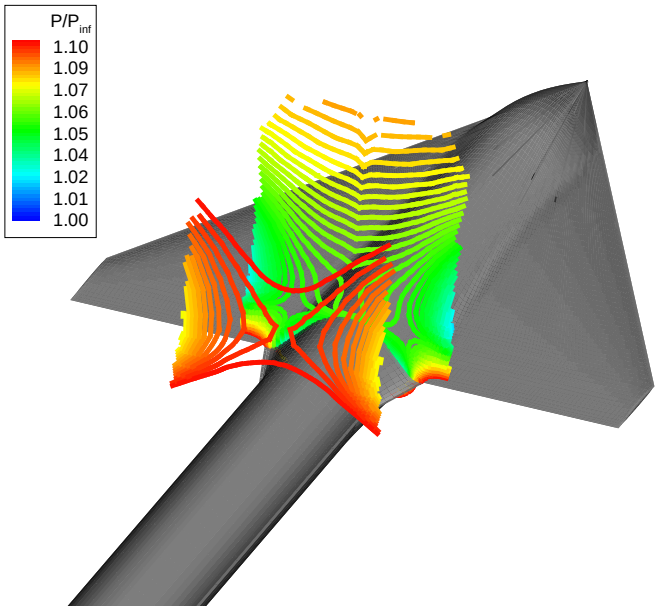

Figure 5.12: *Depiction of interference region forming behind a sting - 65^o delta wing at 17^o incidence, Calculation performed for WEAG THALES JP12.15 Common Exercise I [128]*

Unfortunately there is no useful support information in the paper by Weinberg, therefore one must speculate about the possible interference effects in the experiment. In Weinberg's paper there is mention of a supporting rod attached to the wing lower surface extending in the chordwise direction. It might therefore be assumed that there is some kind of support structure downstream of the wing, either in the form of a vertical support, or simply by the rod (sting) extending downstream. It is also reasonable to speculate that the same support structure was used in all cases. Considering the experiments of Weinberg, as the wing size increases, the position of the vortex core relative to the support (and therefore any interference region such as that depicted in figure 5.12) is likely to influence the results. A smaller wing will tend to have the vortices closer to the support, possibly impinging on a down-

stream structure, or simply being influenced by the separation of the flow from the supporting rod. As the wing is increased in size, the vortex cores will move away from the support (increasingly negotiating any interference region), and may delay vortex breakdown. If the effect of the support structure is dominant over the effect of the side walls (which would be likely with the smaller wings) the trend observed by Weinberg could occur. Another interesting point about the results obtained by Weinberg is that the trend of breakdown moving downstream with increasing model size was dependent on the sweep angle of the wing. The higher swept wing (70^o sweep) showed a consistent trend of breakdown moving downstream with increasing wing size. However, when the sweep angle was reduced (60^o sweep), breakdown was only observed to move downstream when changing from the smallest wing to the medium sized wing. As the wing size increased further, breakdown was not observed to move. It should be recalled that as the sweep angle of a wing is reduced, the trajectory of the vortex cores will naturally move away from any centred interference region. It is therefore possible that for the largest wing the vortex cores were sufficiently far from the support that the wall interference effect became more prominent.

Since the results of Thompson and Nelson show the opposite trend, it is speculated that the support structure in this case has caused a lesser effect than that of the tunnel side walls. It should be noted that the support structure used by Thompson and Nelson was a five bar linkage connected to the wing lower surface of the wing. Therefore there were no support structures downstream of the wing trailing edge in the experiments where breakdown was observed to move upstream with increasing model size. Thus none of the downstream support structure effects discussed in this chapter are applicable.

Pelletier and Nelson also observed that breakdown moved upstream with increasing wing size. The wing was mounted to the roof of the test section via a sting. It should be noted however, that in the experiments of Pelletier and Nelson, the sting size was increased with increasing wing size. It may therefore be speculated that the influence of the sting was consistent in each case, and that it was the wall influence varying the results.

Since at 27^o with the support at $1c_r$ from the wing there is little variation in

breakdown location, it can be concluded that the influence of the vertical support structure in the experimental data of Mitchell [5] (which was around $2c_r$ from the wing) is minimal in comparison to the effect of the ONERA F2 tunnel side walls. The effect of the sting is unmodelled.

5.6 Conclusions

In the previous simulations of test facility interference (chapters 2 and 4) only the test section walls have been considered. In all cases vortex breakdown has been promoted when wind tunnel test sections have been applied. The effect of support structures has therefore been considered in the current chapter. The largest support chosen was of large cross-sectional area (12% frontal area blockage).

Placing support structures downstream of a delta wing has been shown to have little / no effect on the structure of the leading edge vortices prior to vortex breakdown. The only variation is a change in breakdown location. It can therefore be concluded that the only mechanism by which support structures alter the flow is by changing the pressure gradient within the tunnel. Leading edge vortices are known to be sensitive to pressure gradients [51].

The shape and proximity of the support considered in this study has shown that bringing the support close to the wing delays vortex breakdown. This is due to a local acceleration of the flow (a blockage effect) around the support which reduces the local static pressure. Despite there being a large stagnation region in front of the support, the trajectory of the vortical flow is such that it negotiates the stagnation region, and therefore the vortices experience only a local favourable pressure gradient due to the blockage effect. As expected, the response of the vortices has been shown to increase with closer proximity of this blockage effect. Placing the support structure $1c_r$ away from the wing was found to only slightly delay vortex breakdown, since the local favourable pressure gradient around the support is sufficiently far away from the wing to have little influence on the vortices. A narrower support (and therefore lower blockage) of similar geometry produced the same trend, ie. breakdown was delayed.

This evidence indicates that support structure influences are confined to the

production of local pressure gradients, and the response of the vortices (which will vary according to whether or not the vortices impinge on the structure) to the resulting pressure field. It also highlights the importance of considering the support shape when considering any support interference.

For delta wing tests with below model mountings, it is expected that the only corrections required are those for wall effects, since the leading edge vortices are unlikely to experience any support induced axial pressure gradients from the lower surface. A similar case is expected if the downstream structures are at least $1c_r$ from the wing trailing edge, however the effect of the structure attaching the model to the downstream structure must be addressed (for example sting effects).

A possible explanation for the differing trends seen in experiment has also been given. Although this is speculative, it has been based on whether or not the vortices negotiate an interference region. Few of the previous experimental studies considered the effect of support structures, which has been shown to be important.

Chapter 6

Conclusions and future work

6.1 Conclusions

In a paper by Jobe [2] it was shown that there is a wide scattering of vortex breakdown locations for wings of equal sweep at a given incidence. Lowson [91] has suggested that a large proportion of this scattering is due to wing geometry, most importantly in the apex region. Even considering this, scatter remains, and suggesting this is due to some experiments being "better" than others is too simplistic given the sensitivity of the flow to external influences. A more reasonable suggestion is that scattering may be due to fundamental differences in the experiments arising from the test facilities used. It was the aim of this thesis to ascertain the levels of test facility interference on delta wing aerodynamics, to examine how test facilities alter the flow structure (in particular vortex breakdown location) and more generally to improve the understanding of test facility interference on vortical flows.

A CFD investigation of wind tunnel interference effects on delta wing aerodynamics has been conducted. The predictions were first verified and validated, and then used to analyse the effects of separate components of wind tunnels. The effects of blockage, side walls, roof and floor, and support structures have been assessed using both Euler and RANS solutions. Both aerodynamic models produce the same trends for breakdown motion (both steady and pitching), which might be expected for what is widely accepted as an inviscid, Reynolds number independent phenomenon. Two wing geometries have been used in this study, the WEAG-TA15 65^o delta wing and

the ONERA 70^o delta wing.

A search of the available literature on experimental studies of wind tunnel interference has provided contradictory experimental evidence as to the influence of tunnel walls. An experimental study by Weinberg [88] has claimed that vortex breakdown moves downstream with increasing model span-to-tunnel width ratio. However, the opposite behaviour (ie. that breakdown moves towards the apex with increasing model span-to-tunnel width ratio) has been claimed by Thompson and Nelson [89] and Pelletier and Nelson [90]. These contradictory results only serve to highlight the complexity of the flow above delta wings, and the clear sensitivity of the phenomenon of vortex breakdown to external influences.

Verification of the accuracy on the grids used has highlighted a dependency of the solutions to grid resolution. From the available literature this has been found to be common in the prediction of vortical flows. Despite the resolution of the grids being as fine as possible given current computational limitations, grid dependency has been found in both the Euler and RANS simulations. As a result, to ensure that any differences are only due to changes in boundary conditions (such as locations of tunnel walls), in all computations the vortical region of interest has been resolved with a consistent discretisation of the domain. To achieve this a farfield grid was created in such a way that by extracting outer blocks varying tunnel dimensions were obtained.

In order to examine seperately the influence of roof and floor, and side wall proximity, three test cases were defined. These test cases featured a 65^o cropped delta wing at 21^o angle of attack, in square, 3x2, and 2x3 tunnels. The solutions from the tunnel simulations were compared with similar simulations using farfield conditions at the outer boundaries (placed sufficiently far from the wing). The 3x2 and 2x3 tunnels were created by bringing the roof and floor of the square tunnel closer to the wing (the 3x2 tunnel), and by bringing the side walls of the square tunnel closer to the wing (the 2x3 tunnel).

A preliminary study with Euler simulations was described in chapter 2. The Euler simulations have shown that the presence of tunnel walls promotes vortex breakdown. Comparing the square tunnel solutions with those from the 3x2 and 2x3 tunnels, revealed that it is in fact the presence of the tunnel side walls which

promotes vortex breakdown, with roof and floor proximity having little influence on the breakdown location. This conclusion comes from the fact that the breakdown location did not vary when comparing the square and 3x2 tunnel solutions, but was significantly promoted when comparing the square and 2x3 tunnel solutions. This result in itself highlights that in experimental investigations the wing should be orientated such that the side walls are as far away as possible. Another interesting point was that the frontal area blockage was significantly increased when the roof and floor / side walls were brought closer to the wing. Since breakdown did not change when the blockage was increased when changing from the square to 3x2 tunnel, and that the blockage in the 3x2 and 2x3 tunnels is nearly identical, it can also be concluded that blockage effects have little effect on the location of vortex breakdown. Examination of the chordwise distribution of circulation (ie. the vortex strength) indicates that the vortex strength increases. It is also clear that it is the side wall proximity which is dominant in increasing the vortex strength since the strengths from the square and 3x2 tunnels are nearly identical. The increase in vortex strength is due to a tightening of the windings of the leading edge vortex (increased helix angle) which is a result of the additional wall induced upward velocity components. Examination of the tunnel centreline pressure (and also flow visualisation in this region) has indicated that tunnel side walls displace the leading edge vortices upwards off the surface of the wing. This is particularly noticeable in the post-breakdown region aft of the trailing edge.

Euler simulations of the WEAG-TA15 65^o delta wing in sinusoidal pitching motion were performed with the wing placed in the three tunnels mentioned previously. As with the steady case the side walls were found to interfere the most with the flow, promoting vortex breakdown. As the wing incidence increases (ie. on the upstroke) the circulation increases, therefore the side wall interference increases with increasing incidence. The high tunnel interference at high incidences has the effect of delaying breakdown travel to the trailing edge (on the downstroke), due to the time lag associated with the tunnel effects on the breakdown location. As such the tunnel interference effects were found to be strongest on the downstroke of the pitching motion. The delay in breakdown travel towards the trailing edge has the effect of distorting the hysteresis loop of breakdown location.

In chapter 3, the ability of the RANS turbulence models to predict the leeward flow over delta wings was assessed. The flow over the ONERA 70^o wing was considered in detail as there is a large amount of experimental data for validation purposes. It was found that each turbulence model employed predicted different levels of eddy viscosity in the vortex, resulting in varying vortex strengths, secondary separation locations, and vortex breakdown locations. It was also found that as the amount of turbulence predicted in the vortex was reduced (either by refining the grid or altering the source terms in the turbulence models), the core properties increased and delayed vortex breakdown. However, in general the validation of the RANS solutions indicated that the vortical flow above the delta wings was well predicted. It should be noted that the vorticity levels in the core were predicted lower than was found in experiment. This implies that the computed vortex strengths are lower than those found in experiment. This should be kept in mind when considering the levels of tunnel interference discussed in chapter 4.

In chapter 4, the Euler simulations of chapter 2 were repeated using a RANS model of the flow. The Euler simulations of chapter 2 were unable to predict the presence of a secondary vortex. The RANS simulations confirmed all conclusions drawn from the Euler simulations. The influence of the tunnel side walls on the secondary vortices was also assessed. It was observed (most noticeably on the flat upper surface of the ONERA 70^o wing) that the secondary separation location moves towards the leading edge when the wing is placed between tunnel side walls. There was a similar effect on the WEAG-TA15 65^o wing, however, the effect was much less noticeable (it is speculated that this is due to the convex upper surface of the 65^o wing). As mentioned previously the helix angle of the vortices increases with the presence of the tunnel side walls. This increases the strength of the primary vortices due to the increased crossflow momentum (a result of the tighter windings). However, the increased crossflow momentum also increases the strength of the secondary region, thus the adverse pressure gradient experienced by the crossflow after the primary vortex suction peak is essentially unaltered. With the increased crossflow momentum the adverse pressure gradient can be overcome longer, and therefore the secondary separation line moves outboard. As in chapter 2 sinusoidal pitching simulations were performed in the three tunnels considered. Since in the RANS

simulations vortex breakdown was predicted later than in the Euler simulations, breakdown was observed to leave the upper surface of the wing at the lower angles of incidence. As vortex breakdown forms over the wing on the upstroke, there is a loss in the lift curve slope and an eventual increase in the nose up pitching moment. Similar effects were observed in the drag and pitching moment curves. Tunnel interference was observed to be much lower in the low incidence range of the upstroke. As incidence was increased, the differences between the tunnel and farfield solutions became more apparent indicating higher interference. At the higher incidence range of the upstroke and the downstroke of the motion, there appeared to be the largest interference. Due to the high interference at high incidence, in the 2x3 tunnel in particular, it was observed that there is a delay in vortex recovery due to the tendency of the side walls to promote vortex breakdown (which is strongest at high incidence). It should be noted that the delay in vortex recovery in the RANS solutions is less than in the Euler solutions. However it must be recalled that the breakdown reaches the apex in the Euler solutions. It has been shown experimentally [77] that when breakdown reaches the apex and the wing is fully stalled, there is a delay in vortex recovery.

In order to understand why vortex breakdown has moved towards the apex due to the presence of the tunnel side walls, the following points should be considered. Considering the more realistic RANS simulations (though the argument applies also to the Euler results) the following points are made

- The amount of upwash generated is dependent on the side wall location. The 2x3 tunnel induces the greatest upwash, followed by the square and 3x2 tunnels. Averaging the increased effective incidence along the leading edge of the wing it is clear the mean effective incidence of the wing increases.

- The effective incidence of the wing increases along the leading edge (tunnel interference increases toward the trailing edge as the vortices are closer to the side walls) therefore the wing might be considered to behave as if positively cambered. A positively cambered wing is expected to delay vortex breakdown. However it is questionable if the chordwise increasing upwash effect can be modelled as a geometrically cambered wing, and if so, how strong this effect

is.

- The helix angle of the vortices increases due to side wall proximity. The side wall induced upwash tightens the windings of the vortex and therefore increases the vortex strength. Higher helix angles are known to induce vortex breakdown. The increase in helix angle is likely to be due to the increased effective incidence of the wing.

All of these points indicate that the effect of the tunnel side walls is similar to an increase in the effective mean incidence of the wing. The breakdown location could perhaps be corrected by simply applying a $\Delta\alpha$ correction, possibly from charts derived computationally after suitable validation. However as indicated in figure 4.29, and as implied by the method of images, since the local incidence along the leading edge increases towards the trailing edge of the wing, the circulation will grow along the wing in a differing manner (it will most likely grow at a steeper $\frac{\partial\Gamma}{\partial(x/c_r)}$) to that of a wing pitched at the new mean effective incidence. Therefore despite what may be considered an easy correction for the breakdown location, parameters such as upper surface pressure distributions, and loads and moments might not be so easily corrected by simply assuming a higher angle of attack of the wing.

From the previous discussion it is evident that side wall proximity is the most dominant influence in wind tunnel wall interference. It is also clear that it is the wall induced upwash that is the detrimental result of the side walls. Considering the method of images it can be seen that as vortex strength increases, the image vortices also increase in strength, and therefore the wall induced upwash increases. This indicates that the amount of side wall interference is predominantly dependent on the strength of the leading edge vortices. Therefore it can be concluded that tunnel wall interference will be dependent on the model span-to-tunnel width ratio, sweep angle of the wing (lower sweep implies stronger vortices at a given angle of attack), and the angle of attack of the wing. Since the predicted vortex strengths are likely to be lower than in experiment, it can be expected that the tunnel wall interference predicted is lower than that found in experiment.

Despite the grid dependence of individual solutions, the trends of breakdown and vortex response to tunnel walls have been found to be grid independent (the

Euler grids of chapter 2 were considerably coarser than the RANS grids of chapter 4). Further the trends of breakdown motion with tunnel influences are independent of viscous effects (Euler simulations produce identical trends to RANS simulations), which is expected for a widely (if not universally) accepted inviscid phenomenon.

Given the results from the tunnel wall studies it would appear that the main influence of the tunnel walls is to promote vortex breakdown. This agrees with the results of Thompson and Nelson [89] and Pelletier and Nelson [90] but disagrees with the results of Weinberg [88].

In order to assess levels of support interference, the ONERA 70^o wing in the ONERA F2 tunnel was considered. A support with a large frontal area blockage was used. The support was placed at two chordwise locations in order to assess the effect of support proximity on the solutions. It was seen that the leading edge vortices were very sensitive to variations in pressure distributions aft of the trailing edge, due to the presence of supports. It was found that downstream support structures had no effect of the flow structure prior to vortex breakdown. The support shape considered caused a significant acceleration of the flow due to blockage which had the effect of delaying vortex breakdown. A smaller support with a lower blockage ratio was also considered and provided a similar result (though the magnitude of the delay was less). The trajectory of the vortex cores was such that the core flow never experienced the adverse pressure gradient ahead of the support structure. Thus it can be concluded that the effect of downstream support structures is heavily dependent on whether or not the core flow impinges on the structure.

The support structure simulations lead to another interesting suggestion which may help explain the conflicting trends of tunnel interference seen in experiment. The support structure simulations have indicated that the vortices are highly sensitive to local pressure gradients near the trailing edge of the wing. Bringing the support closer to the wing, and therefore decreasing locally the pressure (due to blockage) at the trailing edge, resulted in breakdown moving downstream. If a support such as a sting is used to mount the wing, it may be expected there is a local pressure variation near the centre of the wing where stings are usually mounted. As a wing is increased in size the effect of the sting interference will decrease since the trajectory of the vortices will be such that they are getting further and further

away from the sting with increasing wing size. Therefore if the effect of the sting interference is to induce breakdown, breakdown would be expected to move downstream with increasing wing size. The rod mounting in the experiments of Weinberg may be the reason for the breakdown movement downstream with increasing wing size. Since Thompson and Nelson, and Pelletier and Nelson had no downstream structures, and consistent sting sizes respectively, there is no effect of downstream structures in the case of Thompson and Nelson, and the influence is consistent in the experiments of Pelletier and Nelson. Therefore it is speculated that support interference is the reason for the conflicting experimental results.

6.2 Future work

As with all CFD work the solutions must be validated with experimental data. A systematic experimental investigation (similar to the present work) should be conducted to confirm the results of the test facility interference predicted. The effects of the tunnel boundary layers, diffusers, contraction chambers and freestream flow gradients have not been modelled in any of the current simulations. However, these parameters are specific to a given wind tunnel and vary from tunnel to tunnel. Thus a CFD study with more detailed modelling of the test facility should be conducted in order to provide a solid validation of the results. Further sources of test facility interference are mountings such as stings which should be investigated.

It is recommended that any experimental tests alter the test section geometry as opposed to increasing model size. Support influences have been seen to play an important part, therefore keeping the support influences consistent is necessary to adequately test wind tunnel wall effects. Tunnel geometries can be altered by adding artificial walls. It is also recommended that for tunnel wall interference tests, the model is mounted from beneath the wing as opposed to the use of stings, in this way the tunnel wall interference can be examined without the effect of support interference aft of the trailing edge.

Useful experimental parameters for an accurate validation of the CFD study would be freestream velocity and pressure distributions (boundary conditions), wall pressure distributions, tunnel boundary layer growth data, flow visualisation and

surface pressure data. If CFD can be validated sufficiently, correction charts can be created for both breakdown location and loads and moment data. Given that the test facilities chosen in this study are likely to be at the limits of those a tunnel engineer would use, with suitable correction procedures, larger models could be confidently used for high Reynolds number experiments.

For delta wing aerodynamics in particular, more advanced turbulence modelling should be applied (for example non-linear eddy viscosity models or DES). It has been shown that RANS turbulence models predict unrealistic levels of turbulence and as such modifications are required. Combined with grid resolution effects, this has the effect of smoothing the solution and as such flow gradients (especially core properties) are underpredicted. Even with modifications to the turbulence model, the vortical core flow cannot be predicted to a high level of confidence.

A final important point about the current work is that none of the solutions are temporally refined such that the helical mode of vortex breakdown seen in experiment is resolved. A question which must be addressed is; in the current simulations, does the steady solution represent the time-averaged time accurate solution? It is expected (based on previous experience with unsteady flows) that this is the case, however, time accurate solutions must be conducted to prove this.

Appendix A

The Three-Dimensional Governing Equations

A.1 Introduction

The three-dimensional model equations are presented here in conservative form. A full derivation from first principles can be found in numerous text books such as Anderson [145]. The following is a modification of the theory guide to the two-dimensional version of PMB.

The conservative form of the governing equations is convenient for applications in computational fluid dynamics due to the fact that continuity, energy, and momentum equations are expressed by the same generic equation helping to simplify the logic in a computer program.

A.2 Non-dimensional form

In a three-dimensional Cartesian coordinate system, the non-dimensional form of the equations may be written as

$$\frac{\partial \mathbf{W}}{\partial t} + \frac{\partial (\mathbf{F}^i - \mathbf{F}^v)}{\partial x} + \frac{\partial (\mathbf{G}^i - \mathbf{G}^v)}{\partial y} + \frac{\partial (\mathbf{H}^i - \mathbf{H}^v)}{\partial z} = 0 \tag{A.1}$$

Here the vector $\mathbf{W}$ is the vector of conserved flow variables and is sometimes referred to as the solution vector. It can be written as:

$$\mathbf{W} = \begin{pmatrix} \rho \\ \rho u \\ \rho v \\ \rho w \\ \rho E \end{pmatrix} \tag{A.2}$$

In the above ρ is the density, u, v and w are the components of velocity given by the Cartesian velocity vector $\mathbf{U} = (u, v, w)$. Finally E is the total energy per unit mass.

When deriving the Navier-Stokes equations, the conservative form is obtained using a control volume that is fixed in space as opposed to moving with the fluid. Consequently, we are forced to consider the flux of energy, mass and momentum into and out of the control volume. The flux vectors $\mathbf{F}$, $\mathbf{G}$, and $\mathbf{H}$ consist of inviscid (^{i}) and viscous ($^\nu$) diffusive parts. These are written in full as

$$\mathbf{F}^i = \begin{pmatrix} \rho u \\ \rho u^2 + p \\ \rho uv \\ \rho uw \\ \rho uH \end{pmatrix}$$

$$\mathbf{G}^i = \begin{pmatrix} \rho v \\ \rho vu \\ \rho v^2 + p \\ \rho vw \\ \rho vH \end{pmatrix} \tag{A.3}$$

$$\mathbf{H}^i = \begin{pmatrix} \rho w \\ \rho wu \\ \rho wv \\ \rho w^2 + p \\ \rho wH \end{pmatrix}$$

$$\mathbf{F}^{\nu} = \frac{1}{Re}\begin{pmatrix} 0 \\ \tau_{xx} \\ \tau_{xy} \\ \tau_{xz} \\ u\tau_{xx} + v\tau_{xy} + w\tau_{xz} + q_x \end{pmatrix}$$

$$\mathbf{G}^{\nu} = \frac{1}{Re}\begin{pmatrix} 0 \\ \tau_{xy} \\ \tau_{yy} \\ \tau_{yz} \\ u\tau_{xy} + v\tau_{yy} + w\tau_{yz} + q_y \end{pmatrix} \tag{A.4}$$

$$\mathbf{H}^{\nu} = \frac{1}{Re}\begin{pmatrix} 0 \\ \tau_{xz} \\ \tau_{yz} \\ \tau_{zz} \\ u\tau_{xz} + v\tau_{yz} + w\tau_{zz} + q_z \end{pmatrix}$$

The stress tensor components are written as

$$\begin{aligned}
\tau_{xx} &= -\mu\left(2\frac{\partial u}{\partial x} - \frac{2}{3}\left(\frac{\partial u}{\partial x} + \frac{\partial v}{\partial y} + \frac{\partial w}{\partial z}\right)\right) \\
\tau_{yy} &= -\mu\left(2\frac{\partial v}{\partial y} - \frac{2}{3}\left(\frac{\partial u}{\partial x} + \frac{\partial v}{\partial y} + \frac{\partial w}{\partial z}\right)\right) \\
\tau_{zz} &= -\mu\left(2\frac{\partial w}{\partial z} - \frac{2}{3}\left(\frac{\partial u}{\partial x} + \frac{\partial v}{\partial y} + \frac{\partial w}{\partial z}\right)\right) \\
\tau_{xy} &= -\mu\left(\frac{\partial u}{\partial y} + \frac{\partial v}{\partial x}\right) \\
\tau_{xz} &= -\mu\left(\frac{\partial u}{\partial z} + \frac{\partial w}{\partial x}\right) \\
\tau_{yz} &= -\mu\left(\frac{\partial v}{\partial z} + \frac{\partial w}{\partial y}\right)
\end{aligned} \tag{A.5}$$

and the heat flux vector components are written as

$$\begin{aligned}
q_x &= -\frac{1}{(\gamma-1)M_\infty^2}\frac{\mu}{Pr}\frac{\partial T}{\partial x} \\
q_y &= -\frac{1}{(\gamma-1)M_\infty^2}\frac{\mu}{Pr}\frac{\partial T}{\partial y} \\
q_z &= -\frac{1}{(\gamma-1)M_\infty^2}\frac{\mu}{Pr}\frac{\partial T}{\partial z}
\end{aligned} \tag{A.6}$$

Here γ is the specific heat ratio, Pr is the laminar Prandtl number, T is the static temperature and M_∞ and Re are the freestream Mach number and Reynolds number, respectively. The various flow quantities are related to each other by the perfect gas relations

$$\begin{aligned} H &= E + \frac{p}{\rho} \\ E &= e + \frac{1}{2}\left(u^2 + v^2\right) \\ p &= (\gamma - 1)\,\rho e \\ \frac{p}{\rho} &= \frac{T}{\gamma M_\infty^2} \end{aligned} \tag{A.7}$$

Finally, the laminar viscosity μ is evaluated using Sutherland's law,

$$\frac{\mu}{\mu_0} = \left(\frac{T}{T_0}\right)^{3/2} \frac{T_0 + 110}{T + 110} \tag{A.8}$$

where μ_0 is a reference viscosity at a reference temperature T_0. These can be taken as $\mu_0 = 1.7894\text{x}10^{-5}$ kg/(m.s) with $T_0 = 288.16$ K. All quantities have been non-dimensionalised as follows

$$x = \frac{x^*}{L^*}, \qquad y = \frac{y^*}{L^*}, \qquad t = \frac{t^*}{L^*/V_\infty^*},$$

$$u = \frac{u^*}{V_\infty^*}, \qquad v = \frac{v^*}{V_\infty^*}, \qquad \mu = \frac{\mu^*}{\mu_\infty^*},$$

$$\rho = \frac{\rho^*}{\rho_\infty^*}, \qquad p = \frac{p^*}{\rho_\infty^* V_\infty^{*2}}, \qquad T = \frac{T^*}{T_\infty^*}, \qquad e = \frac{e^*}{V_\infty^{*2}} \tag{A.9}$$

A.3 Reynolds-averaged form

In order to study turbulence one must solve the full N-S equations (called Direct Numerical Simulation - DNS). However these calculations are very large and are currently only possible when examining Reynolds numbers several orders less than those in real applications [112]. Rather than attempt to solve the time evolution of the conserved variables, a somewhat less ambitious method is to calculate the Reynolds averaged form. The Reynolds-averaged form of the Navier-Stokes equations permits turbulent flow to be considered efficiently. The development is not presented here. It is merely noted that fundamental to this approach is the consideration of the flow variables as consisting of two components, a time averaged component and a turbulent fluctuation. For example, density, pressure and velocity components are decomposed as

$$\rho = \bar{\rho} + \rho', \qquad P = \bar{P} + P', \qquad u = \bar{u} + u', \qquad v = \bar{v} + v', \qquad w = \bar{w} + w'.$$

The quantities k (the turbulent kinetic energy), μ_T (the eddy viscosity) and Pr_T (the turbulent Prandtl number) are introduced via the important Boussinesq assumption in an attempt to model the fluctuating-variable stress terms arising from the Reynolds averaging. For a complete discussion of this subject see Anderson et al. [146]. The Reynolds-averaged form of the Navier-Stokes equations are identical to those presented in appendix A.2, except for the stress tensor and heat flux vector components shown below. The variables should be considered as mean flow quantities (superscripts are dropped for clarity). The turbulent nature of the flow is modelled via μ_T and k and a closure hypothesis or turbulence model, for example the SA model (see appendix B.1), the $k-\omega$ model (see appendix B.2), or the SST

model (see appendix B.3).

$$\begin{aligned}
\tau_{xx} &= -(\mu+\mu_T)\left(2\frac{\partial u}{\partial x}-\frac{2}{3}\left(\frac{\partial u}{\partial x}+\frac{\partial v}{\partial y}+\frac{\partial w}{\partial z}\right)\right)+\frac{2}{3}\rho k \\
\tau_{yy} &= -(\mu+\mu_T)\left(2\frac{\partial v}{\partial y}-\frac{2}{3}\left(\frac{\partial u}{\partial x}+\frac{\partial v}{\partial y}+\frac{\partial w}{\partial z}\right)\right)+\frac{2}{3}\rho k \\
\tau_{zz} &= -(\mu+\mu_T)\left(2\frac{\partial w}{\partial z}-\frac{2}{3}\left(\frac{\partial u}{\partial x}+\frac{\partial v}{\partial y}+\frac{\partial w}{\partial z}\right)\right)+\frac{2}{3}\rho k \\
\tau_{xy} &= -(\mu+\mu_T)\left(\frac{\partial u}{\partial y}+\frac{\partial v}{\partial x}\right) \\
\tau_{xz} &= -(\mu+\mu_T)\left(\frac{\partial u}{\partial z}+\frac{\partial w}{\partial x}\right) \\
\tau_{yz} &= -(\mu+\mu_T)\left(\frac{\partial v}{\partial z}+\frac{\partial w}{\partial y}\right)
\end{aligned} \tag{A.10}$$

$$\begin{aligned}
q_x &= -\frac{1}{(\gamma-1)M_\infty^2}\left(\frac{\mu}{Pr}+\frac{\mu_T}{Pr_T}\right)\frac{\partial T}{\partial x} \\
q_y &= -\frac{1}{(\gamma-1)M_\infty^2}\left(\frac{\mu}{Pr}+\frac{\mu_T}{Pr_T}\right)\frac{\partial T}{\partial y} \\
q_z &= -\frac{1}{(\gamma-1)M_\infty^2}\left(\frac{\mu}{Pr}+\frac{\mu_T}{Pr_T}\right)\frac{\partial T}{\partial z}
\end{aligned} \tag{A.11}$$

A.4 Curvilinear form

The model equations are written in curvilinear (ξ,η,ζ) form to facilitate use on curvilinear grids of arbitrary local orientation and density. A space transformation from the Cartesian co-ordinate system to the local coordinate system must then be introduced

$$\begin{aligned} \xi &= \xi(x,y,z) \\ \eta &= \eta(x,y,z) \\ \zeta &= \zeta(x,y,z) \\ t &= t \end{aligned}$$

The Jacobian determinant of the transformation is given by

$$J = \frac{\partial(\xi,\eta,\zeta)}{\partial(x,y,z)}$$

The equation A.1 can then be written as

$$\frac{\partial \hat{\mathbf{W}}}{\partial t} + \frac{\partial(\hat{\mathbf{F}}^i - \hat{\mathbf{F}}^v)}{\partial \xi} + \frac{\partial(\hat{\mathbf{G}}^i - \hat{\mathbf{G}}^v)}{\partial \eta} + \frac{\partial(\hat{\mathbf{H}}^i - \hat{\mathbf{H}}^v)}{\partial \zeta} = 0 \tag{A.12}$$

where

$$\begin{aligned} \hat{\mathbf{W}} &= \frac{\mathbf{W}}{J} \\ \hat{\mathbf{F}}^i &= \frac{1}{J}\left(\xi_x \mathbf{F}^i + \xi_y \mathbf{G}^i + \xi_z \mathbf{H}^i\right) \\ \hat{\mathbf{G}}^i &= \frac{1}{J}\left(\eta_x \mathbf{F}^i + \eta_y \mathbf{G}^i + \eta_z \mathbf{H}^i\right) \\ \hat{\mathbf{H}}^i &= \frac{1}{J}\left(\zeta_x \mathbf{F}^i + \zeta_y \mathbf{G}^i + \zeta_z \mathbf{H}^i\right) \\ \hat{\mathbf{F}}^v &= \frac{1}{J}\left(\xi_x \mathbf{F}^v + \xi_y \mathbf{G}^v + \xi_z \mathbf{H}^v\right) \\ \hat{\mathbf{G}}^v &= \frac{1}{J}\left(\eta_x \mathbf{F}^v + \eta_y \mathbf{G}^v + \eta_z \mathbf{H}^v\right) \\ \hat{\mathbf{H}}^v &= \frac{1}{J}\left(\zeta_x \mathbf{F}^v + \zeta_y \mathbf{G}^v + \zeta_z \mathbf{H}^v\right) \end{aligned} \tag{A.13}$$

The expressions for the inviscid fluxes can be simplified somewhat by defining

$$\begin{aligned} U &= \xi_x u + \xi_y v + \zeta_z w \\ V &= \eta_x u + \eta_y v + \zeta_z w \\ W &= \zeta_x u + \zeta_y v + \zeta_z w \end{aligned} \tag{A.14}$$

The inviscid fluxes can then be written as

$$\hat{\mathbf{F}}^i = \begin{pmatrix} \rho U \\ \rho u U + \xi_x p \\ \rho v U + \xi_y p \\ \rho w U + \xi_z p \\ \rho U H \end{pmatrix}$$

$$\hat{\mathbf{G}}^i = \begin{pmatrix} \rho V \\ \rho u V + \eta_x p \\ \rho v V + \eta_y p \\ \rho w V + \eta_z p \\ \rho V H \end{pmatrix} \tag{A.15}$$

$$\hat{\mathbf{H}}^i = \begin{pmatrix} \rho W \\ \rho u W + \zeta_x p \\ \rho v W + \zeta_y p \\ \rho w W + \zeta_z p \\ \rho W H \end{pmatrix}$$

The derivative terms found in the viscous fluxes are evaluated using the chain rule, for example

$$\frac{\partial u}{\partial x} = \xi_x \frac{\partial u}{\partial \xi} + \eta_x \frac{\partial u}{\partial \eta} + \zeta_x \frac{\partial u}{\partial \zeta}$$

The evaluation of the metrics of the transformation is clearly important, and is described in full in Anderson et al. [146].

A.5 Steady State Solver

The Navier-Stokes equations are discretised using a cell-centred finite volume approach. The computational domain is divided into a finite number of non-overlapping control-volumes, and the governing equations are applied to each cell in turn. Also, the Navier-Stokes equations are re-written in a curvilinear co-ordinate system which simplifies the formulation of the discretised terms since body-conforming grids are adopted here. The spatial discretisation of equation A.12 leads to a set of ordinary differential equations in time,

$$\frac{d}{dt}\left(\mathbf{W}_{i,j,k}V_{i,j,k}\right) = -\mathbf{R}_{i,j,k}\left(\mathbf{W}\right) \tag{A.16}$$

where $\mathbf{W}$ and $\mathbf{R}$ are the vectors of cell conserved variables and residuals respectively. The convective terms are discretised using Osher's upwind scheme (Osher et al. [147]) for its robustness, accuracy, and stability properties. MUSCL variable extrapolation is used to provide second-order accuracy with the Van Albada limiter to prevent spurious oscillations around shock waves. Boundary conditions are set by using ghost cells on the exterior of the computational domain. In the farfield ghost cells are set at the freestream conditions. At solid boundaries the no-slip condition is set for viscous flows, or ghost values are extrapolated from the interior (ensuring the normal component of the velocity on the solid wall is zero) for Euler flow.

The integration in time of equation A.16 to a steady-state solution is performed using an implicit time-marching scheme by

$$\frac{\mathbf{W}^{n+1}_{i,j,k} - \mathbf{W}^{n}_{i,j,k}}{\Delta t} = -\frac{1}{V_{i,j,k}}\mathbf{R}_{\mathbf{i,j,k}}\left(\mathbf{W}^{n+1}_{i,j,k}\right) \tag{A.17}$$

where $n+1$ denotes the time $(n+1) * \Delta t$. Equation A.17 represents a system

of non-linear algebraic equations and to simplify the solution procedure, the flux residual $\mathbf{R_{i,j,k}}\left(\mathbf{W^{n+1}_{i,j,k}}\right)$ is linearised in time as follows,

$$\begin{aligned}
\mathbf{R_{i,j,k}}\left(\mathbf{W}^{n+1}\right) &= \mathbf{R_{i,j,k}}\left(\mathbf{W}^{n}\right) + \frac{\partial \mathbf{R_{i,j,k}}}{\partial t}\Delta t + O(\Delta t^2) \\
&\approx \mathbf{R_{i,j,k}}^{n}\left(\mathbf{W}^{n}\right) + \frac{\partial \mathbf{R_{i,j,k}}}{\partial \mathbf{W_{i,j,k}}}\frac{\partial \mathbf{W_{i,j,k}}}{\partial t}\Delta t \\
&\approx \mathbf{R_{i,j,k}}^{n}\left(\mathbf{W}^{n}\right) + \frac{\partial \mathbf{R_{i,j,k}}}{\partial \mathbf{W_{i,j,k}}}\Delta \mathbf{W_{i,j,k}} \qquad \text{(A.18)}
\end{aligned}$$

where $\Delta\mathbf{W_{i,j,k}} = \mathbf{W_{i,j,k}}^{n+1} - \mathbf{W_{i,j,k}}^{n}$. EquationA.17 now becomes the following linear system

$$\left[\frac{V_{i,j,k}}{\Delta t}\mathbf{I} + \frac{\partial \mathbf{R_{i,j,k}}}{\partial \mathbf{W_{i,j,k}}}\right]\Delta \mathbf{W_{i,j,k}} = -\mathbf{R}^{n}_{i,j,k}\left(\mathbf{W^{n}}\right) \qquad \text{(A.19)}$$

The complexity of a direct method to compute a linear system is of the order of $\mathcal{N}^3$, which becomes prohibitive when the total number of equations $\mathcal{N}$ becomes large. On the other hand, iterative techniques such as Conjugate Gradient (CG) methods are capable of solving large systems of equations more efficiently in terms of time and memory. CG methods find an approximation to the solution of a linear system by minimising a suitable residual error function in a finite-dimensional space of potential solution vectors. Several algorithms, such as BiCG, CGSTAB, CGS and GMRES, have been tested (see Badcock et al. [148]) and it was concluded that the choice of method is not as crucial as the preconditioning. The current results use a Generalised Conjugate Gradient method - see Axelsson [149].

A Krylov subspace algorithm is used to solve the linear system. The preconditioning strategy is based on a Block Incomplete Lower-Upper (BILU) factorisation (Axelsson [149]) since it appears to be the most promising and has the same sparsity pattern as the Jacobian matrix (BILU(0)) - i.e. the sparsity pattern of the Lower

and Upper matrices is defined with respect to the sparsity of the unfactored matrix for simplicity. Furthermore the BILU(0) factorisation is decoupled between blocks to improve parallel efficiency and this approach does not seem to have a major impact on the effectiveness of the preconditioner as the number of blocks increases.

Implicit schemes require particular treatment during the early stages of the iterative procedure. The usual approach in starting the method is to take a small CFL number and to increase it later on. However, it was found that smoothing out the initial flow doing some explicit iterations, and then switching to the implicit algorithm was equally efficient. In the present method, a specified number of forward Euler iterations are executed before switching to the implicit scheme.

The formulation leads to a Jacobian Matrix with a number of non-zero entries per row. Trying to reduce the number of non-zero entries would have several advantages. First, the memory requirements are lowered. Second, the resolution of the linear system by the GCG method is faster in terms of CPU-time since all the matrix-vector multiplications involved require less operation counts. Finally, the linear system is easier to solve since the approximate Jacobian matrix is more diagonally dominant. A full discussion of the Jacobian formulation is given in Cantariti et al. [150].

The steady state solver for the turbulent case is formulated and solved in an identical manner to that described above for the mean flow. The eddy-viscosity is regarded calculated from the latest values of k and ω (for example) and is used to advance the mean flow solution and then this new solution is used to update the turbulence solution, freezing the mean flow values. An approximate Jacobian is used for the source term by only taking into account the contribution of the dissipation terms $\hat{\mathbf{D}}_k$ and $\hat{\mathbf{D}}_\omega$ i.e. no account of the production terms is taken on the left hand side of the system. This approach has a stability advantage as described in Wilcox [112].

A.6 Unsteady State Solver

The formulation is described for the turbulent case. The laminar and inviscid cases represent a simplification of this.

Following the pseudo-time formulation (Jameson [151]), the updated mean flow solution is calculated by solving the steady state problems

$$\mathbf{R}^*_{i,j,k} = \frac{3\mathbf{w}^{n+1}_{i,j,k} - 4\mathbf{w}^{n}_{i,j,k} + \mathbf{w}^{n-1}_{i,j,k}}{2\Delta t} + \mathbf{R}_{i,j,k}(\tilde{\mathbf{w}}^{k_m}_{i,j,k}, \tilde{\mathbf{q}}^{k_t}_{i,j,k}) = 0 \tag{A.20}$$

$$\mathbf{Q}^*_{i,j,k} = \frac{3\mathbf{q}^{n+1}_{i,j,k} - 4\mathbf{q}^{n}_{i,j,k} + \mathbf{q}^{n-1}_{i,j,k}}{2\Delta t} + \mathbf{Q}_{i,j}(\tilde{\mathbf{w}}^{l_m}_{i,j,k}, \tilde{\mathbf{q}}^{l_t}_{i,j,k}) = 0. \tag{A.21}$$

Here k_m, k_t, l_m and l_t give the time level of the variables used in the spatial discretisation. Here the grid is moved rigidly but if grid deformation was required then time varying areas would be required in the expression for the real time derivative in equations A.20 and A.21. If $k_m = k_t = l_m = l_t = n + 1$ then the mean and turbulent quantities are advanced in real time in a fully coupled manner. However, if $k_m = l_m = l_t = n + 1$ and $k_t = n$ then the equations are advanced in sequence in real time, i.e. the mean flow is updated using frozen turbulence values and then the turbulent values are updated using the latest mean flow solution. This has the advantage that the only modification, when compared with the laminar case, to the discretisation of the mean flow equations is the addition of the eddy viscosity from the previous time step. The turbulence model only influences the mean flow solution through the eddy viscosity and so any two equation model can be used without modifying the mean flow solver. Hence, the implementation is simplified by using a sequenced solution in real time. However, the uncoupling could adversely effect the stability and accuracy of the real time stepping, with the likely consequence of limiting the size of the real time step that can be used.

Equations (A.20) and (A.21) represent a coupled nonlinear system of equations. These can be solved by introducing an iteration through *pseudo time* τ to the steady state, as given by

$$\frac{\mathbf{w}_{i,j}^{n+1,m+1} - \mathbf{w}_{i,j}^{n+1,m}}{\Delta\tau} + \frac{3\mathbf{w}_{i,j}^{k_m} - 4\mathbf{w}_{i,j}^{n} + \mathbf{w}_{i,j}^{n-1}}{2\Delta t} + \mathbf{R}_{i,j}(\tilde{\mathbf{w}}_{i,j}^{k_m}, \tilde{\mathbf{q}}_{i,j}^{k_t}) = 0 \tag{A.22}$$

$$\frac{\mathbf{q}_{i,j}^{n+1,m+1} - \mathbf{q}_{i,j}^{n+1,m}}{\Delta\tau} + \frac{3\mathbf{q}_{i,j}^{l_t} - 4\mathbf{q}_{i,j}^{n} + \mathbf{q}_{i,j}^{n-1}}{2\Delta t} + \mathbf{Q}_{i,j}(\tilde{\mathbf{w}}_{i,j}^{l_m}, \tilde{\mathbf{q}}_{i,j}^{l_t}) = 0. \tag{A.23}$$

where the $m-th$ pseudo-time iterate at the $n+1th$ real time step are denoted by $\mathbf{w}^{n+1,m}$ and $\mathbf{q}^{n+1,m}$ respectively. The iteration scheme used only effects the efficiency of the method and hence we can sequence the solution in pseudo time without compromising accuracy. Examples of For example, using explicit time stepping we can calculate $\mathbf{w}^{n+1,m+1}$ using $k_m = n+1, m$ and $k_t = n+1, m$ and $\mathbf{q}^{n+1,m+1}$ using $l_m = n+1, m+1$ and $l_t = n+1, m$. For implicit time stepping in pseudo time we can use $k_m = l_m = l_t = n+1, m+1$ and $k_t = n+1, m$. In both of these cases the solution of the equations is decoupled by freezing values but at convergence the real time stepping proceeds with no sequencing error. It is easy to recover a solution which is sequenced in real time from this formulation by setting $k_t = n$ throughout the calculation of the pseudo steady state. This facilitates a comparison of the current pseudo time sequencing with the more common real time sequencing. In the code the pseudo steady-state problems are solved using the implicit steady state solver described in detail in section A.5.

Appendix B

One and two-equation turbulence models

A brief description of the turbulence models implemented in PMB3D are presented. Conversion to curvilinear form has been covered in section A.4 and the application to the turbulence models represents a continuation of this. The original formulation of the equations is presented.

B.1 The Spalart-Allmaras (SA) Turbulence Model

The Spalart-Allmaras turbulence model [152] is a 1-equation model (inspired by the Baldwin-Lomax turbulence model [111]) and is defined as follows.

Eddy Viscosity Function

$$\nu_T = \tilde{\nu} f_{v1} \tag{B.1}$$

where

$$f_{v1} = \frac{\chi^3}{\chi^3 + c_{v1}^3}, \quad \chi \equiv \frac{\tilde{\nu}}{\nu} \tag{B.2}$$

Convective Transport Equation of the Eddy Viscosity

$$\frac{D\tilde{\nu}}{Dt} = c_{b1}\tilde{S}\tilde{\nu} + \frac{1}{\sigma}[\nabla.((\nu+\tilde{\nu})\nabla\tilde{\nu}) + c_{b2}(\nabla\tilde{\nu})^2] - c_{w1}f_w\left[\frac{\tilde{\nu}}{d}\right]^2 \tag{B.3}$$

where

$$\tilde{S} \equiv S + \frac{\tilde{\nu}}{\kappa^2 d^2}f_{v2}, \quad f_{v2} = 1 - \frac{\chi}{1+\chi f_{v1}} \tag{B.4}$$

and

$$f_w = g\left[\frac{1+c_{w3}^6}{g^6+c_{w3}^6}\right]^{1/6}, \quad g = r + c_{w2}(r^6 - r), \quad r \equiv \frac{\tilde{\nu}}{\tilde{S}\kappa^2 d^2}$$

Closure Coefficients

$$c_{b1} = 0.135, \quad \sigma = 2/3, \quad c_{b2} = 0.622, \quad \kappa = 0.41,$$

$$c_{w1} = 2.762, \quad c_{w2} = 0.3, \quad c_{w3} = 2, \quad c_{v1} = 7.1$$

$$c_{w1} = 2.762, \quad c_{w2} = 0.3, \quad c_{w3} = 2, \quad c_{v1} = 7.1 \tag{B.5}$$

B.2 The k - ω Turbulence Model

The k-ω turbulence model of Wilcox [112] can be written as follows in non-dimensional form.

Eddy Viscosity

$$\mu_T = \rho k/\omega \tag{B.6}$$

Turbulence Kinetic Energy

$$\rho\frac{\partial k}{\partial t} + \rho\mathbf{V}.\nabla k - \frac{1}{Re}\nabla.\left[(\mu + \sigma^*\mu_T)\nabla k\right] = P_k - \beta^*\rho k\omega \tag{B.7}$$

Specific Dissipation Rate

$$\rho\frac{\partial\omega}{\partial t}+\rho\mathbf{V}.\nabla\omega-\frac{1}{Re}\nabla.\left[\left(\mu+\sigma\mu_T\right)\nabla\omega\right] \;=\; P_\omega-\beta\rho\omega^2 \tag{B.8}$$

Closure Coefficients

$$\alpha=5/9,\qquad \beta=3/40,\qquad \beta^*=9/100,\qquad \sigma=1/2,\qquad \sigma^*=1/2 \tag{B.9}$$

In the above relations the production terms of k and ω, P_k and P_ω respectively, are

$$P_k=\mu_T P-\frac{2}{3}\rho k S \tag{B.10}$$

$$P_\omega=\alpha\frac{\omega}{k}P_k \tag{B.11}$$

and

$$P \;=\; \left[\left(\nabla\mathbf{V}+\nabla\mathbf{V}^T\right):\nabla\mathbf{V}-\frac{2}{3}\left(\nabla.\mathbf{V}\right)^2\right] \tag{B.12}$$

$$S \;=\; \nabla.\mathbf{V} \tag{B.13}$$

The equations as shown above use the same non-dimensional quantities as in section A.2, with the addition of

$$k=\frac{k^*Re}{U_\infty^{*2}},\qquad \omega=\frac{\omega^*L^*}{U_\infty^*},\qquad \mu_T=\frac{\mu_T^*}{\mu_\infty^*} \tag{B.14}$$

The equations for k and ω can be written in a curvilinear form analogous to that used for the mean flow equations in section A.4.

B.3 The Shear Stress Transport (SST) Turbulence Model

The SST turbulence model of Menter [153] is defined as follows.

Eddy Viscosity

$$\mu_T = \frac{\rho k/\omega}{max\left[1; \Omega F_2/\left(a_1\omega\right)\right]} \quad a_1 = 0.31 \tag{B.15}$$

In turbulent boundary layers the maximum value of the eddy viscosity is limited by forcing the turbulent shear stress to be bounded by the turbulent kinetic energy times a_1. This effect is achieved an auxiliary function F_2 and an absolute value of the vorticity, Ω. This auxiliary function is defined as a function of the wall distance (y) as

$$F_2 = \tanh\left[\left(\max\left[2\frac{\sqrt{k}}{0.09\omega y}; \frac{500\mu}{\rho y^2\omega}\right]\right)^2\right] \tag{B.16}$$

Turbulence Kinetic Energy

The two transport equations of the model are defined below with a blending function F_1 for the model coefficients of the original ω and ϵ model equations. The transport equation are given by

$$\rho\frac{\partial k}{\partial t} + \rho\mathbf{V}.\nabla k - \frac{1}{Re}\nabla.\left[\left(\mu + \sigma^*\mu_T\right)\nabla k\right] = P_k - \beta^*\rho k\omega \tag{B.17}$$

Specific Dissipation Rate

$$\rho\frac{\partial \omega}{\partial t} + \rho\mathbf{V}.\nabla\omega - \frac{1}{Re}\nabla.\left[\left(\mu + \sigma_\omega\mu_T\right)\nabla\omega\right] = P_\omega - \beta\rho\omega^2$$

$$+2\left(1 - F_1\right)\frac{\rho\sigma_{\omega 2}}{\omega}\nabla k\nabla\omega \tag{B.18}$$

Closure Coefficients

The function F_1 is designed to blend the model coefficients of the original $k-\omega$ model in boundary layer zones with the transformed $k-\epsilon$ model in free-shear layer freestream zones. This function takes the value of one on no-slip surfaces and near one over a large portion of the boundary layer, and goes to zero at the boundary layer edge. This auxiliary blending function, F_1, is defined as

$$F_1 = \tanh\left[\left[\min\left(\max\left[\frac{\sqrt{k}}{0.09\omega y}; \frac{500\mu}{\rho y^2 \omega}\right]; \frac{4\rho\sigma_{\omega 2} k}{CD_{k\omega} y^2}\right)\right]^4\right] \tag{B.19}$$

where

$$CD_{k\omega} = \max\left[\frac{2\rho\sigma_{\omega 2}}{\omega}\nabla k \nabla\omega; 10^{-}20\right]$$

where $CD_{k\omega}$ stands for cross-diffusion in the $k-\omega$ model. The constants are

$$a_1 = 0.31, \quad \beta^* = 0.09, \quad \kappa = 0.41 \tag{B.20}$$

The model coefficients β, γ, σ_k, and σ_ω denoted with the symbol ϕ are defined by blending the coefficients of the original $k-\omega$ model, denoted as ϕ_1, with those of the transformed $k-\epsilon$ model, denoted ϕ_2.

$$\phi = F_1\phi_1 + (1 - F_1)\phi_2,$$

where

$$\phi = [\sigma_k, \sigma_\omega, \beta, \gamma] \tag{B.21}$$

with the coefficients of the original models defined as

- Inner model coefficients

$$\sigma_{k1} = 0.85, \quad \sigma_{\omega 1} = 0.5, \quad \beta_1 = 0.075,$$

$$\gamma_1 = \beta_1/\beta^* - \sigma_{\omega 1}\kappa^2/\sqrt{\beta^*} = 0.553 \tag{B.22}$$

- Outer model coefficients

$$\sigma_{k2} = 1.0, \quad \sigma_{\omega 2} = 0.856, \quad \beta_2 = 0.0828,$$

$$\gamma_2 = \beta_2/\beta^* - \sigma_{\omega 2}\kappa^2/\sqrt{\beta^*} = 0.440 \tag{B.23}$$

Bibliography

[1] Moin and Kim. "Tackling turbulence with supercomputing". *Scientific American*, January 1997.

[2] Jobe, C. E. "Vortex breakdown location over 65^o delta wings empiricism and experiment". *AIAA-98-2526*, 1998.

[3] Hoeijmakers, H. W. M. "Modeling and numerical simulation of vortex flow in aerodynamics". *AGARD-CP-494 Vortex Flow Aerodynamics*, 1, October 1990.

[4] Hummel, D. "On the vortex formation over a slender wing at large incidence". *AGARD CP-247, Paper 15*, 1979.

[5] Mitchell, A. M. "Caractérisation et contrôle de l'éclatement tourbillonnaire sure une aile delta aux hautes incidences". *Thèse de doctorat de l'Université Paris 6*, 2000.

[6] Lowson, M. V. "Visualisation measurements of vortex flows". *J. Aircraft*, 28(5):320–327, 1991.

[7] Parker, A. G. "Aerodynamic characteristics of slender wings with sharp leading edges". *J. Aircraft*, 13(3):161–168, 1976.

[8] Polhamus, E. "Predictions of vortex-lift characteristics by a leading-edge suction analogy". *J. Aircraft*, 8(4):193–199, 1971.

[9] Wentz, W.H., and Kohlman, D.L. "Vortex breakdown on slender sharp-edged wings". *J. Aircraft*, 8(3), March 1971.

[10] Hemsch, M.J., and Luckring, J.M. "Connection between leading-edge sweep, vortex lift, and vortex strength for delta wings". *J. Aircraft, Engineering Notes*, 27(5), May 1990.

[11] Leibovich, S. "Vortex stability and breakdown: Survey and Extension". *AIAA Journal*, 22(9):1192–1206, December 1984.

[12] Visser, K. D. and Nelson, R. C. "Measurements of circulation and vorticity in the leading-edge vortex of a delta wing". *AIAA Journal*, 31(1):104–111, January 1993.

[13] Johari, H. and Moreira, J. "Direct measurement of delta-wing vortex circulation". *AIAA Journal*, 36(12):2195–2203, December 1998.

[14] Cornelius, K. C. "Analysis of vortex bursting utilizing three-dimensional laser measurements". *J. Aircraft*, 32(2):297–306, March-April 1995.

[15] Honkan, A. and Andreopoulous, J. "Instantaneous three-dimensional vorticity measurements in vortical flow over a delta wing". *AIAA Journal*, 35(10):1612–1620, October 1997.

[16] Erickson, G.E. "Vortex Flow Correlation". *Tech. Rept. AFWAL-TR-80-3143*, 1980.

[17] Payne, F.E. "The structure of leading edge vortex flows including vortex breakdown". *Ph.D. Dissertation, Univ. of Notre Dame, Notre Dame, IN*, 1987.

[18] Earnshaw, P.B. "An experimental investigation of the structure of a leading-edge vortex". *R.A.E. Tech. Note No. Aero. 2740*, March 1961.

[19] Hall, M. G. "A theory for the core of a leading edge vortex". *Journal of Fluid Mechanics*, 11:209–288, 1961.

[20] Parker, A. G. "Measurements on a delta wing in unsteady flow". *J. Aircraft*, 14(6):547–552, June 1977.

[21] Jupp, M. L., Coton, F. N., and Green, R. B. "A statistical analysis of the surface pressure distribution on a delta wing". *The Aeronautical Journal*, 103:349–357, July 1999.

[22] Green, R. B. "A flow visualisation study of a pitching delta wing". *G.U. Aero. Report 9824, University of Glasgow, Glasgow, UK*, 1998.

[23] Gad-el-Hak, M. and Blackwelder, R. F. "The discrete vortices from a delta wing". *AIAA Journal*, 23(6):961–962, June 1985.

[24] Payne, F. M., Ng, T. T., and Nelson, R. C. "Visualization and wake surveys of vortical flow over a delta wing". *AIAA Journal*, 26(2):137–143, February 1988.

[25] Gad-el-Hak, M. and Blackwelder, R. F. "Control of the discrete vortices from a delta wing". *AIAA Journal*, 25(8):1042–1049, August 1987.

[26] Gordnier, R. E., and Visbal, M. R. "Unsteady vortex structure over a delta wing". *J. Aircraft*, 31(1):243–248, Jan-Feb 1994.

[27] Morton, S., Forsythe, J., Mitchell, A., and Hajek, D. "DES and RANS simulations of delta wing vortical flows". *AIAA 2002-0587*, January 2002.

[28] Mitchell, A. M., Morton, S. A., and Forsythe, J. R. "Analysis of delta wing vortical substructures using detached eddy-simulation". *AIAA 2002-2968*, June 2002.

[29] Werlé, H. "Quelques résultats expérimentaux sur les ailes en flèche, aux faibles vitesses, obtenus en tunnel hydrodynamique". *La Recherche Aéronautique*, 41, Sept.-Oct. 1954.

[30] Peckham, D. H. and Atkinson, S. A. "Preliminary results of low speed wind tunnel tests on a gothic wing of aspect ratio 1.0". *Aeronautical Research Council, TR C.P. 508, London*, April 1957.

[31] Peckham, D. H. "Low speed wind tunnel tests on a series of uncambered slender pointed wings with sharp edges". *A.R.C., R. & M. No. 3186*, December 1958.

[32] Elle, B. J. "An investigation at low speed of the flow near the apex of thin delta wings with sharp leading edges". *A.R.C., R.& M. No.3176*, 1958.

[33] Lambourne, N. C., and Bryer, D. W. "The bursting of leading-edge vortices - some observations and discussion of the phenomenon". *R. & M. 3282, Aeronautical Research Council, UK*, April 1961.

[34] Sarpkaya, T. "On stationary and travelling vortex breakdowns". *J. Fluid Mech.*, 45(3):545–559, 1971.

[35] Payne, F. M., Ng, T. T., and Nelson, R. C. "Experimental study of the velocity field on a delta wing". *AIAA-87-1231*, 1987.

[36] Lowson, M.V. "Some experiments with vortex breakdown". *J. of the Royal Aero. Soc.*, 68, Technical Notes, May 1964.

[37] LeMay, S.P., Batill, S.M., and Nelson, R.C. "Vortex dynamics on a pitching delta wing". *J. Aircraft*, 27(2), February 1990.

[38] Thompson, S. A., Batill, S. M., and Nelson, R. C. "Separated flowfield on a slender wing undergoing transient pitching motions". *J. Aircraft*, 28(8):489–495, August 1991.

[39] Visbal, M. R. "Computational and physical aspects of vortex breakdown on delta wings". *AIAA 95-0585*, January 1995.

[40] Wentz, W.H. "Wind tunnel investigation of vortex breakdown on slender sharp-edged wings". *PhD Thesis, University of Kansas*, 1969.

[41] Huang, X. Z., and Hanff, E. S. "Unsteady behaviour of spiral leading-edge vortex breakdown". *AIAA-96-3408*, 1996.

[42] O'Neil, P. J., Roos, F. W., Kegelman, J. T., Barnett, R. M., and Hawk, J. D. "Investigation of flow characteristics of a developed vortex". *McDonnell Aircraft Company, P.O. Box 516, St. Louis, MO 63166*, NADC-89114-60, 23 May 1989.

[43] Gursul, I. "Criteria for location of vortex breakdown over delta wings". *Aeronautical Journal*, pages 194–196, May 1995.

[44] Greenwell, D. I. and Wood, N. J. "Determination of vortex burst location on delta wings from surface pressure measurements". *AIAA Journal*, 30(11):2736–2739, November 1992.

[45] Robinson, B. A., Barnett, R. M., and Agrawal, S. "Simple numerical criterion for vortex breakdown". *AIAA Journal*, 32(1):116–122, January 1994.

[46] Hall, M. G. "Vortex Breakdown". *Annual Review of Fluid Mechanics*, 4:1192–1206, 1972.

[47] Escuudier, M. "Vortex breakdown: Observations and explanations". *Progress in Aerospace Sciences*, 25:189–229, 1988.

[48] Delery, J. M. "Aspects of vortex breakdown". *Prog. Aerospace Sci.*, 30:1–59, 1994.

[49] Hawk, J. D., Barnett, R. M., and O'Neil, P. J. "Investigation of high angle of attack vortical flow over delta wings". *AIAA-90-0101*, January 1990.

[50] Hall, M. G. "A new approach to vortex breakdown". *proceedings of the 1967 Heat Transfer and Fluid Mechanics Institute, Univ. of California, San Diego, La Jolla, California*, 319-349, 1967.

[51] Sarpkaya, T. "Effect of adverse pressure gradient on vortex breakdown". *AIAA Journal*, 12(5):602–607, May 1974.

[52] Ludweig, H. "Zur Erklärung der Instabilität der über angestellten Deltaflügeln auftretenden freien Wirbelkerne". *Z. Flugwiss*, 10(6):242–249, 1962.

[53] Squire, H. B. "Analysis of the vortex breakdown phenomenon". *Miszellaneen der Angewandten Mechanik, Berlin, Akademie-Verlag*, pages 306–312, 1960.

[54] Benjamin, T. B. "Theory of the vortex breakdown phenomenon". *Journal of Fluid Mechanics*, 14:593–629, 1962.

[55] Leibovich, S. "Waves in parallel or swirling stratified shear flows". *Journal of Fluid Mechanics*, 93:401–412, 1979.

[56] Gursul, I. "A proposed mechanism for the time lag of vortex breakdown location in unsteady flows". *AIAA 2000-0787*, January 2000.

[57] Brown, G. L. and Lopez, J. M. "Axisymmetric vortex breakdown Part II: Physical mechanisms". *Aeronautical Research Laboratories, PO Box 4331, Melbourne Vic., 3001, Austrailia. A. R. L. Aero Rep.*, AR-0004-572(173), 1988.

[58] Nelson, R. C. and Visser, K. D. "Breaking down the delta wing vortex ". *AGARD-CP-494 Vortex flow aerodynamics*, 21, 1990.

[59] Lin, J.-C. and Rockwell, D. "Transient structure of vortex breakdown on a delta wing". *AIAA Journal*, 33(1):6–12, January 1995.

[60] Darmofal, D. L. "The role of vorticity dynamics in vortex breakdown". *AIAA-93-3036*, July 1993.

[61] Gursul, I. "Unsteady flow phenomena over delta wings at high angle of attack". *AIAA Journal*, 32(2):225–231, February 1994.

[62] Mabey, D. G. "Similitude relations for buffet and wing rock on delta wings". *Prog. Aerospace Sci.*, 33:481–511, 1997.

[63] Ashley, H., Katz, J., Jarrah, M. A., and Vaneck, T. "Survey of research on unsteady aerodynamic loading of delta wings". *Journal of Fluids and Structures*, 5:363–390, 1991.

[64] Gad-el-Hak, M. and Ho, C-M. "The pitching delta wing". *AIAA Journal*, 23(11):1660–1665, November 1985.

[65] Gursul, I., and Wensheng, X. "Interaction of vortex breakdown with an oscillating fin". *AIAA Journal*, 39(3):438–446, March 2001.

[66] Miau, J. J., Chang, R. C., Chou, J. H., and Lin, C. K. "Nonuniform motion of leading-edge vortex breakdown on ramp pitching delta wings". *AIAA Journal*, 30(7):1691–1702, July 1992.

[67] Rediniotis, O. K., Klute, S. M., Hoang, N. T., and Telionis, D. P. "Pitching-up motions of delta wings". *AIAA Journal*, 32(5):716–725, 1994.

[68] Visbal, M. R. "Crossflow topology of vortical flows". *AIAA Journal Technical Notes*, 32(5):1085–1087, 1993.

[69] Cipolla, K. M. and Rockwell, D. "Instantaneous crossflow topology on a delta wing in presence of vortex breakdown". *J. Aircraft*, 35(2):218–223, March-April 1998.

[70] Visbal, M. R. "Onset of vortex breakdown above a pitching delta wing". *AIAA Journal*, 32(8):1568–1575, August 1994.

[71] Visbal, M. R., and Gordnier, R. E. "Pitch rate and pitch-axis location effects on vortex breakdown onset". *J. Aircraft*, 32(5):929–935, September-October 1995.

[72] Coton, F. N., Jupp, M. L., and Green, R. B. "Analysis of unsteady pressure signals on a pitching delta wing". *AIAA Journal*, 39(9), September 2001.

[73] Lee, M., and Ho, C-M. "Lift force of delta wings". *Applied Mech Rev*, 43(9):209–221, September 1990.

[74] Hummel, D., and Srinivasan, P. S. "Vortex breakdown effects on the low-speed aerodynamic characteristics of slender delta wings in symmetrical flow". *Journal of the Royal Aeronautical Society*, 71, Technical Notes:319–322, 1967.

[75] Earnshaw, P.B., and Lawford, J.A. "Low-speed wind tunnel experiments on a series of sharp-edged delta wings". *A.R.C., R. & M., No. 3424*, March 1964.

[76] Jarrah, M. A. "Unsteady aerodynamics of delta wings performing maneuvres to high angle of attack". *Ph.D. Dissertation, Stanford University, Stanford, CA*, 1988.

[77] Soltani, M. R., Bragg, M. B., and Brandon, J. M. "Measurements on an oscillating 70-deg delta wing in subsonic flow". *J. Aircraft*, 27(3):211–217, March 1990.

[78] Thompson, S. A., Batill, S. M., and Nelson, R. C. "Delta wing surface pressures for high angle of attack maneuvres". *AIAA-90-2813*, August 1990.

[79] Anderson, J. D., Jr. *"Fundamentals of Aerodynamics Second Edition"*. Aerospace Science Series. McGraw-Hill International Editions, 1991.

[80] Dubuc, L., Cantariti, F., Woodgate, M., Gribben, B., Badcock, K. J., and Richards, B. E. "A grid deformation technique for unsteady flow computations". *International Journal for Numerical Methods in Fluids*, 32:285–311, 2000.

[81] K.J.Badcock, M.Woodgate, K.Stevenson, B.E.Richards, M.Allan, G.S.L.Goura, and R.Menzies. Aerodynamics studies on a Beowulf cluster. In P. Wilders et al., editor, *Parallel Computational Fluid Dynamics Practices and Theory*, pages 39–46, May 2002.

[82] Garner, H. C., and Rogers, E. W. E. "Subsonic wind tunnel wall corrections". *AGARDograph 109*, 1966.

[83] Karou, A. "Separated vortex flow over slender wings between side walls - theoretical and experimental investigation". *Report LR-300, Dept. of Aerospace Engineering, Delft University of Technology*, 1980.

[84] Engineering Sciences Data Unit. "Blockage corrections for bluff bodies in confined flows". *Item 80024, London*, 1980.

[85] Frink, N. T. "Computational study of wind-tunnel wall effects on the flow field around delta wings". *NASA Report 87-2420*, 1987.

[86] Thomas, J. P., and Lan, C. E. "The simulation and correction of wind tunnel wall interference on delta wing lift using Navier-Stokes and Euler solutions". *AIAA-91-3300-CP*, 1991.

[87] Hsing, C-C. A., and Lan, C. E. "Low-speed wall interference assessment / correction with vortex flow effect". *J of Aircraft*, 34(2), March - April 1997.

[88] Weinberg, Z. "Effect of tunnel walls on vortex breakdown location over delta wings". *AIAA Journal*, 30(6), June 1992.

[89] Thompson, S. A., and Nelson, R. C. "Wind tunnel blockage effects on slender wings undergoing large amplitude motions". *AIAA-92-3926*, July 1992.

[90] Pelletier, A., and Nelson, R. C. "Factors influencing vortex breakdown over 70^o delta wings". *AIAA-95-3469-CP*, 1995.

[91] Lowson, M. V., and Riley, A. J. "Vortex breakdown control by delta wing geometry". *J. Aircraft*, 32(4):832–838, 1995.

[92] Verhaagen, N. G., Houtman, E. M., and Verhelst, J. M. "A study of wall effect on the flow over a delta wing". *AIAA-96-2389*, 1996.

[93] Strohmeyer, D., Orlowski, M., Longo, J. M. A., Hummel, D., and Bergmann, A. "An analysis of vortex breakdown predicted by the Euler equations". *ICAS-96-1.6.3*, 1996.

[94] Ceresola, N. "WEAG-TA15 Common Exercise IV - Time accurate Euler calculations of vortical flow on a delta wing in pitching motion - Final report". *Alenia Aeronautica Report, Doc. n. 65/RT/T302/98182*, 24/08/1998.

[95] Arthur, M. T., Brandsma, F., Ceresola, N., and Kordulla, W. "Time accurate Euler calculations of vortical flow on a delta wing in pitching motion". *AIAA-99-3110*, 1999.

[96] Fritz, W. "WEAG TA15 Common Exercise V - Numerical and experimental investigation of a delta wing in rolling motion". *DASA Report Dasa/S/STY/1820*, 2000.

[97] Woodgate, M., Badcock, K., Richards, B. "Time accurate Euler calculations of vortical flow on a delta wing in rolling motion". *European Congress on Computational Methods in Applied Sciences and Engineering (ECCOMAS 2000)*, September 2000.

[98] Görtz, S., and Rizzi, A. "Computing the high-alpha aerodynamics of delta wings - evaluation and analysis". *AIAA-01-0115*, January 2001.

[99] Le Moigne, Y., Rizzi, A., and Johansson, P. "CFD simulations of a delta wing in high-alpha pitch oscillations". *AIAA-01-0862*, January 2001.

[100] Liepmann, H. W., and Roshko, A. "Elements of Gasdynamics". *John Wiley and Sons, New York*, 1957.

[101] Rizzi, A. "Damped Euler-equation method to compute transonic flow around wing-body combinations". *AIAA Journal*, 20(10), October 1982.

[102] Hitzel, S. M. and Schmidt, W. "Slender wings with leading-edge vortex separation: A challenge for panel methods and Euler solvers". *J. Aircraft*, 21(10), October 1984.

[103] Sod, G. A. *"Numerical methods in fluid dynamics'"*. Cambridge University Press, 1985.

[104] Newsome, R. W. "Euler and Navier-Stokes solutions for flow over a conical delta wing". *AIAA Journal*, 24(4), April 1986.

[105] Hirschel, E. H. and Rizzi, A. "The mechanism of vorticity creation in Euler solutions for lifting wings". *Proceedings of symposium on International Vortex Flow Experiment on Euler Code Validation, ISBN 91-97 0914-0-5*, 1-3 October, 1986.

[106] Eberle, A., Rizzi, A., and Hirschel, E. H. "Numerical solutions of the Euler equations for steady flow problems". *Notes on Numerical Fluid Mechanics*, 34, 1992.

[107] Löser, T. "Dynamic force and pressure measurements on an oscillating delta wing at low speeds". *Report IB 129-96/9 DLR Braunschweig*, 1997.

[108] Smith, M. J., and Huttsell, L. J. "Computational evaluation of semispan straked delta wing flowfields conducive to LCO". *AIAA-99-1212*, 1999.

[109] Visbal, M. R., and Gordnier, R. E. "Compressibility effects on vortex breakdown onset above a 75-degree sweep delta wing". *J. Aircraft*, 32(5):936–942, September-October 1995.

[110] Bradshaw, P. "An introduction to turbulence and its measurement". *Pergamon Press*, 1971.

[111] Baldwin, B. S. and Lomax, H. "Thin-layer approximation and algebraic model for separated turbulent flows". *AIAA Paper 78-257*, 1978.

[112] Wilcox, D. C. "Turbulence modelling for CFD". *DCW Industries, Inc., La Cañada, California*, 1993.

[113] Spalart, P. R., Jou, W-H., Strelets, M., and Allmaras, S. R. "Comments on the feasibility of LES for wings, and on a hybrid RANS/LES approach". *Advances in DNS/LES, 1st AFOSR Int. Conf. on DNS/LES*, Aug 4-8, 1997, Greyden Press, Columbus Oh.

[114] Ekaterinaris, J. A., and Schiff, L. B. "Numerical prediction of vortical flow over slender delta wings". *J. Aircraft*, 30(6):935–942, Nov-Dec 1993.

[115] Gordnier, R. E. "Computation of delta-wing roll manuevers". *J of Aircraft*, 32(3), May-June 1995.

[116] Gordnier, R. E. "Numerical simulation of a 65 Deg sweep delta-wing flowfield for static roll angles". *AIAA 95-0082*, January 1995.

[117] Gordnier, R. E. "Numerical simulation of a 65-Degree delta wing flowfield". *J. Aircraft*, 34(4), July-August 1997.

[118] Degani, D. and Schiff, L. B. "Computation of turbulent supersonic flows around pointed bodies having crossflow separation". *Journal of Computational Physics*, 66(1), September 1986.

[119] Agrawal, S., Barnett, R. M., and Robinson, B. A. "Investigation of vortex breakdown on a delta wing using Euler and Navier-Stokes equations". *AGARD-CP-494 Vortex Flow Aerodynamics*, October 1990.

[120] Agrawal, S., Barnett, R. M., and Robinson, B. A. "Numerical investigation of vortex breakdown on a delta wing". *AIAA Journal*, 30(3), March 1992.

[121] Chaderjian, N. M. and Schiff, L. B. "Navier-Stokes predictions of delta wings in roll with vortex breakdown". *AIAA-93-3495-CP*, August 1993.

[122] Ektanerinaris, J. A., and Schiff, L. B. "Navier-Stokes solutions for an oscillating double-delta wing". *J. Aircraft*, 32(2):228–234, March-April 1995.

[123] Chaderjian, N. M., and Schiff, L. B. "Numerical simulation of forced and free-to-roll delta wing motions". *J. Aircraft*, 33(1):93–99, January-February 1996.

[124] Görtz, S. and Rizzi, A. "Computational study of vortex breakdown over swept delta wings". *AIAA-99-3118*, 1999.

[125] Gordnier, R. E. "Computational study of a turbulent delta-wing flowfield using two-equation turbulence models". *AIAA 96-2076*, 1996.

[126] Menter, F. R. "Zonal two equation k-ω turbulence models for aerodynamic flows". *AIAA-93-2906*, July 1993.

[127] Dacles-Mariani, J., Zilliac, G. G., Chow, J. S., and Bradshaw, P. "Numerical / experimental study of a wingtip vortex in the near field". *AIAA Journal*, 33(9):1561–1568, September 1995.

[128] Brandsma, F. J. "WEAG THALES JP12.15 Proposal for Common Exercise I (CEI)". *NLR-Memorandum AT-2001-005*, 2001.

[129] Brandsma, F. J., Kok, J. C., Dol, H. S., and Elsenaar, A. "Leading edge vortex flow computations and comparison with DNW-HST wind tunnel data". *RTO / AVT Vortex Flow Symposium, Loen, Norway*, 2001.

[130] Mitchell, A. M., Molton, P., Barberis, D., and Delery, J. "Characterization of vortex breakdown by flow field and surface measurements". *AIAA-2000-0788*, 2000.

[131] Molton, P. "Etude expérimentale de l'éclatement tourbillonnaire sur aile delta en écoulement incompressible. Caractérisation du champ externe". *ONERA Rapport Technique No53/1147AN*, 1992.

[132] Visser, K. D. and Washburn, A. E. "Transition behaviour on flat plate delta wings". *AIAA-94-1850*, 1994.

[133] Mitchell, A., Molton, P., Barberis, D., and Délery, J. "Control of vortex breakdown location by symmetric and asymmetric blowing". *AIAA 99-3652*, June 1999.

[134] Morton, S. *Presented at RTO AVT-080 Meeting in Aalborg, Denmark, 26-27 September 2002. Results to appear in RTO publication of AVT-080 Task Group*, 2003.

[135] Ericsson, L. E., and Reding, J. P. "Dynamic support interference in high-alpha testing". *J. Aircraft*, 23(12):889–896, December 1986.

[136] Ericsson, L. E. "Another look at high-alpha support interference in rotary tests". *J. Aircraft*, 28(9):584–591, September 1991.

[137] Beyers, M. E. "Unsteady wind-tunnel interference in aircraft dynamic experiments". *J. Aircraft*, 29(6):1122–1129, Nov.-Dec. 1992.

[138] Beyers, M. E., and Ericsson, L. E. "Ground facility interference on aircraft configurations with separated flow". *J. Aircraft*, 30(5):682–688, Sept.-Oct. 1993.

[139] Taylor, G., Gursul, I., and Greenwell, D. "Static hysteresis of vortex breakdown due to support interference". *AIAA 2001-2452*, 2001.

[140] Hummel, D. "Untersuchungen über das Aufplatzen der Wirbel an schlanken Delta Flügeln". *Zeitschrift für Flugwissenschaften*, 13(5):158–168, 1965.

[141] Straka, W. A. "Effect of fuselage on delta wing vortex breakdown". *J. Aircraft*, 31(4):1002–1005, 1994.

[142] Ericsson, L.E. "Effect of fuselage geometry on delta-wing vortex breakdown". *J. Aircraft*, 35(6), November-December 1998.

[143] Ericsson, L. E. "Further analysis of fuselage effects on delta wing aerodynamics". *AIAA 2000-0891*, January 2000.

[144] Taylor, G., Gursul, I., and Greenwell, D. I. "An investigation of support interference in high angle of attack testing". *To appear in AIAA conference proceedings, RENO NV, USA*, January 2003.

[145] Anderson, J. D., Jr. *"Computational Fluid Dynamics - The basics with applications"*. Mechanical Engineering Series. McGraw-Hill International Editions, 1995.

[146] Anderson, D. A., Tannehill, J. C., and Pletcher, R. H. *"Computational fluid mechanics and heat transfer"*. Series in Computational Methods in Mechanics and Thermal Sciences. Hemisphere, New York, 1984.

[147] Osher, S. and Chakravarthy, S. "Upwind schemes and boundary conditions with applications to Euler equations in general geometries". *Journal of Computational Physics*, 50:447–481, 1983.

[148] Badcock, K., Xu, X., Dubuc, L., and Richards, B. *"Preconditioners for high speed flows in aerospace engineering"*, volume 5, pages 287–294. Institute for Computational Fluid Dynamics, Oxford, U.K., 1996.

[149] Axelsson, O. *"Iterative Solution Methods"*. Cambridge University Press, 1994.

[150] Cantariti, F., Dubuc, L., Gribben, B., Woodgate, M., Badcock, K., and Richards, B. "Approximate Jacobians for the solution of the Euler and Navier-Stokes equations". Technical Report 5, Aerospace Engineering Report, University of Glasgow, Glasgow, UK, 1997.

[151] Jameson, A. "Time dependent calculations using multigrid, with applications to unsteady flows past airfoils and wings". *AIAA Paper*, 91-1596, 1991.

[152] Spalart, P. R. and Allmaras, S. R. "A one-equation turbulence model for aerodynamic flows". *AIAA Paper*, 92-0439, 1992.

[153] Menter, F. R. "Zonal two equation kappa-omega turbulence models for aerodynamic flows". *AIAA Paper*, 93-2906, 1993.